The Effect of Particle Size and Shape on Transport through Confined Channels in three-phase Froths

Tarun Bhambhani

Submitted in partial fulfillment of the requirements

for the degree of Doctor of Engineering Science

in the Fu Foundation School of Engineering and Applied Science

COLUMBIA UNIVERSITY

2019

ABSTRACT

The Effect of Particle Size and Shape on Transport through Confined Channels in three-phase Froths

Tarun Bhambhani

Multiphase systems (containing solid, liquid and gas) are increasingly common in a number of industries, with the most complex manifestation being three-phase froth. The interstitial suspension has to navigate tortuous channels and its transport is affected by drag, capillary and gravitational forces. Particle properties such as wettability, size, shape, and morphology results in a number of different types of interactions with the liquid-air interface and can have a significant effect on froth composition and stability. The effect of particle size and shape on its transport through these confined channels is thus of great interest for a number of industrial applications and is the focus of this work. This transport behavior is studied using a three phase transient froth that is produced in the froth flotation process for mineral separation. In this system, hydrophilic non-value particles present in the interstitial liquid phase do not attach to air bubbles, and their removal is desirable. The original hypothesis was that as particles become more anisotropic in shape, there is an increase in the froth interstitial viscosity, which results in reduced drainage rate of particles through the froth. Flotation experiments, froth sampling experiments, and rheological experiments were conducted to test this hypothesis.

Froth zone sampling experiments were conducted using mixtures of sized platy mica, needle-like wollastonite, and fibrous chrysotile, all mixed with low aspect ratio silica in varying amounts. The froth zone suspension compositions were then used to prepare the froth interstitial suspension ex-situ, and bulk rheological measurements were conducted on the suspensions. The

data showed that while the relative viscosities of the suspensions were much higher at even low concentrations of the fibrous ore in the mixture, there was no significant difference when mica was substituted for silica in the mixture at high concentrations (~50 wt%) at the solids volume fraction of interest (~7.5%). The bulk rheological measurements thus could not fully account for the difference in transport behavior between mica and silica. Flotation experiments were conducted with a copper mineral-containing ore augmented with additional hydrophilic minerals mica, silica (low aspect ratio), wollastonite or chrysotile. The results suggest increasing aspect ratios of the added non-value particles result in increased net transport (transport accounting for loss due to drainage) through the froth zone; mica transport is faster than silica. Froth zone sampling experiments (using pure mixtures of above minerals) confirmed that mica net transport was greater than that of silica. It was then hypothesized that this increase was due to increased drag experienced by high aspect ratio mica compared to low aspect ratio silica. The doped ore flotation data also suggested a decrease in transport as size of added platy mica increased until a local transport minimum was reached, beyond which another increase in transport was observed. It was further hypothesized that this was related to confinement of coarse mica particles in the plateau borders when the size of the constriction was comparable to particle size.

Froth sampling experiments under high drag (upward flow dominated) conditions were compared with those under conditions where drag and drainage were more balanced (steady state froths). Under high drag conditions, mica mixtures showed more hydrophilic mineral mass in the froth zone compared to silica mixtures. Under drag and drainage-balanced conditions when the size of mica approached the size of the measured channel size, platy mica was found to be accumulating in the froth. This was not the case for silica particles with settling being more efficient for silica than for mica. The key parameters driving transport of particles through the froth are the bulk rheology of the interstitial suspension (driven by particle size and shape distributions and solids concentration), the size of constrictions in the plateau borders and vertices and the resulting confinement effects, and the mobility or elasticity of the interfaces (driven largely by the hydrophobic particles attached at the interface).

TABLE OF CONTENTS

List of Figures....viii

List of Tables....xxiv

1 Introduction 1

1.1 Multiphase systems and Froths 1

1.2 Froth Flotation for minerals separation 2

1.2.1 The Froth phase in flotation 4

1.3 Motivation and Hypothesis development 6

1.4 Hypotheses 7

1.5 Experimental map 8

1.6 Original Methods and Contributions to the knowledge 9

1.7 Chapter Outlines 11

2 Literature review 14

2.1 Outline 14

2.2 The mining industry and copper 14

2.3 Copper production process 15

2.4 Froth Flotation 17

2.5 Froth Zone in flotation 19

2.5.1 Liquid drainage 21

2.5.2 Bubble coalescence 22
2.5.3 Detachment of hydrophobic particles 22
2.5.4 Suspension drainage and solids removal. 23
2.5.5 Froth Recovery 24
2.5.6 Froth stabilization by particles 24
2.6 Entrainment 25
2.6.1 Entrainment and water recovery 27
2.6.2 Effect of solids density in pulp 30
2.6.3 Effect of particle size 30
2.6.4 Effect of shape and viscosity 32
2.6.5 Other important factors 32
2.6.6 Methods to measure Entrainment 34
2.6.7 Modeling Entrainment 35
2.7 Entrapment 39
2.8 “Equilibrium/steady state” froths vs flotation froths 41
2.9 Drainage of cellular foams 42
2.10 Rheology 46
2.10.1 Measuring rheological properties 50
2.10.2 Effect of particle shape on suspension rheology 52
2.10.3 Rheology of foams and froths 55

2.11 Non-sulfide gangue minerals in flotation 58
  2.11.1 Mineralogy of phyllosilicates 59
  2.11.2 Morphology of the minerals 62
2.12 Hydrophilic phyllosilicates and related problems in flotation 64
  2.12.1 Heterocoagulation or “slime coating” 64
  2.12.2 Modification of slurry rheological properties 65
  2.12.3 Effect of phyllosilicates on entrainment 68
2.13 Gaps in knowledge 71
2.14 Hypothesis statements and experimental plan 73
3 Materials and Methods 78
3.1 Materials- Mineral samples Preparation 78
  3.1.1 High purity muscovite unground 78
  3.1.2 Ground muscovite 78
  3.1.3 Microscopy images 81
  3.1.4 Mica-rich ore sample 83
  3.1.5 Silica 84
  3.1.6 Chalcopyrite 85
  3.1.7 Wollastonite 85
  3.1.8 Fibrous ore 86
3.2 Methods 86

3.2.1 Flotation tests for mixtures of mica-rich Cu ore with mica-free Cu ore................ 86

3.2.2 Flotation tests with high purity mica mixed with base Cu ore and ground together 88

3.2.3 Flotation tests for mica/silica addition of various sizes... 89

3.2.4 Flotation test procedure... 90

3.3 Design of froth sampler... 92

3.3.1 Cell and Housing... 92

3.3.2 Design of sampling device... 92

3.3.3 Operation... 94

3.4 Froth Sampling experiments... 95

3.4.1 Protocol to ensure froth sampler is not leaking... 95

3.4.2 Procedure to test froth sampler for leaks... 95

3.4.3 Running a froth sampling experiment... 96

3.5 Analysis of samples... 99

3.5.1 XRF calibration procedure... 99

3.6 Interpretation of froth sampling data... 100

3.7 Rheology measurements... 101

3.7.1 Developing a protocol for measurement... 101

3.7.2 Selecting of geometry for rheological measurements.. 104

3.7.3 Identifying shear rate range for measurements and geometry selection.............. 106

3.7.4 Reproducibility between samples ... 108

3.7.5 Final protocol for measurements ... 109

4 Results from flotation tests ... 111

4.1 Mica and silica of various sizes added to flotation cell ... 111

4.2 Degree of entrainment ... 116

4.3 Flotation tests on Fibrous ore (containing approximately 1% of fibrous chrysotile) ... 120

4.4 Summary ... 122

4.5 Additional flotation tests ... 124

5 Results from Froth sampling tests ... 126

5.1 Outline ... 126

5.2 Experimental plan for froth sampling ... 126

5.3 Reproducibility of results ... 128

5.3.1 Solids mass, water content and solids density in “nascent” sampling tests for fine silica only ... 129

5.3.2 Effect of mica addition ... 130

5.4 Mica vs silica transported ... 134

5.5 Mica vs silica in the presence of hydrophobic solids ... 135

5.6 Sampling of Steady state froths ... 137

5.7 Fibrous ore mixture tests ... 141

5.8 Behavior of fibrous minerals in nascent sampling vs steady state sampling ... 144

5.9 Effect of silica size in a mixture with fibrous ore 146

5.10 Summary 149

5.11 Additional froth sampling experiments- smaller data sets 151

5.11.1 Nascent froth sampling with mixtures of comparably sized fine mica with fine silica 151

5.11.2 Addition of wide PSD mica in the absence of chalcopyrite 152

5.11.3 Nascent froth sampling with mixtures of ultrafine mica with base fine silica...... 153

5.11.4 Nascent froth sampling of wollastonite/fine silica mixtures in the absence of chalcopyrite 155

5.11.5 Nascent froth sampling experiments with fibrous ore in the absence of chalcopyrite 155

6 Rheology Measurements 158

6.1 Rheology measurements as a function of shear rate 158

6.2 Rheology-Volume Fraction relationships 159

6.3 Rheology of mineral mixtures 164

6.4 Summary 172

6.5 Wollastonite behavior 173

7 Discussion 174

7.1 Outline 174

7.2 Effect of mica on flotation response 174

7.3 Effect of mica size on flotation response 175

7.3.1 Nascent froth sampling results 178

7.3.2 Steady-state sampling results 181

7.3.3 Compositions of froth zone 183

7.3.4 Summary 187

7.4 Mechanisms 188

7.4.1 Confirming hypothesis that increased drag is experienced by platy particles 188

7.4.2 Confirmation of confinement effects and hypotheses 188

7.5 Channel dimensions to confirm confinement effects 193

7.6 Using rheological properties as a function of volume fraction as indicators of transport via bubble flux and bubble entrapment for fibrous ores 197

7.7 Summary 200

8 Summary, Conclusions and Recommendations for future work 203

8.1 Recommendations for future work 208

References 210

LIST OF FIGURES

Figure 1.1: The froth flotation Process (adapted from www.911metallurgist.com)...................... 2

Figure 1.3: Illustrating the various zones in flotation: pulp zone, pulp froth interface, and froth zone (Adapted from RP King , 2000) 6

Figure 1.4: Experimental map for thesis, with the red arrows showing the path followed for hypothesis 1. The path for hypothesis 2 is shown with blue arrows. The orange areas indicate additional information.. 9

Figure 2.1:(a) Mineral Processing and (b) the froth flotation Process (adapted from www.911metallurgist.com)... 17

Figure 2.2: Lamellae, plateau borders and vertices in froths. Green particles are hydrophilic, and black are hydrophobic.. 20

Figure 2.3: Sub processes in froth flotation illustrated (Adapted from Leja, 2004).................... 20

Figure 2.4: Plateau borders with hydrophilic and hydrophobic particles (taken from Leja, 2004) 27

Figure 2.5: (a) relative importance of liquid velocity vs settling on the solids motion at difference heights in the froth and for different particle sizes). (b) Solids concentration in the froth, C, relative to pulp solids concentration Cp, as a function of height in the froth for different particle sizes (Taken from Neethling, 2009).. 29

Figure 2.6: Recovery of sized silica by entrainment as a function of water recovery (Adapted from Engelbrecht and Woodburn, 1975) 30

Figure 2.7: Concentrate grade vs water recovery for globular silica gangue minerals (Adapted from Yianatos and Contreras, 2010)... 30

Figure 2.8: Degree of entrainment vs particle size for silica particles (Adapted from Bisshop and White, 1974) 31

Figure 2.9: Ross's (1992) work on determining degree of entrainment using batch flotation tests 35

Figure 2.10: Entrapment, adapted from Konopacka (2010) 40

Figure 2.11: Steady state (left) and flotation (right) froths. In the steady state froth, there is no net liquid transfer, i.e. FR^{Z}_{up} - FR^{z}_{down} = 0 at any level (z) of the froth. In a flotation froth, the net flow upwards at any level is the volumetric flow out into the concentrate, i.e. FR^{Z}_{up} - FR^{z}_{down} = *FR* (Adapted from Smith and Warren, 1989) 42

Figure 2.12: The interstitial network of aqueous foams consists of nodes connected by constrictions. Particles suspended in the interstitial fluid can be either freely transported or trapped by constrictions. This behavior is described by using the so-called confinement parameter, λ, that compares the particle size to the size of passage through those constrictions d_c. 43

Figure 2.13: Reduced viscous drag (inverse of the reduced drainage velocity V˜ = V/V0 where V and V0 are foam drainage velocity (with and without particles) of foamy suspensions (10 g L_1 TTAB in distilled water with 20% w/w glycerol and polystyrene spherical beads with different concentrations) as a function of the confinement parameter λ, with bubble size Db = 660 mm and liquid fraction ε = 0.1 for different particle volume fractions, ϕp. λc and λ* correspond to the end of the flowing suspension regime and to the minimal foam drainage velocity, respectively. b: Diagram of the reduced particle volume fraction as a function of the confinement parameter in the foam network. The jammed state domain is deduced from experiments. The red and black lines correspond to eqn (5) and (6), respectively. Adapted from Haffner et al (2015). 45

Figure 2.14: Stress vs shear rate responses for particulate suspensions (adapted from Farrokhpay 2012) 47

Figure 2.15: Relative viscosity vs volume fraction for semi dilute suspensions 49

Figure 2.16: Rheometer types (adapted from Mewis and Wagner, 2012) 50

Figure 2.17: Basic geometries of axisymmetric particles: (a) prolate spheroid, (b) oblate spheroid, (c) rod or fiber, (d) disk. 53

Figure 2.18: Zero shear relative viscosity of dispersions of non-spherical particles: tobacco mosaic viruses with different aspect ratios (adapted from Lauffer (1944)). 53

Figure 2.19: (a) Random packing packing fractions vs aspect ratios- small aspect ratio oblate spheroids Pa<1- squares, Pa>1- circles, as well as biaxial spheroids (diamonds), after Donev et al (2004), (b) comparison of simulation and experimental data for the maximum packing fraction or sphero-cylinders as a function of aspect ratio (After Williams and Philipse (2003). 54

Figure 2.20: Shear stresses for dispersions of kaolin clay at various volume fractions, lines are fits (adapted from Jogun and Zokuski, 1999) 55

Figure 2.21: Phyllosilicate group classification according to Deer et al (1992) (Adapted from Ndlovu, 2013) 60

Figure 2.24: Increasing yield stress with increasing fibrous mineral content and resulting impact on Cu recovery (Adapted from Patra 2010, 2012) 66

Figure 2.25: Two types of froth sampling experiments- a) drag dominated, and b) drag-drainage balanced 76

Figure 2.26: Experimental map for thesis, with the red arrows showing the path followed for hypothesis 1. The path for hypothesis 2 is shown with blue arrows. The orange areas indicate additional information 77

Figure 3.1: Particle size distributions for sieved fractions of mica obtained using Horiba 79

Figure 3.2: SEM images of sieved mica- (a) +150µ, (b) 100-150m, (c) 75-100µ, (d) 50-75µ, (e) 20-50µ, (f) -20µ 80

Figure 3.3: Aspect ratio distributions of (a) 50-75µ mica and (b) 75-100µ mica samples prepared in propylene glycol 81

Figure 3.4: 75-100µ silica sample showing mostly conchoidal fracture and varying opacity 82

Figure 3.5: 50-75µ mica sample showing transparent, platy morphology readily apparent with thin plates observed.. 82

Figure 3.6: Images showing ore containing fibrous mineral chrysotile. Long strands of intertwined fibers as long as 1mm are observed, along with some bunches that appear "brush-like" and a host of fine particles.. 83

Figure 3.7: Particle size distribution for silica samples used as obtained using a) sieve analysis, b) Horiba 85

Figure 3.8: Wollastonite Particle size distribution obtained from SDS 86

Figure 3.9: Particle size distributions obtained from grind study of Mica-rich ore...................... 87

Figure 3.10: Particle-size distribution for mica rich ore and base ore 88

Figure 3.11: Protocol for mixtures of mica-rich Cu ore with mica-free Cu ore 88

Figure 3.12: Protocol for flotation tests with high purity mica mixed with mica free ore in the grind 89

Figure 3.13: Flotation testing procedure for studying effect of particle size of muscovite (vs silica) on flotation recovery/grade 92

Figure 3.14: Froth sampler design and dimensions 94

Figure 3.15: Images of froth sampler (a) side view, and (b) Angle view 94

Figure 3.16: Vacuum apparatus to collect froth samples into a 50ml centrifuge tube (a) side view showing a conical flask used to catch any excess slurry. (b) top view showing the assembly..... 96

Figure 3.17: XRF calibration curve to quantify muscovite in a mixture of muscovite and silica by XRF.. 100

Figure 3.18: Interpretation of froth sampling data.. 101

Figure 3.19: Continuous rheology measurement (no mixing) of 40% fine silica suspension 102

Figure 3.20: Effect of improved measurement protocol on increasing vs decreasing shear rate measurement; 40 % solids concentration fine silica suspension 103

Figure 3.21: Rheology measurements using averages of 2-5th second of measurements- 40% fine silica suspension.. 104

Figure 3.22: Helical ribbon data with increasing and decreasing shear rate; 40% solids concentration fine silica suspension.. 105

Figure 3.3.23: Vane vs helical ribbon for decreasing and increasing shear rate for geometry selection; 40% solids concentration fine silica suspension... 106

Figure 3.24: Vane vs helical ribbon under laminar flow; 40% solids concentration silica suspension 108

Figure 3.25: Assessing reproducibility between samples- stress vs shear rate; 40% solids concentration... 109

Figure 4.1: Cumulative Cu Recovery-Grade plot for 25% sized mica or silica added to 75% ground ore: (a) 20-50µ addition, (b) 50-75µ addition, (c) 75-100µ addition, and (d) 100-150µ addition. u indicates µ (micron size).. 112

Figure 4.2: Cumulative Cu Recovery-mass recovery plot for 25% sized mica or silica added to 75% ground ore: (a) 20-50μ addition, (b) 50-75μ addition, (c) 75-100μ addition, and (d) 100-150μ addition 113

Figure 4.3: Cumulative Cu Recovery-grade plot for 50% sized mica or silica (by weight) added to 50% (by weight) ore: (a) 20-50μ addition, (b) 50-75μ addition, (c) 75-100μ addition, and (d) 100-150μ addition 114

Figure 4.4: Cumulative Cu Recovery-mass recovery plot for 50% sized mica or silica (by weight) added to 50% (by weight) ore: (a) 20-50μ addition, (b) 50-75μ addition, (c) 75-100μ addition, and (d) 100-150μ addition 115

Figure 4.5: Cumulative mass recovery for addition of 25% and 50% (by weight) sized mica or silica to 75% or 50% ore 116

Figure 4.6: Illustration the calculation for the degree of entrainment- cumulative non-sulfide gangue recovery on the y axis and the cumulative water recovery on the x-axis........ 117

Figure 4.7: Degree of entrainment (ENT) for 25% addition of mica/silica as a function of particle size 118

Figure 4.8: Degree of entrainment (ENT) for 50% addition of mica/silica........ 119

Figure 4.9: Degree of Entrainment for the fourth concentrate (only) as a function of particle size for 25% mica and silica addition (by weight) mixed with 75% (by weight) ground ore. 120

Figure 4.10: Degree of Entrainment for the fourth concentrate (only) as a function of particle size for 50% mica and silica addition (by weight) mixed with 75% (by weight) ground ore. 120

Figure 4.11: Cu Recovery-grade profile for fibrous ore mixed into the Cu ore at 1%, 4% and 7% (by weight) addition rates. 122

Figure 4.12: Cu Recovery vs mass recovery profile for fibrous ore mixed into the base Cu ore at 1%, 4% and 7% addition rates 122

Figure 4.13: ENT values for 75-100μ mica and silica, and 1% and 4% fibrous ore addition to base ore 122

Figure 4.14: Recovery grade profile for mixture of 87.5% base ore and 12.5% either mica or silica of 75-100μ. Data shows poorer concentrate grade for when even low amounts of mica are present in the ore. 124

Figure 4.15: Recovery grade profile for mixture of various ratios of wollastonite and base fine silica. Data shows poorer concentrate grade when wollastonite is present, with the grade declining with increasing amounts of wollastonite. 125

Figure 5.1: Nascent Froth sampling tests- Assessing reproducibility- 50/50 coarse mica/fine silica experiments using two independently prepared samples, 35% solids concentration in pulp. This plot shows solids mass in each layer. 128

Figure 5.2: Comparing nascent and steady state froth sampling- 100% fine silica, 35% solids concentration slurry 129

Figure 5.3: Nascent froth sampling- Solids concentration, solids mass and water mass for fine silica only. Solids concentration in slurry was 35%. 130

Figure 5.4: Nascent Froth sampling tests- Addition of 50% mica or silica of 20-50μ (a), 50-75μ (b), 75-100μ (c), 100-150μ (d) sizes to 50% fine silica. The plot shows total gangue mass (including mica and silica) in each layer. Solids concentration in pulp is 35%, and no chalcopyrite (sulfide value) is added. The total mass of gangue is significantly higher for 75-100μ and 100-150μ mica mixtures as compared to silica mixtures of the same size. 131

Figure 5.5: Nascent Froth sampling tests- Addition of 50% mica and silica of 20-50μ (a), 50-75μ (b), 75-100μ (c), 100-150μ (d) sizes to 50% fine silica base sample. The plot shows total water mass (including mica and silica) in each layer. Solids concentration in pulp is 35%, and no chalcopyrite (sulfide value) is added. The mass of water is significantly higher for all mica mixtures as compared to silica mixtures of the same size. 133

Figure 5.6: Nascent Froth sampling-50% fine silica mixed with 50% sized mica (a) Total gangue mass from figure 5.4 for mica tests combined (b) Mica (%) in layer as a function of particle size. [35% slurry solids concentration] 135

Figure 5.5.7: Nascent Froth sampling tests with 49% fine silica mixed with (a) 49% 20-50μ mica or silica, (b) 49% 50-75μ mica or silica, (c) 75-100μ mica or silica and (d) 100-150μ mica or silica, and 2% Chalcopyrite by weight (0.7% Cu). Solids concentration in pulp was 35%. Total gangue mass as a function of froth height for 49% mica or silica is shown. Data shows gangue mass slightly higher when mica is added compared to silica for nascent sampling for some sizes. 136

Figure 5.5.8: Nascent Froth sampling tests with 74% fine silica mixed with (a) 24% 20-50μ mica or silica, (b) 24% 50-75μ mica or silica, (c) 24% 75-100μ mica or silica and (d) 24% 100-150μ mica or silica, and 2% Chalcopyrite by weight (0.7% Cu). Solids concentration in pulp was 35%. Total gangue mass as a function of froth height is shown. The data shows significant drop in gangue mass as a function of height for 25% addition as compared to 50% addition. This is because the gangue transport is more dominated by the fine silica. 136

Figure 5.9: Nascent froth sampling for 25% mica addition- Mica (%) in fine silica with 2% chalcopyrite in each layer as a function of particle size 137

Figure 5.10: Froth sampling under nascent (N) and steady-state conditions (SS)- 50% fine silica mixed with 50% 50-75µ mica or silica. No chalcopyrite; 35% solids concentration. Data shows a significant decrease in gangue mass upon extending the duration of the froth when silica is mixed in, and a more significant decrease in gangue mass when mica is mixed in. 138

Figure 5.11: Froth sampling under nascent (N) and steady-state conditions (SS)- 50% fine silica mixed with 50% 75-100µ mica or silica. No chalcopyrite; 35% solids concentration. Data shows a decrease in gangue mass upon extending the duration of the froth when silica is mixed in, and almost equivalent gangue mass when mica is mixed in. 138

Figure 5.12: Froth sampling under nascent (N) and steady-state conditions (SS)- 50% fine silica mixed with 50% 100-150µ mica or silica. No chalcopyrite; 35% solids concentration. Data shows a negligible increase in gangue mass upon extending the duration of the froth when silica is mixed in, and a more significant increase in gangue mass when mica is mixed in. 139

Figure 5.13: Froth sampling- nascent, short delay (2 min) and steady state (5 min). Mixture of 50% fine silica and a) 50% 100-150µ mica, b) 50% 50-75 µ mica. Data shows increase in total gangue mass with time for 100-150µ mica addition, and a decrease at 50-75µ mica addition.. 141

Figure 5.14: Nascent froth sampling- Solids concentration (wt. %) with increasing amounts of coarse-ground fibrous ore added to fine silica with 2% chalcopyrite; 35% solids concentration in pulp. 141

Figure 5.15: Nascent froth sampling- Water mass with increasing amounts of coarse-ground fibrous ore added to fine silica with 2% chalcopyrite. 35% solids concentration in pulp. 142

Figure 5.16: Nascent froth sampling- Total gangue mass with increasing amounts of coarse-ground fibrous ore added to fine silica with 2wt% chalcopyrite in pulp; 35% solids concentration in pulp. 142

Figure 5.17: Nascent froth sampling- (a) Chalcopyrite mass in layer, and b) chalcopyrite relative wt% in layer for increasing amounts of coarse-ground fibrous ore added to fine silica with 2% chalcopyrite (w/w); 35% solids concentration in pulp 143

Figure 5.18: Nascent vs steady state sampling (5 minute delay) - 4% and 7% fibrous mineral addition to silica - a) Solids density in each layer, b) Total gangue mass in each layer, and c) chalcopyrite mass in each layer 145

Figure 5.19: Effect of silica size on nascent froth sampling for 4% and 7% fibrous ore addition to fine silica - a) Solids density in each layer, and b) Total gangue mass in each layer; 35% solids concentration in pulp.. 147

Figure 5.20: Effect of fibrous ore size on nascent froth sampling for 4% fibrous ore addition- a) Solids density in each layer, and b) Total gangue mass in each layer 148

Figure 5.21: Effect of fibrous ore size on nascent froth sampling for 4% fibrous ore addition- water mass in each layer 148

Figure 5.22: Nascent froth sampling experiments- fine mica in various ratios mixed with fine silica (comparably sized). Data shows that total gangue mass increases as more fine mica replaces fine silica in the mixture; solids concentration in the pulp is 35%(w/w) 152

Figure 5.23: Nascent froth sampling experiments- addition of fine mica in various ratios mixed with base fine silica. Data shows that ratio of mica to silica in the froth is higher than what is in the pulp, but this only occurs when at least 40% mica is present. 152

Figure 5.24: Nascent froth sampling experiments- addition of wide particle size distribution mica (WPSD) in various ratios mixed with base fine silica. Data shows that total gangue mass decreases as more WPSD mica is added to the mixture. 153

Figure 5.25: Nascent froth sampling experiments- addition of wide particle size distribution (WPSD) mica in various ratios mixed with fine silica. Data shows that ratio of mica to silica in the froth is lower than what is in the pulp, with the difference being larger when more WPSD mica is in pulp; 35% solids concentration in pulp 153

Figure 5.26: Nascent froth sampling experiments- addition of ultrafine mica in various ratios mixed with base fine silica. Data shows that total gangue mass increases as more ultrafine mica is added to the mixture; 35% solids concentration in pulp 154

Figure 5.27: Nascent froth sampling experiments- addition of ultrafine mica in various ratios mixed with base fine silica. Data shows that ratio of mica to silica in the froth is higher than what is in the pulp, with the difference being greater for when more ultrafine mica is present; 35% solids concentration in pulp 155

Figure 5.28: Nascent froth sampling experiments conducted on mixtures of wollastonite obtained from a commercial producer mixed with base fine silica. Data shows that on its own, wollastonite transports significantly less than the base fine mica. This may be because of its size, which is coarser than the base fine silica. 155

Figure 5.29: Nascent froth sampling of mixtures of Fibrous ore at 1%, 4% and 7% respectively mixed with fine silica. Solids concentration was 35% and no chalcopyrite was used. Data shows froth suspension solids concentration approaching the pulp solids concentration. 156

Figure 5.30: Nascent froth sampling on mixtures of Fibrous ore at 1%, 4% and 7% respectively mixed with fine silica. Solids concentration in the pulp was 35% and no chalcopyrite was used. Data shows total gangue mass reporting to the concentrate at each level increasing as the amount of fibrous ore added increases, more so in the lower layers. 157

Figure 5.31: Nascent froth sampling on mixtures of Fibrous ore at 1%, 4% and 7% respectively mixed with fine silica. Solids concentration in the pulp was 35% and no chalcopyrite was used. Data shows water mass to the concentrate increasing as the amount of fibrous ore added increases, more so in the lower layers. 157

Figure 6.1: Rheogram for silica as a function of Vol % solids........ 159

Figure 6.2: Relative viscosity vs volume fraction for fine silica only........ 161

Figure 6.3: Reproducibility of data from fine silica experiments- log. Relative viscosity vs shear rate........ 161

Figure 6.4: Fine silica η_r vs volume fraction ϕ for a range of shear rates 162

Figure 6.5: Fine Silica Data fit to the Krieger-Doherty and Mooney models 164

Figure 6.6: Effect of Wide PSD mica on η_r vs (ϕ) relationship for 10/s shear rate 164

Figure 6.7: Effect of wide PSD mica on rel. viscosity-volume fraction relationship with fits to Mooney eqn at 10/s shear rate 165

Figure 6.8: Effect of mica particle size on relative viscosity- volume fraction relationship for 50% addition (with fine silica) at 10/s shear rate........ 166

Figure 6.9: Effect of mica particle size on relative viscosity- volume fraction relationship for 25% addition (with 75% fine silica) at 10/s shear rate 167

Figure 6.10: Effect of fibrous ore addition to silica on rheology-volume fraction relationship and Mooney fit at 10/s shear rate........ 169

Figure 6.11: Relative viscosity- volume fraction for 25% sized mica (75% fine silica) compared to fine silica only. The difference between 25% mica/75% fine silica and 100% fine silica tests appears is about 0.3 to 0.5 units regardless of size 170

Figure 6.12: Relative viscosity (η_r) vs volume fraction (ϕ) for 25% mica or silica of 20-50μ (a), 50-75μ (b), 75-100μ (c), mixed with 75% base fine silica. At 0.075ϕ, the difference between mica and silica addition is about 0.1 units or approximately 10%, which is very small. 171

Figure 6.13: Relative viscosity vs volume fraction f for addition of 0.75% , 1.25% and 2.5% fibrous ore to fine silica. The data shows that the relative viscosity increases by about 100% for small increases in fibrous ore content 171

Figure 6.14: Effect of wollastonite addition on relative viscosity-volume fraction relationship 173

Figure 7.1: Flotation tests- Water recovery in the fourth stage of flotation for addition of (a) 25% and (b) 50% mica and silica to 75% and 50% base ore as a function of particle size 178

Figure 7.2: Nascent froth sampling- Total gangue mass with 50% mica or silica addition to 50% base fine silica for two select layers: a) layer 2 (near top of froth) and b) layer 5 (near bottom of froth). Gangue mass is higher when mica is added as compared to when silica is added in layer 5, while there is no significant difference observed in layer 2. Solids concentration in the pulp is 35%, and no chalcopyrite (value mineral) is present. 179

Figure 7.3: Nascent froth sampling- Solids concentration (w/w) with 50% mica or silica addition to 50% fine silica for two select layers: a) layer 2 (near top f froth) and b) layer 5 (near bottom of froth). Solids concentration is higher when mica is added as compared to when silica is added for layer 5, but there is no difference for layer 2. Solids concentration in the pulp is 35%, and no chalcopyrite (value mineral) is present. 180

Figure 7.4: Nascent froth sampling- Water mass (g) with 50% mica or silica addition to 50% base fine silica in two select layers: a) layer 2 (near the top of froth) and b) layer 5 (near the bottom of froth). Water mass is always only slightly higher for when mica is added as compared

to when silica is added for the same size. Solids concentration in the pulp is 35%, and no chalcopyrite (value mineral) is present. 181

Figure 7.5: Total gangue mass in layer 5 (near bottom of froth) in froth sampling tests for nascent (N) and steady state (SS) sampling conditions- 50% of 50-75µ, 75-100µ or 100-150µ mica or silica mixed with 50% fine silica. Solids concentration in the pulp is 35%, and no chalcopyrite (value mineral) is present. 182

Figure 7.6: Solids concentration (wt.%) in layer 5 (near bottom of froth) in froth sampling tests for nascent (N) and steady state (SS) sampling - 50% of 50-75µ, 75-100µ and 100-150µ mica or silica mixed with 50% fine silica. Solids concentration in the pulp is 35%, and no chalcopyrite (value mineral) is present. 183

Figure 7.7: Nascent Froth sampling tests compositional analysis- 50% fine silica mixed with 50% (a) 75-100µ mica or silica, (b) 100-150µ mica or silica. Data shows sized silica or mica mass in each layer of froth. Mica mass is always more than silica of the same size. Solids concentration in the pulp is 35%, and no chalcopyrite (value mineral) is present. Data from layer 6 is removed in some cases because of errors. Data from layer 1 is excluded because of large uncertainty associated with it. 184

Figure 7.8: Nascent Froth sampling tests compositional analysis- 50% fine silica mixed with 50% (a) 75-100µ mica or silica, (b) 100-150µ mica or silica. Data shows fine silica mass in each layer of froth. fine silica mass is the same for mica or silica addition for both sizes. Solids concentration in the pulp is 35%, and no chalcopyrite (value mineral) is present. Data from layer 6 is removed in some cases because of errors. Data from layer 1 is excluded because of large uncertainty associated with it. 184

Figure 7.9: Nascent froth sampling tests- 50% base fine silica mixed with 50% sized platy mica as noted in legend. Data shows that mass of base fine silica decreases slightly as the size of mica added is coarser, and this may be attributed to increased froth stability. 185

Figure 7.10: Nascent froth sampling vs steady-state froth sampling- 50% (w/w) sized mica mixed with 50% base silica- Mica mass in (a) layer 2 and (b) layer 5. Data shows that mica mass for the nascent and steady state sample is the same for sizes 50-75μ and 75-100μ for both layers. However, the mica mass increases for steady state sampling when 100-150μ mica is added. (Solids concentration in pulp is 35%, and no chalcopyrite was added).................................... 186

Figure 7.11: Nascent froth sampling vs steady-state froth sampling- 50% (w/w) sized mica mixed with 50% fine silica- Fine silica mass in (a) layer 2 and (b) layer 5. Data shows that base fine silica mass for the nascent and steady state sample is almost the same for all sizes, suggesting that its transport rate to the froth is balanced by drainage and is unaffected by increase/decrease in mica transport (Solids concentration in pulp is 35%, and no chalcopyrite was added) 187

Figure 7.12: Relative viscosity vs volume fraction (a) 75:25 fine silica: sized mica, and (b) addition of increasing amounts of fibrous ore. The relative viscosity is substantially higher for fibrous ore as compared to mica addition, even at much higher mica concentrations. The blue dotted boxes show the volume fractions in the froth zone obtained from froth sampling experiments. 190

Figure 7.13: Measuring dimensions of plateau borders in froths. Data showed that the size of the plateau borders ranged from 100-300 microns in size. 194

Figure 7.14: Degree of Non-sulfide Gangue Recovery (DNSR) vs confinement parameter generated from flotation tests with the assumption that the size of the constriction is 100 microns: DNSR for (a) 25% mica addition, and (b) 50% mica addition. The onset of confinement

related effects appears to be delayed for 25% mica addition, as compared to 50% mica addition. Confinement effects not observed for silica at 25% addition rate. 195

Figure 7.15: Modes of particle transport and drainage for mica and silica 196

Figure 7.16: Illustration of various modes of particle transport to froth zone as a function of mica size and content in ore. The map illustrates the region where entrainment dominates, the region where entrapment/confinement effects start to contribute to gangue recovery, and the region of target particle size for minimal gangue recovery. 197

Figure 7.17: Relative viscosity-volume fraction relationships for select fibrous/silica and mica/silica mixtures 198

Figure 7.18: Relationship between Mooney fit to rheology data and mechanisms for gangue transport to concentrate 199

LIST OF TABLES

Table 3.1: XRD composition of mica-rich ore sample ... 84

Table 3.2: Mineralogy of fibrous ore sample ... 86

Table 5.1: Experimental plan ... 127

Table 6.1: Goodness of fit for parameters B and ϕ_{max} ... 163

Table 6.2: B and ϕ_{max} parameters for 50% mica addition of all sizes ... 166

Table 6.3: B and ϕ_{max} parameters for 25% mica addition to fine silica of all sizes ... 167

Table 7.1: Critical confinement parameter for 25% and 50% addition rate of mica ... 196

ACKNOWLEDGEMENT

I would like to express sincere gratitude to all those who supported this undertaking and made this work possible: Firstly, to Prof. P. Somasundaran for his critical feedback and patience throughout this journey. His kind and thought-provoking emails after every single visit to Columbia helped me chart the path for this work. I also thank Partha Patra for inspiring confidence and providing feedback throughout this work.

I would also like to thank the management of Cytec/Solvay for supporting this work over the last 6 years, particularly Al Wagner and Mike Moser, who allowed me time to focus on the thesis towards the end of 2018. I thank John Schmitt in the mechanical shop at Solvay for the time he spent fabricating the robust froth sampling device, which lasted the duration of this work with little maintenance needed. I am eternally grateful to Nancy Touba for her efforts toward method development for and quantitation of species in the froth fractions. I also thank Chermeine Riviera for particle size analysis and SEM imaging of mineral samples, and Sarah Aanonsen for assays. I also thank Debbie Waldon at SGS labs for assaying of samples, as well as Chris Gunning for mineralogical analysis.

I would like to thank my family for their enduring emotional support during this work: my parents who worried constantly about my health during this process and tried to take as much off my plate as they could; my sister for her calming voice throughout; and my in-law-family who celebrated each milestone. I acknowledge the numerous sacrifices my wife made taking care of our son as I spent late nights at the office completing this; without her support and love during the tough times this day would not come. I apologize to my son Vihaan for not spending enough

time with him, and look forward to making up for this in the future. If it wasn’t for the light in his eyes, I could not have seen the end of this tunnel.

I sincerely acknowledge D.R.Nagaraj’s encouraging mentorship and tough love over the past 12 years; without his positive influence my career in mineral processing would be short lived, and without his objective questioning of data this work would not be nearly as relevant. Finally, I am forever indebted to Ray Farinato whose astute vision shaped this work; who clarified and re-clarified numerous scientific concepts and problems, spent his precious evenings running froth sampling experiments with me, proof-read multiple versions of the manuscript during weekends, and refused to give up on me; this work is one of many testaments to the dedication with which he has mentored and guided a whole generation of young scientists that have had the pleasure of knowing him.

Dedicated To my family.

This page intentionally left blank.

1 Introduction

1.1 Multiphase systems and Froths

Multiphase (containing solids, liquids and gases) systems are common in industrial processing operations. The most complex industrial manifestation of a multiphase system is particle-laden foam (froth). Foaming is widely encountered in industrial processes: gas is mixed with many materials in order to improve their thermal or acoustical performance or simply to make them lighter and to save raw materials. The matrix of those foamy materials is often composed of a complex fluid, such as a suspension. Typical examples for such mixtures can be found in the production of materials for the building industry (e.g. ceramic foams), in food and cosmetic industries and the separation of minerals in mining. The homogeneity of foamy materials is affected by the drainage of the interstitial phase (the continuous phase between the gas bubbles) and the simultaneous rising of the bubbles, resulting in the degradation of their quality and their functional properties. The drainage of the liquid phase and the resulting increase of the gas volume fraction promote other detrimental aging processes, such as ripening and coalescence. In order to control foam-based systems it is crucial to understand and to control the drainage process. Addition of solid particulates can help increase foam stability and the solids are selected such that suspension drainage is minimized. However, in the separation of minerals using the froth flotation process, increased suspension drainage often produces a cleaner product and is desirable. Optimization objectives can thus vary significantly between these industries. In addition, foams in ceramic and personal care industries are very stable and dry, while those in the separation of minerals are considerably wetter, unstable (i.e. collapse within seconds) and constantly evolving.

The properties of the particles in the liquid phase of the froths can drive their behaviors. Hydrophobic particles can attach to the air bubbles, thus changing the dimensions of the Plateau borders, while hydrophilic particles are present in the liquid phase. Depending on the concentration of the particles, they may undergo Stokes or hindered settling. The size of the particles dictates their ability to pass through the channels. The network of channels that the particles pass through will be dynamic depending on the surfactants used to stabilize the froths, and the particles properties. The transport phenomena of particles of various shapes through tortuous channels in a froth is thus of significant interest to all these industries. In this work, an investigation into the transport phenomena of particles through froth is done using the evolving and unstable mineral froth system.

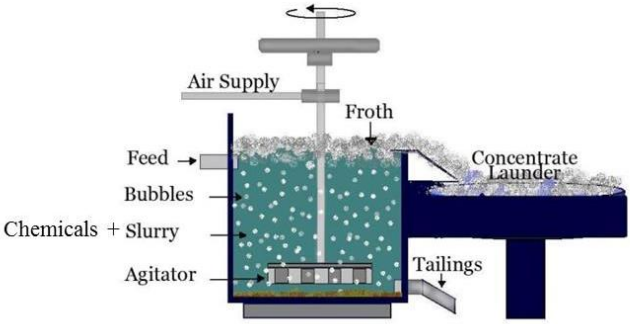

Figure 1.1: The froth flotation Process (adapted from www.911metallurgist.com)

1.2 Froth Flotation for minerals separation

This process involves, for example, the separation of copper sulfide value minerals (1% by weight in the ore) from the non-value silicates (99% by weight) that they are present with obtained from the mining process. [Non-value silicates are sometimes referred to as non-sulfide gangue, NSG, or gangue minerals in this thesis]The ground ore is agitated in a large tank, which can be as big as 300 m^3, with water, while maintaining a solids concentration of 33%. Mineral specific surfactants called collectors are then added to the tank. Collectors have a mineral-specific functional group and a hydrocarbon tail which contains 2-5 carbon atoms, which enables the molecule to adsorb onto the copper mineral surface, and renders the mineral surface hydrophobic. Air bubbles are then passed through the bottom of this agitated tank. The agitation and ensuing turbulent flow ensure that there are collisions between all particles and air bubbles. A select few of these collisions with hydrophobic particles are fruitful, resulting in particle attachment to the air bubbles. The bubble-particle aggregates, while agitated in the turbulent medium, float upwards due to buoyancy forces. Another reagent, called the frother which is a weak surfactant that lowers the surface tension of bubbles, allows formation of a transient froth. This froth sits atop the agitating slurry, as shown in figure 1.1. The top layer of the froth, which contains a higher concentration of hydrophobized particles than the slurry underneath, is continuously removed as the “concentrate” product in commercial applications.

Flotation is thus a probabilistic process, with the outcome dictated by the probability of collisions of valuable particles with bubbles, probability of attachment of the particles to bubbles, and the probability of detachment in the froth. Value minerals are not always fully liberated from the other sulfide and silicate minerals, frequently occurring as binary and ternary particles, with surface exposure of the value minerals ranging from 5% to 100%. There is thus a rate associated with the recovery of value minerals, with fully liberated particles being recovered rapidly, and with partially liberated particles being recovered more slowly. It is for these reasons that the slurry subject to flotation is treated under these conditions for an extended period of time to allow all particles to be recovered. In the time it takes to recover an economically adequate amount of value minerals, the amount of hydrophilic non-value (gangue) mineral content recovered becomes substantial, resulting in a dilution of the product. The flotation outcome, like any separation, is measured in terms of the quality of final product (grade), and the recovery of value minerals present in the feed (ore).

It should be noted that there are (financially-driven) strict specifications on the copper concentrate produced from the flotation process. Typically, concentrate must have a minimum of 25% Cu. There is a specification on the ratio of Cu to Fe, and a similar specification on the non-sulfide gangue mineral content of the concentrate. If these ratios are not met, the processing plants are penalized. It is thus important that the flotation plants minimize the recovery of the non-sulfide gangue minerals. Selectivity is thus paramount in the flotation of base and precious metals associated with sulfide minerals.

1.2.1 The Froth phase in flotation

Froth flotation may be divided into various sub-processes, which take place in the three zones.

a. The largest zone is the slurry or pulp zone, where the solids concentration is 30-35% and the flow is turbulent. This is the region where collisions between hydrophobized particles and bubbles take place; a subset of these collisions is fruitful and lead to attachment of these particles to bubbles. Of all the solids in the pulp, typically 95% of these are the hydrophilic silicate minerals.

b. The bubbles rise due to buoyancy forces and reach the second zone, which is the pulp-froth interface. This is the smallest region, where the rising bubbles collide with the bubbles already at this transition zone, resulting in the detachment of some hydrophobized particles. In this interface, the swarming bubbles carry over the slurry into the froth zone.

c. While most of the gangue slurry is squeezed out from between the rising bubbles, some slurry does make its way into the third zone, which is the froth zone. The froth zone is unagitated, and the flow regime is laminar. As the bubbles rise up, slurry drains back continuously, resulting in both liquid fraction and bubble size changing with the height in the froth. Bubbles that may have been essentially spherical in shape at the pulp-froth interface now appear as polyhedral cells whose surfaces are formed by thin liquid films. As the liquid films separating the bubbles become thinner, <u>coalescence</u> of the bubbles can occur, and some hydrophobic particles may <u>detach</u> from the bubbles. The interstitial suspension containing hydrophilic particles <u>drains</u> due to gravity; it passes through the network of Plateau borders and vertices that are *decorated* with hydrophobic particles. The concentration of interstitial fluid in the froth typically decreases from the bottom to the top of the froth zone, but a finite amount of it is retained even at the very top of the froth zone. At the very top of the froth zone, bubbles burst and hydrophobic particles are transferred to the layer of bubbles underneath. The top of froth loaded with hydrophobic particles is removed as the concentrate, as well as any non-value hydrophilic particles accompanying the interstitial fluid.

The mechanism by which hydrophobized particles are transported to the froth by adherence to the air-water interface of bubbles and recovered in the concentrate is termed *"true" flotation*. As bubbles rise to form the froth, they also carry hydrophilic particles in the interstitial space between the bubbles, and these particles are said to be recovered by *entrainment.* The effect of particle size on entrainment is well known. Unwanted gangue minerals are also sometimes trapped in between hydrophobic particles, and this process is called *entrapment.*

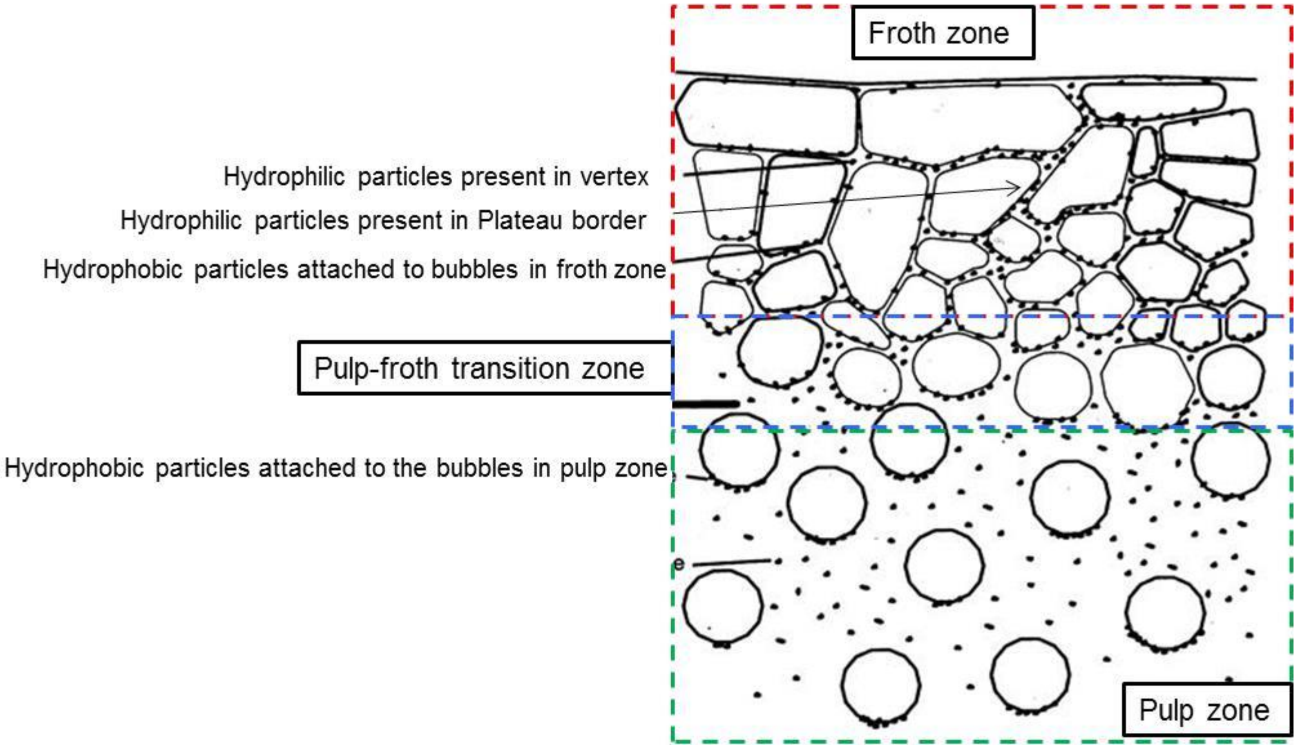

Figure 1.2: Illustrating the various zones in flotation: pulp zone, pulp froth interface, and froth zone (Adapted from RP King , 2000)

1.3 Motivation and Hypothesis development

It has been observed that when certain non-sulfide gangue mineral species are present in the ore, there is a negative effect on flotation concentrate quality. Mineral processing plants cannot ship these concentrates to smelters and have to waste or blend them with other concentrates, if available, leading to millions of dollars in losses. This operational issue has been recognized as a significant problem in the industry, with Jorjani (2011) and Bulatovic (1999) discussing problems at specific plants. The mineral species that have been implicated in causing these issues are serpentines and micas, which are in the category of silicate minerals called phyllosilicates. Muscovite mica, which is part of the phyllosilicate subgroup of silicate minerals, has a highly perfect basal cleavage yielding remarkably thin laminae (sheets) which are often highly elastic. The muscovite particles, when ground, have a platy morphology. However, a scientific understanding of the mechanisms which lead to the poor concentrate grades due to mica is lacking.

The field of rheology involves the study of flow behavior of particulate suspensions. Rheological properties of particulate suspensions are a function of the volume fraction of the dispersed particles, the size distribution and shape distribution of the particles and the viscosity of the continuous phase (suspending liquid).

In past work, Patra (2010) showcase how the rheological properties of mineral suspensions have a tremendous impact on increased transport of gangue to the froth resulting in poor concentrate grade. The increased viscosity observed was attributed to the shape of the problematic mineral chrysotile, which has a fibrous morphology and entangles to form a non-woven network-like structure which gets transferred from the pulp zone to the froth zone. In addition, Kirjavanein (1992) showed that a platy mineral (phlogopite) also increased the viscosity of the pulp zone.

1.4 Hypotheses

The focus of this thesis is the transport of hydrophilic particles through confined channels in the froth zone. The interstitial space in between bubbles is occupied by the suspension of hydrophilic particles carried from the pulp zone. The suspension drains, carrying hydrophilic particles with it, and has to navigate the network of Plateau borders and vertices that are decorated with hydrophobic particles. Based on a review of the literature and observations, it was hypothesized that the material properties of the interstitial suspension, viscosity in particular, is affected by the size distribution, shape/morphology distribution and concentration of the hydrophilic particles present in it. For platy shaped particles, viscosity of the suspension is greater than that for just low aspect ratio silica particles alone. The increased viscosity is implicated in the reduced drainage rates of the suspension through the Plateau borders, resulting in reduced concentrate grades. The platy (moderate aspect ratio) mineral mica is compared to globular (low aspect ratio) silica to study the effect of particle shape for the majority of the work in this thesis, with some experiments being done on fibrous minerals (chrysotile) and plank-shaped mineral (wollastonite).

When it was found that the viscosities at the relevant solids concentrations in the interstitial suspension found in our froths were not affected significantly by coarse platy particles, a revised two-part hypothesis was developed: a) increased platy mica/high aspect ratio mineral transport is related to the higher drag forces experienced by the platy mica particles as compared to the low aspect ratio silica particles, and b) asymmetrical shape of platy particles leads to increased confinement of coarse particles in the plateau borders of the froth, thus resulting in increased transport to the concentrate.

1.5 Experimental map

The experimental map for this thesis is shown in figure below 1.3 below.

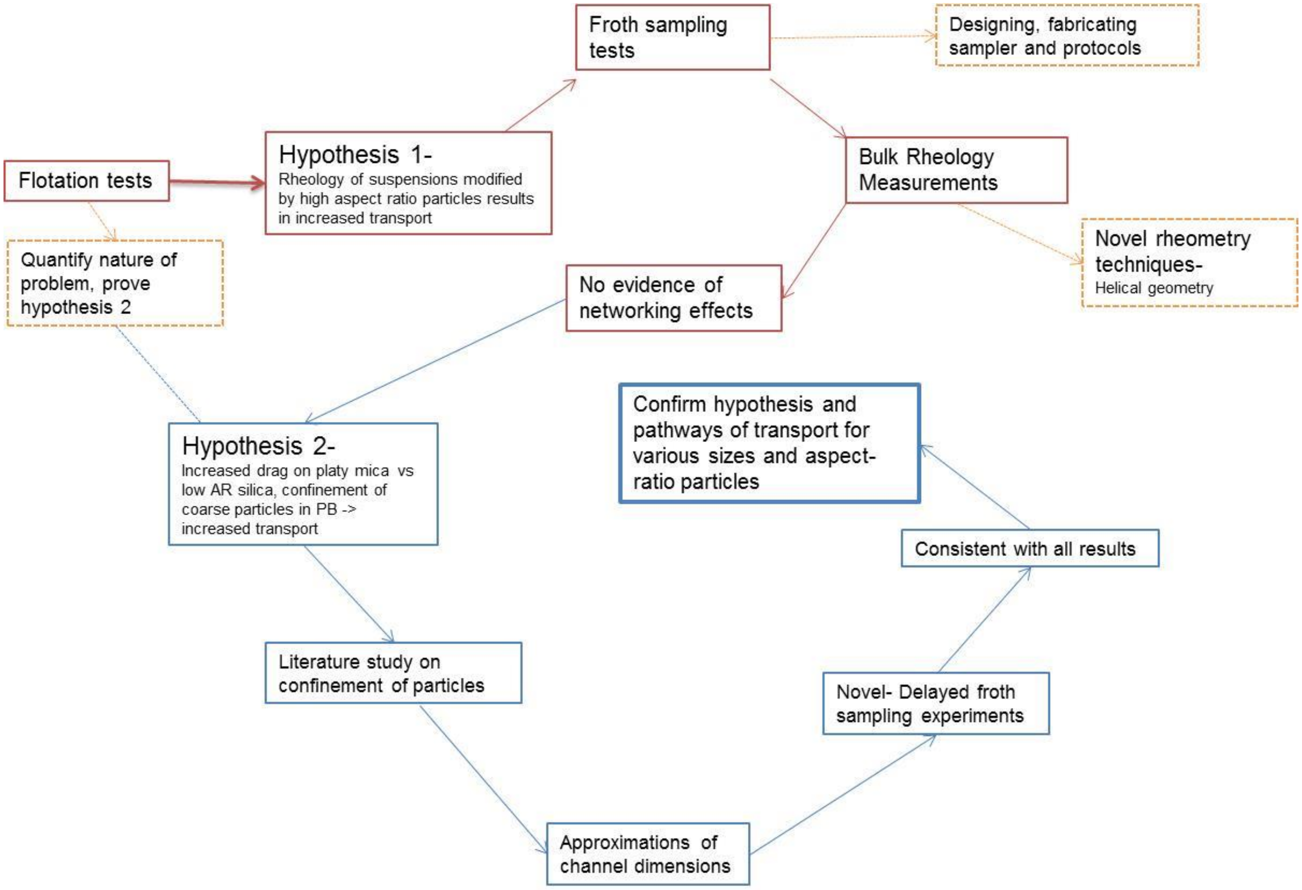

Figure 1.3: Experimental map for thesis, with the red arrows showing the path followed for hypothesis 1. The path for hypothesis 2 is shown with blue arrows. The orange areas indicate additional information

1.6 Original Methods and Contributions to the knowledge

1. The effect of particle shape on transport through confined channels in a transient/unstable three phase froth has been studied. Multiple mechanisms for transport have been studied and identified, attributed to the various types of forces that dominate the transport behavior as particle size and shape change.
2. The behavior of platy phyllosilicate minerals (mica) in the flotation of sulfide ores has been quantified, with their effect on recovery and grade clearly demonstrated as a function of size. Using this data it is possible to predict flotation outcome for any size and concentration of platy or globular hydrophilic gangue minerals.

3. A froth sampling assembly was custom designed and fabricated to test the hypothesis. Protocols were developed to enable the sampling of unstable three-phase froths without any leaks.
4. For the first time in mineral suspensions, helical ribbon geometry was used in a viscometer to generate highly reproducible rheology data, a significant improvement over the existing vane geometry.
5. For the first time, two types of froth sampling (as a function of height in froth) experiments were conducted, i.e. nascent sampling, which results in an upward transport/drag force dominated regime, and steady-state sampling, where drainage of interstitial suspension is balanced by drag. It will be readily apparent in chapter 8, that these experiments are critical for understanding mechanisms of transport of mineral species to and through the froth zone.
6. In order to simulate behavior for real ores, mixtures of platy mica and low aspect ratio/rounded silica were used, as opposed to studying minerals on their own. In addition, a number of experiments were conducted for these minerals in the presence of hydrophobic chalcopyrite particles to ensure results are applicable to mineral flotation.
7. The mechanisms of transport of the platy minerals to the froth were identified:
    a. It was shown that the viscosity of the interstitial suspension at the relevant solids concentrations was not significantly affected by the substitution of platy minerals for silica. Increased froth viscosities, thus, were demonstrated to not be the major factor in the differential transport of platy minerals compared to low-aspect ratio silica.
    b. It was found that platy mica is transported to the froth by entrainment (hydrodynamic transport) when it is <100μ in size. However, the rate of its transport is faster than

that for low-aspect ratio silica particles, and this is attributed to increased drag forces experienced by platy particles, and reduced effect of settling due to gravity.

   c. When coarser than 100μ, it was found that the mica was transported to the concentrate due to entrapment/confinement in plateau borders, whereas the effect was less strong for silica.

8. Experimental findings demonstrated methods to identify pathways for all gangue transport through the froth.

1.7 Chapter Outlines

Chapter 2 includes a review of the existing literature on the froth zone in the flotation process and the factors that impact its behavior. A large section is dedicated to the entrainment mechanism, effect of various material and froth properties on it, and modeling techniques. This is followed by a discussion on rheology of suspensions and froths, including the various models used for these. The last section includes a discussion on phyllosilicate minerals, with detailed descriptions of the mineralogy of muscovite and chrysotile. The existing knowledge of the pathways by which phyllosilicates affect flotation are also included followed by a discussion on gaps in the knowledge, the hypotheses and the experimental plan to fill the gaps in knowledge.

Chapter 3 is on materials and methods. It includes the method of preparation of the various mineral species to be tested. The protocols for flotation tests are included. It also contains detailed drawings of the froth sampling assembly that was designed and fabricated to test the first hypothesis. The protocols established to use this assembly without having leaks and testing it are also included, along with the analytical techniques needed to quantitate mica, chrysotile and wollastonite in a mixture of minerals. For the rheological measurements, the method development to use the helical tool is included, along with the measurement systems evaluation.

Chapter 4 contains the results from the froth flotation tests on mixtures of ore and: a) mica, b) fibrous ore, and c) wollastonite. The results show the impact on of mica and fibrous ore on concentrate grade and recovery. The degree of entrainment for all the entire tests, as well as the final (fourth) concentrate as a function of size of mica added is included. The effect of addition of fibrous ore as well as wollastonite is also shown.

In Chapter 5, the results from the froth sampling tests are shown using a synthetic mixture of fine silica, and either coarse silica, mica, wollastonite, or a fibrous ore, with or without chalcopyrite. The first set of results is in the absence of hydrophobic particles (chalcopyrite made hydrophobic by collector adsorption) with mica and silica of various sizes added at 50% addition rate to the base fine silica for nascent sampling. This is followed by the same tests but in the presence of hydrophobic particles. The results from froth sampling tests on mixtures of fibrous ores and silica are also included.

In Chapter 6, results from the rheological measurements are shown. It includes the relative viscosity-volume fraction curves for mica and silica of various sizes mixed with the fine silica. The results are compared to the data obtained for the fibrous ore. The data suggests that the relative viscosities are very similar for the various sizes of mica and silica at the volume fractions found in the froth interstitial suspension.

In Chapter 7, titled discussion, the results from all experiments are discussed with the goal of identifying transport mechanisms of particles of various shapes and sizes. With differences in bulk measured viscosity being small, the revised was investigated i.e. drag forces are greater on platy mica than silica, and that confinement of particles in the Plateau borders and vertices is driving the increased transport to concentrate of coarse platy gangue minerals. The results from steady state sampling are shown, which suggest that indeed at a critical size, mica appears to be more confined in the channels. Measurements of channel dimensions relative to particle size are shown which help verify the hypothesis. The mechanisms for both coarse and fine platy minerals are summarized and compared to those for rounded silica particles in light of the various forces whose dominance changes with particle shape and size change.

Chapter 8 contains the summary and conclusions, as well as recommendations for future work.

2 Literature review

2.1 Outline

The review starts with a discussion on mining, the flotation process for minerals separation, and the froth zone (including its various sub-processes). This froth is a perfect example of an unstable multiphase froth. While entrainment may be classified as a sub-process of the froth/transition zone, it is central to this work and has been included in its own section. This is followed by a discussion on rheology of suspensions and froths. The last section covers the mineralogy of the non-sulfide gangue minerals that are the subject of this work, namely platy muscovite mica and fibrous chrysotile. This is followed by a discussion on the nature of the problems attributed to these minerals. This followed by an analysis of the gaps in the state of knowledge of the transport mechanisms, the hypotheses for the transport mechanisms, and the experimental plan to test these hypotheses.

2.2 The mining industry and copper

The mining industry remains the single largest mover of material. The importance of the industry may be summarized using the adage “If it cannot be grown, it must be mined”. In the year 2014, 45 billion tons of ore was mined around the world to produce a range of commodities- fuel minerals such as coal, industrial minerals such as potash, soda ash, phosphate and crushed stone, and base and precious metals such as iron, copper, lead, zinc, gold and silver. Industrial and fuel minerals are low-value products and the material moved to produce product is significantly less than for base and precious metals. Production of base and precious metals, particularly copper, is the focus of this thesis. The typical copper content in an ore is 0.5% Cu, and thus a ton of ore mined can yield on average only 5kg of Cu. In the year 2014, 12.1 billion tons of copper ore was moved globally to produce 18 million tons of copper. The US produces about 10% of the world's copper cathode.

2.3 Copper production process

In order to produce the 99.999% Cu that is used in electronics, the ore containing typically 0.5% copper (by weight) needs to be enriched. The Cu occurs either as sulfide or oxide copper minerals. When the copper occurs primarily as oxide minerals, it is enriched using hydrometallurgical techniques. The Cu is leached using dilute sulfuric acid, concentrated using a solvent extraction process, and followed by electrowinning to obtain the pure copper cathode.

When the copper occurs primarily as sulfide minerals, it is treated by the froth flotation process. The largest component in the ore is non-sulfide gangue minerals, which typically comprise 85-95% of the ore. These are mostly sodium and potassium silicates, carbonates and other such minerals. The typical specific gravity of this portion of the ore is 2.6. A small amount of sulfide gangue mineral (e.g. pyrite FeS_2) when present, is typically 2-10% of the ore. The value Cu mineral (e.g. chalcopyrite $CuFeS_2$) is typically 1% of the ore by weight. For these ores, a combination of hydrometallurgy and pyrometallurgy is used to prepare the final copper concentrate which ranges from 20-35% Cu. The upgrading process involves crushing the ore to about 2mm in size. The ore is then typically ground in a ball mill to a particle size distribution such that 80% of the ore is finer than 100 microns in size. This is done to liberate or expose the Cu sulfide mineral surfaces. The ore is then subject to the froth flotation process, which utilizes differences in the wettability of the mineral surfaces to separate it from the gangue minerals. In the first stage of flotation, the concentrate typically contains about 10% copper. The flotation concentrate obtained then is repeatedly subject to the process to generate the final concentrate containing about 25% Cu. At this concentration, it is economical for pyrometallurgy; the concentrate is sent to a smelter and converter, which results in blister copper, which is about 98.5% Cu. This is followed by a sequence of furnaces and refineries to generate 99.999% pure copper cathode to be used in electronics and other applications.

There has been a shift to lower grade ores over the past two decades, due to various factors including the economic advantages of extending the life of older mines over finding and establishing new mines, and scaling factors (West, 2011). Low-grade ores are difficult to process because they are commonly complex and valuable minerals are often associated with gangue minerals at even fine particle sizes, thus requiring finer grinding.

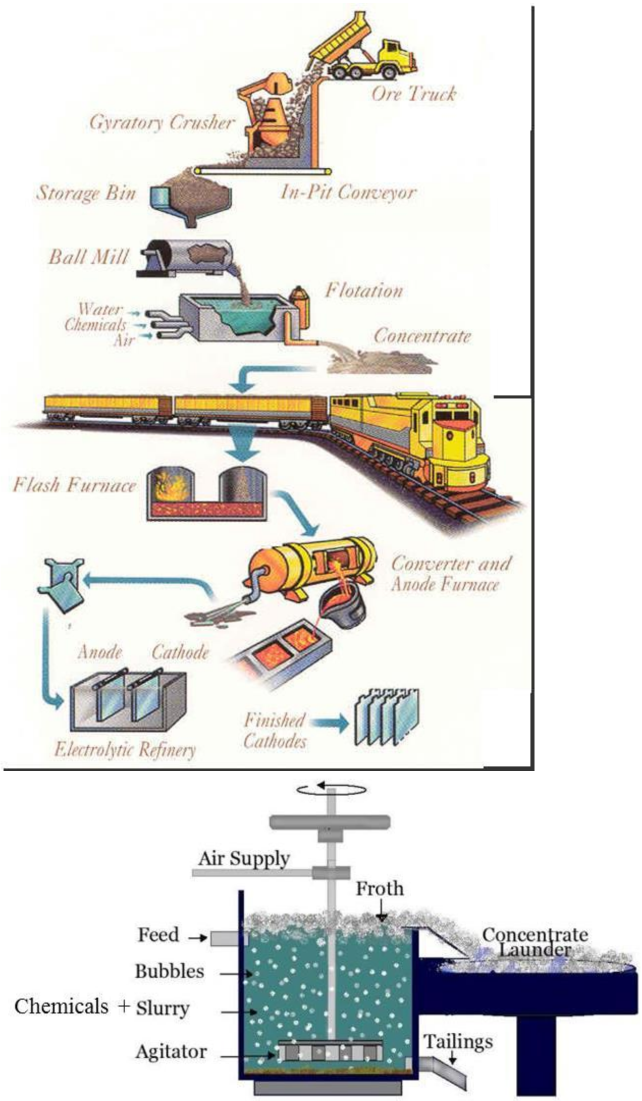

Figure 2.1:(a) Mineral Processing and (b) the froth flotation Process (adapted from www.911metallurgist.com)

2.4 Froth Flotation

The ground ore is agitated in a large tank, which can be as big as 300 m^3, with water, while maintaining a solids concentration of 33%. Surfactants called collectors are then added to the tank. Collectors have a mineral-specific functional group, which enables the molecule to adsorb onto the copper mineral surface, and a hydrocarbon tail which contains 2-5 carbon atoms, and renders the mineral surface hydrophobic. Air bubbles are then passed through the bottom of this tank. The agitation and ensuing turbulent flow ensure that there are collisions between all particles and air bubbles. A select few of these collisions with hydrophobic particles are fruitful, resulting in particle attachment to the air bubbles. The bubble-particle aggregates, while agitating in the turbulent medium, float upwards due to buoyancy forces. Another reagent, called the frother, is also added, which is a weak surfactant that lowers the surface tension of bubbles, allowing them to form a transient froth, which sits atop the agitating slurry, as shown in figure 2.1(b). The top layer of the froth, which contains a higher concentration of hydrophobized particles than the slurry underneath, is removed as the "concentrate" product in commercial applications.

Flotation is thus a probabilistic process, with the outcome dictated by the probability of collisions of valuable particles with bubbles, probability of attachment of the particles to bubbles, and the probability of detachment in the froth. Value minerals are not always fully liberated from the other sulfide and silicate minerals, frequently occurring as binary and ternary particles, with surface exposure of the value minerals ranging from 5% to 100%. There is thus a rate associated with the recovery of value minerals, with fully liberated particles being recovered rapidly, with partially liberated particles being recovered more slowly. It is for these reasons that the slurry subject to flotation is treated under these conditions for an extended period of time to allow all particles to be recovered. In the time it takes to recover an economically adequate amount of value minerals, the amount of hydrophilic non-value (gangue) mineral content recovered becomes substantial, resulting in a dilution of the product. The flotation outcome, like any separation, is measured in terms of the quality of final product (grade), and the recovery of value minerals present in the feed (ore).

It should be noted that there are strict specifications on the copper concentrate produced from the flotation process. Typically, concentrate must have a minimum of 25% Cu. There is a specification on the ratio of Cu to Fe, and a similar specification on the non-sulfide gangue mineral content of the concentrate. If these ratios are not met, the processing plants are penalized. It is thus important that the flotation plants minimize the recovery of the non-sulfide gangue minerals. Selectivity is thus paramount in the flotation of base and precious metals associated with sulfide minerals.

2.5 Froth Zone in flotation

The term foam refers to a two phase system consisting of air and liquid, and froth refers to a three phase structure consisting of air bubbles, liquid (water) and solids (particles). Foams are dispersions of gas bubbles in a volume of liquid stabilized by surface active agents and are typically composed of polyhedral gas bubbles with liquid films residing in between bubbles. The three films meet at Plateau borders and vertices represent the junction of three Plateau borders (Harvey et al, 2005). Froth has a similar structure to foam, but in flotation froth, hydrophobic solid particles are attached to the surface of liquid films, and the Plateau borders and vertices between bubbles contain both hydrophobic and hydrophilic particles as shown in figure 2.2. The concentration of hydrophobic particles in the froth is higher in the initial stages of flotation but decreases as the content of these particles is depleted with time.

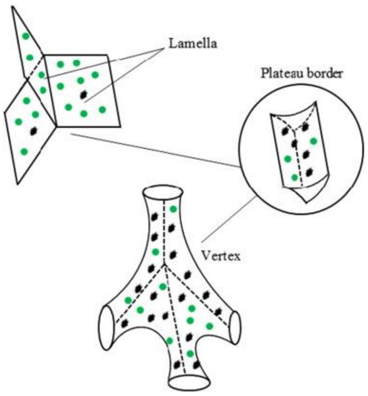

Figure 2.2: Lamellae, plateau borders and vertices in froths. Green particles are hydrophilic, and black are hydrophobic.

The function of the froth zone in flotation is largely to enhance the overall selectivity of the flotation process. The froth achieves this by reducing the recovery of gangue mineral to the concentrate stream, while preferentially retaining the attached material. This increases the concentrate grade whilst limiting as far as possible the reduction in recovery of values. As the bubbles rise up, *suspension drains* back continuously, resulting in both liquid fraction and bubble size changing with the froth height. Bubbles that may have been essentially spherical in shape at the pulp-froth interface now appear as polyhedral cells whose surfaces are formed by thin liquid films. As the liquid films separating the bubbles become thinner, coalescence of the bubbles occurs, and *particles detach* from the bubbles and return back into the liquid zone if they are not picked up in the froth. Finally, at the top of the froth, the *bubbles burst* and hydrophobic particles attached deposit on the layer of bubbles underneath. The airflow rate is such that a froth bed is maintained, and does not overflow the bank in laboratory scale testing, while a gentle overflow is maintained at plant scale. Figure 2.3 illustrates the sub-processes in the froth zone.

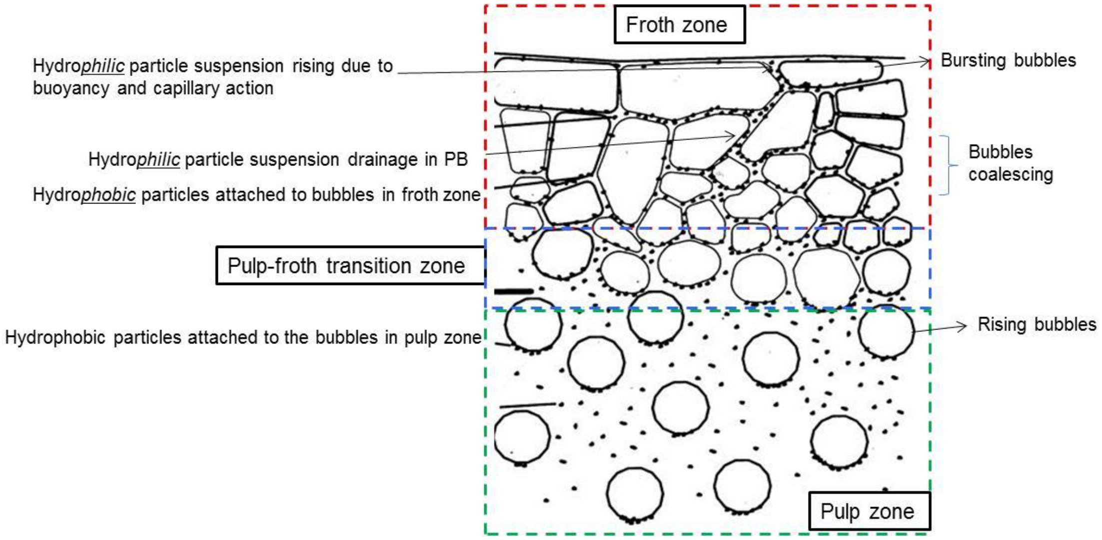

Figure 2.3: Sub processes in froth flotation illustrated (Adapted from Leja, 2004)

The froth also rejects some unwanted gangue minerals that are unselectively transported into the froth with water (entrainment). This zone is therefore an important part of the flotation process as it further refines the concentrate produced and determines the recovery and grade of metal concentrate (Wills and Napier-Munn, 2006). The role of the froth phase in cleaning the concentrate has been recognized for many years. It is no wonder that the various phenomena occurring in the froth phase have been investigated with great interest, with a comprehensive review recently published by Ata (2012).

2.5.1 Liquid drainage

Liquid drainage was first modeled by drawing analogies from flow in porous media and fluidized beds, which is a good first approximation. However, as the liquid fraction decreases and the bubbles grow in size, they are no longer spherical and drainage of liquid becomes dominated by the capillary and gravitational forces, and viscous losses can affect the liquid drainage rate. In addition, the disjoining pressure keeps the film from draining through steric or electrostatic forces, which are affected by ionic strength, ion type and temperature. The drainage is also affected by the hydrophobic particles at the interfaces. Studies in 2-dimensional cellular foams assume that al the liquid is drained through the plateau border and the contribution from films is negligible (Verbist et al, 2004), which laid the foundation for foam drainage in flotation froths. Theories developed for cellular foam, of course, cannot be translated directly to mineral foams because mineral froths have a relatively high liquid content and contain significant amount of solids. Neethling and Cilliers (2009) published a model for liquid flux upwards in terms of the cross-sectional Plateau border area A (*dA/dy*). Below the overflow lip, the liquid flux is:

$$\frac{dA}{dy} = \frac{\lambda k_1 A^2 + \lambda J_g A - \frac{Q_l}{A_{col}}}{\lambda k_2 \sqrt{A}} \text{ where } k_1 = \frac{\rho g}{3C_{PB}\mu} \text{ and } k_2 = \frac{\left(\sqrt{\sqrt{3}-\frac{\pi}{2}}\right)\gamma}{6C_{PB}\mu} \tag{2.1}$$

In these equations ρ and μ are the fluid density and viscosity, γ is surface tension and g is the gravitational acceleration. Q_l is the volumetric liquid flowrate into the froth and overflowing the lip, A_{col} is the cross- sectional area of the froth column and J_g is the superficial velocity of the gas into the froth. The Plateau border area, A, is related to the liquid content, ε, by the Plateau border length per volume of froth, λ using the relation ε = λA.

And above the lip, the liquid flux is:

$$\frac{d^2A}{dy^2} = \frac{-2k_1 A\frac{dA}{dy} - \frac{k_2}{2\sqrt{A}}\left(\frac{dA}{dy}\right)^2 + J_g\left(\frac{h_f - y}{h_{over}}.\alpha + (1-\alpha)\right)\left(\frac{dA}{dy} + \frac{A}{\lambda}\frac{d\lambda}{dy}\right)}{k_2.\sqrt{A}} \tag{2.2}$$

The interstitial slurry viscosity (μ) is part of both the k_1 and k_2 terms and is shown to be critical to drainage.

2.5.2 Bubble coalescence

Bubble coalescence occurs when the thin liquid films that separate two adjacent bubbles ruptures as the liquid content in the froth falls below a critical value. Ireland (2009) found that bubble coalescence was attributed to mechanical perturbations such as vibrations and bubble oscillations, verifying Neethling's (2001) assumptions. The role of hydrophobic particles in inducing bubble coalescence is critical, with the contact angle determining whether the particle will stabilize the film or will contribute to film failure (Aveyard et al, 1992).

2.5.3 Detachment of hydrophobic particles

The major reason for the detachment of hydrophobic particles is bubble coalescence. It has been shown that most detachment occurs at the pulp/froth interface, and can be as high as 60% (Falutsu and Dobby, 1989). The pulp/froth interface is the region where bubbles rising from the liquid underneath start to crowd and pack together. Bubbles coalesce predominantly in this region, and this coalescence is vigorous and tends to lead to chaotic dynamics which may lead to particle disturbance and eventual detachment (Ata 2009).

2.5.4 Suspension drainage and solids removal.

As bubbles rise, the interstitial suspension flows down due to density difference between the air and liquid. The solids experience drag forces from the flowing liquid and also flow downward. The interstitial suspension contains mainly gangue minerals and its drainage is the critical process affecting grade. Cutting and Devenish (1975) used an equilibrium froth cell, in which froth is not removed but allowed to come to a dynamic equilibrium with the pulp. They observed different modes of drainage, namely drainage around air bubbles, and column drainage (rapid descent) and subduction drainage (related to accumulation of solids on froth, where they clump up, reach an unstable mass, and sink). The drainage behavior depends on factors such as the viscosity of the froth, particle properties such as the size, density and hydrophobicity. Most hydrophilic minerals and weakly attached particles are rejected rapidly at the wettest portion of the froth which corresponds to the base of the froth near the pulp-froth interface. At the upper layer where the froth shows relatively dry characteristics, the solids removal is rather slow. The particles become more vulnerable to entrapment in the interstices of the bubbles in this region, since the liquid film thickness is not sufficiently large to allow the particles to drain out (Szatkowski, 1987). Froths loaded with very hydrophobic particles have been reported to provide a suitable platform for entrapment (Ata, 2004) as shown in figure 2.8. *Entrainment and* *entrapment*, which apply to hydrophilic particles, are discussed in detail in later sections of this chapter.

2.5.5 Froth Recovery

Froth recovery is the fraction of valuable mineral entering the froth phase and attached to air bubbles that reports to the concentrate and is often used as a measure of froth phase performance. This approach focuses on the gross behavior of the froth, and offers limited insight into the nature of the process. Nevertheless it is an important input for modeling of flotation plants. The concept was first introduced by Finch and Dobby (1990) and can be expressed by the ratio of overall flotation rate constant to the collection zone rate constant. The pulp phase recovery ranges from 60-99%, and the froth recovery can range from 10 to 90%. For modelling froth recovery, Gorain et al (1998) showed that there is a relationship between froth recovery and froth retention time, which can be measured. Zanin et al (2009) defined froth retention time in terms of froth stability. Neethling (2008) related froth recovery to particle detachment in the froth, settling of particles within the froth, and air recovery using a first-principles model, but it is difficult to measure some of the variables used in this model. Four methods have been proposed for measuring froth recovery in practice: a) changing froth depth (Vera et al, 1999), b) mass balance technique (Savassi et al, 1997), c) measuring bubble loading which can be used to calculate froth recovery (Savassi et al, 1997 and Seaman, 2004), and d) measurement of froth dropback which allows for calculation of froth recovery (Rahaman, 2013).

2.5.6 Froth stabilization by particles

The presence of solids has a profound effect on characteristics of froth as well as its stability. Ata’s (2012) review covers numerous publications on the role of hydrophobic particles in stabilizing froths. Kaptay's (2006) theoretical analysis showed that particles smaller than 3μ in diameter are required to completely stabilize thin films. Sufficiently hydrophobic particles with submicron dimensions adsorb at the air-water interface and create a barrier against coalescence. Mineral froths contains particles of much larger size, so are prone to coalescence and bursting and this is beneficial because mineral froths need to collapse once they move to the launder. When the contact angle between a bubble and particle is too large particles can detach rapidly as they can destroy the film, and if the contact angle is too small, particles can detach rapidly due to smaller contact area. Optimum contact angles (moderately hydrophobic particles) have been found to stabilize froth (Johansson and Pugh, 1996, Ata, 2002). Barbian (2003) measured the performance of industrial cells using dynamic froth stability tests. The froth stability factor obtained was correlated with air recovery for practical purposes. Air recovery is defined as the fraction of air entering the flotation cell that overflows the weir in unburst bubbles and was first introduced by Moys (1984) to assess physical behavior of froths in the plant. It is easily measured, and has therefore found significant practical application (Hadler and Cilliers, 2009). There is a linear relationship between air recovery and froth stability.

2.6 Entrainment

The term entrainment when used in the froth flotation literature, refers to the transfer process by which mineral particles suspended in water enter the flotation froth, move upwards, and leave the flotation cell with the mineral particles recovered by true flotation. It thus touches, in a way, almost all of the above described sub-processes. There are two steps involved: Particle transfer from the pulp phase to the froth phase, and rise through the froth phase to be recovered in the concentrate. Entrainment is non-selective, and can involve both hydrophobic and hydrophilic particles, but the contribution from hydrophobic particles is small and can be ignored. There are three main theories to explain transfer of hydrophilic particles to the froth zone as discussed by Savassi (1998):

1. Boundary layer theory- hydrophilic mineral particles are transported to the froth phase in the bubble lamella, i.e. the thin layer of water surrounding the bubble.
2. Bubble wake theory- the hydrophilic mineral particles are transported to the froth phase in the wake of an ascending bubble.
3. Bubble swarm theory- the region below the pulp-froth interface is congested with bubbles as the bubbles slow down and crowd together. Some water including suspended solids is squeezed upwards due to the buoyancy of the bubble swarm. Each subsequent swarm arriving at the pulp-froth interface thus pushes more particles and water into the froth.

The water containing hydrophilic particles can also drain back from froth into the pulp. The mechanisms range from drainage through plateau borders, collapse of froth causing rapid transfer of water and solids downwards in the local area of the froth, and sedimentation induced by gravity or shear (Cutting, 1989). Recovery of particles by entrainment is thus the result of a trade-off between the transfer of suspended solids upwards in the froth phase and the drainage of particles downwards through the pulp-froth interface and back into the pulp phase.

The plateau borders in the froth are particularly important for entrainment, as they provide the liquid channels for entrained solids (Figure 2.4). The Plateau borders also contain most of the liquid present within the froth. The Plateau borders are formed by the thin water films (lamellae) meeting at 120^o. In the Plateau borders, the unattached hydrophilic and hydrophobic particles move freely in the water, undergo settling and experience hydrodynamic drag.

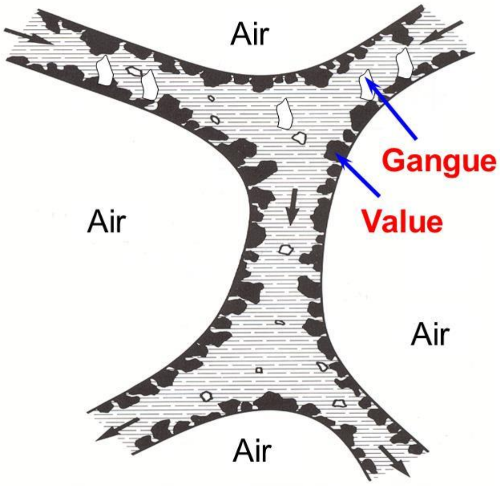

Figure 2.4: Plateau borders with hydrophilic and hydrophobic particles (taken from Leja, 2004)

2.6.1 Entrainment and water recovery

Entrainment mechanisms are related to state of suspended solids in the pulp phase or the water film of the bubbles, the drainage in the water film of the bubbles, the drainage in the froth phase and the water recovery. The degree of entrainment (ENT_i) was proposed to describe the classification effect of the drainage of entrained particles (Johnson 1972, Bisshop and White, 1976, Smith and Warren, 1989, Savassi et al, 1998). The degree of entrainment is defined as the ratio of the mass of mineral of size *i* per unit mass of water in the concentrate recovered by entrainment to the mass of mineral of size *i* per unit mass of water in the pulp (Johnson 1972).

$$ENT_i = \frac{(mass\ of\ free\ gangue\ per\ unit\ mass\ of\ water)_{concentrate,i}}{(mass\ of\ free\ gangue\ per\ unit\ mass\ of\ water)_{tailings,i}} \tag{2.3}$$

It indicates the relative transfer of hydrophilic solids from the pulp to the froth. It can be calculated either using size-by-size assays of both the concentrate and the pulp, or by the amount of gangue and water in the concentrate and pulp. Overall recovery by entrainment may thus be expressed as a function of degree of entrainment and water recovery.

$$R_{ent,i} = ENT_i . R_w \tag{2.4}$$

Where $R_{ent,i}$ is the recovery of particles in the *i*th size fraction by entrainment and R_w is the water recovery. Note that the degree of entrainment is sometimes generalized to the term “entrainment factor” when particles of all sizes are integrated together (Ross, 1989).

Neethling and Cilliers (2009) modeled the recovery of globular silica particles by entrainment, and compared their results to plant data. Figure 2.5 (a) shows the relative importance of upward liquid velocity and particle settling velocity, as determined numerically for spherical silica particles with a relative value of *1* indicating liquid velocity is dominant. Immediately above the pulp-froth interface, for all particle sizes, the particle settling velocity dominates. Progressively higher in the froth, there is a transition to an upward liquid velocity dominated system. The rate of change of relative importance with height depends critically on the particle size; for very small particles, this occurs at a very short distance into the froth from the pulp froth interface, while for larger particles, this transition only takes place much higher in the froth. The entrainment of particles into the froth, in spite of the dominance of their settling velocity, against the upward liquid velocity at the interface, is due to diffusion-related dispersion, as shown by calculations of the Plateau border Peclet number (Lee, 2005).

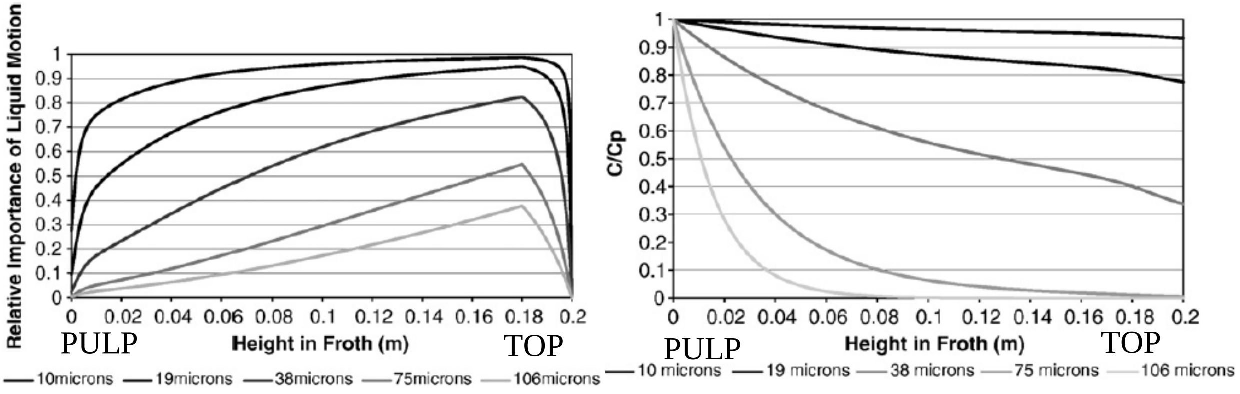

Figure 2.5: (a) relative importance of liquid velocity vs settling on the solids motion at difference heights in the froth and for different particle sizes). (b) Solids concentration in the froth, C, relative to pulp solids concentration Cp, as a function of height in the froth for different particle sizes (Taken from Neethling, 2009)

Figure 2.5 (b) shows that there is a strong decrease in solids concentration with height, from its value at the interface in the regions of the froth where the particle settling velocity may become dominant. Particles move due to diffusion-mediated dispersion from the highest concentration at the pulp–froth interface to progressively lower concentrations higher in the froth.

Studies by Jowett (1966) first demonstrated the linear relationship between water recovery and the recovery of hydrophilic particles. In general, the correlation between recovery by entrainment and the water recovery shows a linear plot trend for ultrafine particles, and a parabolic trend for coarser particles (Engelbrecht and Woodburn, 1975) as shown in figure 2.6. An increase in the amount of water brings more suspended solids into the froth phase. The relationship between water recovery and entrained solids can also be indicated by the effect of water recovery on the concentrate grade as shown by Yianatos and Contreras (2010). This inverse relationship is because a higher recovery of water in a cell results in a wetter froth, followed by a higher proportion of gangue minerals reporting to the concentrate as shown in figure 2.7.

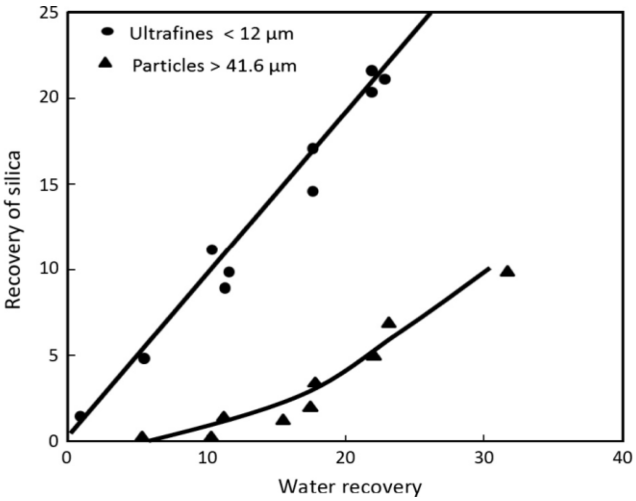

Figure 2.6: Recovery of sized silica by entrainment as a function of water recovery (Adapted from Engelbrecht and Woodburn, 1975)

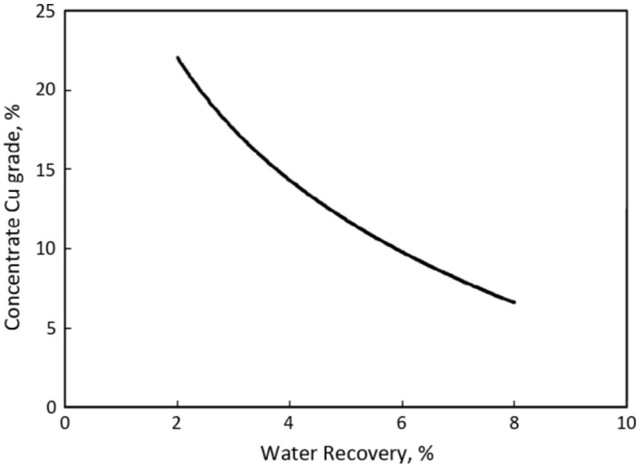

Figure 2.7: Concentrate grade vs water recovery for globular silica gangue minerals (Adapted from Yianatos and Contreras, 2010)

2.6.2 Effect of solids density in pulp

Another factor determining entrainment is solids density in the pulp phase, with lower solids densities resulting in reduced recovery via entrainment. This has been verified by a number of researchers, starting with Johnson (1974). For a greater mass of a mineral in a size fraction suspended in a unit mass of water in the pulp, a greater mass of solids per unit mass of water in the concentrate will result from the entrainment mechanism. With large cells in use today, the settling effect of coarse particles in the upper portions of the pulp phase does occur and the cell is not perfectly mixed, resulting in a classification effect in the pulp phase which must be accounted for as it affects entrainment. Data from Johnson (2005) shows that recovery of fine and intermediate-sized gangue particles is much higher in the perfectly mixed cells, than in the poorly mixed ones.

2.6.3 Effect of particle size

Smith and Warren (1989) suggested that recovery of hydrophilic particles increases significantly as the particle size decreases. They further this by explaining that the froth phase thus acts as a classifier, allowing fine particles to pass, but slowing down passage of the coarser ones. Figure 2.8 shows a plot of the degree of entrainment vs particle size, and it is no wonder that the shape looks like that of a classification curve for a hydrocyclone. The degree of entrainment is known to fall between zero and one, with zero representing the condition of total drainage where there is no entrained recovery of particles regardless of the water recovered, and one represents the condition when there is no drainage and the concentration of particles in the water in the concentrate (due to entrainment) is the same at that in the pulp phase (Runge, 2010). The data indicates that coarse particles drain more readily from the voids between the bubbles than the fine particles. Most publications estimate a range of cutoff size for entrainment, suggesting that particles coarser than 40-60μ are unlikely to be entrained. The specific size at which entrainment is of no significance in recovering particles, it is governed by the froth properties (froth height, froth structure, airflow rate) and the state of solids suspension (Savassi et al, 1998).

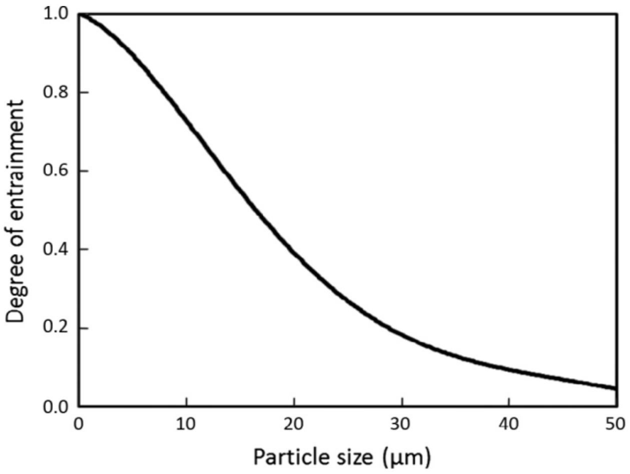

Figure 2.8: Degree of entrainment vs particle size for silica particles (Adapted from Bisshop and White, 1974)

The relative importance of upward liquid velocity versus settling velocity has been investigated by Neethling and Cilliers (2009) and is strongly dependent on particle size. They have shown that immediately above the pulp/froth interface, for all particle sizes, the particle settling velocity dominates and that, higher in the froth, there is a transition to an upward liquid velocity dominated system. The entrainment of particles into the froth in spite of the dominance of their settling velocity against the upward liquid velocity at the interface is due to diffusion-mediated dispersion as shown in Figure 2.3 (a) above.

2.6.4 Effect of shape and viscosity

Kirjavanein (1996) used quartz and phlogopite (flaky) minerals at different slurry densities and studied their entrainment. He observed that entrainment was high with phlogopite and attributed it to slurry viscosity, and proposed a mathematical model, without a clear demonstration of the mechanisms. Another limitation was that the size of the particles used in this work was 20μ, so it is not really applicable to flotation plants today treating slurries of 150μ size. Viscosity affects the state of solids suspension in the pulp phase, resulting in poor gas dispersion due to turbulence damping Shabalala et al (2011). Rheological properties of the froth zone were recently done by Li et al (2016). Shi and Zheng (2003) observed that high froth viscosity led to an increase in froth retention time, decreased water holdup in the froth phase, and provided a longer time for entrained quartz to drain back into the pulp phase.

2.6.5 Other important factors

Impeller speed also affects entrainment by modifying the state of suspension of solids in the pulp. *Particle density* or specific gravity is also important; in Bisshop’s (1974) work, it ranked second to particle size in the order of importance. However, for sulfide ores where the gangue comprises mostly of silicate minerals with minor differences in density, this effect is expected to be small.

Zheng's (2006) work discusses the mixed role of *gas rate* on entrainment. Increasing the gas rate results in greater amount of water and suspended solids carried over from the pulp to the froth phase. In the froth, however, gas rate also determines the extent of drainage of water and suspended solids by changing the structure of the froth, and the retention time of the water and suspended solids in the froth phase (Zheng, 2006). In the froth phase, it should be noted that too high a gas rate may cause an unstable froth and a possible effect on froth structure, resulting in an effect on entrainment. Increasing airflow rate boosts froth rising velocity and shortens the froth retention time, thus changing the drainage of suspended particles; a lower proportion of particles per unit mass of water tended to drain back to the pulp from the froth. Thus, the effect is not just that of increasing water recovery, but also truly affecting the entrainment process.

Zheng's (2006) work also highlights the effect of *froth height*; increasing height results in lesser recovery of gangue by entrainment because increasing froth height extends the froth residence time and promotes drainage of particles per unit mass of water in the froth phase back to the pulp phase.

Froth retention time is the time particles and bubbles exist within the froth phase, and consists of two time periods: a) the time for the froth to move vertically from the base of the froth phase to the level of the concentrate launder lip, and b) the time for froth to move horizontally to the edge of the flotation cell. However, in the literature, it only takes the vertical froth transportation into account for modelling, and this is also more applicable for bench-scale testing (froth is scraped manually, as opposed to allowing it to overflow). Froth retention time is determined by froth height and superficial gas velocity, and consequently longer retention times translate to lower recovery of minerals by entrainment. As mentioned earlier, changing froth retention time also changes other froth properties such as thickness of the lamellae and plateau borders, the froth viscosity, and the rate of bubble coalescence and bursting, which promotes drainage in particular areas within the froth (Zheng, 2006), thus affecting entrainment.

Another factor investigated in this regard is the froth structure, which depends on a number of other factors: water content, gas rate, bubble size, and the content of hydrophobic particles, and the concentration and type of frothers, collectors and other reagents (Savassi, 1998). As these change, the thickness of the lamellae and length of the plateau borders change, thus affecting water recovery and entrainment. A loose froth structure conducive to the motion of water affects the amount of gangue minerals entrained to the concentrate. Froth stability is one measure of froth structure and it refers to the rate of bubble coalescence and bubble bursting. Froths with relatively low coalescence and small bubbles not only allow the recovery of attached particles, but also promote the recovery of gangue minerals by entrainment.

2.6.6 Methods to measure Entrainment

Entrainment can be measured by various methods, and Wang's (2015) review lists all the various techniques. Trahar (1981) first studied this by comparing batch flotation tests with and without collector to determine relative contributions of true flotation and entrainment. Warren (1985) tried to do this by changing airflow rates and froth depth, which is more complicated and time consuming, and susceptible to more errors. Ross (1981) calculated transfer factors to determine contributions from true flotation and entrainment using a single batch flotation test as shown in

Figure 2.7. The key assumptions are that entrained particles are recovered at the end of the batch flotation tests, and the transfer factor decreases linearly with flotation time.

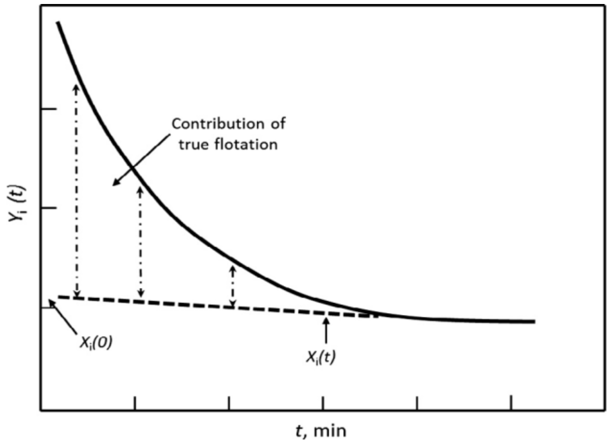

Figure 2.9: Ross's (1992) work on determining degree of entrainment using batch flotation tests

2.6.7 Modeling Entrainment

A number of different models have been proposed to characterize entrainment. There are two kinds, those that predict entrainment flow directly, and those that estimate degree of entrainment and the classification effect in the pulp which may be used to calculate entrainment. Maachar and Dobby’s (1992) model estimates entrainment directly in a column, and is applicable only to column flotation. Moys (1978) conducted a number of tests under varying conditions and developed a model that involved a number of parameters such as gas rate, product removal rate, particle specific gravity, froth height, and water recovery rate and requires certain fitting parameters. Neethling and Cilliers developed a model from first principles, shown in equation 2.4 below:

$$F_{y,Entrained} = -f(Q, Q_{air}) \times \frac{\varepsilon_F}{\varepsilon_P} \times \frac{\partial C_{S_i}}{\partial y} + \left(Q - v_{settling,i} \times \varepsilon_F\right) \times \frac{C_{S_i}}{\varepsilon_P} \qquad (2.5)$$

where $F_{y,Entrained}$ is the vertical flux of the gangue at a point y, $f(Q, Q_{Air})$ is the dispersion function, dependent on the air and water flux, among other variables, ε_F is the fractional slurry content of the froth, ε_P is the fractional water content of the Plateau borders, C_{si} is the concentration of solids of class i within the Plateau boarders, Q is water flux, while $v_{Settling,i}$ is the hindered settling velocity of particle type i. This mathematical model asserts that the vertical flux of the gangue at any point is the outcome of the (usually) upward motion of the liquid, the downward settling of the particles under gravity and the diffusion-mediated dispersion of solids.

2.6.7.1 Estimating entrainment recovery from degree of entrainment- empirical models

In order to calculate recovery by entrainment from the degree of entrainment, the following equations may be used.

$$R_{ent,i} = \frac{ENT_i.R_w}{1-(1-ENT_i).R_w}.CF_i \qquad (2.6)$$

where $R_{ent,i}$ is the recovery by entrainment, R_w is the water recovery, CF_i is the classification function describing the state of solids suspension in the pulp, and ENT_i is the degree of entrainment.

Ross and Van Deventer(1988) modelled the degree of entrainment by studying froth for 3 different size fractions collected at different heights for an ore sample. The degree of entrainment is expressed as

$$X_i = 1.0429[\log(d_i) - 1][\rho_s - 1] \tag{2.7}$$

where X_i is the degree of entrainment of the *i*th size fraction, d_i is the particle diameter, and ρ_s represents the density of mineral (g/cm^3). This model does not account for froth retention time.

Bisshop and White (1976) developed a semi-empirical model relating degree of entrainment to the residence time in the froth phase, particle size, and density of particles as shown below.

$$ENT_i = \frac{1+\alpha.\tau_{fw}}{1+\beta.\tau_{fw}}$$

$$\alpha = k_1.\left(\rho_s - \rho_p\right)$$

$$\beta_i = \alpha.\exp(k_2.d_i) \tag{2.8}$$

where ENT_i is the degree of entrainment of the *i*th size fraction on the basis of the tailings, α and β_i are the drainage parameters of water and entrained particles, respectively, τ_{fw} is the residence time of entrained material in the froth (froth volume divided by the volumetric flow of entrained material in the concentrate), ρ_s and ρ_p represent the specific gravity of the entrained solids and the pulp, respectively, d_i represents the entrained particle size, while k_1 and k_2 are empirical parameters. The empirical parameters k_1 and k_2 in the equations are determined by the experimental system and operating conditions used in the given system. However, in this model, volumetric flow rate of entrained solids may be calculated if entrainment index is known. If volumetric flow rate of entrained materials is not known, this model cannot work (Savassi et al, 1998). Zheng et al (2006) fitted the data from a 3m^3 cell to this model and found that the curve predicts entrainment but becomes irregular if data is erroneous; i.e. the slope is flexible and parameters are overly affected by errors in data.

Kirjavanein (1992) investigated entrainment of two hydrophilic particles, quartz and phlogopite in the absence of hydrophobic particles, and related the entrainment factor to a number of parameters as follows:

$$P = \frac{w^{0.7}}{w^{0.7} + b\psi\eta^{0.5\psi} m^{0.5\psi-0.4}} \tag{2.9}$$

where P is the entrainment factor (the ratio of the recovery of gangue and water), w is the water recovery (kg/m^2/s), m is the particle mass (π_g), ρ is the slurry viscosity (mPa s), Ψ is a dynamic shape factor, and b is a constant. However, this work was done in the absence of hydrophobic particles and is only applicable to those two mineral species alone.

Savassi (1998) developed a model for entrainment as shown below:

$$ENT_i = \frac{2}{\exp\left[2.292\left(\frac{d_i}{\zeta}\right)^{adj}\right] + \exp\left[-2.292\left(\frac{d_i}{\zeta}\right)^{adj}\right]} \tag{2.10}$$

$$adj = 1 - \frac{\ln(\frac{1}{\delta})}{\exp\left(\frac{d_i}{\zeta}\right)}$$

where d_i is the particle size, ζ is the entrainment parameter defined as the particle size for which the degree of entrainment is 0.20, and δ is the drainage parameter which is related to the degree of preferential drainage of coarse particles. The model was derived using a hyperbolic secant function modified to fit certain boundary conditions:

when d_i-> ∞, ENT_i–> 0

when d_i-> 0, ENT_i–> 1

when d_i-> ζ , ENT_ι–> 0.2

Even as this dataset appears to fit a number of different plant data sets, it accounts for particle size only, and no other parameters. Zheng (2006) tried to fit this model to plant data and found that while it worked well for fine and medium-sized particles, the model underestimated recovery at the coarse size, and he attributed this to the entrapment mechanism.

Yianatos and Contreras (2010) developed a model similar to Savassi's,

$$EF_i = \exp\left(-0.693\left(\frac{d_{p,i}}{\delta}\right)^{\phi}\ \right) \tag{2.11}$$

where EF_i is the entrainment factor representing the gangue/water recovery ratio, $d_{p,i}$ is the mean particle size of class i, parameter δ corresponds to the mean particle size at $EF_i = 0.5$ for each data set, while ϕ is the drainage parameter depending on the mineral characteristics and cell operating conditions (i.e. cell design and water recovery). The model complies with the following boundary conditions:

when EF_i-> 1, $d_{p,i}/\delta$ –> 0

when EF_i-> 0.5, $d_{p,i}/\delta$ –> 1

when EF_i-> 0, $d_{p,i}/\delta$ –> ∞

Parameter δ in Eq. (5) was shown to be related to the water recovery and is also a function of the particle size distribution in the region just below the pulp/froth interface, cell design and operating conditions of the flotation system.

2.7 Entrapment

Another mechanism for recovery of non-sulfide gangue is entrapment, first proposed by Gaudin (1923). He postulated that entrained particles could be trapped in between valuable particles attached to the walls of the liquid channels. Such attached particles project a substantial distance into the channel narrowing the effective drainage pathway. The mechanism was invoked to explain higher than expected recoveries of gangue in the presence of strongly floating species. Since then, this definition has been expanded and three main mechanisms have been identified that may contribute to entrapment- a) increasing thickness of froth lamellae and plateau borders reduces to a value similar to or less than particle size (Neethling, 2002), and the free drainage of particles may cease; b) the flotation of composite particles without complete liberation of gangue minerals (Zheng, 2006), and c) occlusion of gangue particles within the floccs or aggregates of hydrophobic value minerals (Polat, 2003), which is what Gaudin (1923) was referring to. Mechanism (a) was shown in Konopacka (2010).

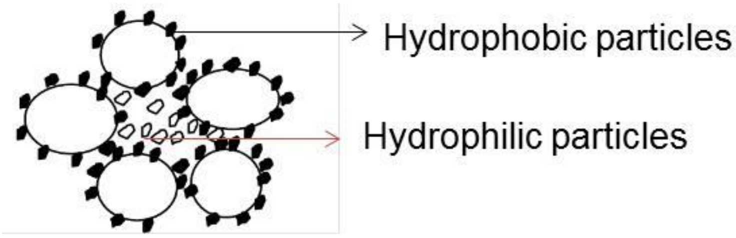

Figure 2.10: Entrapment, adapted from Konopacka (2010)

Hemmings (1980) indicated that his observation of a higher concentration of recovered +9μ particles in the froth compared with the pulp (i.e., $ENT_i > 1$) was due to an entrapment process. It is clear that several process factors must combine before entrapment has a noticeable effect on gangue recovery. In particular the froth must be highly mineralized, very dry at the removal level and/or contain relatively large entrained particles. It is not surprising therefore that not all authors have found entrapment to be significant. Trahar (1981), for example, found that the recovery of ultrafine quartz gangue was independent of the presence of strongly floating chalcopyrite, indicating that entrapment was not affecting the entrainment process in this system. Wang (2013) found that in coal flotation, entrapment played a significant role in the recovery of particles below 38μ, and this appears to be related to mechanism (c) above. He found that it was insignificant when particle size was greater than 38 microns. Zheng (2006) when using Savassi's (1998) model to fit the experimental data for silica, observed that the model fit the data well for the fine and intermediate sized particles, but not for the coarse sized particles, where it underestimated degree of entrainment, and attributed it to entrapment.

2.8 "Equilibrium/steady state" froths vs flotation froths

If a froth is raised in a flotation cell in which froth overflow is prevented, then, at constant aeration rate, eventually the froth column reaches a steady state height where the coalescence of bubbles at the top is matched by the rate at which air is supplied through the pulp. This has been referred to in the literature as equilibrium froth (Smith and Warren, 1989), however, a more appropriate term is "steady-state froth". In these froths, although water (suspension of hydrophilic particles) is always entrained with the rising bubbles, the volumetric flow at any level z, FR^{Z}_{up} will be balanced by the downwards flow by drainage, FR^{z}_{down}, as shown in figure 10 below.

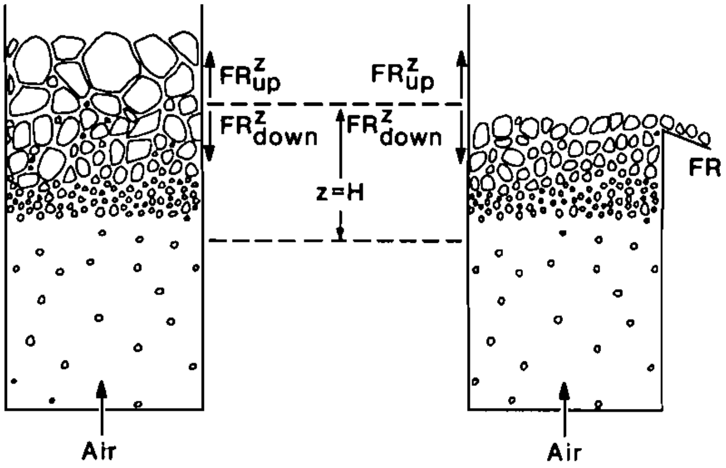

Figure 2.11: Steady state (left) and flotation (right) froths. In the steady state froth, there is no net liquid transfer, i.e. FR^{Z}_{up} - FR^{z}_{down} = 0 at any level (z) of the froth. In a flotation froth, the net flow upwards at any level is the volumetric flow out into the concentrate, i.e. FR^{Z}_{up} - FR^{z}_{down} = *FR* (Adapted from Smith and Warren, 1989)

In a flotation froth, both water and solids are recovered into the concentrate from a level below that of the equilibrium froth height. In this case, the net volumetric flow of water upwards at any level will equal the recovery rate of water out into the concentrate, i.e., FR^{Z}_{up} - FR^{z}_{down} = *FR*, as shown in Figure 10. Moys (1978) measured grades of both values and gangue in "equilibrium" (steady-state) and flotation froths indicating that significant differences in water content were obtained. Watson and Grainger-Allen used this steady-state froth to study froth stability and to separate it from pulp zone processes. Ross (1992) used this cell to study drainage behavior and to determine transfer factors for values and gangue.

2.9 Drainage of cellular foams

Cellular foams are those having a significantly lower liquid content than mineral froths. Cellular foams are also highly stable and last for days, as compared to mineral froths, which last for a few seconds. They are stabilized by very strong surfactants, as compared to weak surfactants (frothers) used for mineral froths. In these foams, the role of solids is typically to stabilize the foam. Forced drainage experiments have been conducted using these foams using water as well as particulate suspensions. To explain foam drainage in the presence of particles, several mechanisms have been proposed, such as rheology of the suspension, and clogging in the confined regions of the plateau borders (Haffner, 2014). Among them, one of the important parameters controlling the drainage behavior of foams with hydrophilic particles is the confinement parameter, $\lambda = d_p/d_c$, which relates the diameter of the particle d_p to the maximum diameter of the circle inscribed in the plateau border cross section, d_c (figure 2.12). The hydrophilic particles are trapped in network of aqueous foams either by the mechanism of collective trapping- jamming of the suspension for $\lambda<1$ or by the individual capture of the particles by the foam constrictions for $\lambda>1$.

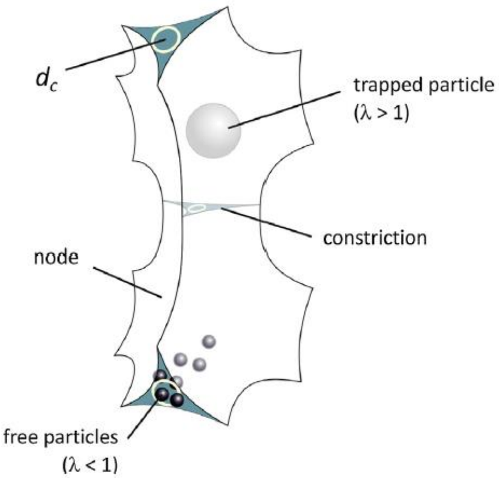

Figure 2.12: The interstitial network of aqueous foams consists of nodes connected by constrictions. Particles suspended in the interstitial fluid can be either freely transported or trapped by constrictions. This behavior is described by using the so-called confinement parameter, λ, that compares the particle size to the size of passage through those constrictions d_c.

The other important parameter is the volume fraction of particles in the interstitial phase of the foam, ϕ_p. It has been found the foam drainage velocity is sufficiently reduced when ϕp is sufficiently high even if $\lambda<1$. Haffner (2015) investigated the joint effects of the volume fraction of particles in the interstitial phase of the foam, ϕ_p and the confinement parameter λ on the foam drainage in the presence of hydrophilic particles. In this study, all the regimes and transitions of reduced foam drainage velocity induced by the presence of hydrophilic particles are identified experimentally based on ϕp and λ. The authors identified the particle inclusion/exclusion transition, which refers to the transition from full inclusion to full exclusion of the solid particles with respect to the foam network. This transition makes the foam drainage velocity evolve from its minimal value (fully included particles) to its maximal value (fully excluded particles) due to the decrease in fraction of the particle surface area in contact with the foam network and consequently the reduction of the drag experienced by the draining liquid. Different regimes are identified by the two values of the confinement parameter, λ_c and λ^*, that correspond to the end of the flowing suspension regime and to the minimum foam drainage velocity respectively. Specifically, five regimes are identified for the low and moderate particle volume fractions (ϕ_p <0.4):

a) Flowing suspension regime ($\lambda<\lambda_c$), where the drainage velocity is almost constant for $\phi_p<0.16$ or decrease slightly
b) Capture transition regime ($\lambda_c < \lambda < \lambda^*$), where the drainage velocity decreases significantly (for $\phi_p< 0.4$)
c) Maximum frictional drag regime ($\lambda=\lambda^*$), where the drainage velocity becomes minimal
d) Particle exclusion transition regime ($\lambda^* < \lambda < 10$), where the drainage velocity increases to the values that are close to the velocities in the first regime
e) Minimal frictional drag regime ($\lambda<10$), where the increase in the drainage velocity is much less pronounced than the one in the previous regime.

The authors also identify the region of the jammed state for $\lambda<1$

$$\frac{\varphi_p^{pack}(\lambda)}{\varphi_p^{pack}(0)} \sim 1 - \frac{\lambda}{3} + 0.1\lambda^2 \tag{2.12}$$

And for λ>λ*

$$\varphi_p^{pack} \sim 6\,\frac{1-\varepsilon}{\varepsilon}\left(\frac{\lambda}{C(\varepsilon)}\right)^3 0.72\,\frac{C(\varepsilon)}{\lambda} - 1 \tag{2.13}$$

Where ε=0.1, ϕ_p^{pack} (λ) is the critical particle volume fraction beyond which the particle packing occurs, ϕ_p^{pack} (0) represents the value of ϕ_p^{pack} (λ) for unconfined conditions, and

$$C(\varepsilon) = (1 + 0.57e^{0.27})/(0.27\sqrt{e} + 3.17e^{2.75} \tag{2.14}$$

obtained from numerical simulations of foam structures.

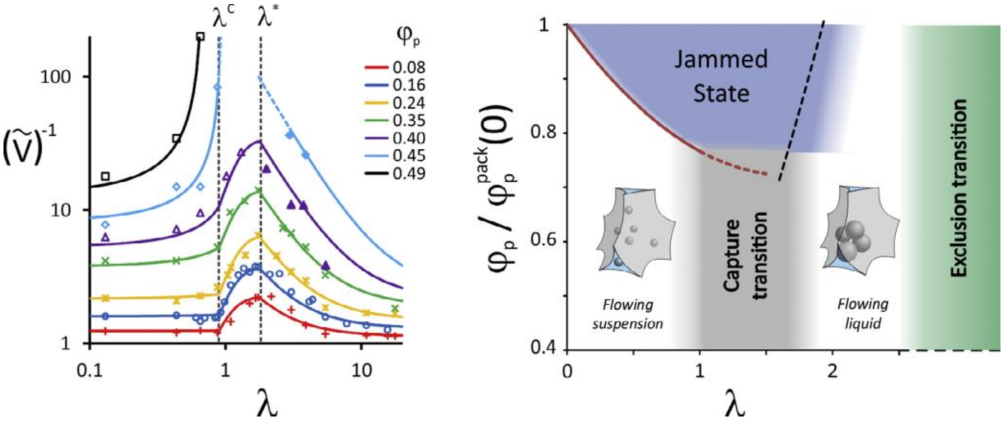

Figure 2.13: Reduced viscous drag (inverse of the reduced drainage velocity $\tilde{V} = V/V_0$ where V and V_0 are foam drainage velocity (with and without particles) of foamy suspensions (10 g L_{-1} TTAB in distilled water with 20% w/w glycerol and polystyrene spherical beads with different concentrations) as a function of the confinement parameter λ, with bubble size D_b = 660 mm and liquid fraction ε = 0.1 for different particle volume fractions, ϕ_p. λ_c and λ* correspond to the end of the flowing suspension regime and to the minimal foam drainage velocity, respectively. b: Diagram of the reduced particle volume fraction as a function of the confinement parameter in the foam network. The jammed state domain is deduced from experiments. The red and black lines correspond to eqn (5) and (6), respectively. Adapted from Haffner et al (2015).

As mentioned earlier, these foams have a very low liquid content, and not all findings are applicable. However, the idea of using λ or confinement parameter is a useful tool to study drainage. In particular, it becomes useful for the study of confinement/entrapment as will be discussed in the hypothesis section.

2.10 Rheology

Rheology is the science of flow and deformation of matter. The rheological behavior of a material is typically characterized by the plot of shear stress associated with the shear rate measured by a rheometer. A number of rheograms are illustrated in figure 2.14 below. A fluid may exhibit either Newtonian or non-Newtonian behavior, with the latter including dilatant, plastic, pseudoplastic or Bingham behaviors. A Newtonian fluid exhibits a linear increase of the shear stress as a function of the shear rate. Two important rheological terms which are often associated with rheology studies are: yield stress, which is the intercept of the flow curve on the shear stress axis at zero shear rates; and viscosity, which is the slope of the line connecting the particular point on the flow curve with the origin. The viscosity is constant throughout the entire shear rate range for Newtonian fluids. For non-Newtonian fluids, this is not the case, and the viscosity of a non-Newtonian fluid under specific conditions is referred to as the apparent viscosity. It has been shown that the material flow is significantly different below and above the yield stress (Barnes, 1999).

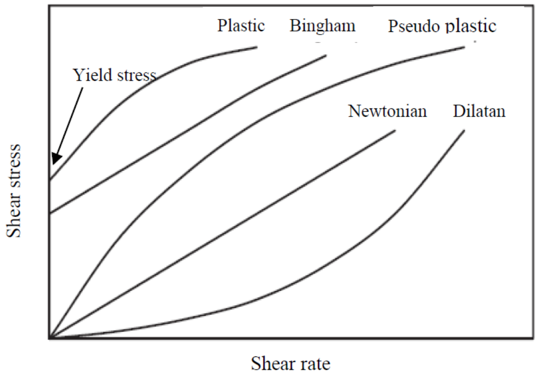

Figure 2.14: Stress vs shear rate responses for particulate suspensions (adapted from Farrokhpay 2012)

Plastic/pseudoplastic behavior is characterized by a reduction in apparent viscosity as the shear rate increases (shear thinning). In mineral suspensions, this is attributed the gradual breakdown of particle aggregates, releasing any trapped inter-aggregate bulk fluid and leading to a decrease in effective solid concentration, which is manifest as a decrease in apparent viscosity. Shear thinning behavior is typical of phyllosilicate minerals, where particles which tend to assume random orientations are progressively aligned in the direction of the flow with increasing shear (Shaw, 1992).

Particle-particle interactions dominate the suspension at intermediate volume fractions, and the material behaves as an elastic solid. When subject to stress, such systems resist flow until the applied stress exceeds the inherent elastic strength of the particulate network. The network of interconnected particles fails and the material shifts to a more liquid like (viscous) state with less resistance to flow (Barnes, 1989). The critical stress where this occurs is termed the yield stress. In other words, it is the minimum force per unit area required in initiating the flow of a suspension in the limit of low shear. This is a useful indicator of changes in the degree of aggregation of suspensions. Viscosity η is a measure of the suspension resistance to flow against applied shear stress. It is a useful parameter in mineral processing applications in determining the effects of process variables such as impeller speed, process time and temperature on suspension flow behavior and subsequent process performance (Bakker, 2010).

The rheology of suspensions depends on the characteristics of the continuous phase and the discrete phase. The viscosity of the suspension η is directly proportional to the viscosity of the liquid (η_l), which might be Newtonian or non-Newtonian. Most rheological models are expressed in terms of the relative viscosity of the suspension η_r (Mewis and Wagner, 2012) defined as

$$\eta_r = \eta/\eta_l \tag{2.15}$$

The relative viscosity of a suspension is a function of the shear rate, the volume fraction of the solid and the particle shape (Mewis and Wagner, 2012). In dilute suspensions (<0.1% v/v), particle-particle interactions are insignificant and the viscosity of the suspension is similar to that of the suspending liquid. Einstein (1956) proposed a theoretical model for relative viscosity of dilute suspensions:

$$\eta_r = 1 + B\phi \tag{2.16}$$

Where B is the intrinsic viscosity and ϕ is the volume fraction of the suspended solids. Einstein also derived that the B is 2.5 for rigid spheres.

Between ϕ of 0.05 and 0.15, the regime is called “semi-dilute” and the interaction between particles starts to influence suspension rheology by dissipating shearing energy, resulting in a significant deviation from linearity. While the effect of particle interactions is complex, it may be expressed as a Taylor expansion in powers of the solids volume fraction:

$$\eta_r = 1 + 2.5\phi + c_2\phi^2 + c_3\phi^3 \tag{2.17}$$

The coefficient c_2 reflects not only contributions from hydrodynamic particle interactions, but also inter-particle forces. Batchelor and Green (1972) identified the coefficient c_2 as 7.6 for spheres.

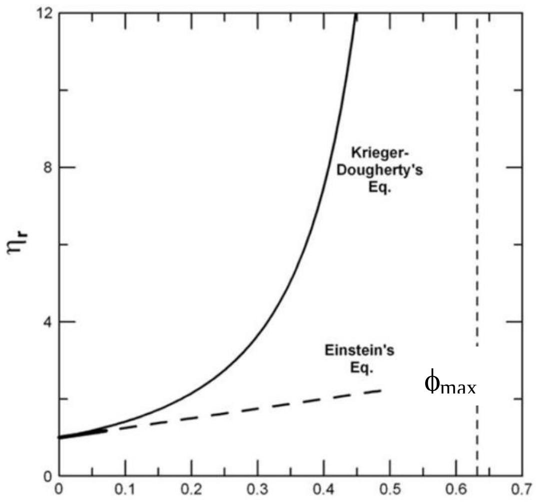

Figure 2.15: Relative viscosity vs volume fraction for semi dilute suspensions

As ϕ increases beyond 0.15, the regime is termed "concentrated", where the role of microstructure is important. Increasing viscosity results in rapidly growing viscosities that finally diverge at maximum packing, which is a dominating characteristic for concentrated suspensions. This is termed ϕ_{max} and its actual value depends on shape, size distribution and packing protocol. A number of semi-empirical equations have been proposed to describe the viscosity-concentration relations of suspensions.

A number of different models have been developed to fit data, but there are two which are most popular. The first one was proposed by Krieger and Doherty (1959)

$$\eta_r = \left(1 - \frac{\phi}{\phi_{max}}\right)^{-B\phi_{max}} \tag{2.18}$$

where B is 2.5 in the case of spheres, like in Einstein's situation.

The second most popular one is the Mooney Equation (1951)

$$\eta_r = \exp\left(\frac{B\phi}{1-\frac{\phi}{\phi_{max}}}\right) \tag{2.19}$$

2.10.1 Measuring rheological properties

There are two types of rheometers: a) the ones where motion is caused by moving one of the walls, which drags the fluid along, i.e. drag flow, and b) one where the sample is forced through a channel by means of pressure. Rotational rheometers are based on drag flow and are the most common devices for measuring rheology of industrial suspensions owing to the small amount of samples required, the ease of completing measurements, and the ease of data analysis. Rotational rheometers involve the relative rotation about a common axis of one of three geometries: coaxial cylinders, cone and plate, or parallel plates, as shown in the figure 2.16 below. The gap between the stationary and rotating parts needs to be as small as possible to avoid velocity gradients in the gap. The most typical type of coaxial geometry is the concentric cylinder rheometer, in which the inner cylinder rotates and the outer cylinder is fixed (or vice-versa). The material filling in the gap between the cylinders is sheared by the rotating cylinder; owing to its viscous nature, the material resists the cylinder rotation and a torque is detected by the rheometer. The relative rotational speed between the two cylinders is converted to a shear rate, and the torque detected is converted to a shear stress. Experiments may be conducted under viscometric flow (steady) or dynamically by using oscillatory techniques.

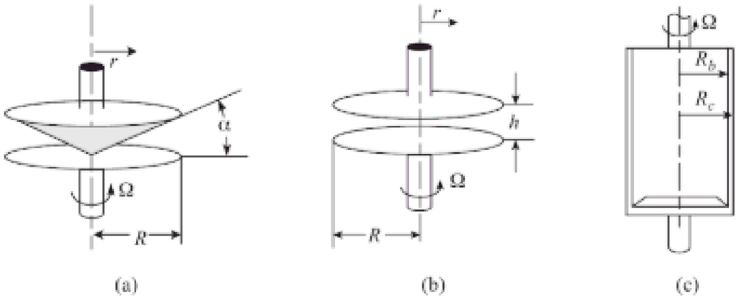

Figure 2.16: Rheometer types (adapted from Mewis and Wagner, 2012)

A key problem for rheological measurements for mineral suspensions is the aggregation and rapid settling of particles (Kawatra and Bakshi, 1996). Using a couette rheometer this problem can be addressed. Smaller gap sizes are optimal, but the coarse particles in mineral suspensions do not allow for very small gaps. Increasing the gap size results in non-uniform shearing across the annulus, this results in artifacts in the dataset. Several correction factors have been proposed, such as the Couette flow, Bingham approximation and the Tikhonov approximation (Boger, 1999, Barnes and Nguyen, 2001).

Constitutive relationships can be used to approximate rheological properties based on steady shear data. Newtonian fluid behavior can be characterized by the Newtonian model, while the Hershel Buckley model, provides a generalized model for non-Newtonian fluid behavior from which other non-Newtonian models can be derived. This is dependent on the presence of a yield stress and the value of the flow behavior index n, which is representative of shear thickening/thinning characteristics of the suspension. A power law model may be used when the suspension is either pseudoplastic or dilatant; when n>1, the fluid is dilatant and when n<1, the fluid is pseudoplastic. Mineral suspensions often report as pseudoplastic with n<1 or n=1. The yield stress is approximated by extrapolating curves of shear stress vs shear rate to zero or low shear, and the viscosity term is derived from the appropriate mathematical model. The Bingham and Casson model is often used in the classification of the rheological behavior of a mineral suspension. The various models are shown below:

Newtonian model: $\tau = \eta_p \gamma$

Herschel Buckley model: $\tau = \eta_0 + \eta_p \gamma^n$

Power Law model: $\tau = \eta_p \gamma^n$ where n>1

Pseudo plastic: $\tau = \eta_p \gamma^n$ where $n<1$

Bingham Plastic model: $\tau = \eta_0 + \eta_p \gamma^n$

Casson model: $\tau^{1/2} = \eta_0 + \eta_p \gamma^{1/2}$

Where τ is the stress, η_p is the viscosity and γ is the shear rate and n is the flow index described above.

2.10.2 Effect of particle shape on suspension rheology

Particles come in a variety of shapes, and this has an effect on their suspension rheology. Fibers and platelets constitute two simple shapes that represent deviation from sphericity, and are shown in figure 2.13 below. When such particles are subject to shear flow they will be dragged along and rotate, as with spherical particles. However, hydrodynamic stresses will depend on the relative orientations of the particles with respect to the direction of the flow, resulting in a time-dependent motion of the particle in steady shear flow. Consequently, the rheology of a suspension of non-spherical particles will depend on orientation. All the shapes can be characterized by an aspect ratio, defined as a ration of the dimension along the symmetry axis to that in the cross direction. The aspect ratio can be larger or smaller than unity; the spheroids are then prolate or oblate, with aspect ratio greater or lesser than 1 respectively.

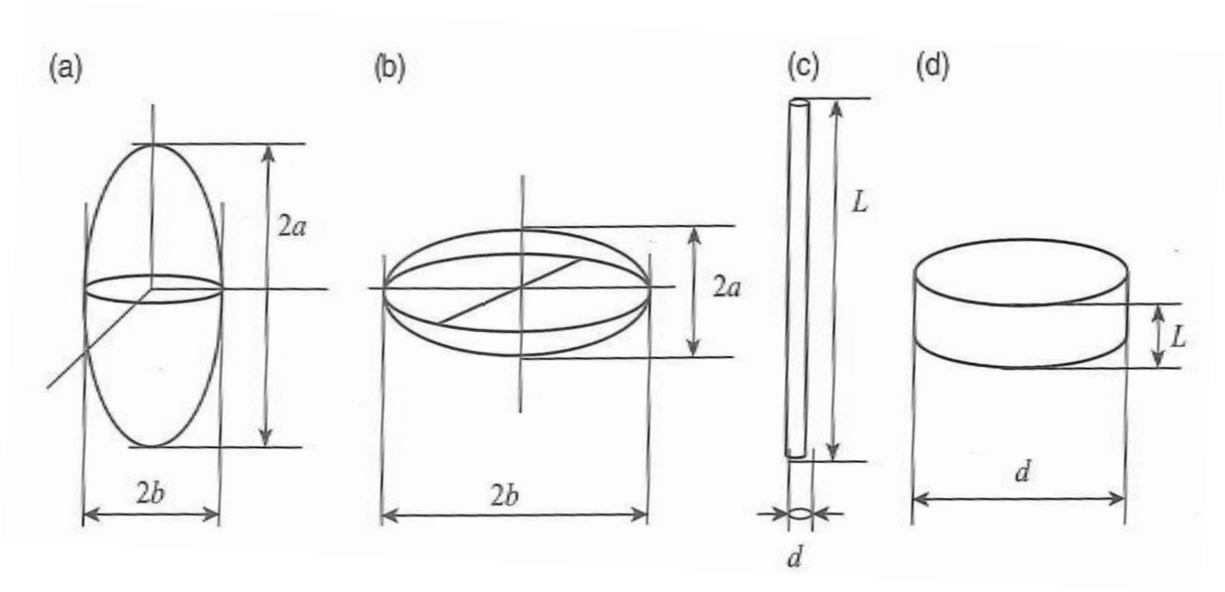

Figure 2.17: Basic geometries of axisymmetric particles: (a) prolate spheroid, (b) oblate spheroid, (c) rod or fiber, (d) disk.

Lauffer (1944) showed the effect of aspect ratio on zero shear viscosity using tobacco mosaic viruses with various aspect ratios. Viscosity increases with increasing aspect ratio and becomes substantially higher than that for spheres.

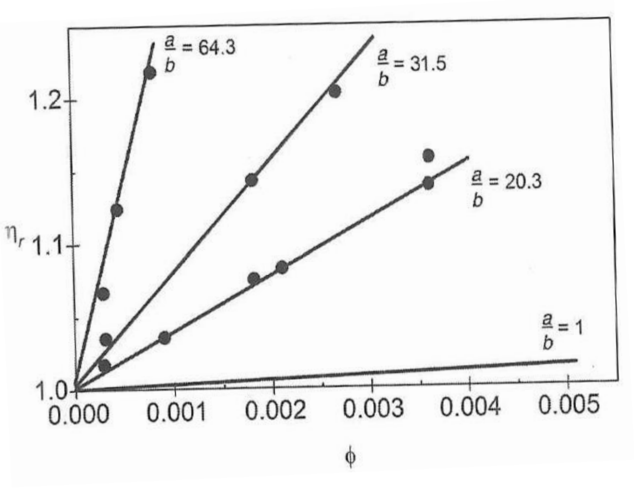

Figure 2.18: Zero shear relative viscosity of dispersions of non-spherical particles: tobacco mosaic viruses with different aspect ratios (adapted from Lauffer (1944)).

While these results are for dilute suspensions, the same can be said for concentrated suspensions as well. Volume fraction dependence on viscosity can be correlated by considering the maximum packing fraction. For nearly spherical particles, maximum random packing increases substantially with anisotropy, from 0.638 to nearly 0.74 as shown in Figure 2.15. At higher aspect ratios, however, there is a substantial decrease in maximum packing fraction, as shown in figure 2.15 (b) for sphero-cylinders.

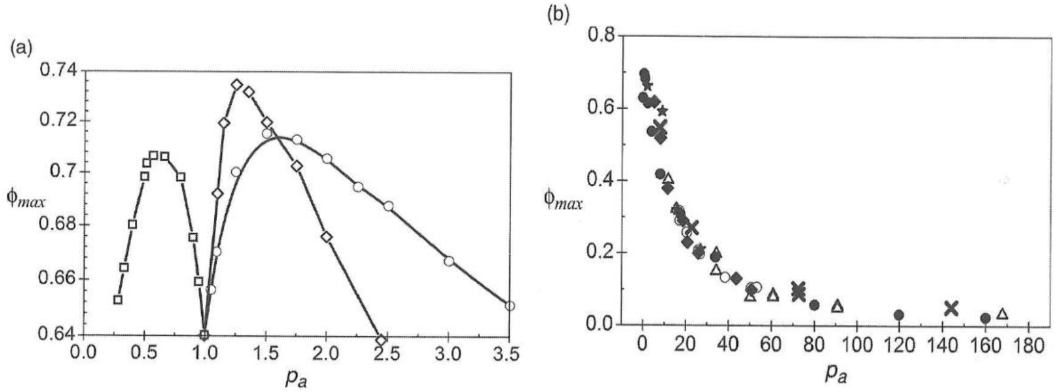

Figure 2.19: (a) Random packing packing fractions vs aspect ratios- small aspect ratio oblate spheroids Pa<1- squares, Pa>1- circles, as well as biaxial spheroids (diamonds), after Donev et al (2004), (b) comparison of simulation and experimental data for the maximum packing fraction or sphero-cylinders as a function of aspect ratio (After Williams and Philipse (2003).

Considering effect of aspect ratio on maximum packing, higher viscosities can be expected for suspensions of long slender objects than spheres at high volume fractions. However a maximum has been observed, and this is related to improved alignment with increasing concentration. Alignment greatly increases maximum packing fraction.

Viscosity-volume fraction relationships have been developed for the dilute, semi-dilute and concentrated regimes as a function of aspect ratio. Separate relationships are required for low Per (rotational Peclet number) limit and the high Peclet number limit, which are included in Mewis and Wagner (2012). In the concentrate regime, for long slender particles, inverse proportionality between ϕ_{max} and aspect ratio has been proposed, and the Krieger Doherty or Maron Pierce equations have been used to fit the data, with B being an adjustable fitting parameter (Egres and Wagner, 2005). This has been the approach in the current work as well.

Dispersions of plate like particles such as clays show increased ordering and alignment under flow with increasing volume fraction. However, experiments on clay dispersions suggest the flow alignment becomes independent of volume fraction for concentrated systems. Results for dispersions of kaolin clay (Pa ~ 10-12) shown in Figure 2.16 illustrate a nearly constant viscosity at low concentrations, and follow the Herschel-Buckley model at high concentrations, where a yield stress is evident. The samples show ageing and have a dependence on shear history.

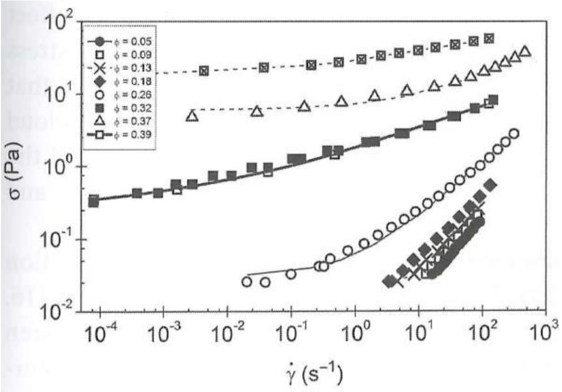

Figure 2.20: Shear stresses for dispersions of kaolin clay at various volume fractions, lines are fits (adapted from Jogun and Zokuski, 1999)

In the mineral processing field, suspension rheology has been studied widely. Extensive reviews have been completed by Farrokhpay (2012). The effect of slurry rheology on grinding performance is well understood (Klimpel, 1999, Shi and Napier-Munn, 2002). In addition the effect of pulp rheology on kinetics of flotation in the pulp phase has been described in section 2.11.2 below.

2.10.3 Rheology of foams and froths

Foams are gas-bubble dispersions in an aqueous solution, with a packing fraction above a critical value (Cohen-Addad and Hohler, 2014). When gas volume fraction is less than 0.73, bubbles disperse in the liquid phase without being attached to one another; when gas volume fraction is greater than 0.73, bubbles start to pack and are separated by thin-plane-parallel films called lamellae forming polyhedral cells. The thin lamellae meet in lines called plateau borders and the lines meet at vertices (Bikerman, 1973). In a foam, volume fraction of air is very high and exceeds packing concentration of rigid sphere suspensions (Herzhaft, 1999). Foam rheology is affected by bulk liquid rheology, gas volume fraction, and the bubble size. In wet foams, in which air bubbles disperse in the continuous phase as rigid spheres, probability of bubble collisions is low, although bubbles do confine each other, and the disjoining pressure plays a role determining the stability of the film. When shear is applied to wet foam, the energy is dissipated largely due to the shearing of the liquid in the foam; consequently, the foam rheology is dominated by the bulk fluid rheology. In a foam with medium water content, energy dissipation occurs as a result of shearing of both the bubbles and the liquid.

The resistance to bubble deformation is the foam dilatational rheology. This is determined by the bubble surface tension, in turn influenced by bubble size and surfactant concentration. The resistance to bubble rearrangement is the shear rheology, which is defined as the friction between the lamellae (Maestro et al, 2015). Bikerman noted that the lamella was significantly more viscous than the bulk liquid, owing to the surfactant induced reduction in surface mobility. The length of the lamella in a given volume of froth is determined by the bubble size. A bigger mean bubble size in the froth reflects lower total lamella length, and so for a foam with medium water content, the foam rheology is determined by the liquid rheology, gas holdup and bubble size. In dry foams, when volume fraction of water is low, energy is dissipated mainly to shear bubbles and foam rheology is dominated by bubble size. In addition, the foam has a yield stress. A capillary viscometer is the instrument of choice for studying foam rheology (Mewis and Wagner, 2012).

The presence of solid particles at a gas-liquid interface changes its rheological and morphological characteristics. Levine (1999) noted that once particles arrive at the interface, they remain trapped irreversibly, and no partitioning of the particles between the fluid phases occurs due to the high detachment energies involved. Interfacial surface tension decreases and the rigidity of the interface increases. The higher the interfacial packing density, the more rigid the interface, and the higher the dilatational viscosity (Maestro et al, 2015). Studying flotation froth rheology is challenging as the froth breaks or collapses in seconds. Shi and Zheng used a vane rheometer due to the advantages described in section 2.6.1 and measured froth viscosity and observed useful correlations for recovery and grade. Li (2016) improved on this technique by using a vane protected from horizontal flow motions by a cylinder, and measured the relationships between froth properties such as airflow rate and bubble size, and its rheological properties. In this work, it was demonstrated that mineral froths are shear thinning and have a minor yield stress. A model structure was developed relating the apparent viscosity of a flotation froth to other properties as shown below:

$$\eta = (\varepsilon_f - 0.73)\left(\frac{D_{32}\dot{\gamma}}{2k_0\vartheta}\right)^{-0.5} \tag{2.20}$$

where η is the apparent viscosity of the froth, ε_f is the gas hold-up, D_{32} is the Sauter mean bubble diameter in the froth (defined as the diameter of a sphere that has the same volume/surface area ratio as a particle of interest), $\dot{\gamma}$ is the shear rate, ϑ is the fraction of lamellae covered by solids, and k_0 is a fitting constant.

A number of researchers are focused on the study of rheology of foams and froths. However, in this work, the focus is the rheology of the froth interstitial suspension.

2.11 Non-sulfide gangue minerals in flotation

In the flotation of sulfide minerals from their ores, the value minerals only represent 1-2% (w/w) of the ore. The largest component in the ore is non-sulfide gangue minerals, which typically comprise 85-95% of the ore. These are mostly sodium and potassium silicates, aluminosilicates, carbonates and oxides-hydroxyoxides. The silicate minerals are typically the most prominent species. They are classified into six or seven categories based on the structure of the silicate anion:

a. Neosilicate such as those in the olivine group
b. Sorosilicates such as those in the epidote group
c. Cyclosilicates such as those in the tourmaline group
d. Inosilicates such as those in the pyroxene and amphibole groups
e. Phyllosilicates such as micas and clays
f. Tectosilicates such as quartz and feldspars.

In the flotation of sulfide minerals, the most problematic silicate group is the phyllosilicates. The nature of the problems observed in flotation attributed to these minerals varies. One class of problems involves the mineral talc, which is part of the phyllosilicate family. Talc represents the final alteration product of the various magnesium silicate minerals serpentine, pyroxene, amphibole and olivine. Talc is naturally hydrophobic, and when present in ores, reports to the concentrate by true flotation. It competes with value Cu or Ni minerals for space in the froth zone, thus reducing their flotation rate and contaminating the concentrate. When more than 2-3%

of the ore is talc, it must be either recovered by flotation prior to recovery of value metal containing minerals, or its flotation rate must be depressed by the addition of depressants. Similar problems are encountered when organic carbon is present in the ore. This class of problems is not part of this thesis. The second class of problems is one where the non-sulfide gangue minerals are hydrophilic in nature. These are described in section 2.9 below.

2.11.1 Mineralogy of phyllosilicates

Phyllosilicates comprise tetrahedral ‘T’ and octahedral ‘O’ layers which are the building blocks of this group of minerals. A tetrahedral layer consists of silica tetrahedral units. Within each unit, four oxygen atoms are arranged symmetrically around a silicon atom. Successive tetrahedra are held together by shared apical oxygen atoms to form rings of tetrahedral T layers. An octahedral unit consists of a central cation in a six-fold co-ordination bonded to six hydroxyl groups, resulting in octahedral symmetry. These hydroxyl groups are linked to other surrounding metal atoms. The cations in the octahedral unit can either be divalent (Mg^{2+}) or trivalent (Al^{3+}). When the cations are divalent, charge balance is maintained when each cation site is occupied and each hydroxyl group is surrounded by three cations forming a trioctahedral structure as in brucite ($Mg(OH)_2$). In the case of trivalent cations, one out of every there cation site is unoccupied and each hydroxyl group is then surrounded by two cations in a dioctahedral structure as is observed in the mineral gibbsite ($Al(OH)_3$). Thus, the phyllosilicates may be classified as dioctahedral and trioctahedral as identified by Klein and Dutrow (1998).

Variations in T and O layer configurations result in minerals of similar structure, but different physical and chemical properties. Consequently, many different classifications exist in the literature (e.g. Dixon and Weed, 1989 and Hurlbut and Sharp, 1998). The classification most appropriate for this work and also used by Ndlovu (2013) is the one used in Deer et al (1992), and is shown in figure Figure 2.21 below.

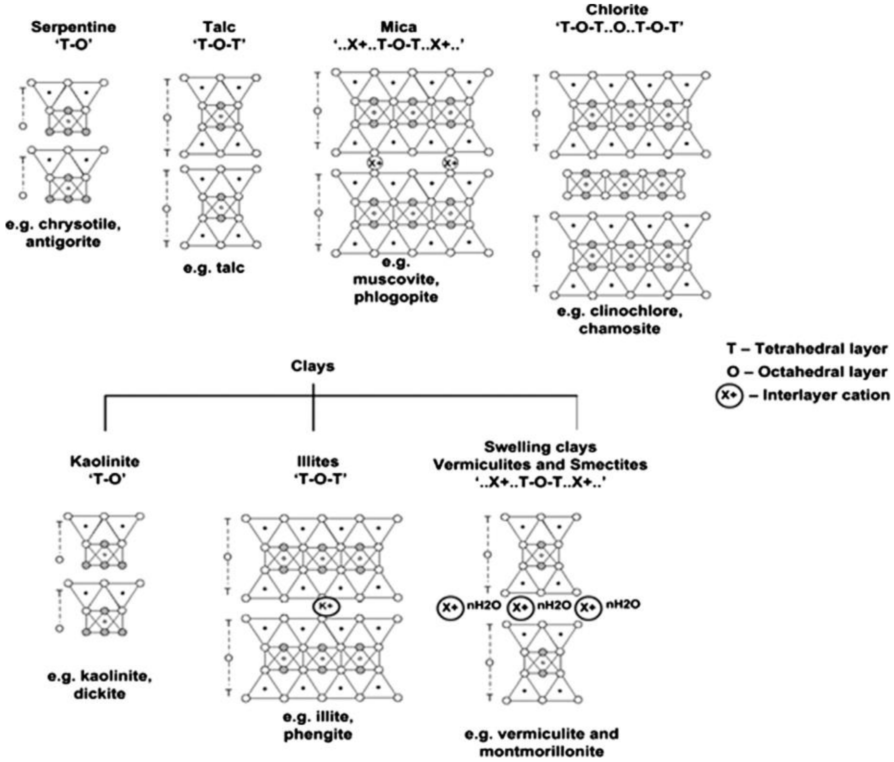

Figure 2.21: Phyllosilicate group classification according to Deer et al (1992) (Adapted from Ndlovu, 2013)

Here, the phyllosilicates are grouped according to the proportion of tetrahedral and octahedral layers, and the interlayer connections that may occur between successive structural units. The groups that emerge are serpentinites, talc/pyrophyllite, micas, chlorites and clay minerals. The clay minerals group is further classified into non-swelling clays (kaolinite and illite), and swelling clays (smetcites and vermiculites). Ndlovu (2013) notes additional important details, which deserve mention here: “There is a distinct different between clays and clay minerals. Clays are sediments which comprise clay minerals and accessory ‘non-clay’ minerals, while clay minerals are pure sheet silicates that are responsible for the classic properties of clay, such as plasticity when wet and hardness when dry or heated. By this definition, bentonite, for example, is a type of clay which is composed mostly of montmorillonite clay mineral and will mimic the properties of montmorillonite, but can include other non-clay minerals or phyllosilicate minerals such as quartz. The difficulty with clay minerals stems from their ability change from one form to another (interstratification), such that they typically comprise alternate layers of other clays in either ordered an regular or highly unordered and irregular sequences. In such cases, mineral identification is difficult as they tend to mask each other.

2.11.1.1 Mineralogy of muscovite

Muscovite $[K_2Al_4Si_6Al_2O_{20}(OH,F)_4]$ is typically produced by the metamorphism of impure limestones. In low grade environments, it is formed by recrystallization of illites $(K_{1.5-1.0}Al_4[Si_{6.5-7}OAl_{1.5-2.0}O_{20}](OH)_4$ and other clay minerals (Deer et al, 1992). It is a 2:1 dioctahedral phyllosilicate mineral with a gibbsite ‘O’ layer sandwiched between two inward pointing silica T layers to form T-O-T units, balancing a negative charge which is thought to be due to the isomorphous substitution of about ¼ of higher valence Si^{4+} cations with Al^{3+} cations of a lower valence in the tetrahedral layer. The negative charges are balanced by interlayer K+ ions which hold subsequent T-O-T structures together.

2.11.1.2 Chrysotile mineralogy

Chrysotile is a trioctahedral magnesium silicate and is a polymorph of serpentine. It forms through the hydrothermal alteration of olivines $[(Mg,Fe)_2SiO_4]$ and pyroxenes $[(Ca,Na,Fe)(Mn,Cr,Al)(Si,Al)_2O_6)]$ (Kirjavanein and Heiskanen, 2007). Unlike symmetrical 2:1 sheet minerals like muscovite, serpentine minerals consist of a silica tetrahedral layer bonded to a brucite octahedral layer in a 1:1 ratio, to form T-O sheets. However, there is a mismatch between these layers, causing a strain in the T-O lattice. The adaptation of the T and O layers to this mismatch results results in the formation of three polymorphs, antigorite, lizardite and chrysotile. In antigorite, the strain is relieved by the bending and periodic rotating of the T layers, resulting in corrugated structures. Alternatively, the minor substitution of Al^{3+} for Si^{4+} ions in the T-layers results in the formation of lizardite. In the case of chrysotile, the strain is relieved by the extension of the brucite O layer to form convoluted T-O tubes with the silica T layer bent on the inside and the brucite layer exposed on the outer face of the tube (Klein and Hurlbut, 1993). The bending of the T-O sheets results in long, spiral chrysotile fiber like microstructure. This internal spiral configuration means that the T-O edge occurs at the end of each tube and runs along the length of it. The continuous curvature of the chrysotile T-O microstructure results in a much more complex morphology than the familiar plate/stacked composition of most phyllosilicate minerals. Individual chrysotile particles typically have a long, thin, fibrous morphology and are able to orient themselves in several different directions in suspension (Ney, 1973).

2.11.2 Morphology of the minerals

The morphology of the various mineral species is critical to the hypothesis of this thesis. The movement of particles in a fluid is dependent on shape, as the shape influences drag. The drag experienced by the particles affects the particle orientation, packing and flow behavior and thus the rheological properties in suspension. It is well known that suspension rheology is more pronounced with a larger deviation from sphericity, with higher yield stresses and viscosities observed in suspensions containing platy and needle/rod shaped particles relative to spherical particles (Barnes et al, 1989).

The morphology is analyzed by using SEM. As noted by Ndlovu (2013), one cannot make inferences on the particle networks and agglomeration behavior of the minerals from the images given the highly randomized structure that arises from the capillary forces as samples dry during preparation for SEM imaging. However, differences in particle packing behavior and resultant apparent volumes arising from differences in shape can be deduced. The morphology can be used to determine the aspect ratio of the mineral in question. The aspect ratio is defined as the ratio of the length of the basal plane to the thickness of the edge for mica. Particle crystallinity also contributes particle alignment and rheology; crystalline particles have smooth surfaces which enhance alignment along basal planes. Particles of low crystallinity comprise complex rough structures and particle alignment is compromised by randomized formation of surface microstructures (Zbik and Smart, 1998).

The morphological characterization is critical as the light scattering based particle size instruments are designed and calibrated with the assumption that the particles tested are largely spherical. The typical non spherical morphology of phyllosilicate minerals renders the application and results of these robust methods potentially misleading, particularly when viewed in isolation.

Quartz consists of rounded/angular particles [Sharpened wedge like particles are observed, some hexagonal and cubic particles are present]. Ndlovu (2013) mentions that the shapes are subject to geological origin, and breakage mechanism attributed to the size reduction process used to prepare the sample. Despite this, aspect ratio of silica is about 1. The most efficient arrangement of these particles occurs by the close packing of congruent particles, with smaller particles likely filling the gaps between larger particles (Laskowski and Pugh, 1992).

Muscovite typically consists of long thin platy particles with with platy morphology preserved even as particles are ground. Plates sometimes appear stacked due to friction that occurs between the grinding media and muscovite particles during size reduction. This causes spreading of the surface flakes in directions parallel to the shearing movement and likely results in thinning and superimposition of the plates (Ndlovu, 2013). Deer et al (1992) state that the basal face area for muscovite can be 50-80 times the edge area. The muscovite platelets are smooth crystalline surfaces.

The fibrous ore contains about 1% chrysotile by weight. The chrysotile fibers are visible in the SEM images shown in the next chapter. The fiber thickness is less than 0.1 microns, with lengths from 100-500 microns, resulting in an aspect ratio of between 1000 and 10000. The flexibility of the fibers is also demonstrated. Together with the long, thin morphology, the flexibility results in a large effective volume swept by the fiber, which is significantly more than the actual volume of the fiber. The fibers are entangled within themselves and with adjacent fibers resulting in a mesh like structure. Other particles are observed to be trapped within this network structure.

2.12 Hydrophilic phyllosilicates and related problems in flotation

When hydrophilic phyllosilicates are present in the ore, another class of problems in flotation is observed. Ndlovu’s (2013) review article covers the impact of phyllosilicates in the mineral processing industry. The phyllosilicates have the potential to significantly affect the planning operation and economics of mineral processing plants. There are three main pathways by which these minerals are known to interfere with flotation:

2.12.1 Heterocoagulation or “slime coating”

This refers to the coating of these gangue minerals on value minerals such as chalcopyrite. The silicates are hydrophilic and thus the coating prevents collector adsorption on the values resulting in slower kinetics and even lower recoveries (Arnold and Aplan 1986). Because the minerals that coat the values are generally fine in size, this phenomenon is termed slime coating. Slime coating can be attributed to non-silicate minerals as well. For the coating to occur, there must be an attractive force between the silicate and the value mineral. For the longest time, electrostatic attractions were deemed responsible for the slime coating (Fuerstenau, 1958). However, the ensuing research showed that the charge wasn't the only factor controlling the slime coating, and the DLVO and extended DLVO theory provided a better explanation of the observed data (Yu et al, 2017). Some authors suggest that grinding can also produce fines, and van-der Waals forces can then cause slime coatings (Chen, 1999). Ma et al (2014) note that calcium released from hydrolysis of gypsum reacted with Na_2CO_3 in the slurry to produce calcium carbonate precipitate which affected the recovery of a molybdenum ore. Vasudeven's (2010) work showed that the presence of aqueous species Ca and Mg species can have a significant effect on recovery, with the precipitate species being gypsum ($CaSO_4$). Edwards (1980) demonstrated the use of SEM to visually observe slime coatings. Electrokinetic measurements, induction time measurements, interfaction force measurements by AFM and QCM-D measurements can also be used to observe slime coatings. The factors affecting slime coatings include pH, ionic strength, electrolytes, mechanical energy in the system (turbulence) and material properties of the minerals. In most cases, it was found that the use of dispersants such as CMC, sodium silicate and polymers could restore the recoveries (Vasudevan et al, 2010). Physical methods such as desliming, high intensity conditioning and ultrasonic treatments were also found to alleviate the problem.

2.12.2 Modification of slurry rheological properties

These effects are related to dispersion/aggregation state of the silicate minerals. At low concentrations, no aggregates form and suspensions exhibit Newtonian behavior. Increasing solids concentration results in interactions between the particles and deviation from Newtonian behavior. A number of studies show a strong relationship between flotation performance and pulp rheological properties. The silicate minerals influence the rheological properties, thus changing the hydrodynamics within the cells to affect the various sub-processes in flotation including gas dispersion and particle bubble attachment, and the mobility of particles and mineralized bubbles in the pulp phase (Bakker, 2009). In the case of poor gas dispersion, the small bubbles generated within the vicinity of the impeller are not efficiently dispersed throughout the cell by bulk fluid flow due to the high viscosity of the slurry. This is exacerbated by the formation of region with yielded fluid (cavern) within the vicinity of the impeller, while the rest of the slurry remains stagnant (Bakker et al, 2009, Shabalala et al 2011). Patra et al (2010, 2012) identified that serpentine minerals form a network like structure in the pulp phase which gets lifted into the froth phase via bubble flux/bubble entrapment. The structure formation is readily detected with a significant increase in yield stress and viscosity and attests to the role of pulp rheology. The result, in this case, is poor final concentrate grade and slower Ni flotation kinetics at the low serpentine content, and poor recovery to no flotation at very high serpentine content (Figure 2.24)

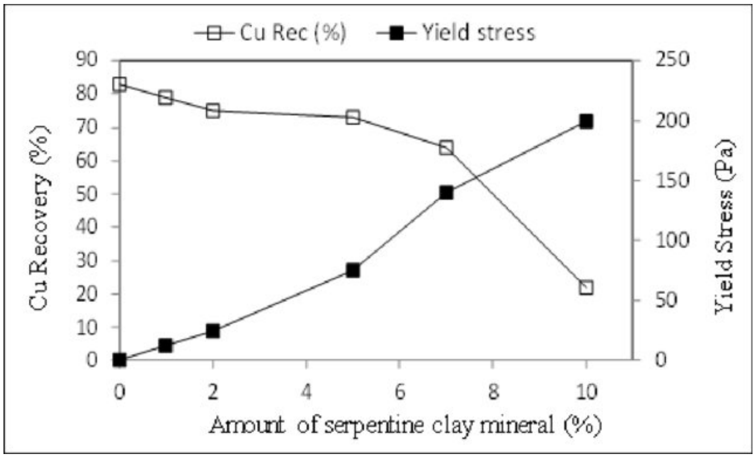

Figure 2.22: Increasing yield stress with increasing fibrous mineral content and resulting impact on Cu recovery (Adapted from Patra 2010, 2012)

The increase is viscosity results in a decrease in turbulent energy dissipation. Owing to different compositions, structures and charge properties, the other phyllosilicates form different network structures and thus affect flotation in different ways. Ndlovu (2013) compared the rheological properties of suspensions of various clays minerals and reported a critical concentration beyond which the non-linear increases in yield stress and viscosity were observed, which correlated with the onset of problems in flotation. While chrysotile had a critical concentration of 0.7% by volume, montmorillionite had a critical concentration of 4% by volume, kaolinite was problematic beyond 10% by volume, and illite and muscovite did not show yield stresses even at 30% solids by volume. In this work the yield stress behavior was compared to quartz, which did not show a yield stress even at 40% by volume, highlighting the rheological complexity of phyllosilicates. This study also concludes that it is unlikely that typical concentrations of kaolinite, illite and muscovite will be problematic in flotation, given the high volume concentrations needed to affect rheological behavior.

Subsequent studies focused on kaolinite, bentonite and mica minerals, with the goal of establishing a correlation between rheological properties and flotation performance. Cruz et al (2015) show the formation of structures and aggregates when kaolinite and bentonite particles are present in the slurry (bentonite being mostly montmorillonite) using SEM image analysis. Zhang and Peng (2015) show a decrease in the flotation recovery, and an increase in apparent viscosity with the addition of bentonite at 15% by weight, and their work was confirmed by Wang (2015) and Basnayaka et al (2017) who demonstrated the effect of bentonite on gold ore. None of these studies mentioned the effect on concentrate grade or mass recovery as being a problem, which is disputed by Farrokhpay (2016). Farrokhpay (2016) demonstrated that montmorillonite influences pulp rheology and flotation recovery and grade, but illite and kaolinite do not. Farrokhpay (2018) demonstrated that a minor effect on pulp rheology was indeed observed for muscovite, which coincided with an effect on concentrate grade; a more plausible explanation is increased entrainment. Zhang and Peng (2015) reported minor effects from crystallinity of the mineral species, with poorly crystalline minerals showing higher viscosities due to increased frictional interaction between surfaces.

2.12.3 Effect of phyllosilicates on entrainment

From the above review, it is apparent that chrysotile and montomorillonite (swelling clays) have a significant impact on pulp rheology translating to slow flotation kinetics, poor gas dispersion and reduced concentrate grade. The other minerals, namely illite, kaolinite, and mica show an effect on concentrate grade, but significantly smaller effects on rheological properties. Minor changes in rheological properties can be attributed to increased particle-particle frictional interactions arising from their morphological asymmetry, but this does not affect flotation recovery. However, their asymmetrical shape can affect entrainment, which is the subject of this section. As described in the section 2.3, entrainment is a mechanical transfer process where particles suspended in water are recovered in the water between bubbles enter the froth from the pulp-froth interface, survive the drainage of water, and are transported to the concentrate. Entrainment is nonselective and primarily responsible for recovery of fine particles. As these phyllosilicates such as kaolinite and illite are soft and tend to be ground fine, they are more likely to be entrained, and negatively affect concentrate grade. Zhang (2015) demonstrated lower concentrate grade with kaolinite compared to flotation of the same ore with 15% quartz that had the same size distribution with kaolinite. The entrainment was correlated to the formation of loose network structures with low density. Illite did not demonstrate the significant effect on concentrate grade. Zhang (2015) also demonstrated that in the presence of sea water, formation of cross-linked network structures were observed, resulting in higher entrainment. Addition of lime and gypsum resulted in more entrainment due to interactions with Ca^{2+} in strengthening the network structure. Addition of gypsum reversed this effect for bentonite, resulting in higher recoveries, but grade suffered as a result of entrainment.

A number of researchers have connected increased entrainment to the formation of network structures by phyllosilicates through the change in pulp rheology and froth rheology. It is not clear whether increased viscosity was truly the cause of increased entrainment. Wang (2015) found that froth stability decreased with the addition of bentonite owing to the increase in pulp viscosity; this was probably attributed to fewer particles making their way into the froth phase resulting in an unstable froth. Tests conducted by Kirjavanein (1992) using phlogopite and quartz at different slurry densities showed that the recovery by entrainment was influenced by slurry viscosity. In this case, an increase in slurry viscosity was not demonstrated *to be a cause* for increased entrainment.

Wiese (2015) demonstrated that particles of 40µ with different shapes have different degrees of entrainment. It was observed that wollastonite and its mixtures reported a higher degree of entrainment than rounded ballotini, or spherical particles. In another paper, Wiese (2016) expanded on the above work and demonstrated that mixtures of ballotini and chromite had a significantly higher degree of entrainment for 25µ size particles, and this was attributed to the increased froth stability. In both these papers, the authors suggest the increased drag forces encountered by non-spherical particles are responsible for increased recovery by entrainment. The drag forces on particles of different shapes can be described by the relationship shown in Eq. 18 below:

$$F_D = \frac{1}{2}\rho v^2 C_D A \tag{2.21}$$

where F is the drag force, C_D is the drag coefficient, ν is the velocity of the particle relative to the fluid, ρ is the density of the fluid and A is the area of the orthographic projection of the object on a plane perpendicular to the direction of motion. The drag coefficient, C_D, is in turn dependent on the Reynolds number which can be determined using relationships such as shown in Eq. 19.

$$C_D = \frac{24}{Re} \times f_D\ (Re) \tag{2.22}$$

where f_D is the drag correction factor. Equations to determine f_D can be found in various references (e.g. Nguyen and Schulze, 2004).Two examples for determining f_D are shown in Eqs. 2.23 and 2.24.

$$F_d = 1 + 0.169Re^{2/3} \qquad 0 < Re \leq 700 \tag{2.23}$$

$$F_d = 1 + 0.216Re^{2/3} + 0.0118Re \quad 0 < Re \leq 1000 \tag{2.24}$$

The drag coefficient is independent of the mass of the particle and hence if ρ, ν and A are approximately constant then cylindrical shaped particles will have a higher drag force compared to spheres. This will result in the asymmetric particles moving up through the liquid and being recovered through entrainment to a greater extent than the spherical particles.

Forbes et al (2014) identified that both slime coating and rheological behavior affected flotation recovery when kaolinite was present above 70% (w/w) in the mineral mixture, with the kaolinite prepared as 80% passing 15µ. Farrokhpay's (2016) suggested that there is an effect on concentrate grade but no effect on recovery with kaolinite, although they only investigated addition of 30% (w/w), with kaolinite being prepared to 80% passing 15μ.

2.13 Gaps in knowledge

In studying the literature of the mechanisms of transfer of hydrophilic solids to the concentrate, often the word entrainment is used as an all-encompassing term as the mechanism for gangue mineral recovery, despite having multiple sub-processes associated with it. At least two main sub processes may be identified: particle transfer to the froth zone, and transfer of particles through the froth zone to the concentrate. Both of these sub-processes have different mechanisms as well as different rates associated with them, and thus need to be modeled differently. This is indeed done for hydrophobic particles, with the term froth recovery being used as described in section 2.5.4, but not for hydrophilic particles. An important first step is taken by Amelunxen (2017) who tried to separate the two sub-processes for batch flotation tests. However, there are some assumptions in this work, such as that all particles being transferred to the froth zone will be recovered by entrainment in bench scale tests, that need to be addressed. In assessing the impact of these minerals, calling the recovery of these minerals as related to entrainment is insufficient because the specific mechanisms may vary.

A review of the literature from flotation tests on the impact of phyllosilicate minerals of intermediate aspect ratio (i.e. muscovite) suggests mixed results. Wiese’s (2015) work on single minerals shows no impact of mica on entrainment. Farrokhpay’s (2018) work shows that there is a decrease in both recovery and grade when mica is added although the size of mica is not specified. There is lack of understanding of the impact on recovery and grade and the amount of mica that has to be present in an ore to impact flotation. This is particularly important given the presence of mica and other clay minerals in many ore bodies around the world (Connelly, 2011, Jorjani, 2011).

The mechanisms or pathways by which muscovite and other intermediate aspect-ratio silicates impact flotation are unclear. Farrokhpay (2018) observes that there is an impact of mica addition on rheological properties and attributes the impact on flotation to entrainment. Wiese (2016), however, does not see an impact on entrainment. Indeed, for a number of phyllosilicate minerals such as kaolinite, montmorillonite and muscovite, most studies note that there is a change in rheological properties but the mechanism by which these minerals affect flotation is not clear. As discussed above, for chrysotile, Patra (2010) have illustrated clearly that reduced gas dispersion leads to lower recoveries, and high viscosities leads to transport of gangue “network” to froth via bubble flux/bubble entrapment. However, for intermediate aspect ratio minerals, visual observations suggest that viscosities of the pulp for these minerals are not nearly as high as for chrysotile. Increased entrainment is observed by Wiese (2016), and attributed to increased drag forces experienced by the particles, but this implies no correlation to the rheology/viscosity effects.

Rheological measurements of mineral slurries are conducted using vane geometry in a rheometer. However, problems due to settling of the solids often complicate measurements. The wide-particle size distribution results in some very coarse particles being present in the ore, and if annular gap is too large, there are velocity gradients that are difficult to account for. At very high shear rates, secondary flows are observed, which lead to Taylor vortices leading to erroneous results.

Few publications discuss effects on flotation for mixtures of particles of different shapes and morphologies (asymmetric phyllosilicates) with other rounded minerals such as quartz, which is what is typically observed in ores. In studies where this is done, the effects are not studied as a function of particle size, whose effect on entrainment is stronger than particle shape.

Very little has been done to differentiate between entrainment and entrapment in the flotation literature. For the most part, entrapment as a mechanism has been ignored and only cited when data does not fit typical degree of entrainment vs particle size curves. This is because the studying of entrapment is difficult.

2.14 Hypothesis statements and experimental plan

Based on the critical analysis of the literature, the following initial hypotheses were developed:

a. Increasing muscovite content in an ore will impact flotation grade significantly.
b. The effect of mica on flotation recovery is a function of its particle size.
c. The effect of muscovite on flotation performance is related to its shape and morphology.
d. The material properties of the interstitial suspension, viscosity in particular, is affected by the size, shape/morphology and concentration of the hydrophilic particles present in it. For platy particles, viscosity of the suspension is greater than that for just globular silica particles alone.
e. The increased viscosity is implicated in the reduced drainage rates of the suspension through the plateau borders, resulting in reduced concentrate grades.
f. Bulk rheological measurements of froth interstitial suspensions can explain and predict the observed impact on flotation response.

Bulk rheological measurements indicated that the difference between relative viscosities between mica and silica of the same size were too small. Bulk rheological measurements thus cannot be used to explain the observed higher retention rates of mica in the froth zone. To this end, a second hypothesis was developed.

Hypothesis 2 states that the increased retention of mica as compared to silica is related to its confinement in the plateau borders and vertices, and thus confinement behavior is a function of particle size as well.

The experimental work to test these hypotheses is as follows

1. A thorough assessment of the impact of mica on flotation outcome was conducted. This was done with three types of flotation tests
    a. Addition of mica crushed to -2mm size in varying amounts (12.5%, 25% and 50%) to the grinding mill alongside a mica-free ore followed by flotation tests.
    b. Grinding a mica-rich ore to prepare a slurry, and mixing it with a mica-free ore in varying amounts (25%, 50% and 75%), followed by flotation tests.
    c. Addition of mica prepared to various sizes fractions- 0-20μ, 20-50μ, 50-75μ, 75-100μ, 100-150μ, and >150μ in varying amounts (25% and 50%) to mica-free ore, to assess the effect of size.
    d. For comparison, an ore rich in chrysotile was also tested, as done in Patra et al (2010).
2. In order to: a) study the effect of entrainment in a deeper (more realistic, i.e. closer to industrial depths), and b) to study the effect of particles shape on entrainment as a function of height, and c) obtain concentrations of species in the froth interstitial fluid, froth sampling tests were conducted on mixtures of mica and silica of 6 sieved size-

fractions, with a base fine silica, both in the absence and presence of chalcopyrite at two ratios. The results were compared with the findings from froth sampling tests where chrysotile was added to converge on the mechanisms resulting in the transport of these various species.

In this regard, it is important to mention the role of the froth sampling equipment and experimental setup. In the initial phase of the work, experiments were conducted by raising and sampling a nascent froth, which took 10-25s to build depending on particle size of mica/silica mixture. The sampling of the nascent froth is concerned largely with the transport of material into the froth zone as froth is still being built and has not reached its maximum height. The airflow rate is deliberately higher than required for height to reach the top of the sampler. It is thus suggestive of the rate of upward transport of the interstitial suspension. Sampling of the steady-state froth included experiments conducted by: a) raising froth b) reducing airflow rate to maintain the froth height (c) waiting 5 minutes for the froth to reach a steady-state (or a pseudo steady-state). This results in a situation where, as described in section 2.5, the upward flow rate of the interstitial suspension is completely balanced by its drainage rate. These experiments provide insights into the drainage behavior of the suspension. This is illustrated in Figure 23 below. In comparison, for flotation froths there is a net upward flow of the interstitial suspension. The drainage in steady-state froths, thus, is higher than that for flotation froths.

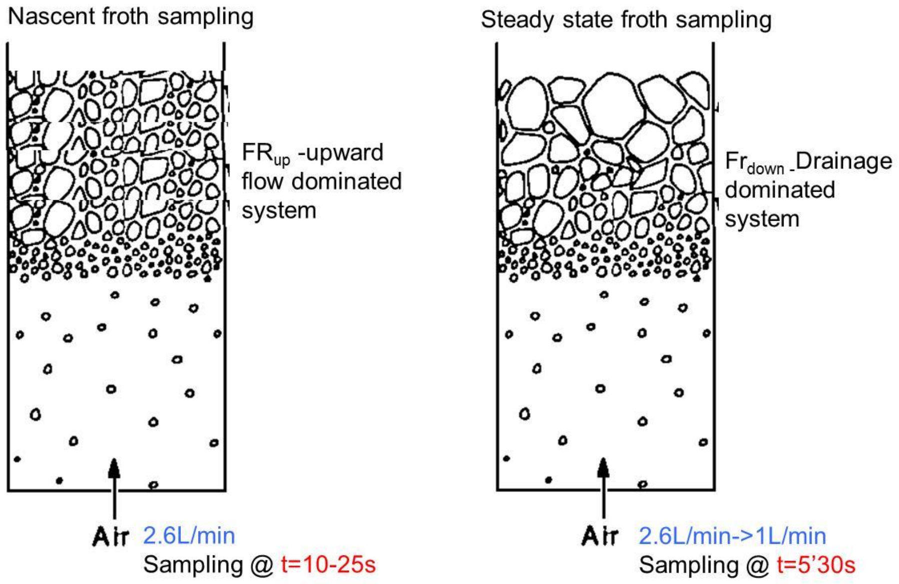

Figure 2.23: Two types of froth sampling experiments- a) drag dominated, and b) drag-drainage balanced

3. The rheological properties of the interstitial fluid were studied. Bulk rheology measurements of the froth interstitial suspension prepared ex-situ were conducted. The concentrations of muscovite and silica (of all sizes) in the interstitial fluid were obtained and rheological tests conducted at a series of volume fractions, and compared with a known problematic system (i.e. chrysotile mixture with silica).
4. In order test hypothesis 2 an experimental setup using a prism mirror attached to the froth sampler was used to image the froth zone. This was used to obtain the dimensions of the plateau borders.

The experimental plan is shown again in Figure 2.24.

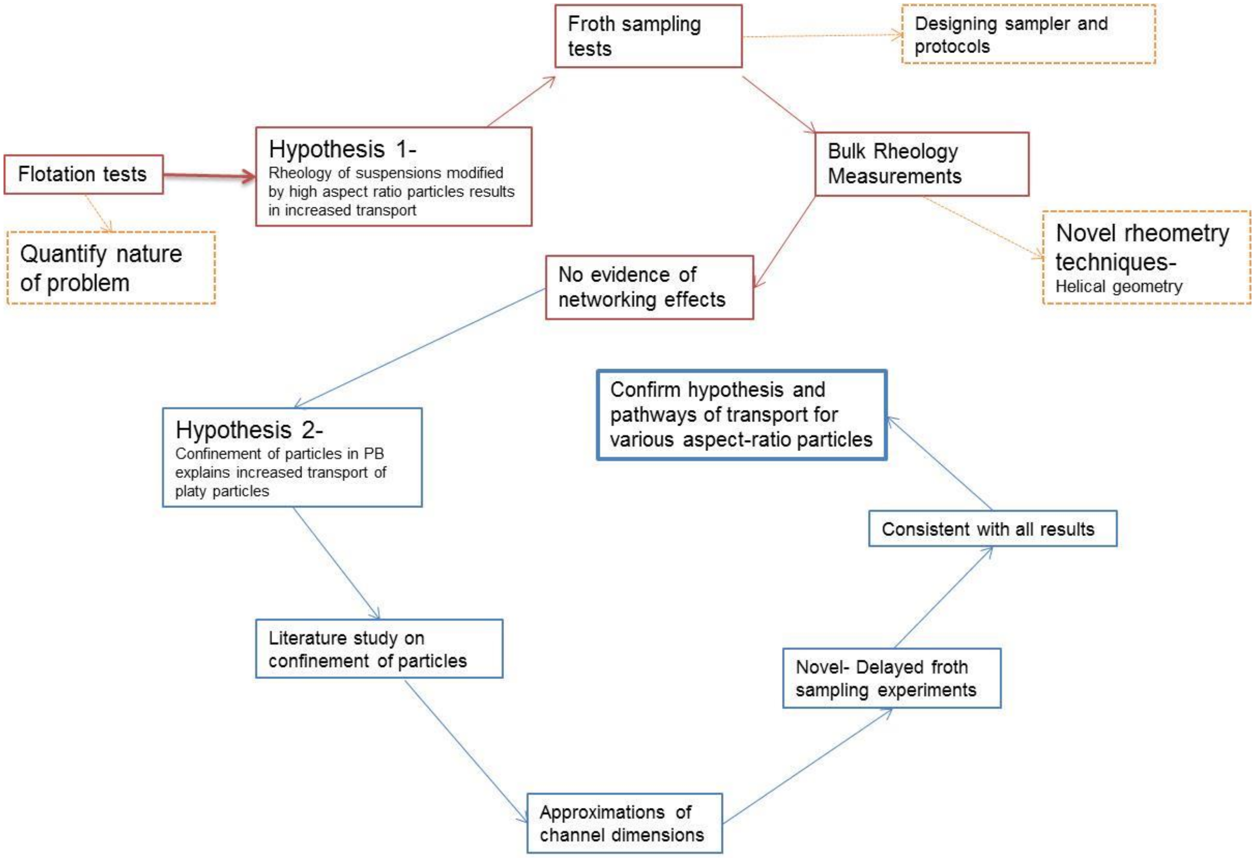

Figure 2.24: Experimental map for thesis, with the red arrows showing the path followed for hypothesis 1. The path for hypothesis 2 is shown with blue arrows. The orange areas indicate additional information

3 Materials and Methods

3.1 Materials- Mineral samples Preparation

3.1.1 High purity muscovite unground

A muscovite sample was obtained from Ward's science. XRD suggests that the sample is very pure (~90% muscovite mica). The same was first broken into pieces using a hammer, and the resulting pieces were manually crushed using a steel plunger in a metal vessel. The discharge was passed through a 2mm sieve. And the retained material was manually crushed again until it passed through the 2mm sieve. This material was added to the mill along with the designated ore for some flotation tests.

3.1.2 Ground muscovite

Ground muscovite was obtained from a commercial mica supplier Pacer Minerals. Their DP700 brand of muscovite is mined in South Dakota and micronized to produce mica of a wide particle size distribution. DP 700 was used as-is in some flotation tests to represent mica that is "as-ground in the mill". Additionally, this mica was then wet sieved through a stack consisting of screens of the following size: 150µ, 100µ, 75µ, 50µ, and 20µ. The wet-sieved material was then dewatered using a vacuum filter, and then dried in a commercial oven at 80C for 6 hours. The sample was then dry-sieved using a Ro-Tap and the resulting size fractions were used in flotation and froth sampling experiments.

Wet screening was used to separate the muscovite because dry screened muscovite, when observed through optical microscopy, showed the presence of a significant number of very fine particles (finer than 10µ) in the mica sample of 100-150µ size. Fine particles can attach to coarse particles, and thus dry sieving alone does not always produce particle size distributions of the right size.

Particle size analysis of the various sieved fractions, as well as the wide particle size distribution mica starting sample (DP700), using the Horiba LA-950 Particle size analyzer (forward angle light scattering based-instrument) is shown below:

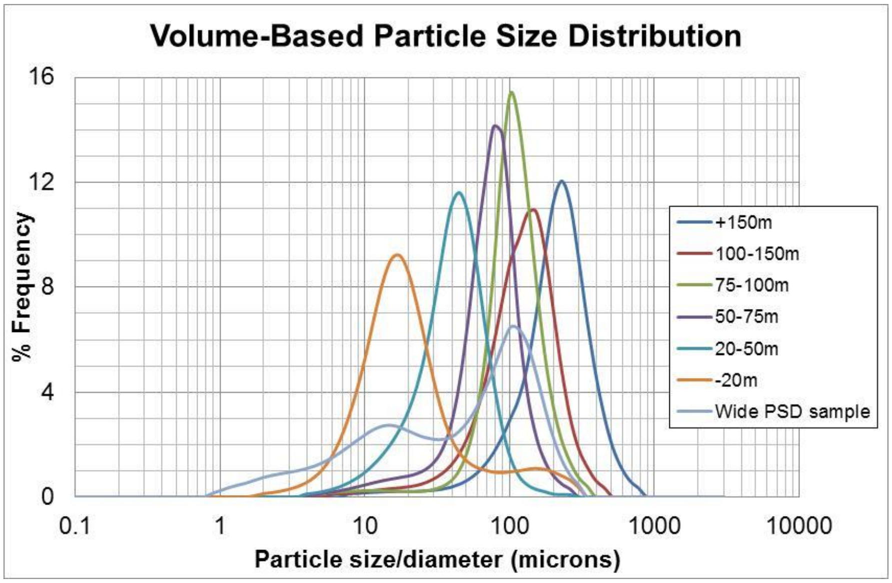

Figure 3.1: Particle size distributions for sieved fractions of mica obtained using Horiba

3.1.2.1 SEM imaging of mica

A Zeiss Sigma VP SEM was used to confirm particle sizes obtained using the Horiba particle size analyzer. The images taken are shown in figure 3.2 below with platy morphology clearly visible.

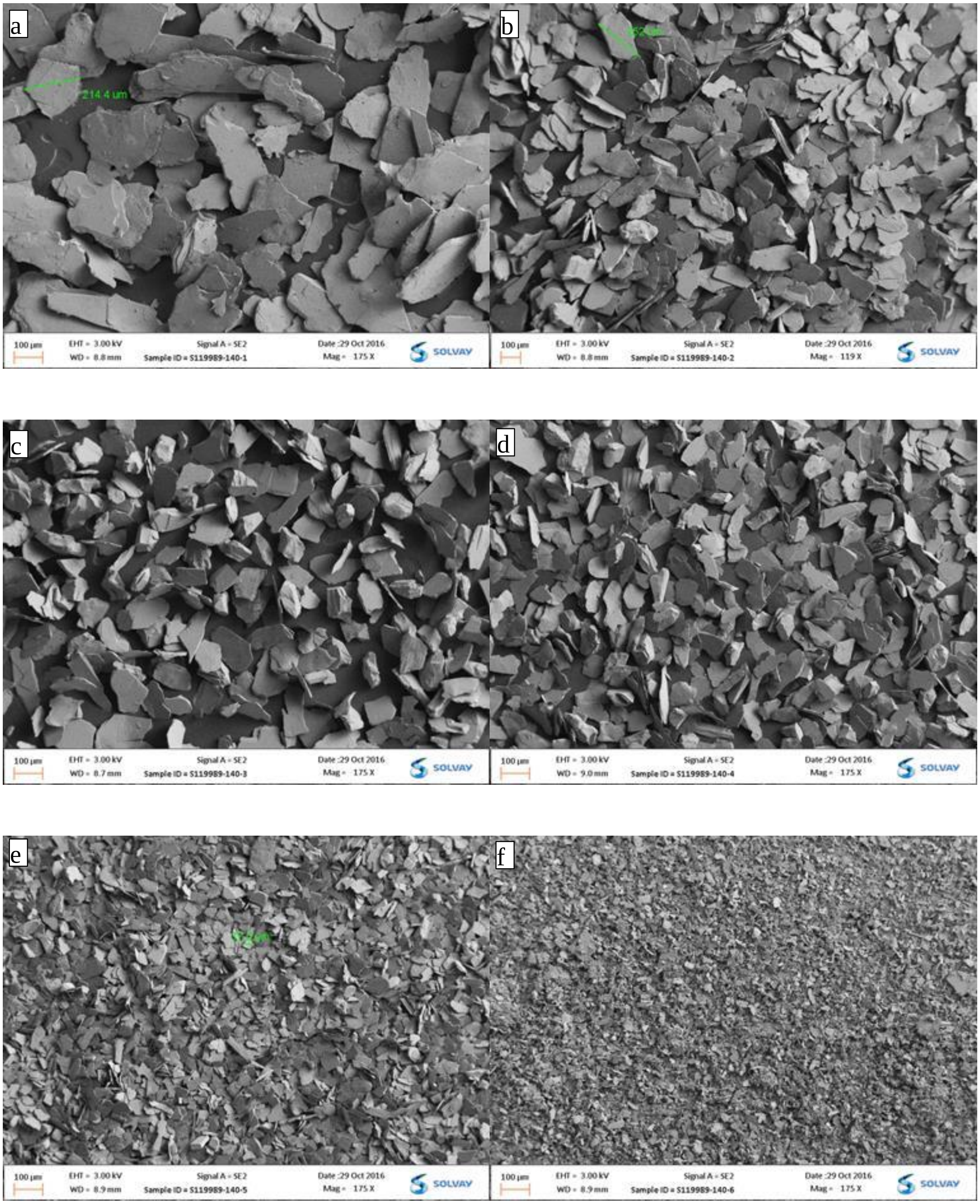

Figure 3.2: SEM images of sieved mica- (a) +150µ, (b) 100-150m, (c) 75-100µ, (d) 50-75µ, (e) 20-50µ, (f) -20µ

3.1.2.2 Aspect ratio of mica

In addition, the aspect ratio distributions of two of the mica samples was obtained using the FLOWCAM instrument made by fluid imaging technologies.

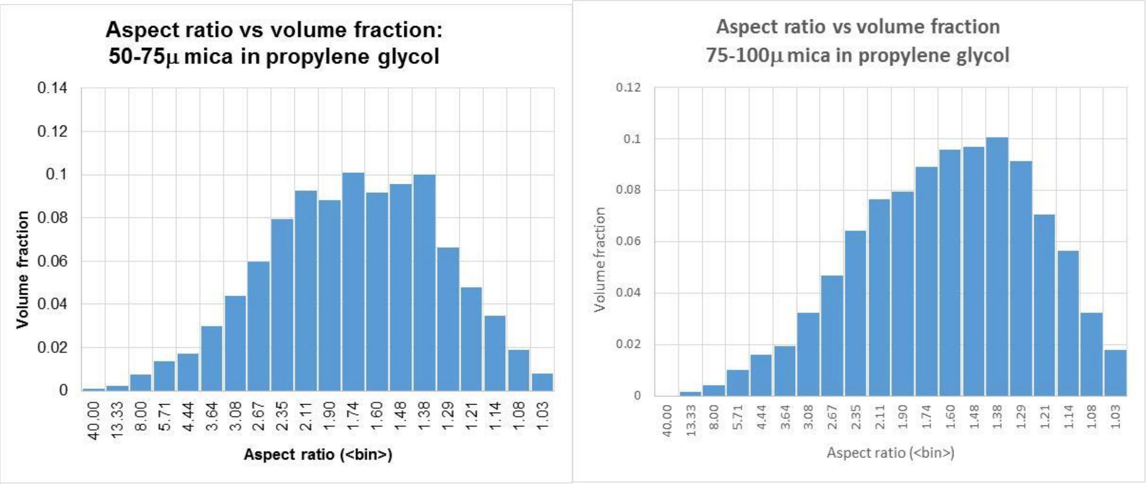

Figure 3.3: Aspect ratio distributions of (a) 50-75μ mica and (b) 75-100μ mica samples prepared in propylene glycol

The instrument identified that the aspect ratio of mica is between 1.5 and 2. However, given that the flow is through a rectangular channel 300μ thick, the plates tend to align themselves in the direction of the flow perpendicular to the viewing direction, and the aspect ratio distribution obtained is mostly an average of the basal plane dimensions. In other words, the thickness of the edge is not obtained, which is the aspect ratio of greater interest for mica. Knowing that the thickness of the edge is approximately 5-10 micron (Kaufman et al, 1974 and the SEM images shown in the previous section), the aspect ratio (face/edge) ranged between 2 to 6, depending on the size.

3.1.3 Microscopy images

Samples of silica, mica and quartz were observed under the microscope to confirm shape and morphology. The images were taken using an Olympus BH-2 microscope connected to a Sony

DXC-S500 color camera. The images were obtained and labeled using the software “Spot Advanced version 5.2”.

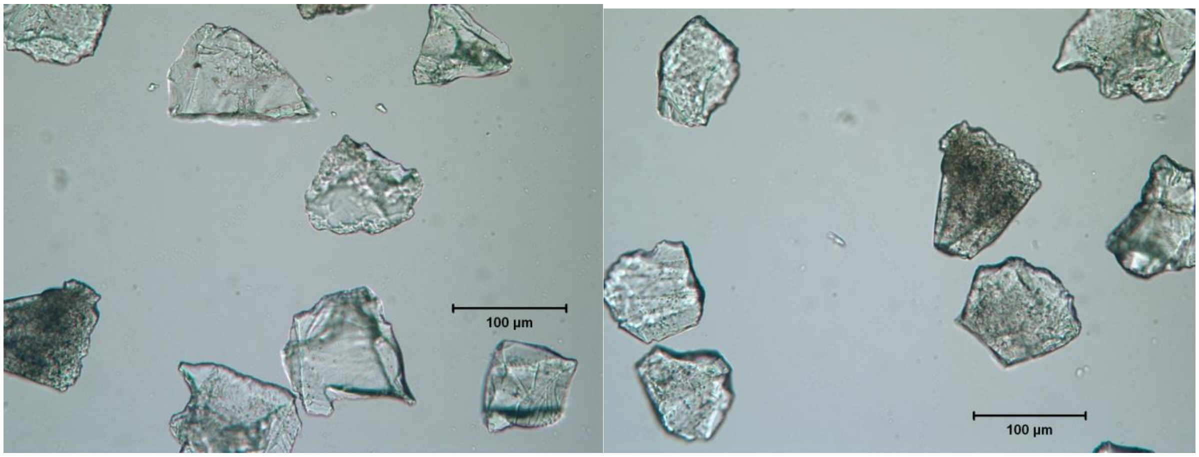

Figure 3.4: 75-100µ silica sample showing mostly conchoidal fracture and varying opacity

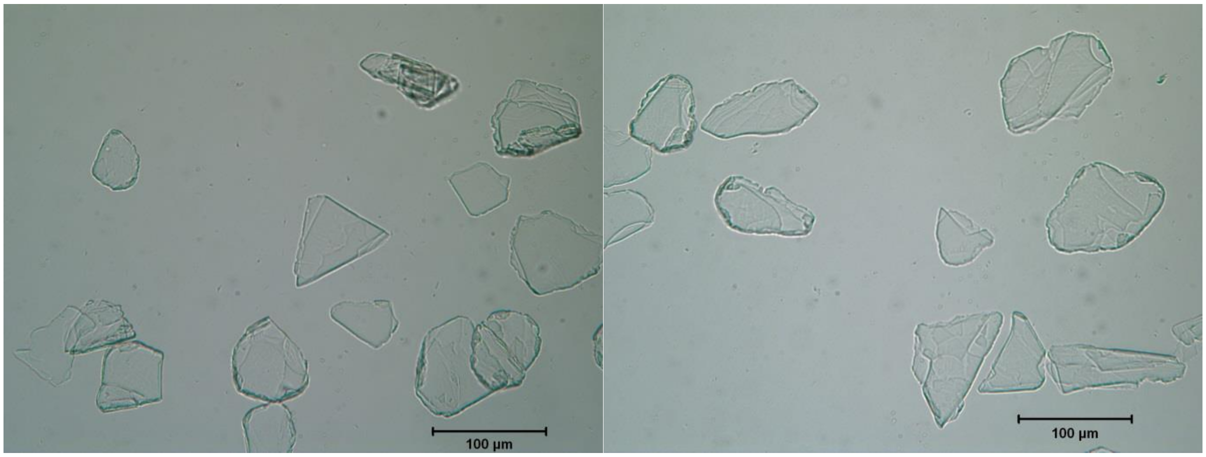

Figure 3.5: 50-75µ mica sample showing transparent, platy morphology readily apparent with thin plates observed

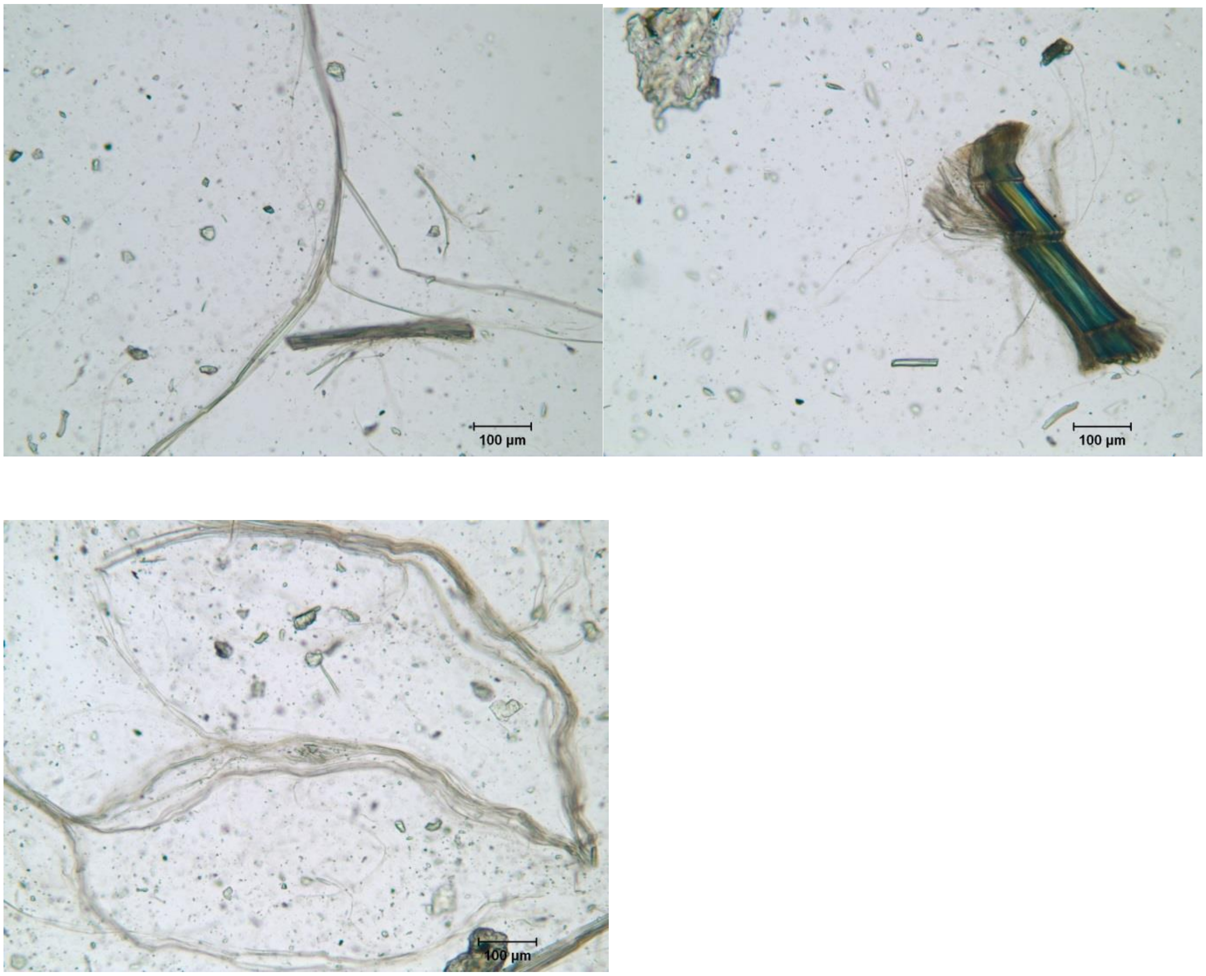

Figure 3.6: Images showing ore containing fibrous mineral chrysotile. Long strands of intertwined fibers as long as 1mm are observed, along with some bunches that appear "brush-like" and a host of fine particles.

3.1.4 Mica-rich ore sample

The mineralogy of the mica-rich ore sample was determined. The XRD instrument was the Bruker AXS D8 Advanced diffractometer. Co radiation was used with voltage and current 40kV and 35mA respectively, with a step time of 0.2s, a step of 0.2^o and a 2θ range of $3\text{-}70^o$. PDF2/PDF4 powder diffraction databases issued by the International Center for Diffraction Data (ICDD) were used to interpret the patterns. DiffracPlus Eva software was used for processing the data. The detection limit was identified as 0.5 to 2%, strongly dependent on crystallinity.

Table 3.1: XRD composition of mica-rich ore sample

	Size fraction					
Mineral	+150µ	100–150 µ	75–100µ	50–75µ	20–50µ	–20µ
	(wt %)	(wt %)	(wt %)	(wt %)	(wt %)	(wt %)
Quartz	41	44.7	34.1	33.6	28	19.2
Albite	13.8	17.1	17.8	17.5	20.8	31.6
Muscovite	23.8	18.4	22.3	21.5	20.9	11.3
Biotite	3.1	4.8	0.8	13.6	5.6	13.8
Phlogopite	4.2	4.7	8.9	2.9	8.8	4.7
Magnesio-hornblende	3.3	4	10.8	4.7	2.4	4.6
Chamosite	8.5	3.1	2.1	2.4	2.5	3
Chalcopyrite	0.8	0.9	-	-	1.1	5.2
Siderite	0.9	1.1	1.3	1.2	1.3	0.6
Magnetite	0.3	0.9	0.6	0.7	1.3	0.6
Hematite	0.3	0.4	0.3	0.8	1.5	0.9
Jarosite	-	-	-	-	2.6	1.2
Rutile	-	-	0.9	0.3	1.1	1.3
Diopside	-	-	-	-	2	1.3
Ilmenite	-	-	-	0.7	-	-
Iron	-	-	-	-	-	0.7
Total Platy mineral content	39.6	31	34.1	40.4	37.8	32.8

3.1.5 Silica

2 types of silica were used for these experiments. The so called “fine” silica was obtained from Allied Compounds. The so called “coarse” silica was obtained from Unimin Corporation. The brand name for the silica product is called “Sil-co-sil 250”. The particle size distributions of the fine and coarse silica obtained from sieving are shown below. The coarse silica sample was used to prepare silica of various size fractions, also using wet sieving. The particle size distributions of the original samples are shown below:

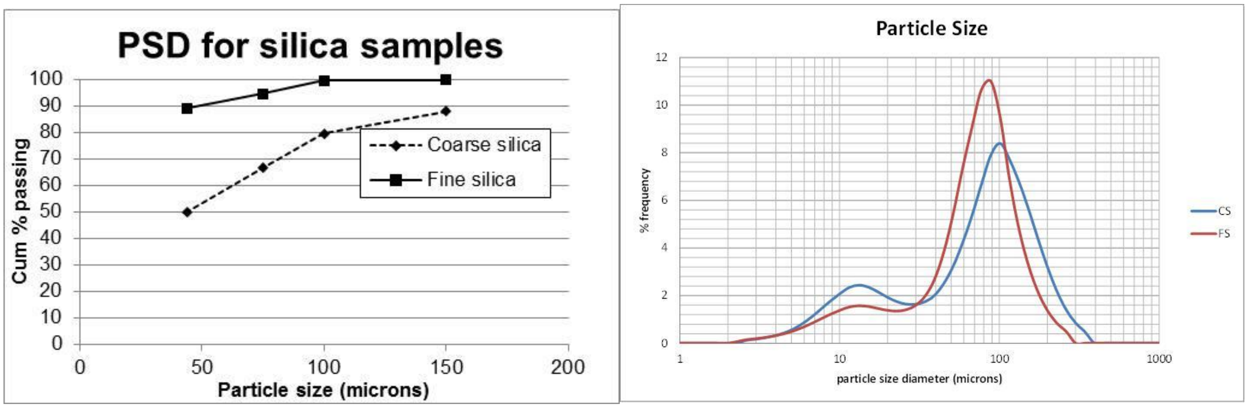

Figure 3.7: Particle size distribution for silica samples used as obtained using a) sieve analysis, b) Horiba

3.1.6 Chalcopyrite

Research grade chalcopyrite CuFeS2 sample was obtained from Wards Sciences and hand crushed/ground using a mortar and pestle to -75µ and +40 µ and sieved. The sample was then stored in a freezer to ensure that it did not oxidize, and removed only just prior to addition to the flotation cell.

3.1.7 Wollastonite

The wollastonite used in these flotation tests is obtained from King Industries. The coarsest available wollastonite sample is called VanSil WG. Its particle size distribution, obtained from their MSDS is shown below.

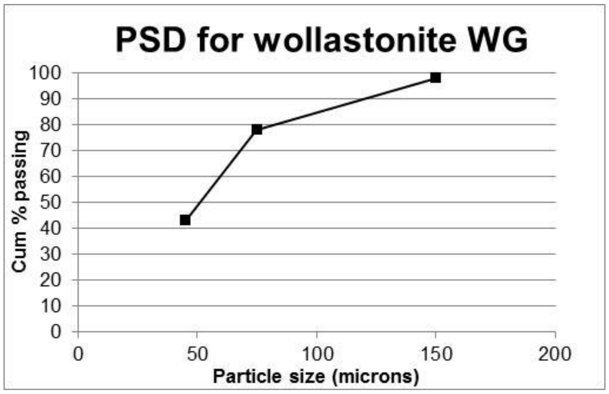

Figure 3.8: Wollastonite Particle size distribution obtained from SDS

3.1.8 Fibrous ore

An ore containing the fibrous mineral serpentine was obtained and has been discussed in previous publications by the author (Patra et al, 2014). The composition of this ore sample, as obtained through semi-quantitative XRD is shown in table 1 below.

Table 3.2: Mineralogy of fibrous ore sample

Mineral	Fibrous ore sample (wt %)
Clinochrysotile (partially fibrous)	62.6
Lizardite	21.1
Clinochlore	7.1
Magnetite	4.2
Pyrrhotite	1.6
Ankerite	0.8
Quartz	0.7
Chromite	0.7
Pentlandite	0.7
Calcite	0.3

3.2 Methods

3.2.1 Flotation tests for mixtures of mica-rich Cu ore with mica-free Cu ore

An ore sample containing a large amount of muscovite mica was obtained from a mine in Africa. The ore sample had a feed Cu content of 0.4%. This mine has often complained of poor concentrate grade, particularly when mica content in the ore is high. The target grind specification at this plant is 80% passing 100µ. This ore sample was ground for 6, 10 and 15 minutes in the mill. The ground ore was wet screened at 150µ and 75µ microns to remove fines, and the products were dry-sieved using the same screen stack, i.e. 210, 150, 100, 75, 50 and 20µ. The results from these tests are shown in the plot below, along with the mill feed particle-size distribution.

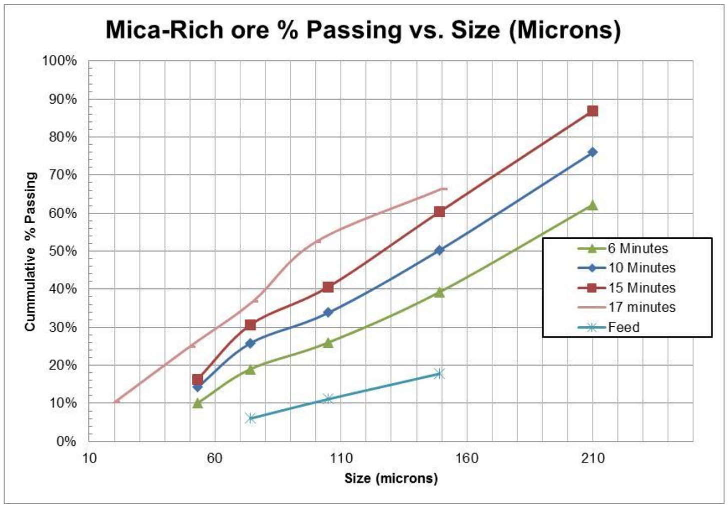

Figure 3.9: Particle size distributions obtained from grind study of Mica-rich ore

The reader will notice that this ore sample shows a bimodal distribution suggesting preferential grinding, which is unusual, but is the result of the presence of large amounts of mica.

The ore with which this mica-rich ore was to be mixed was prepared to achieve approximately the same particle size distribution at 75µ. The grind curves for mica-rich ore and the base Cu ore are shown in the plot below.

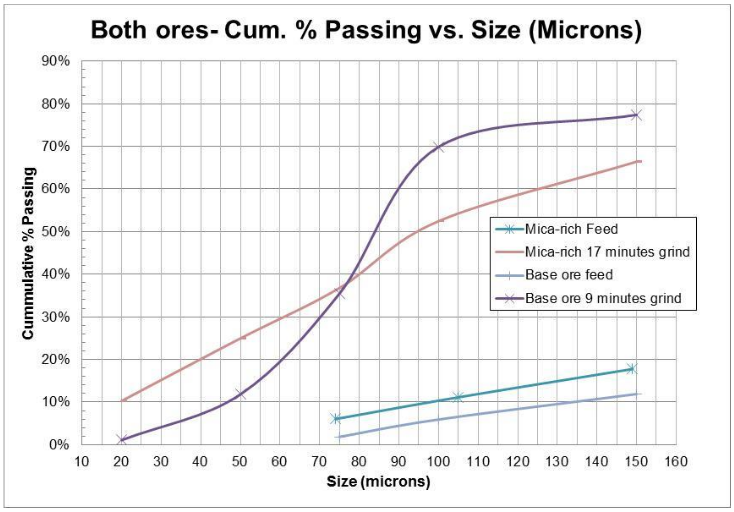

Figure 3.10: Particle-size distribution for mica rich ore and base ore

The mica-rich ore and base ore were ground separately, and then mixed together in desired ratios for the flotation tests as shown in the figure 3.11 below.

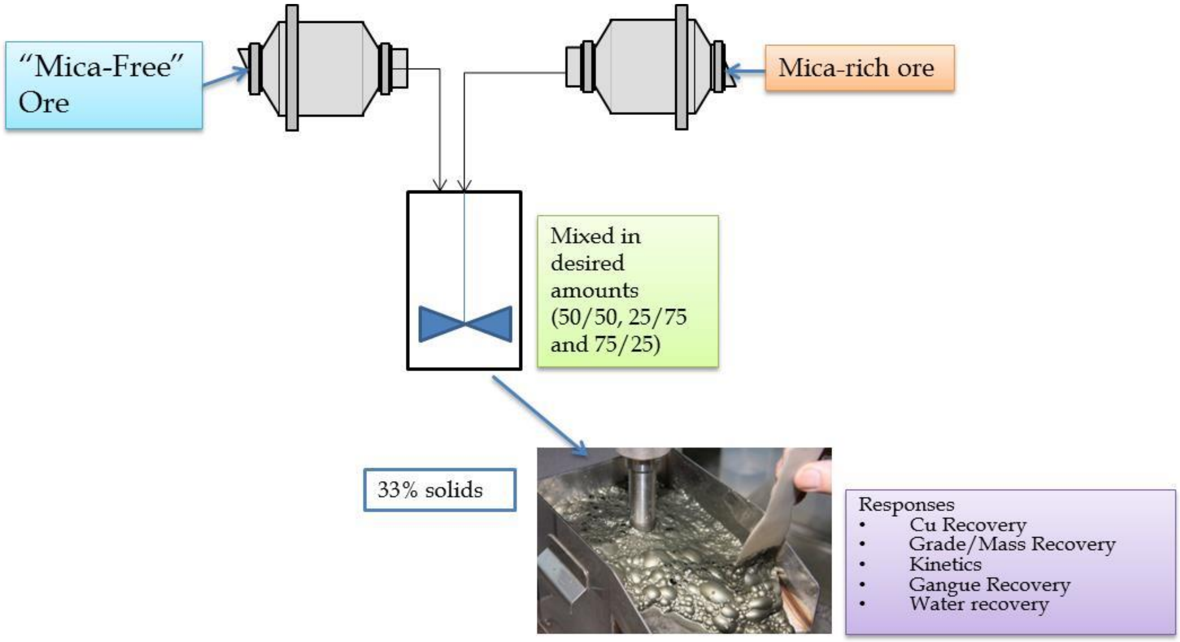

Figure 3.11: Protocol for mixtures of mica-rich Cu ore with mica-free Cu ore

3.2.2 Flotation tests with high purity mica mixed with base Cu ore and ground together

In order to conduct tests with well-defined mica content, but with mica ground with the ore, a separate series of tests was conducted. The desired amount of high-purity mica crushed to -2mm as described in section 1.1 was added to the mill, along with the mica-free ore for a total mass of 500g. The mica was thus ground with the mica-free ore. The amount of lime added for the mica-free ore alone was 2g, and was adjusted down to represent the amount of mica-rich ore. For example, for the test where 50% of pure mica was added to the grinding mill, 1g of lime was used. The ore sample was ground in the mill for 9 minutes to achieve the target particle size distribution of 80% -75μThe collector used in these tests was sodium isobutyl xanthate, dosed at 5 and 15 g/t in the first and fourth flotation stages. The frother was methyl isobutyl carbinol, dosed at 40 g/t in the first and 20g/t in the fourth flotation stages. Figure 3.12 shows this protocol.

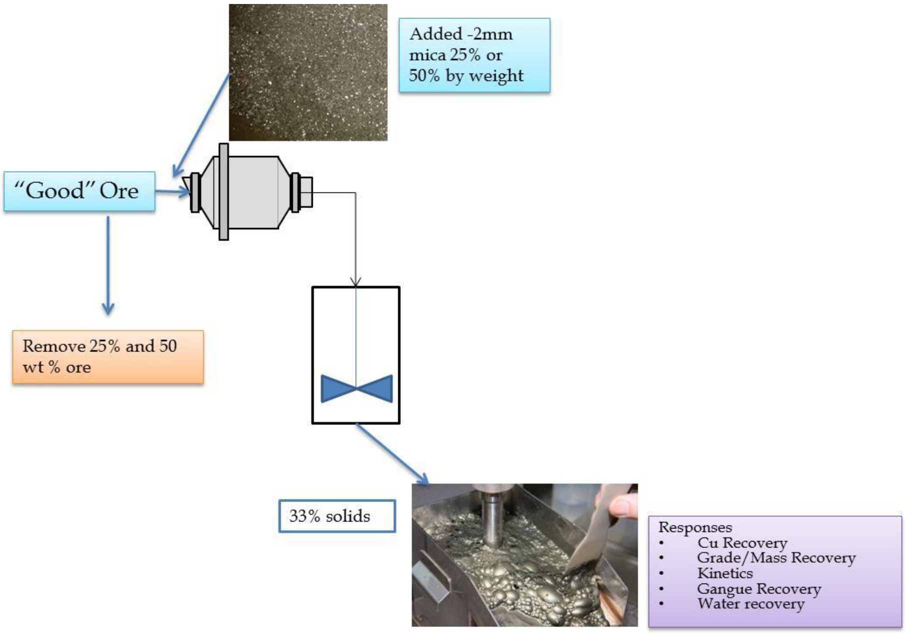

Figure 3.12: Protocol for flotation tests with high purity mica mixed with mica free ore in the grind

3.2.3 Flotation tests for mica/silica addition of various sizes

A Cu ore averaging 0.4% Cu by weight was obtained from a North American Cu operation. This was the second mica-free ore into which the various gangue minerals (muscovite and silica) of various sizes were mixed. 0.75g of lime per 500g of ore charge was used for these flotation tests. Volume of slurry commensurate with the amount of mineral to be added was removed from the flotation cell as it was agitated at 800 rpm. Volumetric removal of sample was done to minimize inhomogeneity during sampling. The desired mass of the mineral of desired size fraction was then added to the pulp with the slurry still agitating, and makeup water was added to attain the original pulp density of 34% (wt. /wt.) solids. The flotation cell was 1.25L in capacity. The collector used in these tests was diisobutyl dithiophosphate, dosed at 20 and 10 g/t in the first and fourth flotation stages respectively. The frother was a mixture of methyl isobutyl carbinol and polypropylene glycol (85/15), dosed at 20 g/t in the first and 10g/t in the fourth flotation stages respectively.

3.2.4 Flotation test procedure

Ore obtained from the mine was crushed to -10 mesh using laboratory crushers, and split into 500g charges using a rotary splitter after thorough mixing. A 500g ore charge was ground in a laboratory FLSmidth rod mill containing 60% solids with the desired amount of lime to achieve the target particle-size distribution and pH. The grinding mill discharge was transferred to a 1.2L flotation cell and makeup water was added, resulting in a flotation solids density of 34%. The froth depth was kept at 1 inch from the lip with the impeller turned off. Two minutes of conditioning time was allotted to ensure mixing of the mineral and ore before flotation. The collector and frother were added at the desired dosage rate. The pulp was conditioned with collector and frother for 2 minutes prior to flotation. The airflow rate for flotation was maintained between 3 and 3.7 liters per minute for the duration of the test while keeping the froth depth constant. The minor adjustments in airflow rate are unlikely to have had any effect on flotation kinetics. The froth was scraped at 10 second intervals, and three concentrates were collected at time 0.5, 1.5, and 3.5 minutes respectively. After the third concentrate, the airflow as turned off, and additional collector and frother were added. Additional water was added to bring the water level to 1 inch from the lip. An additional concentrate was collected, bringing the total flotation time to 6.5 minutes. After 6.5 minutes it was readily apparent that all of the Cu had been recovered in all tests. Four concentrates were thus collected; they were dried, weighed and analyzed for Cu, Fe, S and acid-insolubles (representative of non-sulfide minerals). The analysis was conducted by a standard method- dissolution of the sample in aqua regia followed by AAS (atomic absorption spectroscopy) on the supernatant. The residue from the acid leach was weighed and reported as acid-insoluble (non-sulfide minerals). A LECO analyzer was used to quantify S.

A diagram of the experimental procedure is shown in Figure 3.13 below.

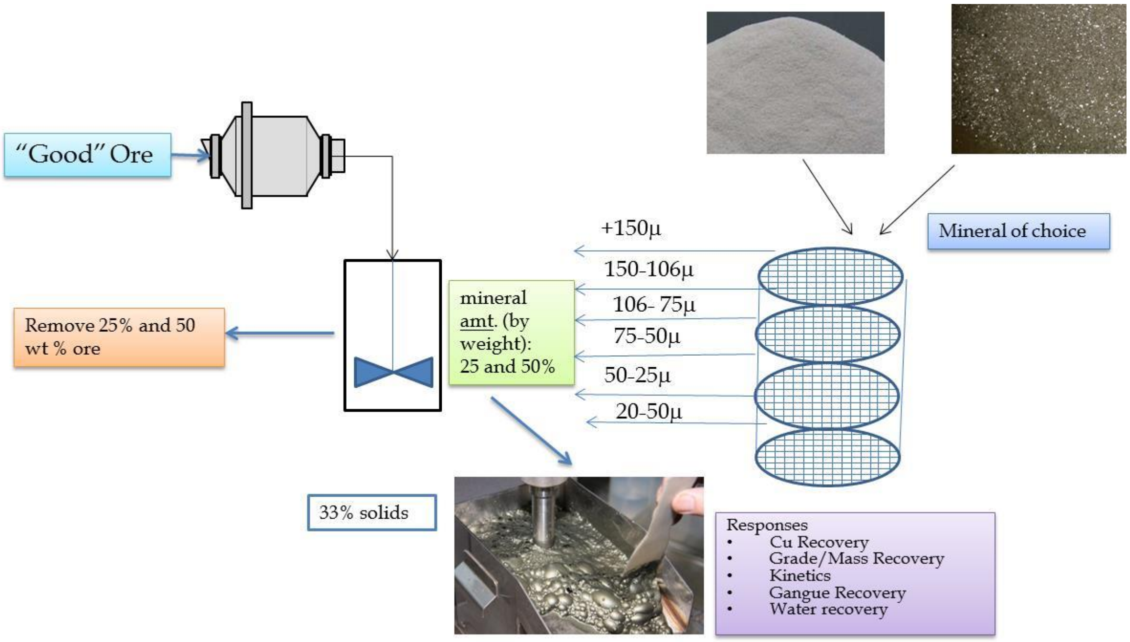

Figure 3.13: Flotation testing procedure for studying effect of particle size of muscovite (vs silica) on flotation recovery/grade

3.3 Design of froth sampler

3.3.1 Cell and Housing

A bottom driven flotation cell was used for the froth sampling as opposed to the typical top driven (e.g. Denver) to ensure that the entire froth surface is sampled. The cell, made of polycarbonate, is 1.5L in capacity. For a 33% solids test, the cell accommodates 500g of ore or mineral sample. There are two orifices in the bottom through which air travels, with a flowmeter to regulate airflow. A baffle is added to the bottom of the cell to enable adequate mixing. There is a valve to discharge the contents of the cell at the bottom left. The impeller is driven by a 40 hp motor capable of 2000rpm. Slurry (grinding mill discharge) or solids and water are added directly into the top of the cell. The motor is housed in a solid steel frame, and has wheels for easy transport. The motor is protected from water with generous weather stripping. Weather stripping is also included on the top of the steel frame to contain water spills.

3.3.2 Design of sampling device

The design and dimensions of the froth sampling device is shown below in figure 3.13. It has two components, namely the fixed piece and the mobile piece.

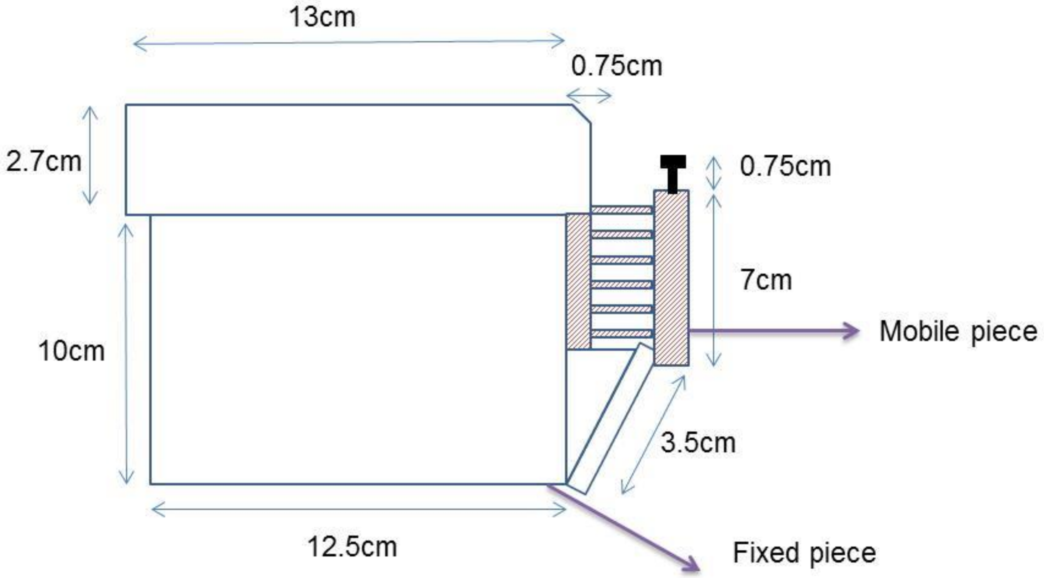
13cm
0.75cm
2.7cm
0.75cm
7cm
Mobile piece
10cm
3.5cm
12.5cm
Fixed piece

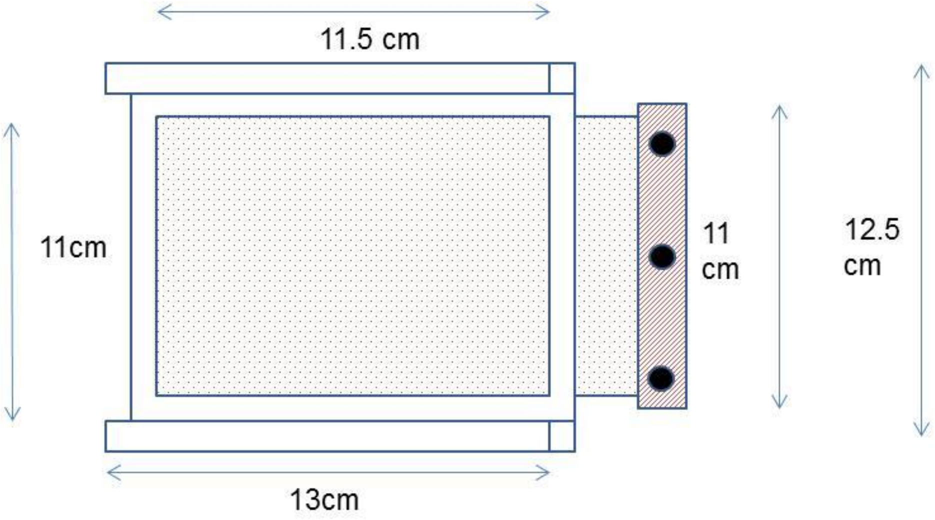
11.5 cm
11cm
11
cm
12.5
cm
13cm

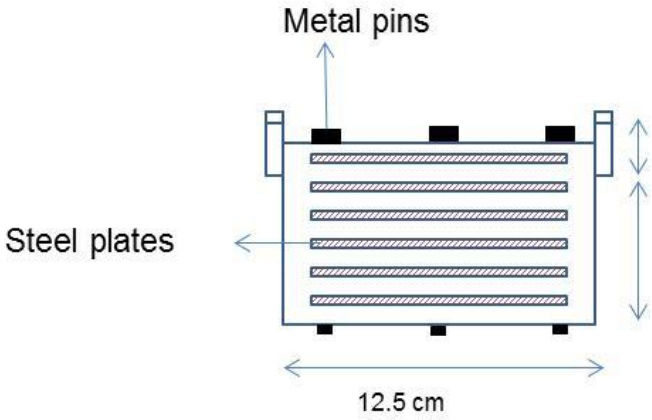
Metal pins
Steel plates
12.5 cm

Figure 3.14: Froth sampler design and dimensions

Figure 3.15: Images of froth sampler (a) side view, and (b) Angle view

The froth sampler consists of two pieces, the fixed and the mobile pieces. The fixed piece is constructed from Delrin with 1mm thick slots placed 1cm apart each. A total of six slots are used for these experiments. For the fixed piece there is a 3cm gap between the top of the unaeratedslurry and the first sample of froth. The 3cm gap is to account for the air holdup in the cell, and to ensure that we are sampling the froth and not the pulp froth interface. The mobile piece was constructed using is a 3cm thick single piece of Delrin that secures sampling trays with help of 3 locking pins; the pins are long enough to secure all trays. The sampling trays, which attach to the mobile piece, are made of 1mm stainless steel to ensure they do not bend during the rapid inserting motion required to collect a sample.The use of delrin and stainless steel ensured that the mobile piece was sturdy. The fixed piece is mounted on the flotation cell, while the mobile piece is lined up just into the slots before the start of the experiment.

3.3.3 Operation

When adding solids and water separately, it is important to add the water first, and the impeller should be turned on. The rotation speed deemed adequate for froth sampling was 1000rpm. The airflow rate deemed appropriate for a silica suspension at 33% solids to raise a 9cm high froth was about 2.56 liters per minute. The surface area of the cell is 123cm^2, and thus the superficial air velocity (Jg) in the cell was about 0.5 cm/s. This compares well to large flotation cells in plants that have a J_g of 0.2-1 cm/s.

3.4 Froth Sampling experiments

3.4.1 Protocol to ensure froth sampler is not leaking

It took about 30 experiments to develop a workable protocol for the froth sampler such that there were no leaks. The following steps were taken to achieve a non-leaking froth sampler.

1. The edges of the steel plates are coated with a light layer of silicone grease.
2. The slots are covered with a moderate layer of grease that act as a barrier for the slurry
3. After 2 froth sampling experiments, clean the slots thoroughly, and scrape the slots inside the froth sampler to remove grease and mineral samples lodged in the slots.

3.4.2 Procedure to test froth sampler for leaks

In order to test the froth sampler for leaks, first a known amount of silica is placed on each plate. A known amount of water is then added. The vacuum apparatus is used to suck up the silica/water slurry into a conical tube and is shown in figure 3.15 below.

Figure 3.16: Vacuum apparatus to collect froth samples into a 50ml centrifuge tube (a) side view showing a conical flask used to catch any excess slurry. (b) top view showing the assembly

This process is repeated for all 6 layers, resulting in 6 conical tubes filled with silica slurry. The tubes are weighed, centrifuged to remove excess water, and dried in an oven at 80C overnight. The difference in weights from the amounts originally added to the amount in the tubes was measured. If the error was greater than 3%, Silicone RTV sealant was used to seal the edges of the froth sampler. The procedure was repeated to check for leaks. The losses in solid (silica) and liquid phases were found to be less than 2 and 3% respectively. This level of accuracy was deemed sufficient for the froth sampling experiments. In addition, experiments were conducted by placing methylene blue dye on one of the layers during an experimental run, and if dye was found in any other layer than the one in which it was deliberately placed, additional Silicone RTV sealant was used to seal the edges of the froth sampler.

3.4.3 Running a froth sampling experiment

1. Six 50ml centrifuge tubes and one 15ml centrifuge tube were labeled and their weights recorded in a notebook.
2. A very small amount of silicone grease is added to each steel plate on the three edges that will contact the froth/slurry and in the delrin slots. This is to ensure smooth sliding of the

steel plates into the slots during the sampling experiment and to prevent water leaks. The excess grease was cleaned with a paper towel. The froth sampler was then assembled by attaching the steel plates to the holder. The three metal pins were then inserted to tighten the assembly.

3. In order to test for blockages in the air lines, a small amount of water was added to the bottom-driven cell. The airflow was turned on to check if any of the air vents were clogged. If they were clogged, bubbling would be observed only from a single point in the froth sampler instead of from two points (there are two vents). The vents were unclogged by pumping water through the vent using a syringe. The vents were then rechecked to ensure both are unclogged. The dirty water was then removed, and about 200ml of fresh water was added to the cell. The removable baffle was also inserted at this time.
4. A 500g sample to be used for froth sampling experiment was prepared and added to the flotation cell containing about 200ml of water after agitation was turned on. The flotation cell was then filled with water to the 1.25L mark. The slurry remained agitated and the impeller speed set to 1000 rpm.
5. Using a microliter syringe, an appropriate amount of collector was inserted into the agitating slurry followed by an appropriate amount of frother. The needle was dipped in the slurry to ensure appropriate dosing and cleaned with a paper towel. The froth sampler was then attached to the flotation cell. Note that the steel plates were out of the flotation cell at this time (in ready position). A clear plexiglass plate was placed on top of the assembly, which provided an indicator of froth height and indicated when it was time to sample.

6. The airflow was then started to raise the froth. When the froth is just above the level of the topmost steel plate, the steel plates were inserted into the froth sampler as fast as possible. At the same time, the airflow valve was shut and impeller switched off to prevent leaks. For the steady-state froth sampling, the froth was raised by turning on the air, and adjusted to maintain the full froth height for the designated time (2 or 5 minutes) before inserting the plates.
7. The vacuum line for vacuuming apparatus was turned on and checked for adequate suction.
8. The first sample collection tube was attached to the vacuum assembly. It was ensured that the line feeding sample into the tube is placed lower than the line drawing excess vacuum into the Erlenmeyer flask to prevent sample from overflowing into the Erlenmeyer flask.
9. A small plastic card was used to thoroughly mix the sample on the collection plate. The material was dragged to the center of the sample plate.
10. The vacuum line was used to transfer sample from the steel plate to the first centrifuge tube.
11. Additional water (weighed) was added from a syringe to wet the sample if necessary. The plastic card was used to move material to the center of the sampling plate. The vacuum was used to transfer additional material to the sample collection tube. This step was repeated 2 times until the steel plate appears clean. The sample collection tube 1 was removed from the vacuum apparatus and capped. Steps 6 through 9 are repeated for samples 2,3,4,5 and 6.
12. The weight of all the centrifuge tubes with sample and water were recorded. The tubes were placed in a centrifuge for 4 minutes to obtain a clear supernatant. A visual check

was conducted to confirm that the supernatant was clear. If it wasn't, the samples were run in the centrifuge for an additional two minutes. The supernatant was removed using a dropper/pipette and tubes were placed in the oven at 80C overnight to dry completely. The dried tubes were weighed the following morning. The solid in the tubes was analyzed by XRF to quantitate muscovite, wollastonite, silica, chalcopyrite and fibrous mineral serpentine.

3.5 Analysis of samples

3.5.1 XRF calibration procedure.

To homogenize and obtain a representative sample, the mineral mixture in each layer was prepared by hand pulverizing using a mortar and pestle. An aliquot was prepared using 0.25 g of sample and 6.5 g of flux and fused to prepare a glass bead. The beads were analyzed using a Rigaku Primus II WD-XRF. A calibration on the XRF was done using mixtures of pure muscovite and silica. The 6 point calibration curve was linear, and is shown in Figure 3.17 below.

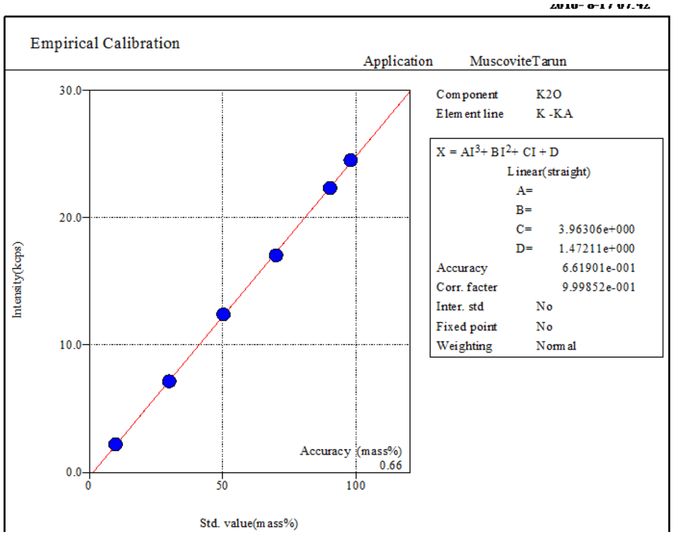

Empirical Calibration

Application MuscoviteTarun

Component K2O
Element line K -KA

X = AI3+ BI2+ CI + D
Linear(straight)
A=
B=
C= 3.96306e+000
D= 1.47211e+000
Accuracy 6.61901e-001
Corr. facter 9.99852e-001
Inter. std No
Fixed point No
Weighting Normal

Figure 3.17: XRF calibration curve to quantify muscovite in a mixture of muscovite and silica by XRF

3.6 Interpretation of froth sampling data

The results from the froth sampling tests are shown in plots like Figure 3.17. The height in the froth is plotted on the y-axis, with marking for the top shown as layer 0, and subsequent layers indicated as layers -1,-2,-3,-4,-5 and -6 each. The concentration of the species in question is plotted on the x-axis, with the concentration increasing from left to right. Recall from section 2.3 the description of the froth phase of flotation. In the very bottom layer (closes to the pulp phase, there is a significant amount of hydrophilic particles entrained in the froth. As liquid drains from the froth, hydrophilic particles start draining with it, and the concentration of hydrophilic particles decreases with increasing height. If a hydrophilic mineral species is being entrained more than another, its plot is further to the right. In contrast, the content of hydrophobic particles increases as a function of height (as the hydrophilic particles drain out). In addition, when hydrophobic particles (chalcopyrite rendered hydrophobic by collector adsorption) was used in the tests, and coarse particles were used (which resulted in a froth that was not as strong), the froth would collapse into the center of the cell. Results from these tests show a higher concentration of hydrophobic particles in the middle layers (3,4) than in the upper layers (1,2) resulting in an awkwardly-shaped curve.

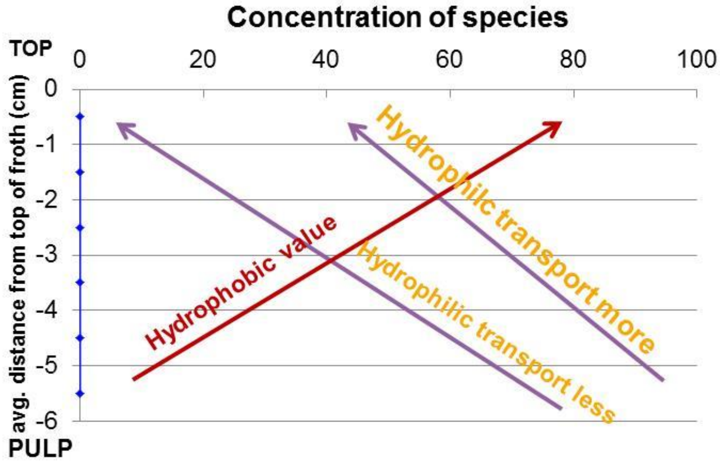

Figure 3.18: Interpretation of froth sampling data

3.7 Rheology measurements

For measurement systems evaluation the file silica suspension prepared as a 40% solution (w/w) was used. The focus was to develop the protocol first using the vane geometry, ramping rotation rate up and down to check for deviations that may be attributed to settling. Once the basic protocols were established, tests were conducted using the same 40% (w/w) fine silica suspension to select the geometry and the shear rate of operation. The rheometer used for these measurements was a TA instruments Discovery DHR-3 hybrid rheometer.

3.7.1 Developing a protocol for measurement

The experiments were started with a simple measurement protocol as follows: the low and high end of the shear rates were selected as 1/s and 120/s. The highest shear rate was identified as that where rheological measurements could be conducted without driving sample out of the container due to turbulence. A silica sample of 40% solids (w/w) was used. The program was instructed to make 20 measurements in one minute, or one measurement every three seconds. The rheometer recorded the stress at a given shear rate during the third second of operation at the shear rate, before switching to the next shear rate. Each experiment was conducted ramping up from shear rate of 1 to 120/s and then immediately ramping down i.e. 120/s to 1/s, and each experiment was repeated twice. The plot of stress vs shear rate is shown in the graph below.

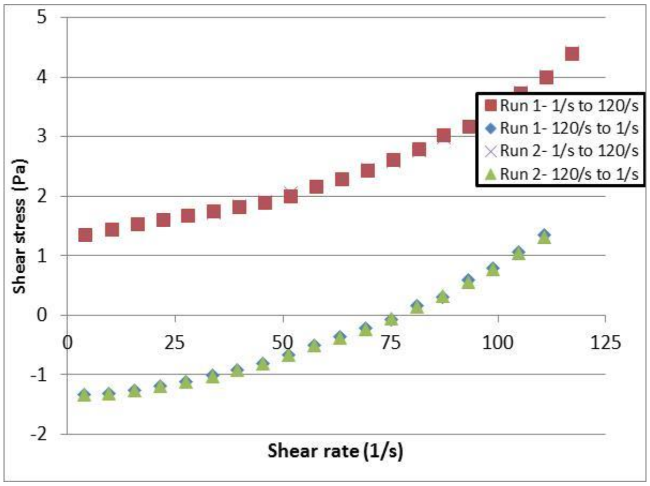

Figure 3.19: Continuous rheology measurement (no mixing) of 40% fine silica suspension

The plot shows that the stress is negative for when the experiment is run the reverse direction, i.e. 120/s to 1/s, which cannot be the case. This is likely because of the sample settling and artifacts in the data from autocorrelation (i.e. current run being influenced by the previous run). For this reason, it was decided that an agitation step must be conducted before each measurement to restore the sample to a “fully suspended state” before experiments are conducted. A protocol was thus developed whereby the sample was agitated at a shear rate of 150/s for 7 seconds and then held at zero shear for 5 seconds to allow the flow to cease. Following this, a measurement was conducted for 5 seconds. Experimental data using this protocol for ramping up (increasing shear rate) and ramping down (decreasing shear rate) experiments is shown in the plot below. The average of the 2nd measurement for three repeat tests is shown below.

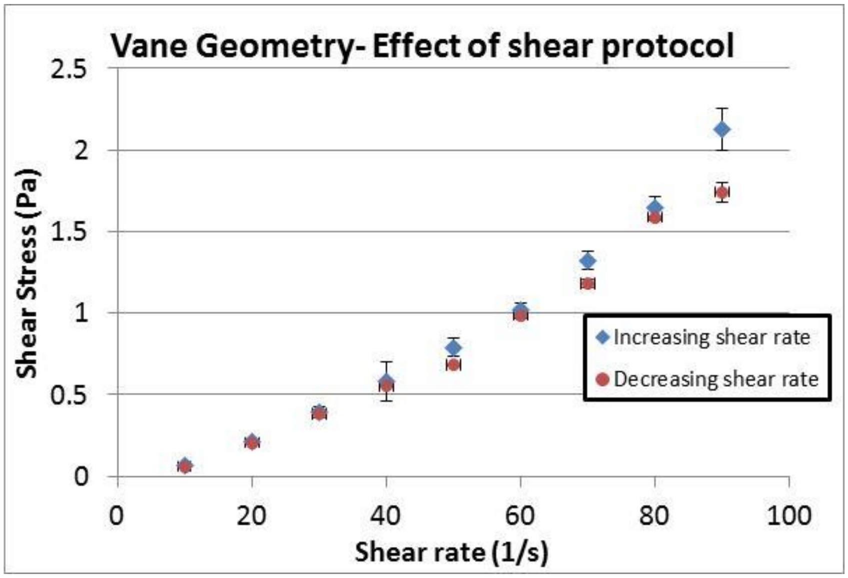

Figure 3.20: Effect of improved measurement protocol on increasing vs decreasing shear rate measurement; 40 % solids concentration fine silica suspension

The data shows that for both forward and reverse direction, the measured stresses are positive thus confirming that the protocol allows for reliable measurements. However, there are still some differences between the increasing and decreasing shear rate measurements, and it was hypothesized that using the stress obtained in the 2nd second of measurement was perhaps the reason for the inaccuracy. Instead, an average of the 2nd, 3rd, 4th and 5th measurements was obtained and the rheology measured. The data is showed in figure 3.21 below.

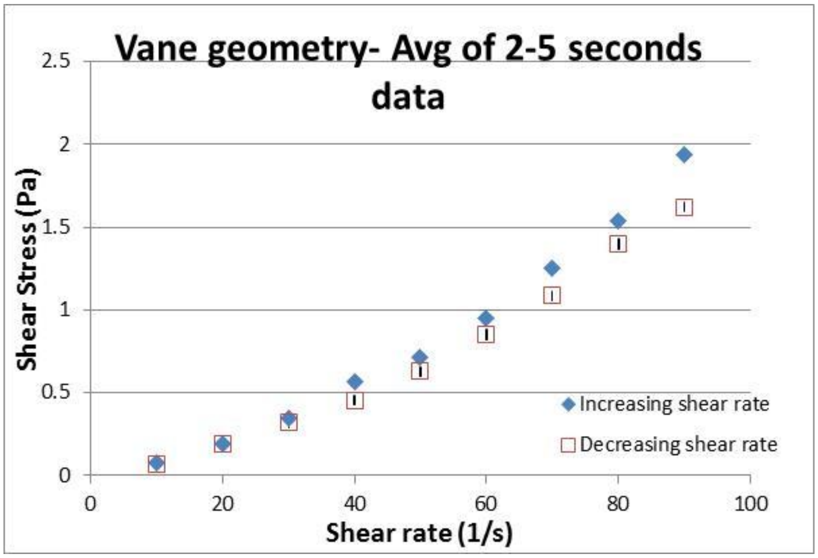

Figure 3.21: Rheology measurements using averages of 2-5th second of measurements- 40% fine silica suspension

The data in figure 3.21 above suggests a more consistent pattern, with the data following a reasonable trend. Using the average value, the errors are also considerably smaller than those with the 2nd second measurement. It was thus decided to use the average of the 2nd, 3rd, 4th and 5th second of measurements. However, it is apparent that there is still a significant difference between the increasing and decreasing shear rate measurement. It was then hypothesized that this may be related to settling of the sample. Flow in the vane geometry is not turbulent enough to allow for mixing of the entire sample. For this reason, alternative geometries were explored.

3.7.2 Selecting of geometry for rheological measurements

The Discovery HR-3rheometer comes with several geometries that may be used to conduct the rheology tests. The first is the traditional couette geometry. We recognize that the likelihood of wall slip is very high with this geometry, as is the likelihood of settling. For this reason the couette is disqualified. The other options included the vane and the helical ribbon geometries. The vane has a long history of being using for mineral suspensions. Nguyen and Boger first recommended its use in 1983. Wall slip is minimized because of the design. In addition, the vane geometry enables reasonable mixing of the slurry, thus countering the settling problem. The helical ribbon has not been used in mineral suspensions. However, the principle of helical flow has been used in some rheometers with vanes to reduce the settling problem (Akroyd, 2003). The key challenge with the helical ribbon is to develop an appropriate equation to convert the measured torque to the shear stress, and the angular velocity to shear rate. Recent publications by Ait-Kadi et al (2004) suggest that the couette analogy may be used to obtain a stress constant and a strain constant that can be used as a simple multiplying factor to conduct the above mentioned conversions. An oil of known Newtonian viscosity (0.1Pa.s obtained from Brookfield Instruments) was used to obtain the stress and strain constants to make these conversions.

The data obtained from the helical ribbon geometries is shown below:

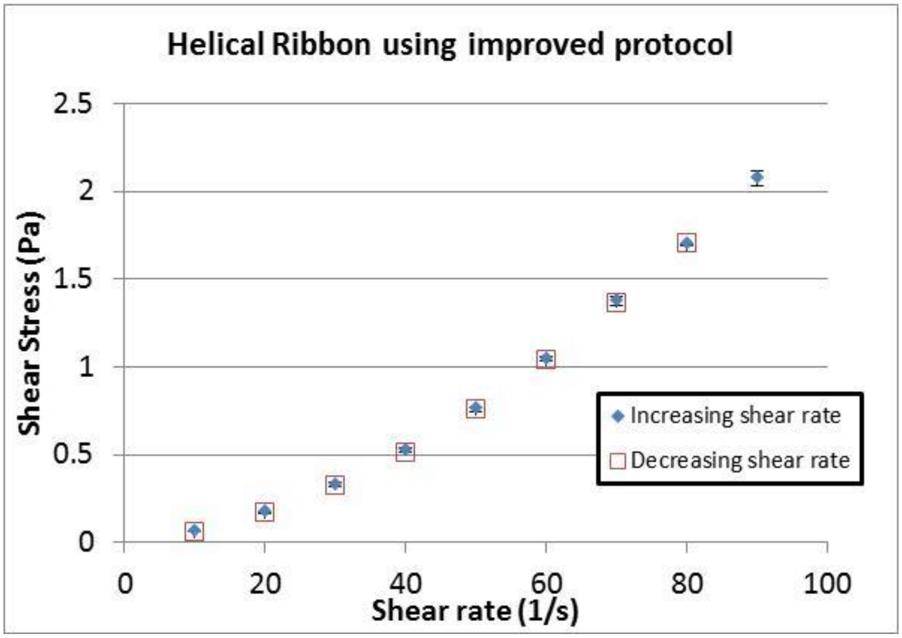

Figure 3.22: Helical ribbon data with increasing and decreasing shear rate; 40% solids concentration fine silica suspension

It is readily apparent that the helical ribbon, owing to its larger area, combined with its ability to suspend particles well, results in a significantly more consistent and reproducible measurement than the vane geometry. A comparison between the two geometries is shown in the plot below.

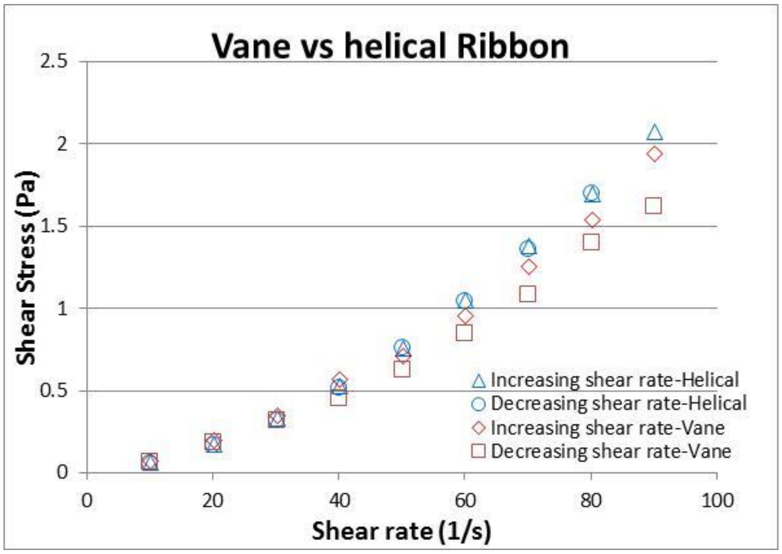

Figure 3.3.23: Vane vs helical ribbon for decreasing and increasing shear rate for geometry selection; 40% solids concentration fine silica suspension

For this reason, the helical ribbon was chosen as the geometry of choice for the remainder of the experiments.

3.7.3 Identifying shear rate range for measurements and geometry selection

As discussed earlier, the shear stress measured for a given shear rate can directly yield an apparent viscosity and related material properties. The stress is a function of the shear rate, and thus selection of shear rate is critical. In order to determine the appropriate shear rate, re-examining figure 3.23 is in order. It is apparent that there is curvature in the stress vs shear rate curve. Figure 2.13 (literature review section) shows that this type of response is characteristic of a thixotropic material. Since mineral slurries are known to pseudoplastic an error in measurement was suspected. The curvature may be attributed to the effect of turbulence. According to Li (2017) and Shi and Napier-Munn (1996)-

"When the vane is rotating and the cup is at rest, the fluid near the vane is subjected to a higher centrifugal force, which results in a tendency for the fluid to be propelled outwards. At a certain Reynolds number, vortices appear in the flow whose axes are located along the vane circumference rotating alternatively in opposite directions"

They further state that the onset of turbulence can be characterized by using the Taylor number T_a, defined as follows:

$$T_a = \frac{(R_c - R_b) U_b \rho}{\mu} \cdot \sqrt{\frac{\mathrm{R_c} - \mathrm{R_b}}{\mathrm{R_b}}} \tag{1}$$

where U_b is the peripheral velocity of the vane (measured in revolutions per minute or rpm), μ and ρ are the fluid viscosity and density, respectively, and R_c and R_b are the radii of the cup and vane, respectively. Three regimes of flow between the rotating vane and the cup may be defined using the Taylor number, as shown in Table 3.2 below (Schlichting and Gerston, 2000).

Table 3.2 Flow regimes based on Ta number (Schlichting and Gerston, 2000)

T_a *number*	$T_a < 41.3$	$41.3 < T_a < 400$	$T_a > 400$
Flow regime	Laminar	Laminar and vortices	Turbulent

Using equation 3.11 above, it was determined that to stay under a Ta of 41.3, the maximum peripheral rotation rate of the vane to achieve laminar flow is 60 rpm, which translates to 11/s shear rate. The higher shear rates were definitely in the “laminar and vortices” region, which caused the curvature in the shear stress vs shear rate plot. As a result, all the measurements were conducted from a shear rate of 13/s to 7/s, which translates to 60 to 22 rpm. The rheological tests conducted earlier were then repeated as shown in Figure 3.24 below.

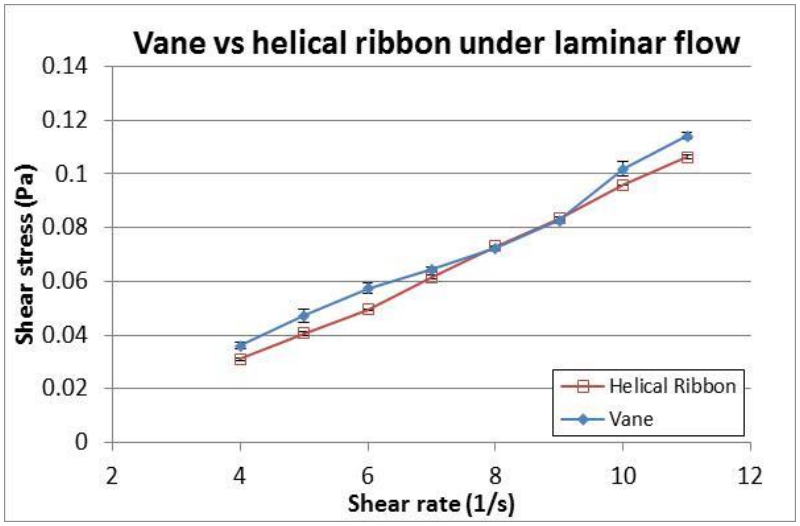

Figure 3.24: Vane vs helical ribbon under laminar flow; 40% solids concentration silica suspension

The results from this plot suggest that under laminar flow conditions, the vane measurements are more variable. We see a bend in the shape of the rheogram. However, for the helical ribbon, this bend is not observed, the plot is linear as expected for a pseudoplastic fluid in this shear-region. Additional experimental runs at 30% and 50% solids concentration (not shown) confirm that indeed, the helical ribbon data is more precise. For this reason we selected the helical tool for these experiments.

3.7.4 Reproducibility between samples

Experiments were also conducted with multiple freshly prepared suspension samples to ascertain the reproducibility associated with preparation of samples. Figure 3.25 shows a rheogram with data from two samples.

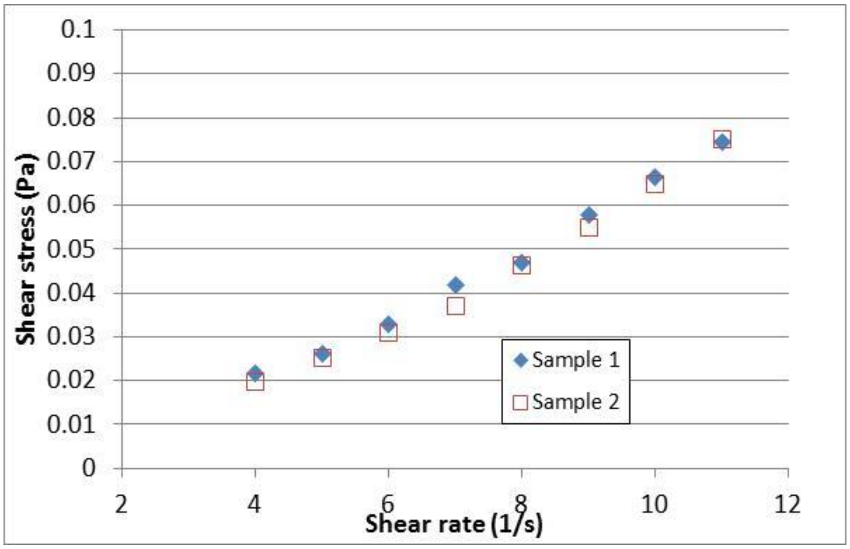

Figure 3.25: Assessing reproducibility between samples- stress vs shear rate; 40% solids concentration

The data suggests that the variation between the two experiments were very small, with standard deviation being less than 1%.

3.7.5 Final protocol for measurements

Based on all this work, the final protocol for measurements was identified as follows:

The silica and/or other mineral species were weighed and added to the 80ml glass sample holder in which the measurements were to be conducted. Water that is needed to achieve the highest volume fraction to be measured was added. The suspension was hand mixed to ensure homogeneity. A rheology test was conducted from the highest shear rate (13/s) to the lowest shear rate (7/s), with appropriate mixing and waiting times as described earlier in this section. The sample was then diluted with water to achieve the volume fraction for the next measurement in the sample holder itself. The rheology experiment was then conducted at this volume fraction from the highest to the lowest shear rate, and on until the sample holder was full. Then, at a shear rate of 120/s the slurry was agitated using the helical geometry itself, and 10ml of slurry was removed from the sample holder and disposed. Another measurement was taken with the sample remaining in the holder and the measured relative viscosities were compared with the previous sample to ensure that the sample removal process did not result in a change in concentration of the minerals or volume fraction of solids. Additional experiments were then conducted by adding water to achieve lower volume fractions, followed by another step to remove slurry. A total of 3 slurry removal steps were required to achieve volume fractions from approximately 45% to 7.5%. Conducting measurements at high volume fractions was difficult due to a) slurry ejection, and b) very high shear stresses beyond the capabilities of the instrument. The highest volume fraction thus varied from sample to sample.

4 Results from flotation tests

4.1 Mica and silica of various sizes added to flotation cell

A number of different types of plots are made for the results from the flotation tests, all of which contribute to the analysis of the data. This includes Cu recovery-grade curves, Cu recovery vs mass recovery curves, and non-sulfide gangue vs water recovery curves.

To generate the recovery-grade curves, the *cumulative recovery of Cu is plotted on the y-axis and cumulative concentrate grade of Cu is plotted on the x-axis*. Typical grade recovery curves start in the bottom right on the plot, with higher grades and low recoveries. In the first concentrates, the liberated fast floating hydrophobic Cu species are being recovered. The curve moves towards the top-left as the slow floating Cu minerals (poorly liberated binaries and ternary particles) start floating. However, since the rate of flotation of these minerals is slow, the concentrates produced during the later stages, particularly in the third and fourth stages of flotation, contain a lot of non-sulfide gangue minerals that are understood to be recovered by entrainment. As a result, a rightward shift in the grade- recovery curve is indicative of more selective flotation response, and would be considered more “desirable”. Each curve of 4 points corresponds to a single flotation test with each point corresponding to a concentrate collected (see Figure 4.1 for illustration).

The Cu recovery-grade plots for the addition of 25% mica or silica (75% mica-free ore) by weight are shown in figure 4.1. For ease of understanding, the curves for addition of 25% mica or silica of the same size are shown in the same plot. It is readily apparent that for almost all sizes of mica and silica at the 25% addition rate, the plot for silica sits to the right of that of mica, except for the 100-150μ size, where the two plots are very close to each other. In the case of the

100-150μ data set, it appears that the final concentrate grade for the mica addition is still considerably lower than that for the silica. This suggests that concentrates produced when mica is the added mineral are significantly more diluted than for those where silica is added. The size of mineral added, thus, does affect flotation rate.

Another type of plot that provides useful insights is the Cu recovery vs cumulative mass recovery. Mass, in this case, refers to the mass of the concentrate (dry), and the mass recovery is the fraction of mass in the feed that is recovered. Here, if less gangue was transported to the concentrate, the curve would shift leftward.

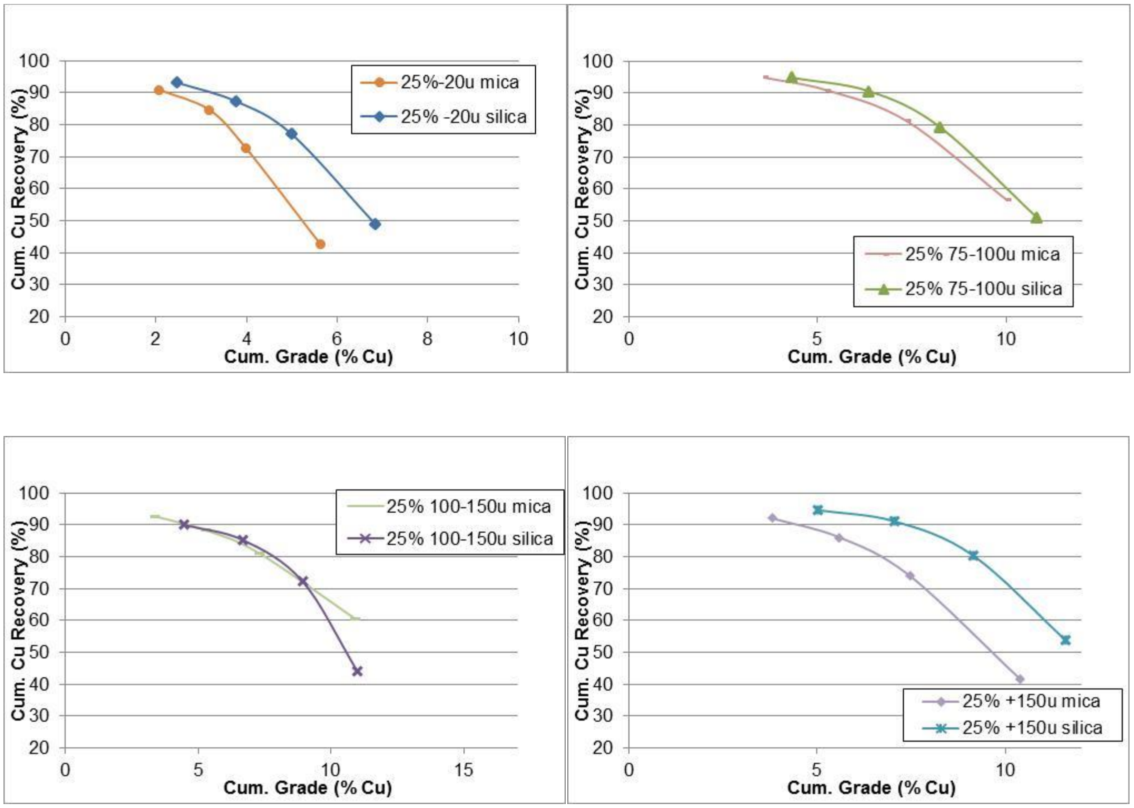

Figure 4.1: Cumulative Cu Recovery-Grade plot for 25% sized mica or silica added to 75% ground ore: (a) 20-50μ addition, (b) 50-75μ addition, (c) 75-100μ addition, and (d) 100-150μ addition. u indicates μ (micron size)

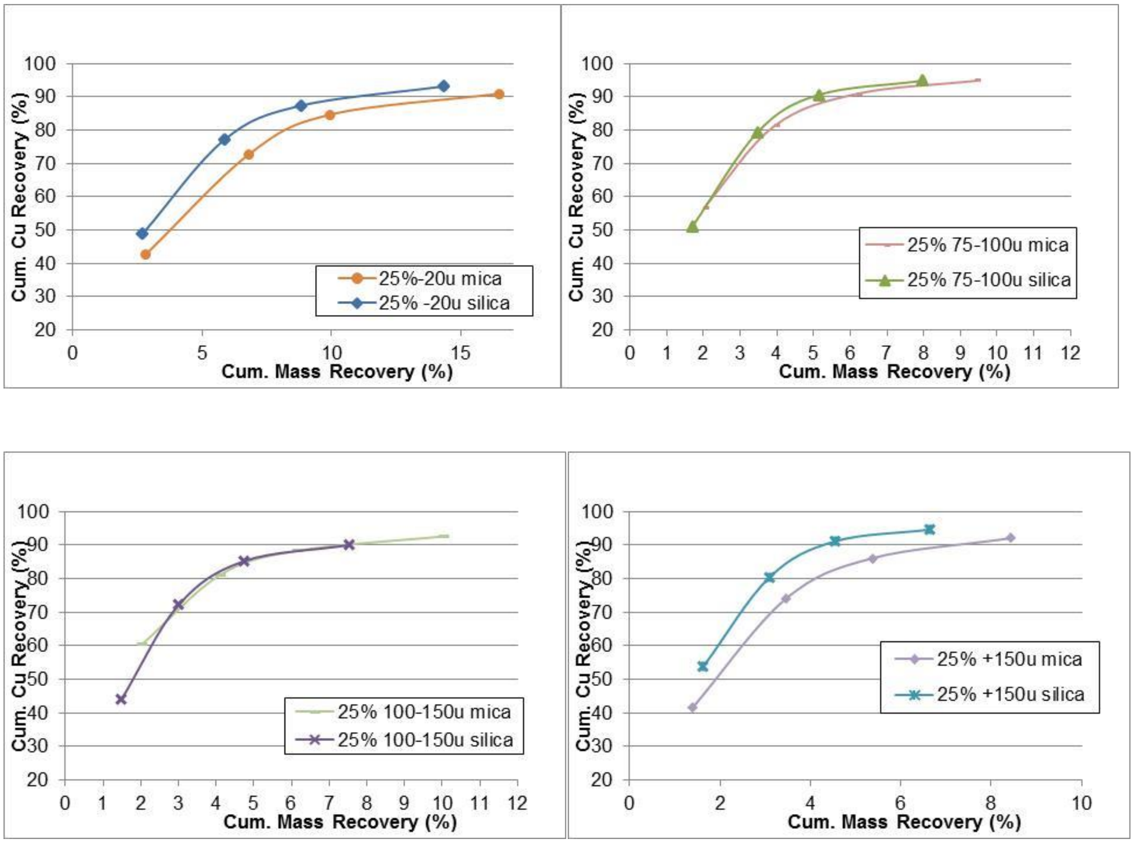

Figure 4.2: Cumulative Cu Recovery-mass recovery plot for 25% sized mica or silica added to 75% ground ore: (a) 20-50µ addition, (b) 50-75µ addition, (c) 75-100µ addition, and (d) 100-150µ addition

Figure 4.2 shows the Cu recovery vs mass recovery plot for 25% addition of mica or silica (75% base ore). The data shows that the silica addition curves are to the left of the mica addition curves, showing addition gangue transport with mica. This is apparent in the 100-150u size plot, where mass recovery is above 10%, as compared to when silica is added, where the recovery is 7.5%, a 25% increase.

The next set of plots is those for which 50% mica or silica are added (50% base ore). The recovery grade plots are shown in figure 4.3 below

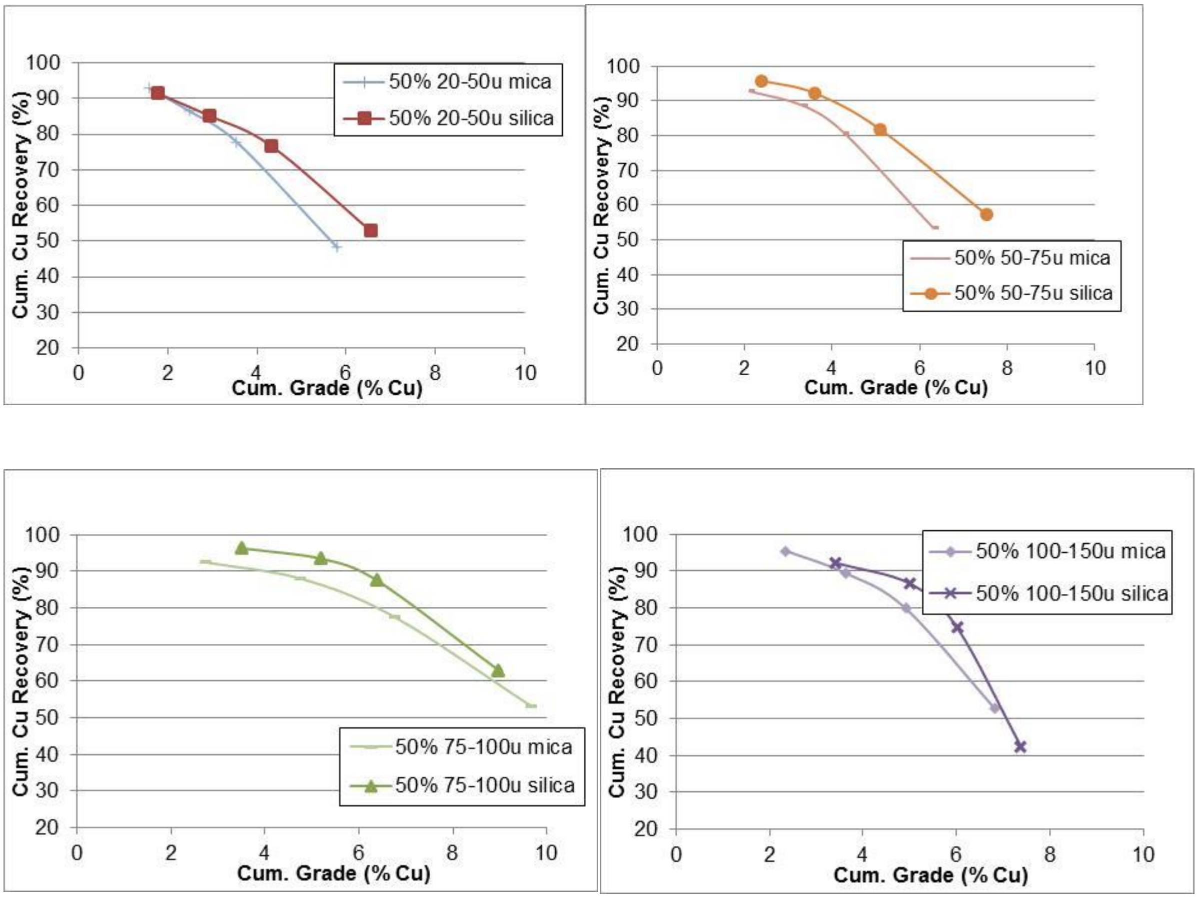

Figure 4.3: Cumulative Cu Recovery-grade plot for 50% sized mica or silica (by weight) added to 50% (by weight) ore: (a) 20-50µ addition, (b) 50-75µ addition, (c) 75-100µ addition, and (d) 100-150µ addition

Similar to the plots at 25% addition, the 50% addition plots show how the curve with mica is always to the left of the curve with silica. This suggests that the concentrates produced with mica are more dilute as compared to those produced with silica. Furthermore, in this dataset, the 100-150µ sized mica and silica plots are not coincident.

Figure 4.4 shows the Cu recovery vs mass recovery plot for 50% addition of mica or silica. Curves for the silica tests are always to the right of the mica tests, suggesting diluted concentrates with mica addition of all sizes. It is noted here that the minor difference in recoveries is within the margin of experimental error given the low grade of Cu in the samples after silica or mica is added to it. Once again, the 100-150u plots appear coincident with the mass recovery with mica is much higher, a 20% increase.

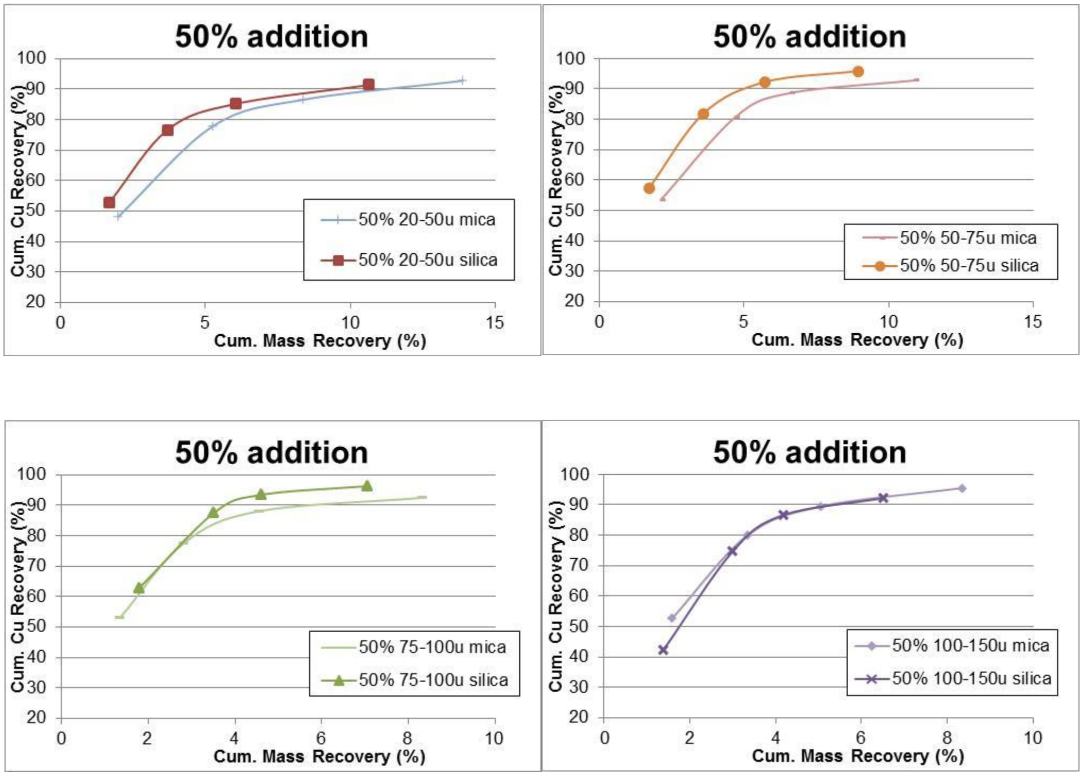

Figure 4.4: Cumulative Cu Recovery-mass recovery plot for 50% sized mica or silica (by weight) added to 50% (by weight) ore: (a) 20-50µ addition, (b) 50-75µ addition, (c) 75-100µ addition, and (d) 100-150µ addition

The cumulative mass recovery plots are instructive in comparing between the various sizes of mica and silica, as the amount of value sulfide minerals are small compared to the non-sulfide gangue. Figure 4.5 shows the cumulative mass recoveries of mica and silica added at 25% and

50%. The 25% plot shows a substantial decrease in mass recovery with increasing particle size.

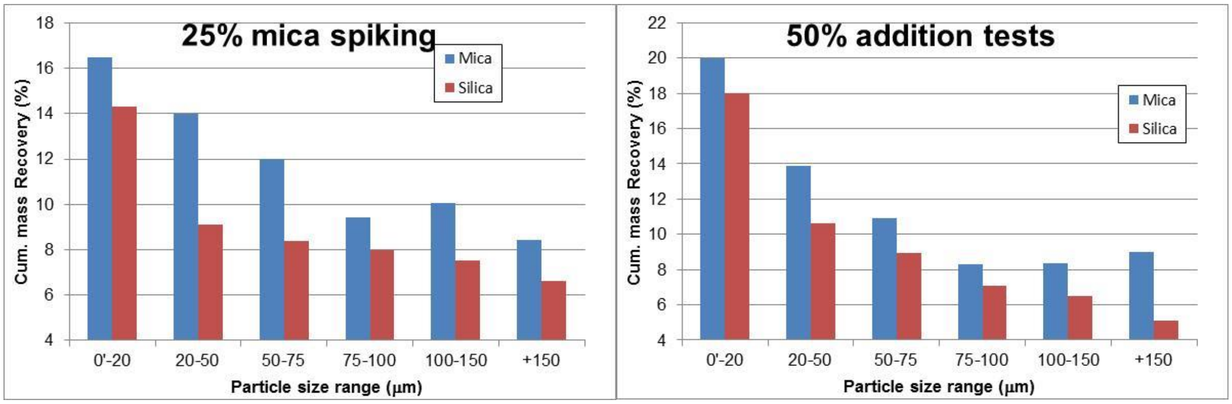

Figure 4.5: Cumulative mass recovery for addition of 25% and 50% (by weight) sized mica or silica to 75% or 50% ore

This suggests lesser dilution of concentrate with non-sulfide gangue minerals as a larger size of mica or silica is blended with the base ore. Given that the mechanism of transport for non-sulfide gangue minerals is presumed to be entrainment, the mass recovery plots appear, in this case, to be a viable proxy for degree of entrainment. However, there is a shift in the mass recovery plot for mica at 100-150μ. At this size, the mass recovery does not decrease any further, instead, increasing slightly from 9 to 10%. It then decreases back to 8.5% for the +150μ test. For the 50% addition, a similar mass recovery trend is observed for mica addition at the 100-150μ size, i.e. the mass recovery remains almost constant from 75-100 to 100-150μ.

4.2 Degree of entrainment

As discussed in the chapter 2, the degree of entrainment may be calculated as the slope between the line connecting the cumulative mass of particles recovered by entrainment, and the cumulative mass of water recovered, in the same time interval. The cumulative mass of entrained material was calculated by subtracting the total mass of chalcopyrite and pyrite from the total mass of material recovered (the assumption being that chalcopyrite and pyrite floating are recovered by true flotation, and the remaining mass consists of non-sulfide gangue). The calculation is shown in figure 4.6 below. In this situation, the ENT for mica addition is 0.27 and ENT for silica addition is 0.20.

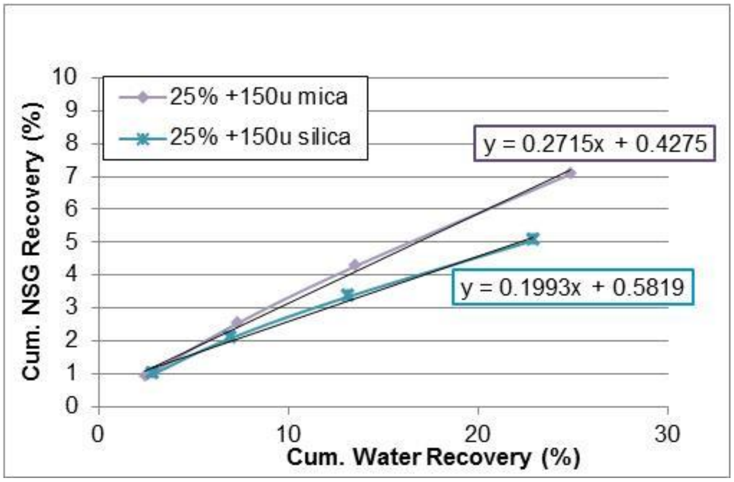

Figure 4.6: Illustration the calculation for the degree of entrainment- cumulative non-sulfide gangue recovery on the y axis and the cumulative water recovery on the x-axis.

It is also noted here that the line connecting silica recovery with water recovery for a given test is almost a straight line. According to Smith and Warren (1989), the line connecting the two should be a straight line when particles of a defined size are used, while the line appears parabolic when particles of multiple sizes are used. The data suggests that line is driven by particles of a narrow size fraction, thus the effect of mica/silica addition is certainly observed in this dataset. In other words, the curves are not driven by the ore alone.

The degree of entrainment (ENT) curves as functions of particle size for 25% addition rate of mica or silica are shown in figure 4.7.

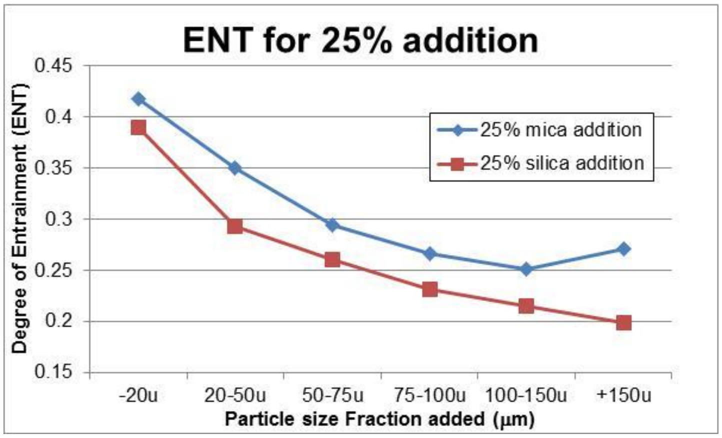

Figure 4.7: Degree of entrainment (ENT) for 25% addition of mica/silica as a function of particle size

Some key observations from the data are as follows:

a. There is a considerable change in ENT values and so the data are dominated by the particle size of the mineral added, even though the addition makes for only 25% of the blend.

b. The ENT curve for mica is above that of silica for all points except for the -20µ size, where both points are very close to each other.

c. The decrease in ENT is steady for mica addition, but decreases sharply for silica addition after -20υ size, followed by a steady decrease to +150υ.

d. However, there is a peculiar trend in the curve for the 100-150µ size mica; an increase in the ENT value, from 0.25 to ~0.3, suggesting increased entrainment with increasing particle size, which is theoretically not possible by entrainment.

The ENT vs particle size fraction curves for 50% addition of mica/silica are shown in figure 4.8 below. The trends are similar to those seen in the 25% curves except for a one key difference: ENT decreases until the particle size approaches 75-100µ. Thereafter, there is an increase in ENT for both mica and silica. The increase is susbtantially higher for mica than it is for silica.

Thus, the effect that seems to be minor, and only occuring at 150μ for 25% addition, now occurs at 100-150μ for 25% addition, and seems to occur for silica as well.

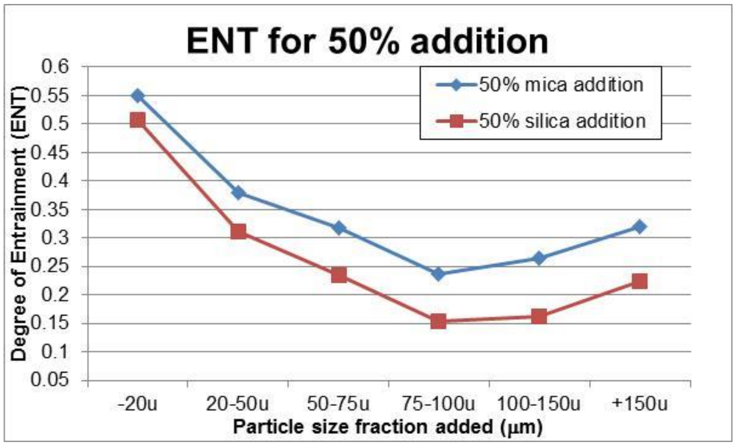

Figure 4.8: Degree of entrainment (ENT) for 50% addition of mica/silica

According to Zheng (2006), the reason why they saw a plateau in the ENT vs particle size curve was the recovery of coarse particles by entrapment. The paper is missing additional details, and efforts are made in this thesis to further this idea.

To do this, the ENT values for the individual concentrates are obtained. This is used to assess the effect of hydrophobic value minerals on ENT; the hydrophobic mineral content in the froth phase decreases from the first concentrate (C1) to the last concentrate C4. The ENT vs particle size curves for the final (4th) concentrate only are shown in figure 4.9 below.

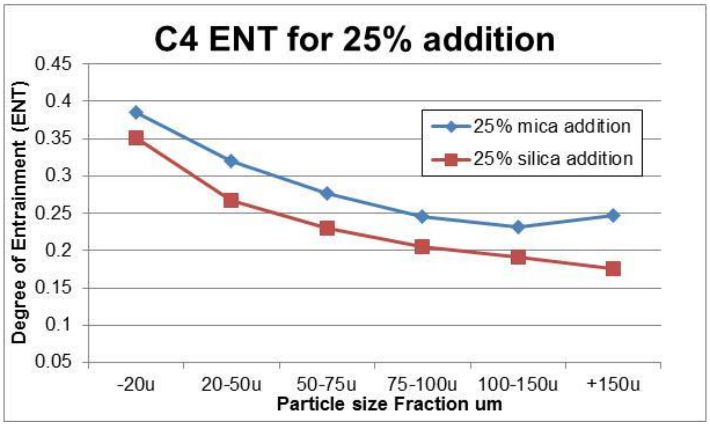

Figure 4.9: Degree of Entrainment for the fourth concentrate (only) as a function of particle size for 25% mica and silica addition (by weight) mixed with 75% (by weight) ground ore.

The ENT values for the fourth concentrate (only) show that the trends are similar to the overall ENT. This suggests that the change in direction of the ENT curve is maintained even when the hydrophobic solids content is very low, i.e. the final concentrate. Finally, the ENT curves for 50% addition rate are shown in Figure 4.10 below. The curves are similar to those for overall ENT values, with the only difference being that the ENT for silica does not appear to increase past 100µ size, rather, it remains constant, along the lines of what was observed by Zheng (2006).

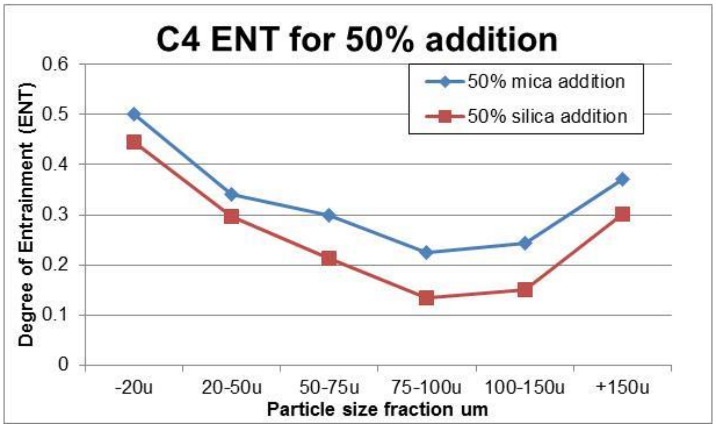

Figure 4.10: Degree of Entrainment for the fourth concentrate (only) as a function of particle size for 50% mica and silica addition (by weight) mixed with 75% (by weight) ground ore.

4.3 Flotation tests on Fibrous ore (containing approximately 1% of fibrous chrysotile)

To elucidate the mechanisms of transport of mica, flotation tests were conducted with systems for which the transport mechanisms are known. In Patra (2010), the author discusses the mechanisms for grade dilution attributed to fibrous minerals, namely “network transport via bubble flux”, and is explained in detail in the literature review section. In this system, substantial increases in slurry viscosity translate to increases in froth viscosity and thus serves as an appropriate comparative for studying whether froth interstitial viscosity is responsible for platy mica as well. Flotation tests were conducted by mixing into the base ore increasing amounts of fibrous-ore. The results from these tests are shown in Figure 4.11. The data shows a significant decrease leftward shift in the recovery-grade curve when increasingly more fibrous minerals are added to the system. It is also noted that the airflow rate had to be reduced substantially for addition of fibrous ore at 4% and 7% levels, so the impact of fibrous minerals is muted from that effect. The shift from 4% to 7% is not as apparent, and this is attributed to the need to reduce airflow rate to the lowest setting to maintain the same froth depth when the ore is mixed with 7% by weight of fibrous ore, or else the slurry would overflow without scraping (an unacceptable condition). The reduced airflow rate thus results in a physical limit on the recovery of concentrate, which is near what is possible at the 4% fibrous ore addition level. The impact is visible on the Cu recovery vs mass recovery plot as shown in Figure 4.12, with the 4% and 7% addition curves almost coincident, and thus not really representative of the flotation response. Finally, the ENT values for fibrous ore addition at 1% and 4% are shown in figure 4.13 below. The data shows an increase in ENT values are more fibrous material is added (recognizing that the 4% value is lower than what it should be). It is also apparent that the ENT values are very much higher than what is observed with silica and mica.

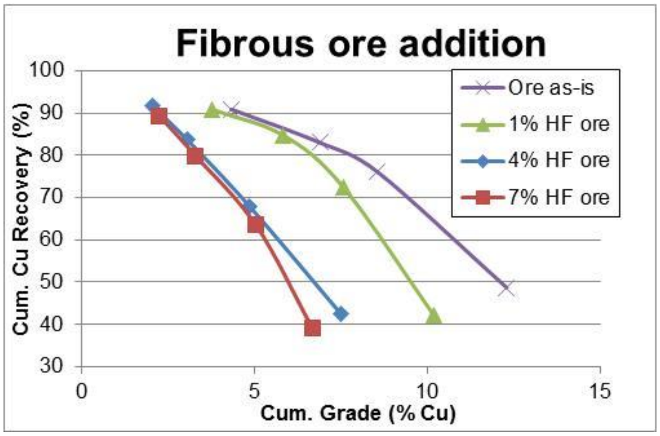

Figure 4.11: Cu Recovery-grade profile for fibrous ore mixed into the Cu ore at 1%, 4% and 7% (by weight) addition rates.

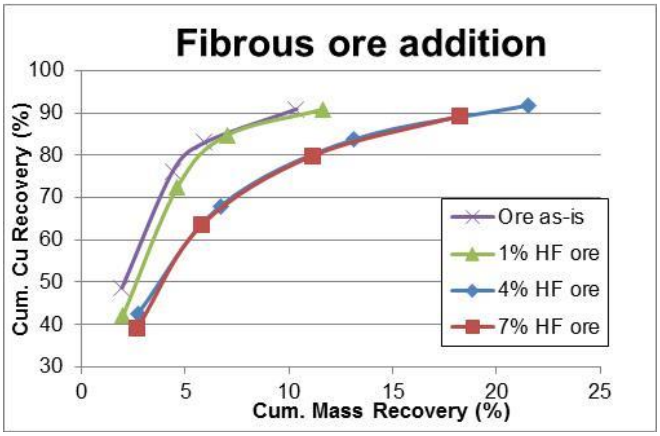

Figure 4.12: Cu Recovery vs mass recovery profile for fibrous ore mixed into the base Cu ore at 1%, 4% and 7% addition rates

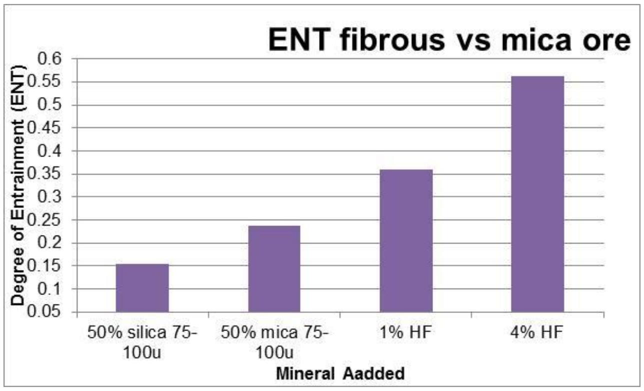

Figure 4.13: ENT values for 75-100µ mica and silica, and 1% and 4% fibrous ore addition to base ore

4.4 Summary

The data from the flotation tests demonstrates the following

1. Addition of mica results in leftward shifts in the recovery-grade curves, regardless of mica size added, for the 25% addition rate and the 50% addition rate. The exception to this is the 100-150υ size range, where the recovery is substantially lower.

2. Addition of mica results in a significant increase in the degree of entrainment (ENT) as compared to addition of silica of the same size. This is valid for all size fractions except -20μ.
3. There is a decrease in degree of entrainment with particle size as expected for both mica and silica at 25% addition rate (to ore). However, at +150μ, there is a reversal of this trend, with an increase in ENT values, which cannot be explained by the entrainment mechanism.
4. This trend continues for the 50% addition rate (to ore). There is a progressive decrease, but, this time, at 100-150μ size there is a reversal in the trend, with progressive increases in ENT for the coarser sizes
5. The ENT values for the final concentrate (only) suggest that there is no increase in ENT with silica, but there is a decrease with mica added at the coarse size ranges.

To further the understanding of the mechanisms attributed to the increased transport of mica, and the shape of the ENT vs particle size curve, froth sampling using a pure mineral system was conducted.

4.5 Additional flotation tests

Additional flotation tests were conducted, by addition of 12.5% mica of size 75-100μ. The results from these experiments are shown in figure 4.14 below. The data shows that the curve for silica is still to the right of mica, indicating that concentrate (product) quality is affected even when very small amounts of mica are present.

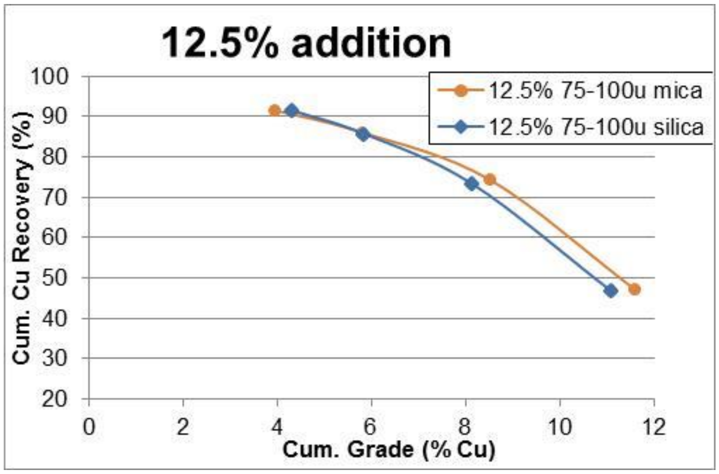

Figure 4.14: Recovery grade profile for mixture of 87.5% base ore and 12.5% either mica or silica of 75-100μ. Data shows poorer concentrate grade for when even low amounts of mica are present in the ore.

Flotation tests were also conducted by adding the plank-like wollastonite mineral in various ratios to the ore mixture. The results show a significant impact of wollastonite addition, with a decrease in product quality as more wollastonite is added.

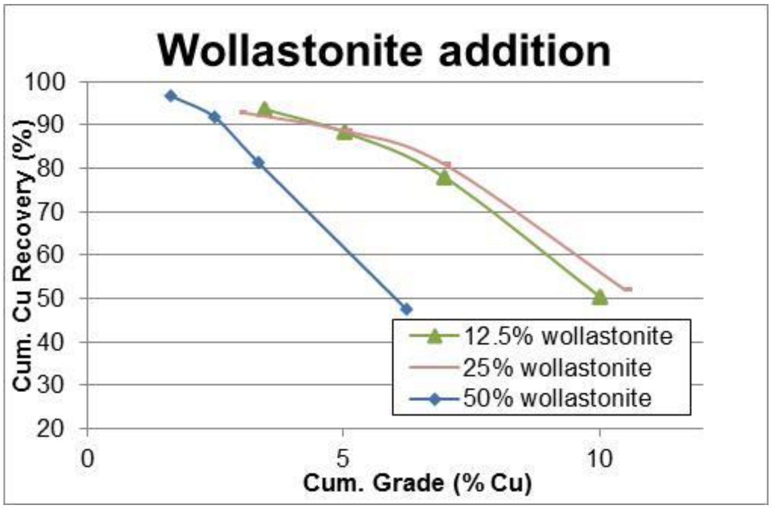

Figure 4.15: Recovery grade profile for mixture of various ratios of wollastonite and base fine silica. Data shows poorer concentrate grade when wollastonite is present, with the grade declining with increasing amounts of wollastonite.

5 Results from Froth sampling tests

5.1 Outline

Froth sampling tests were conducted in a bottom-driven flotation cell, as described in Chapter 3. The goal of these tests was to study the froth as a function of depth and to obtain compositional information on the various constituents as a function of depth. The data would be used to generate appropriate bulk slurries ex-situ, (replicating froth interstitial compositions) for rheological measurements. These experiments in themselves provide valuable insights into mechanisms driving the transport of value and gangue minerals into and through the froth zone. The first set of results includes those conducted on mica and silica mixtures, in the absence of hydrophobic solids. The second set includes results on mica and silica mixtures in the presence of hydrophobic solids. The third set includes results with mixtures of silica and an ore containing the fibrous mineral chrysotile. Froth sampling experiments were conducted under nascent (high drag conditions) and steady state (balanced drainage and drag conditions) sampling conditions.

5.2 Experimental plan for froth sampling

The experimental plan for froth sampling is shown in the figure below. Experiments that are included in the "additional experiments" section are not shown here.

Table 5.1: Experimental plan

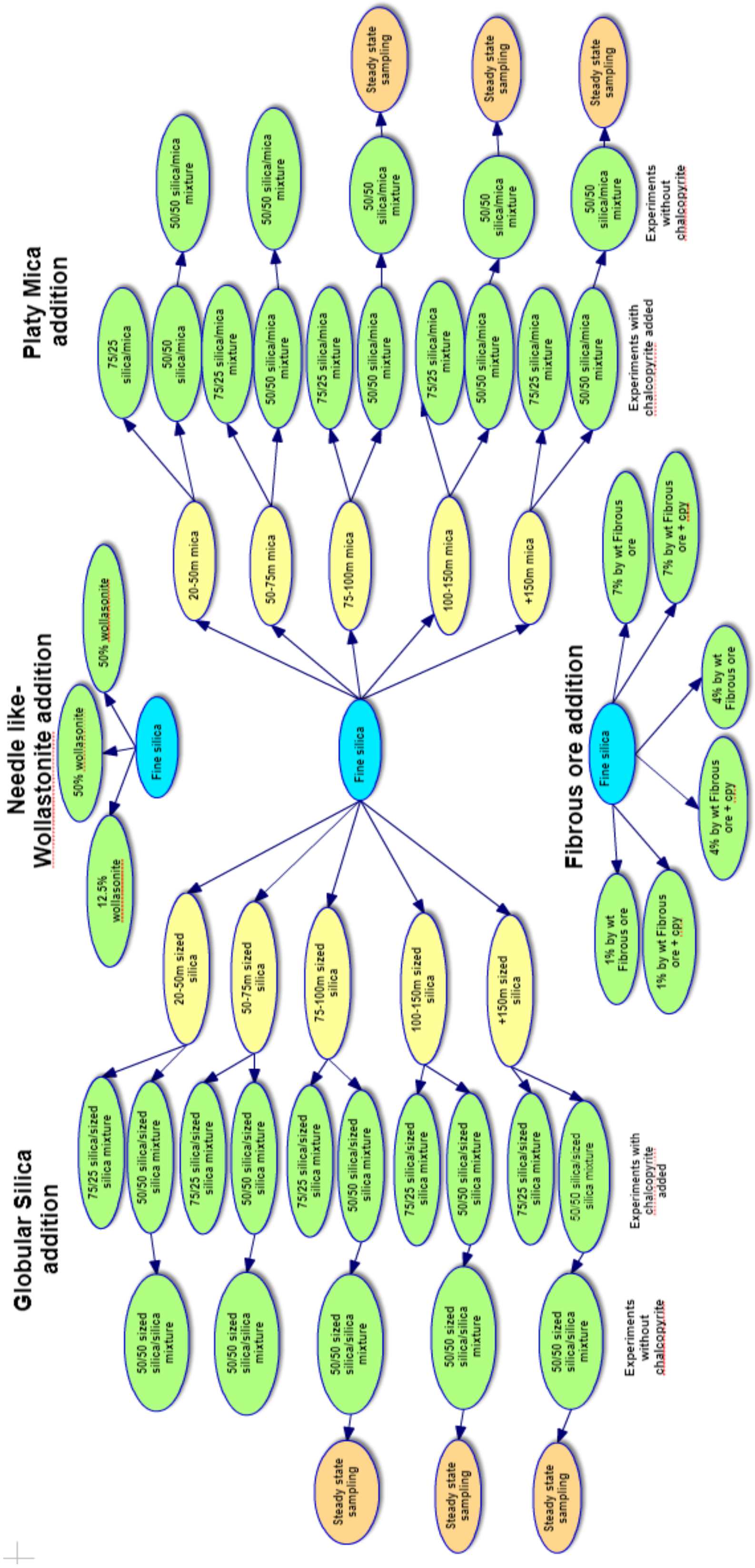

5.3 Reproducibility of results

To confirm that the froth sampling equipment was working as desired, replicate runs were conducted using a sample of 50% wide particle size distribution mica and 50% fine silica (w/w). The experiments were conducted by raising the froth and sampling as soon as the froth reached the top of the sampler (nascent sampling, ~30 seconds after turning air on). The results are shown in figure 5.1 below.

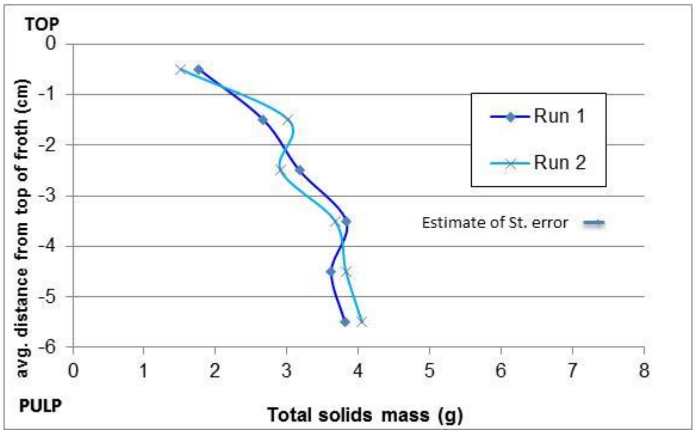

Figure 5.1: Nascent Froth sampling tests- Assessing reproducibility- 50/50 coarse mica/fine silica experiments using two independently prepared samples, 35% solids concentration in pulp. This plot shows solids mass in each layer.

As expected, the mass of hydrophilic mineral recovered in the froth decreases as the top of the froth is approached (section 2.2) for these nascent froth sampling experiments, where the system is upward transport/drag dominated. When froth sampling is delayed, the system is drainage dominated, and the concentration of hydrophilic minerals is the bare minimum needed to maintain a froth bed after much fine silica has drained out, as shown in figure 5.2.

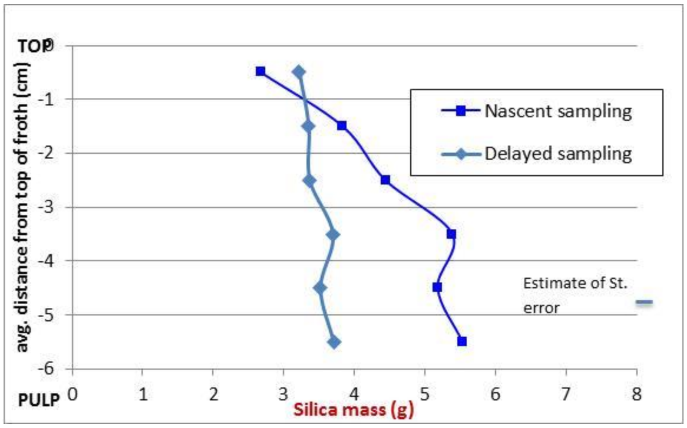

Figure 5.2: Comparing nascent and steady state froth sampling- 100% fine silica, 35% solids concentration slurry

5.3.1 Solids mass, water content and solids density in “nascent” sampling tests for fine silica only

The solids concentration (w/w), solids mass and water mass as a function of depth are shown in Figure 5.3 below. The data shows that the solids concentration remains relatively constant as a function of depth. However, both silica mass and water mass decrease slightly, but in proportion. This is because in this test the froth is still building up, and the fine hydrophilic solids and water and transported together. Note also that the froth solids concentration is less than the pulp solids concentration. This is explained by the fact that a fraction of solids (~30%) are rejected at the pulp-froth interface, as explained in section 2.2.

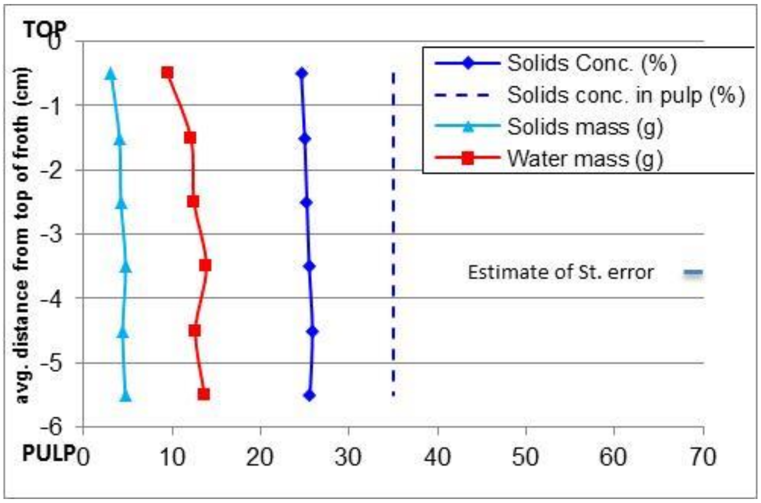

Figure 5.3: Nascent froth sampling- Solids concentration, solids mass and water mass for fine silica only. Solids concentration in slurry was 35%.

5.3.2 Effect of mica addition

In the first set of experiments, the fine silica was replaced with 50% by weight of mica of various size fractions. The treatment is similar to the flotation tests, except, instead of the base Cuore, we use fine silica. As discussed earlier, this allows for accurate quantitation of the mica and silica in each layer. Figure 5.4 shows the results from these froth sampling tests. Layer 1 is excluded from these results because of the high variability in that layer (attributed to slight differences in final height of froth before nascent sampling).

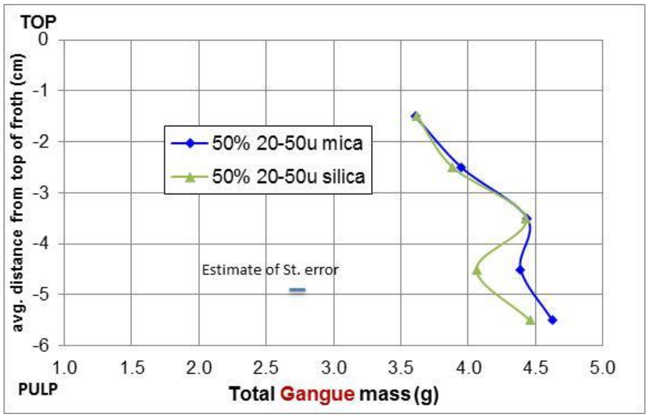

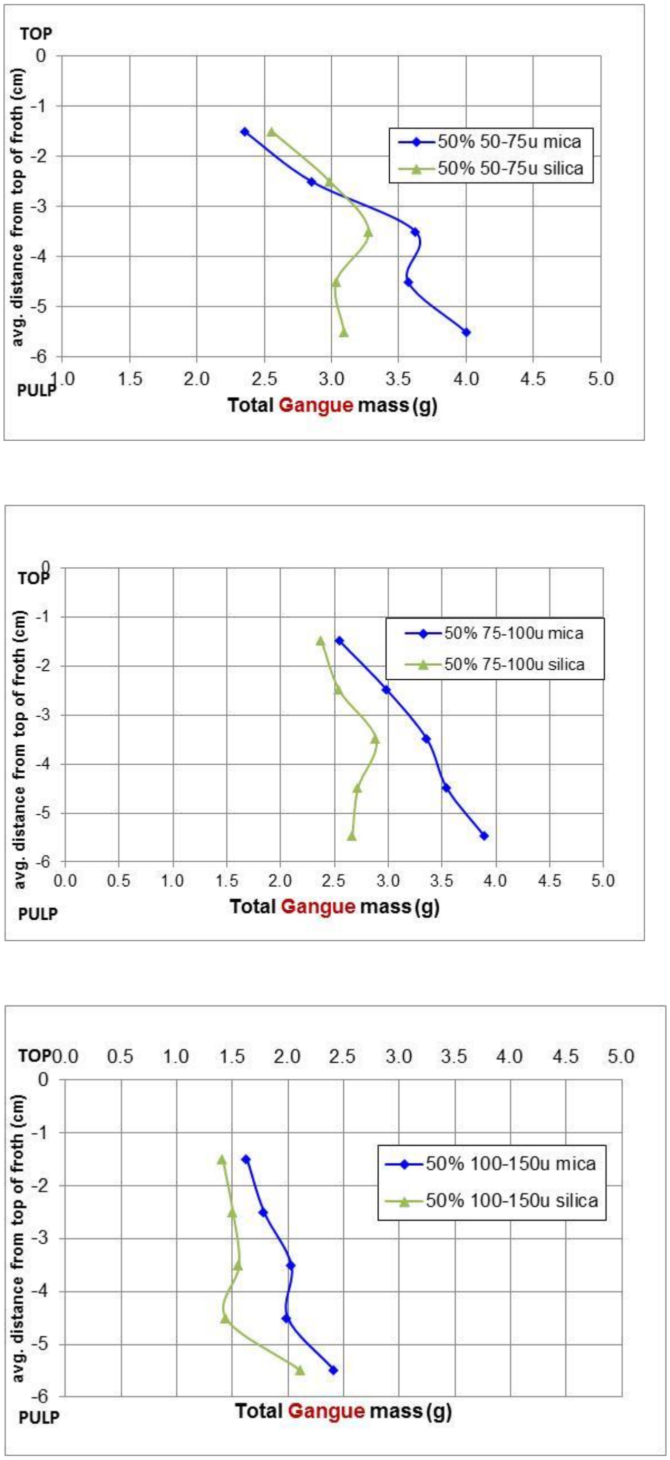

Figure 5.4: Nascent Froth sampling tests- Addition of 50% mica or silica of 20-50μ (a), 50-75μ (b), 75-100μ (c), 100-150μ (d) sizes to 50% fine silica. The plot shows total gangue mass (including mica and silica) in each layer. Solids concentration in pulp is 35%, and no chalcopyrite (sulfide value) is added. The total mass of gangue is significantly higher for 75-100μ and 100-150μ mica mixtures as compared to silica mixtures of the same size.

The following observations can be made:

a. The total mass of material transported to the froth (as soon as it is formed) decreases as the particle size of silica/mica added increases. This is in line with the observations from flotation tests.
b. The total mass of material transported is very similar for mica and silica of the lowest size fraction, i.e. 20-50μ. At coarser size fractions, a clear difference is observed, with the amount of material transported to the froth for the mica addition tests being higher than that for the silica addition tests.
c. The results for 50-75μ mica and 75-100μ mica are very similar, but there is a drop in total mass from 20-50μ to 50-75μ, and another drop from 75-100μ to 100-150μ.
d. The amount of material in the froth zone decreases from bottom layer to top layer for all sizes, except for the 100-150μ size mica over most of the froth depth.

The water content of the froth as a function of froth depth for the above experiments is shown in figure 5.5 below. The data suggests that there is more water in the froth when mica is added at 50%, as compared to when silica is added in the same ratio, regardless of size of mica/silica added. However,

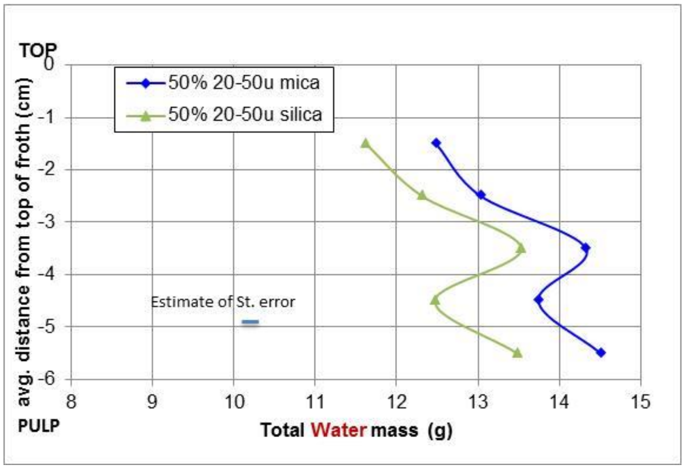

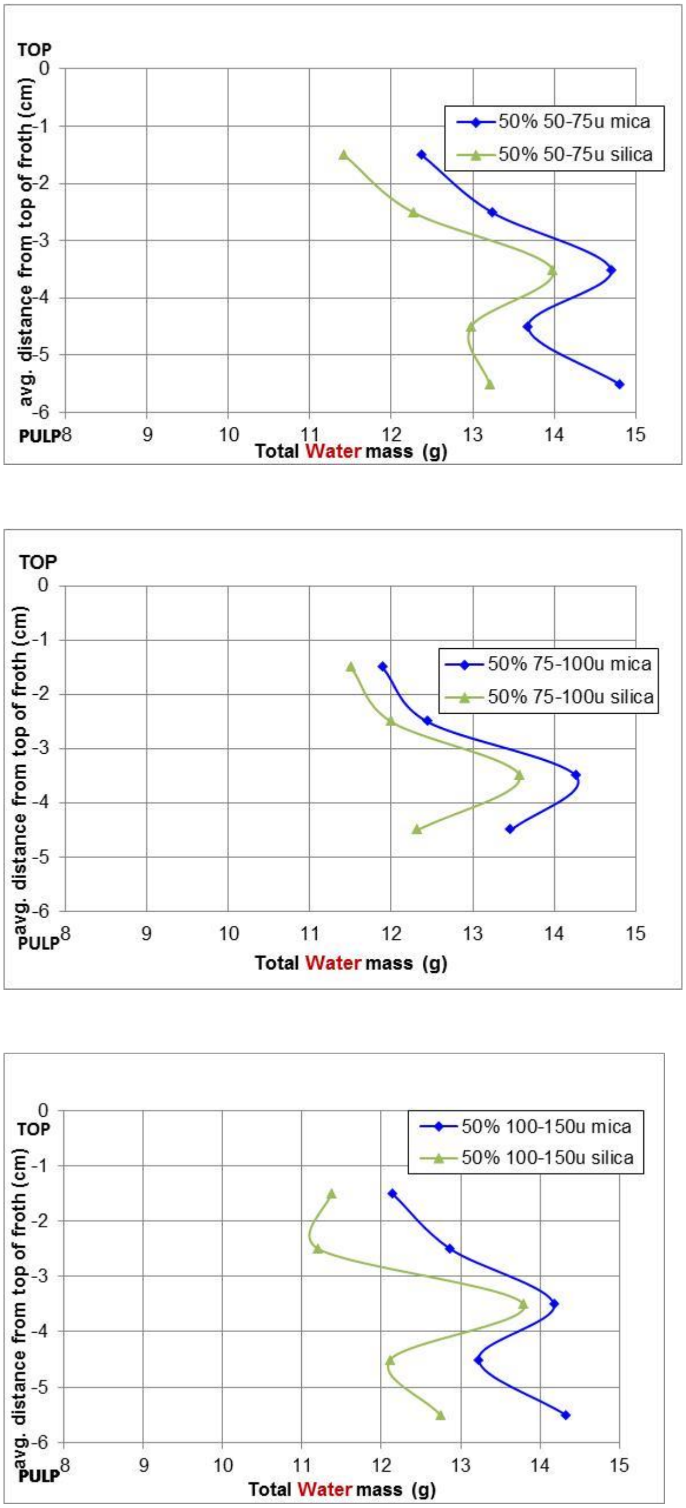

Figure 5.5: Nascent Froth sampling tests- Addition of 50% mica and silica of 20-50μ (a), 50-75μ (b), 75-100μ (c), 100-150μ (d) sizes to 50% fine silica base sample. The plot shows total water mass (including mica and silica) in each layer. Solids concentration in pulp is 35%, and no chalcopyrite (sulfide value) is added. The mass of water is significantly higher for all mica mixtures as compared to silica mixtures of the same size.

there is no significant difference in the amount of water in the froth for any size of mica or silica added. This indicates that the amount of water moving into and through the froth during the initial buildup of the froth is similar, regardless of particle size of mica or silica added. Even as the pulp/froth interface is able to act as a classifier, not allowing coarser particles to be transported, this does not affect the amount of water moving into the froth. The bends in the shapes of the curves may be explained partially by the leaks in a given layer. The total gangue mass from all the mica tests is plotted in figure 5.6(a) below. The results show the steady decrease in total gangue mass transported to the froth phase as the size of mica (mixed 50:50 with fine silica) is increased. The decrease is substantial, with the total gangue mass with 50% 100-150μ and +150μ mica being approximately one half of the mass with 50% 20-50μ mica.

5.4 Mica vs silica transported

For the above tests, the amount of mica present in each layer is shown as a function of particle size of mica in figure 5.6 (b) below. The plot shows that there generally is a decrease in mica recovered relative to fine silica as a function of mica particle size when the froth is raised and sampled in ~30 seconds. Again, this is along the lines of what is expected in the results from the flotation tests.

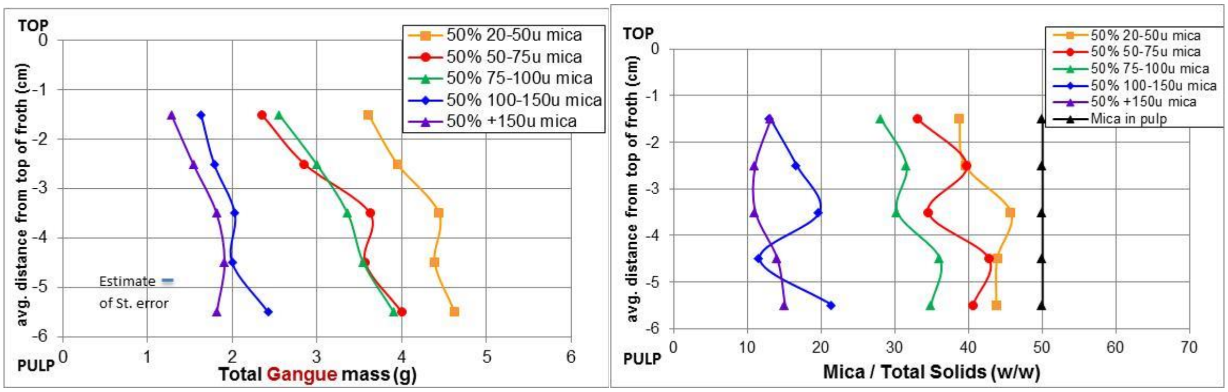

Figure 5.6: Nascent Froth sampling-50% fine silica mixed with 50% sized mica (a) Total gangue mass from figure 5.4 for mica tests combined (b) Mica (%) in layer as a function of particle size. [35% slurry solids concentration]

5.5 Mica vs silica in the presence of hydrophobic solids

The results from nascent froth sampling tests are summarized in figure 5.7 below, which shows the total gangue mass in each froth layer for the addition of 49% sized mica or silica to 49% fine silica and 2% chalcopyrite (made hydrophobic by adsorbed collectors). The data are grouped by mica or silica size. The results in the presence of hydrophobic solids (chalcopyrite) are very similar to those obtained without hydrophobic solids (section 5.2 above). There is a decreased transport of total gangue (hydrophilic) into the froth as a function of its particle size. Total gangue transport when mica is added remains higher than or almost equal to when silica of the same size is added.

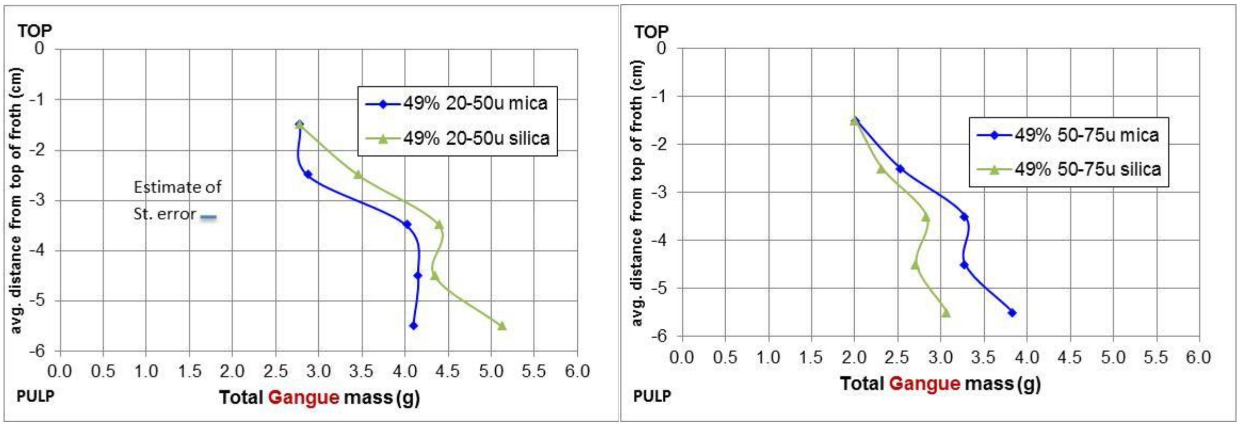

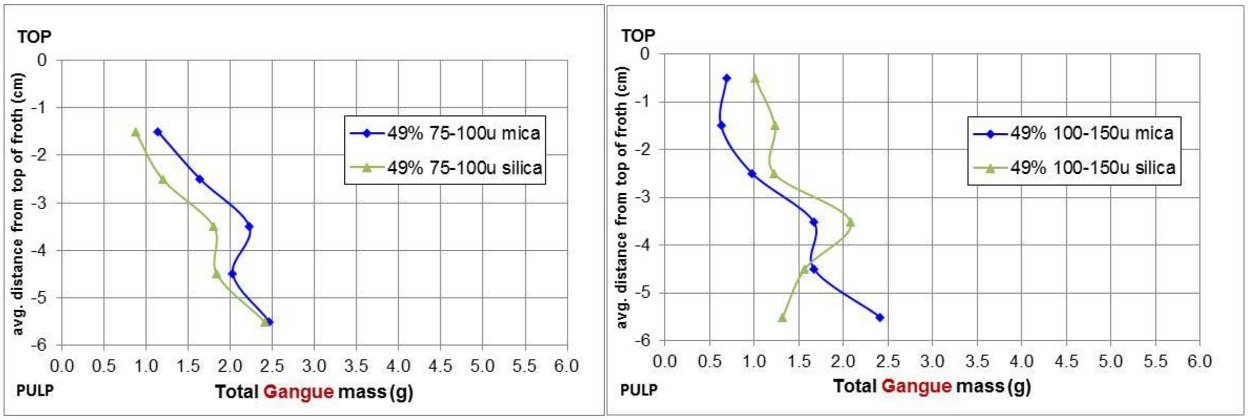

Figure 5.5.7: Nascent Froth sampling tests with 49% fine silica mixed with (a) 49% 20-50µ mica or silica, (b) 49% 50-75µ mica or silica, (c) 75-100µ mica or silica and (d) 100-150µ mica or silica, and 2% Chalcopyrite by weight (0.7% Cu). Solids concentration in pulp was 35%. Total gangue mass as a function of froth height for 49% mica or silica is shown. Data shows gangue mass slightly higher when mica is added compared to silica for nascent sampling for some sizes.

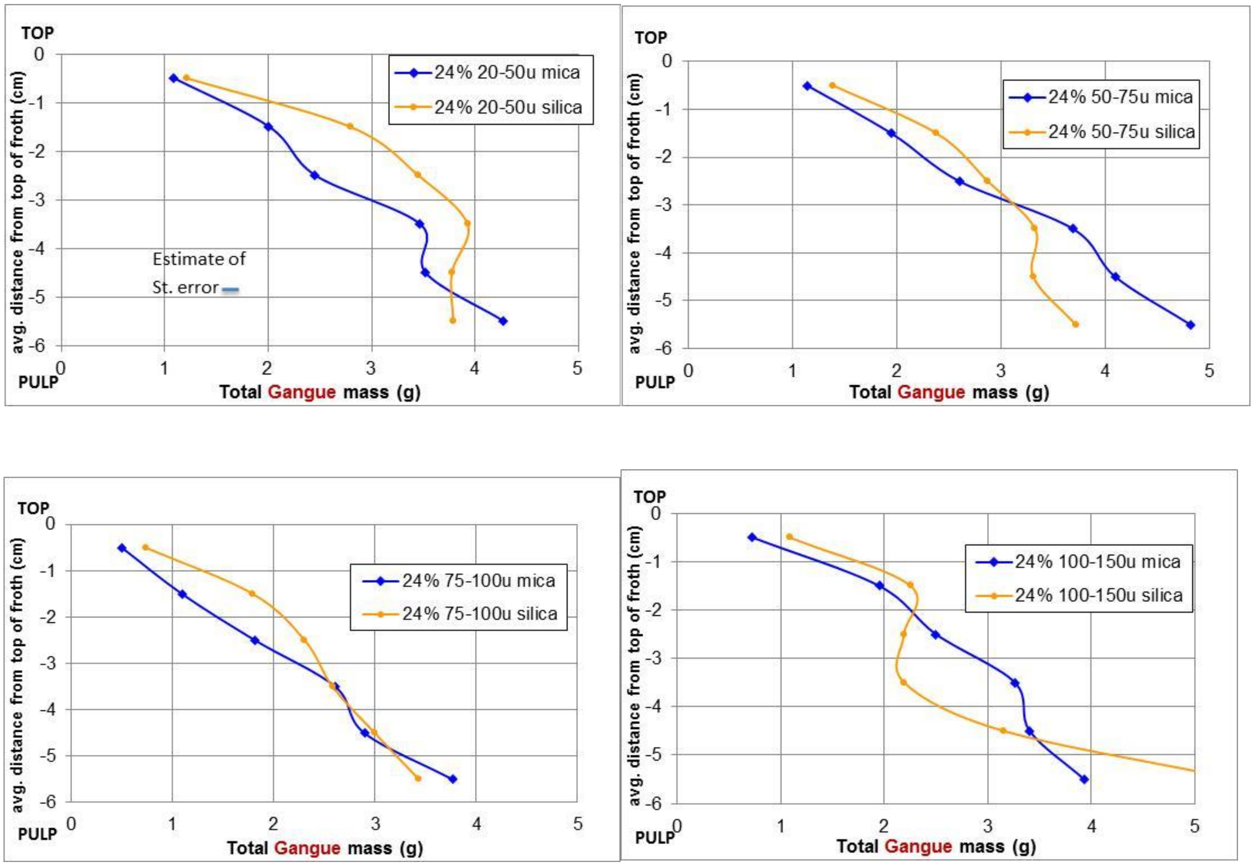

Figure 5.5.8: Nascent Froth sampling tests with 74% fine silica mixed with (a) 24% 20-50µ mica or silica, (b) 24% 50-75µ mica or silica, (c) 24% 75-100µ mica or silica and (d) 24% 100-150µ mica or silica, and 2% Chalcopyrite by weight (0.7% Cu). Solids concentration in pulp was 35%. Total gangue mass as a function of froth height is shown. The data shows

significant drop in gangue mass as a function of height for 25% addition as compared to 50% addition. This is because the gangue transport is more dominated by the fine silica.

The results for 25% mica or silica (~24%) addition are shown in figure 5.8 above. There is no significant difference in the mass recoveries regardless of size of mica or silica added. The data suggests that the initial transport (nascent sampling) at 25% mica or silica addition is not dominated by the sized mica or silica added. Instead, it is dominated by the fine silica that constitutes the majority of the mineral mixture. Another species playing a critical role is the hydrophobic chalcopyrite itself; this is evident in the shape of the curves, which show the total gangue mass decreasing much faster as the top of the froth is approached than for the 50% addition rate.

The fraction of the transported material that is mica is shown in figure 5.9 below. The transport does appear to be dominated by the fine silica.

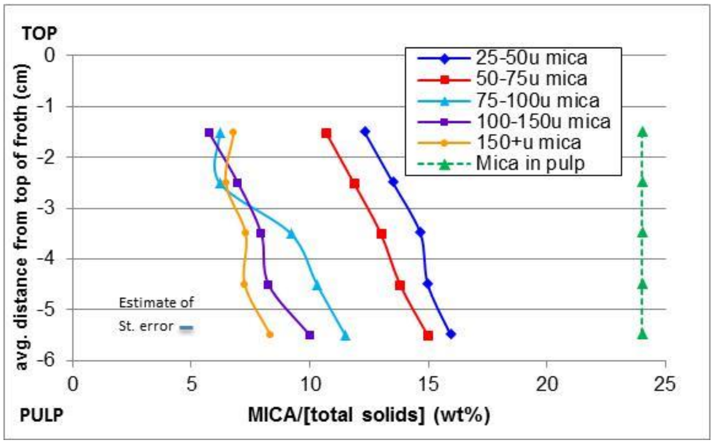

Figure 5.9: Nascent froth sampling for 25% mica addition- Mica (%) in fine silica with 2% chalcopyrite in each layer as a function of particle size

5.6 Sampling of Steady state froths

As discussed in the experimental section, for the steady state froth sampling experiments, a delay duration of 5 minutes was used. The results from froth sampling tests for steady-state sampling are compared with those for nascent sampling and grouped by size. Plots are shown in Figures 5.10, 5.11 and 5.12.

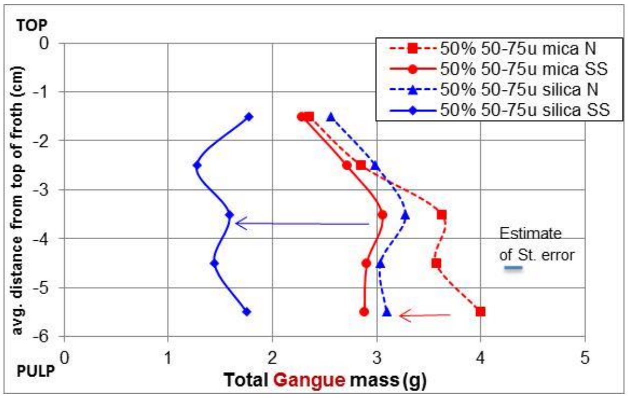

Figure 5.10: Froth sampling under nascent (N) and steady-state conditions (SS)- 50% fine silica mixed with 50% 50-75µ mica or silica. No chalcopyrite; 35% solids concentration. Data shows a significant decrease in gangue mass upon extending the duration of the froth when silica is mixed in, and a more significant decrease in gangue mass when mica is mixed in.

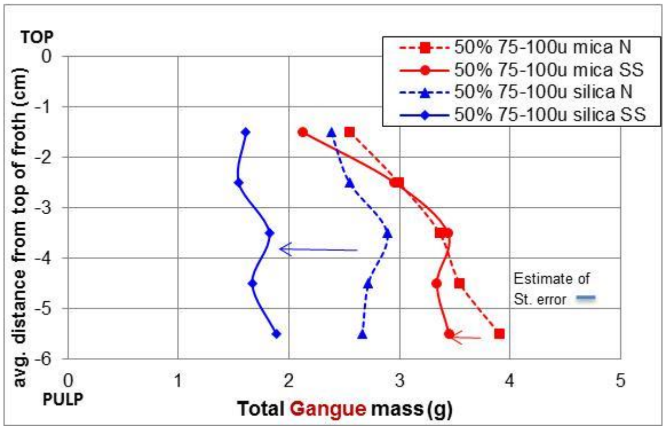

Figure 5.11: Froth sampling under nascent (N) and steady-state conditions (SS)- 50% fine silica mixed with 50% 75-100µ mica or silica. No chalcopyrite; 35% solids concentration. Data shows a decrease in gangue mass upon extending the duration of the froth when silica is mixed in, and almost equivalent gangue mass when mica is mixed in.

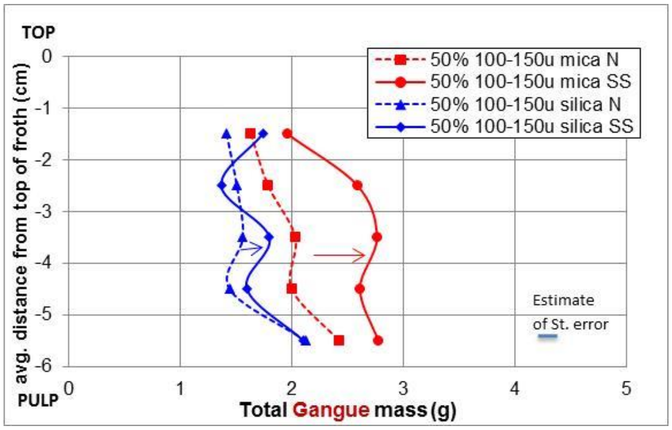

Figure 5.12: Froth sampling under nascent (N) and steady-state conditions (SS)- 50% fine silica mixed with 50% 100-150µ mica or silica. No chalcopyrite; 35% solids concentration. Data shows a negligible increase in gangue mass upon extending the duration of the froth when silica is mixed in, and a more significant increase in gangue mass when mica is mixed in.

The data shows the following:

1. For the finest size tested, i.e. 50-75µ, for silica (Figure 5.10) , there appears to be a significant decline in silica in all layers when a steady state sample (5 minutes) is taken, as compared to nascent sampling, suggesting significant drainage in the steady-state froth.
2. However, for the same size of mica (50-75µ), there appears to be a very small decline in total gangue mass for the steady-state sampling condition. This suggests that in the steady-state froth, over time, the silica is able drain from the froth a lot faster than mica.
3. A very similar trend is seen for the 75-100µ size samples. There is a significant reduction in total gangue mass in all layers for silica addition, and a negligible reduction in gangue mass for the mica addition. This is attributed to faster drainage of silica compared to mica in steady-state froths.
4. However, at the 100-150µ size silica, there is an unusual trend. The transport of 100-150µ silica appears to be slightly more for the delayed sample. At best, it appears that the

transport is equal, suggesting that these coarse silica particles are not able to drain from the froth as well as the finer silica

5. For the 100-150μ mica addition, the gap between the nascent and steady-state sample is wider, with considerably more material present in the froth for steady-state sampling as compared to the nascent sampling. The reasons for this will be part of the discussion section.

To ensure the validity of the above trend, an additional test was conducted by sampling after a delay of only 2 minutes and the data is shown in Figure 5.13 below.

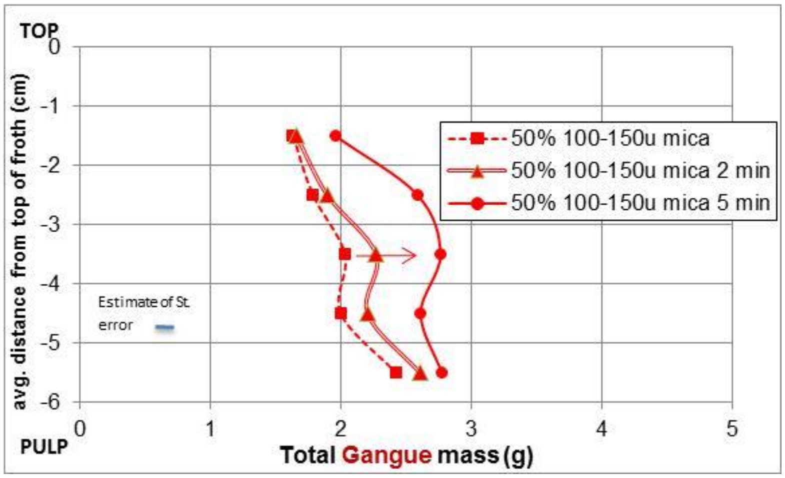

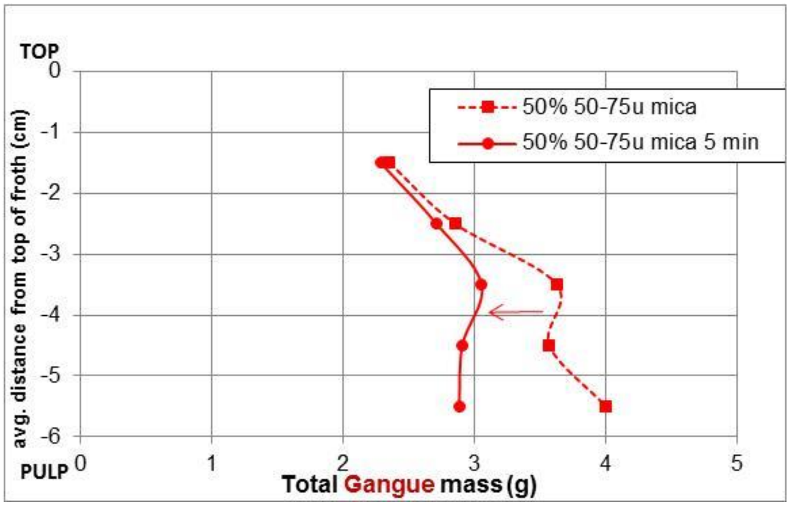

Figure 5.13: Froth sampling- nascent, short delay (2 min) and steady state (5 min). Mixture of 50% fine silica and a) 50% 100-150µ mica, b) 50% 50-75 µ mica. Data shows increase in total gangue mass with time for 100-150µ mica addition, and a decrease at 50-75µ mica addition.

The plot shows that there is indeed slightly more material in the froth during a 2-minute delay than during nascent sampling. In addition, in this intermediate test, the mass appears to steadily build up starting with the lower layers (3, 4 and 5) showing more mass than the upper layers. The steady-state sample (5 minutes) shows increased mass in all layers, in comparison to the 50-75µ mica (b), for which there is a decrease in mass for the steady-state sample.

5.7 Fibrous ore mixture tests

The results in this section illustrate the effects of addition of fibrous ore on nascent and steady-state froths to help understand mechanisms driving transport of the various gangue mineral species. The tests illustrated here are conducted in the presence of hydrophobic solids (i.e. 2% chalcopyrite). Recall that the fibrous ore likely contains about 1% by weight fibrous minerals and that these have a very broad length distribution.

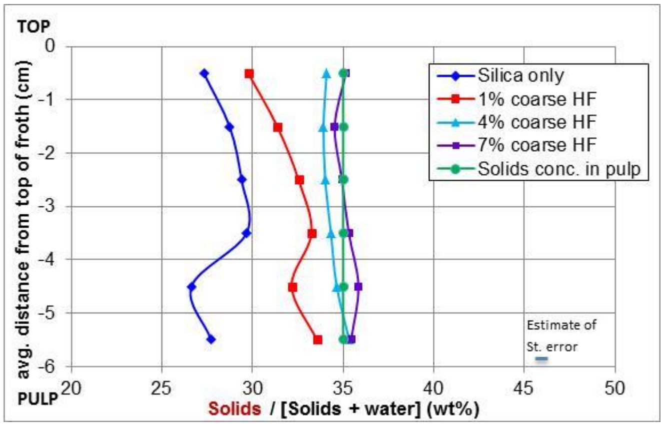

Figure 5.14: Nascent froth sampling- Solids concentration (wt. %) with increasing amounts of coarse-ground fibrous ore added to fine silica with 2% chalcopyrite; 35% solids concentration in pulp.

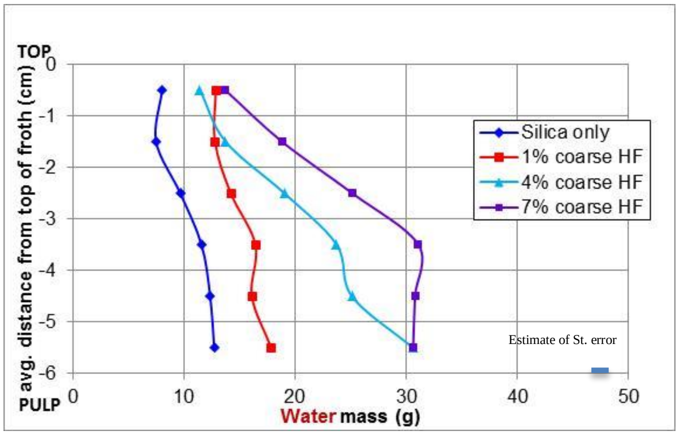

Figure 5.15: Nascent froth sampling- Water mass with increasing amounts of coarse-ground fibrous ore added to fine silica with 2% chalcopyrite. 35% solids concentration in pulp.

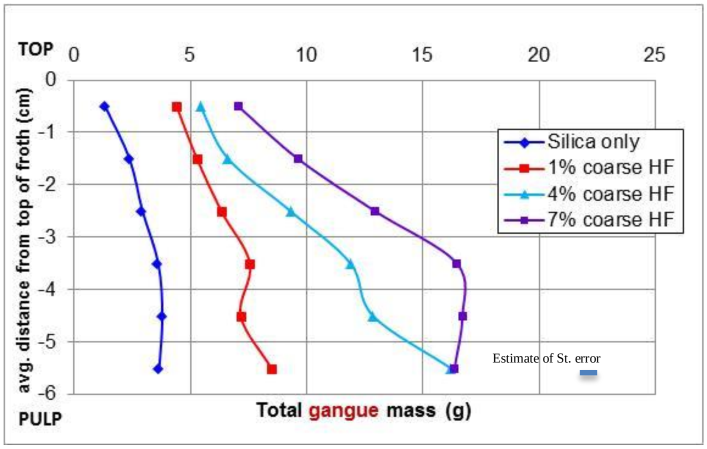

Figure 5.16: Nascent froth sampling- Total gangue mass with increasing amounts of coarse-ground fibrous ore added to fine silica with 2wt% chalcopyrite in pulp; 35% solids concentration in pulp.

The first plot (figure 5.14) shows the solids concentration in the froth zone, which changes significantly as the amount of fibrous mineral content is increased. It approaches a maximum of 35%, which is the solids concentration of the slurry, but does not increase beyond it. This provides further evidence for the “network transport through bubble flux” mechanism, as demonstrated in Patra (2010). The solids density remains constant going up to the top of the froth. This is also not typical; there should be decrease in solids content as a function of height even under nascent sampling conditions, and can also be explained by the mechanism above.

Figure 5.15 shows the water mass in the froth zone, which increases unevenly with height in the froth with increasing the fibrous ore content. It is noted here that the airflow rate for the 7% fibrous ore addition is lower than the 4% fibrous ore addition, which is lower than the 1% fibrous ore addition. This is because the higher viscosities from increasing fibrous ore addition result in significantly deeper froths. As the network is stronger with more fibrous minerals being transported, the amount of water that it can hold also increases. Figure 5.16 shows the increasing gangue mass in the froth, which follows the trends for water recovery. The coincident decrease in water mass and total gangue mass and no effect on solids density is a clear indicator that even as the channels thin in the upper layers and drainage occurs, the high viscosity results in drainage of solids and liquid at the same rate.

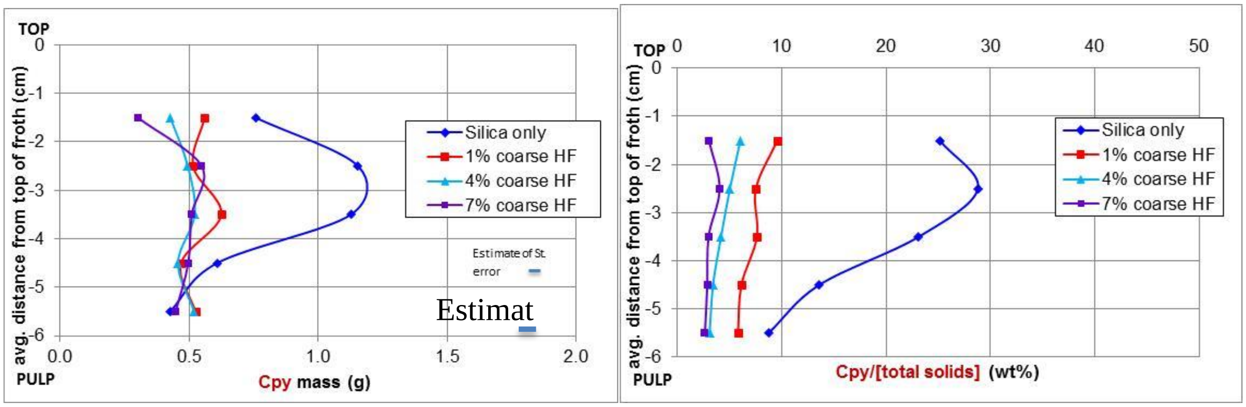

Figure 5.17: Nascent froth sampling- (a) Chalcopyrite mass in layer, and b) chalcopyrite relative wt% in layer for increasing amounts of coarse-ground fibrous ore added to fine silica with 2% chalcopyrite (w/w); 35% solids concentration in pulp

Figure 5.17 highlights the effect of fibrous ore addition on flotation of hydrophobic values (chalcopyrite). 5.17(a) suggests that chalcopyrite mass is unchanged regardless of the fibrous mineral content in the mineral mixture. However, the chalcopyrite transport is less than when silica without fibrous ore is used, suggesting that the viscous froth obstructs chalcopyrite transport and affects recovery, as is shown in Patra (2010). In the case of Patra et al (2010), the recovery impact was only observed at 4% coarse HF addition, suggesting that at low fibrous content, after the fibrous minerals are removed in the first concentrate, recovery is eventually possible. This suggests an impact on flotation kinetics at low fibrous content, but recovery impact at higher fibrous mineral content. Note: the unusual shape of the silica (no fibrous ore) curve is due to a collapse of the top of the froth laden with hydrophobic solids which was observed as the froth was building up.

5.8 Behavior of fibrous minerals in nascent sampling vs steady state sampling

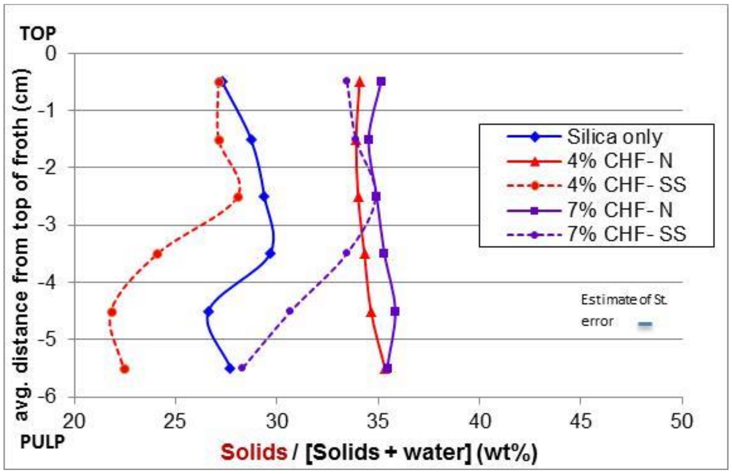

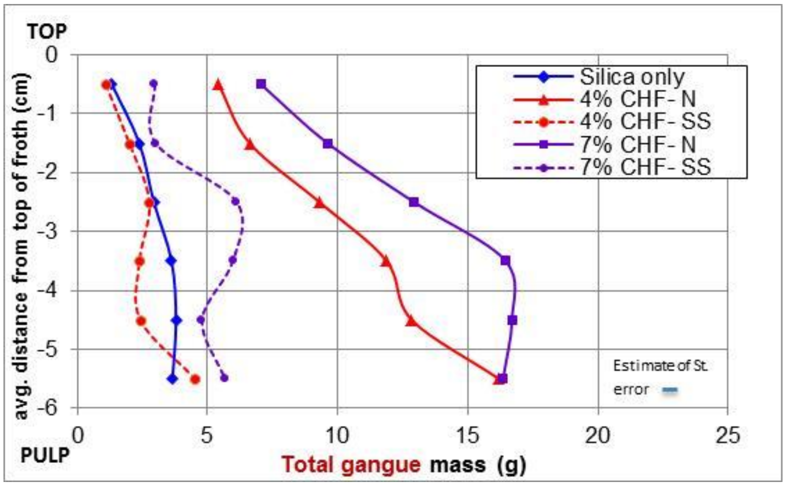

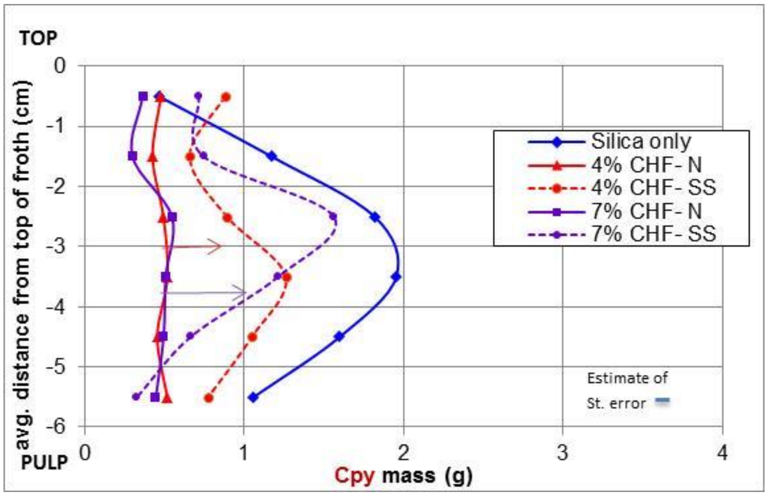

Figure 5.18: Nascent vs steady state sampling (5 minute delay) - 4% and 7% fibrous mineral addition to silica - a) Solids density in each layer, b) Total gangue mass in each layer, and c) chalcopyrite mass in each layer

Figure 5.18 shows the results from froth sampling with fibrous ore addition, when the sampling is conducted under nascent conditions and under steady state (5 minute delay). In 5.18 (a) it is observed that there is a substantial decrease in solids concentration at all levels with 4% fibrous ore is added, but less and only at the lower levels when 7% fibrous ore is added. The 7% addition thus marks a transition to reduced drainage. In 5.18 (b) it is observed that the total gangue mass decreased substantially when the sampling is delayed. At the 4% fibrous ore addition level, the total gangue mass decreased to an amount that is almost equal to that observed for the silica (only) test. At the 7% fibrous ore addition level the reduced amount of gangue mass nears the amount with silica only, but is still slightly above it. These data suggest that fibrous minerals form a structure that, even as it leads to transport of significant amounts of gangue into the froth, does allow for drainage albeit at reduced levels. Finally, in 5.18(c) it is noted that the chalcopyrite mass in each layer increases for the steady-state sample as compared to the nascent sampled froth for both 4% and 7% fibrous ore addition rates. This suggests that there is an upward flow of chalcopyrite into the froth over time; as the plateau borders and vertices drain to remove silica, chalcopyrite is able to take its place.

5.9 Effect of silica size in a mixture with fibrous ore

Figure 5.19 shows the effect of silica size in the presence of fibrous ores as a function of silica size in each layer. The data shows a substantial decrease in both the solids concentration (a) and the total gangue mass (b) when a coarser silica size is used for the nascent froth sampling tests. The network generated by the mixture of coarser sized silica with fibrous ore is substantially weaker than that generated by the finer-sized silica that is the baseline for all of these tests. The silica size, and more generally the non-fibrous gangue size, plays a significant role in the strength of the network-like structure formed by the fibrous minerals.

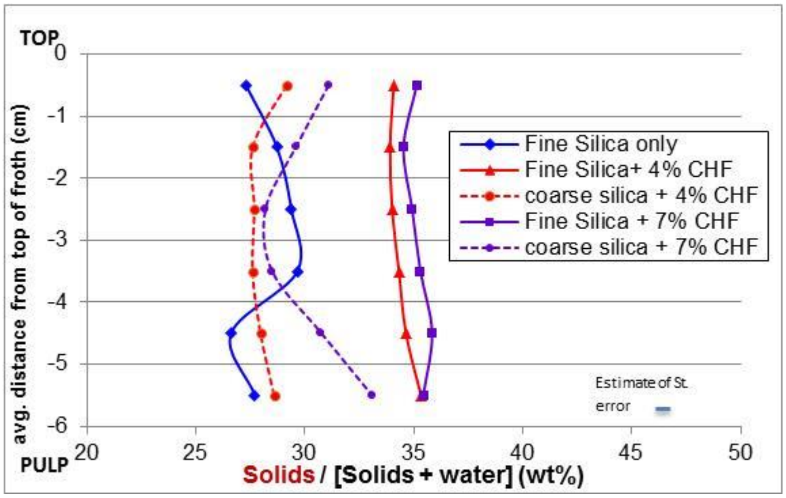

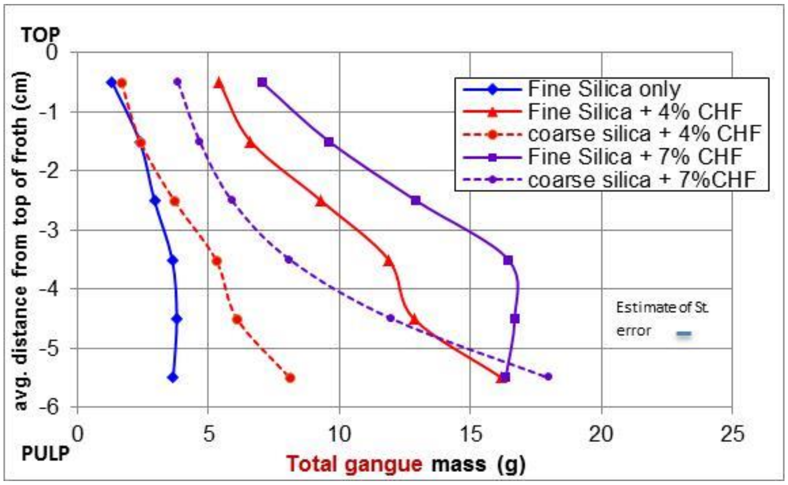

Figure 5.19: Effect of silica size on nascent froth sampling for 4% and 7% fibrous ore addition to fine silica - a) Solids density in each layer, and b) Total gangue mass in each layer; 35% solids concentration in pulp

Figure 5.20 shows the effect of addition of fibrous ore size to fine silica. To prepare this sample, the fibrous ore was ground for twice as long as the coarse high-fiber ore sample. Of course, a particle size distribution curve cannot be generated easily with fibrous ores because they entangle in the sieves. However, suffice to say that the longer grind time likely produced shorter fibers. The solids density (5.20a) does not change very much with addition of finer-sized fibrous ore. This is likely because 35% solids, (which is the solids concentration of the pulp) is the likely maximum amount possible. However, there is an increase in total gangue mass (b), and water mass (figure 5.21), and a decrease in chalcopyrite mass (not shown). Finer-ground fibrous ore is likely to form a stronger network for particle transport than the coarse-ground fibrous ore due to either shorter or more fibers being present.

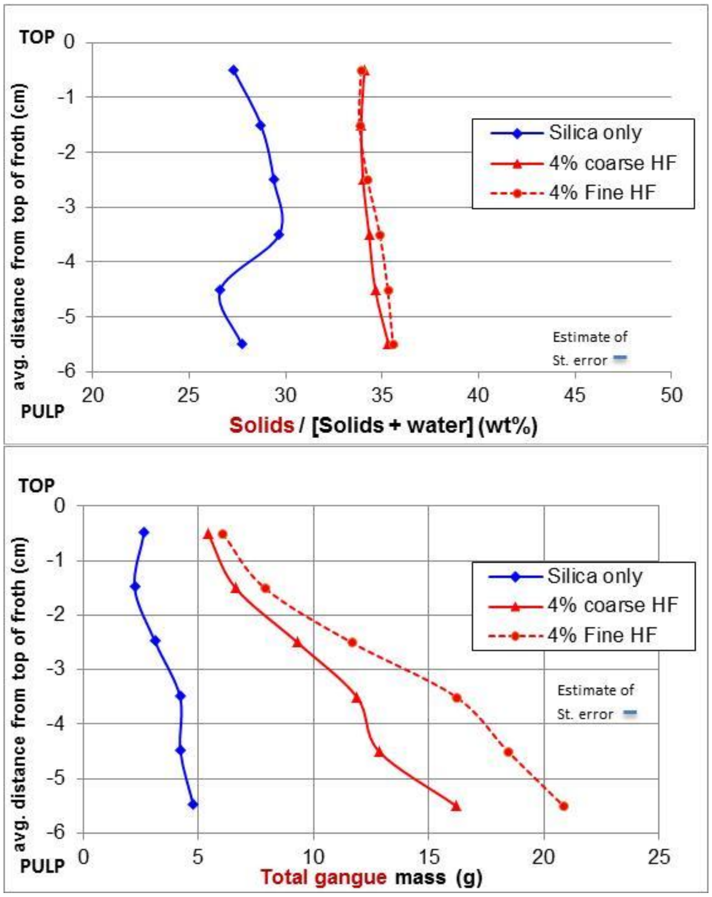

Figure 5.20: Effect of fibrous ore size on nascent froth sampling for 4% fibrous ore addition- a) Solids density in each layer, and b) Total gangue mass in each layer

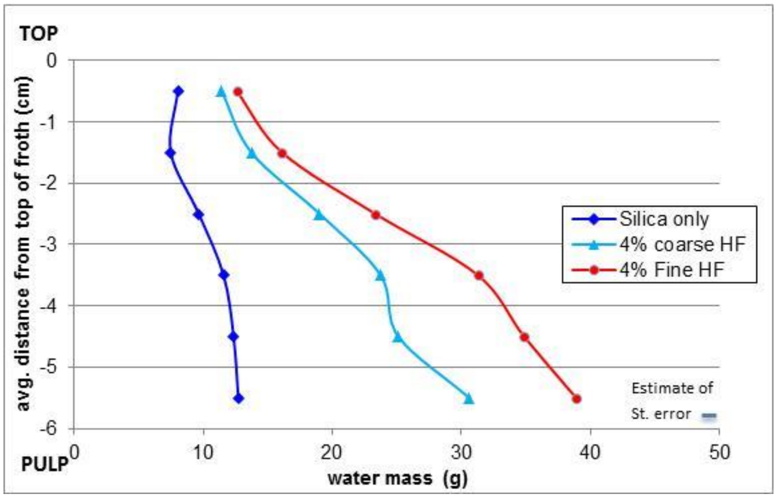

Figure 5.21: Effect of fibrous ore size on nascent froth sampling for 4% fibrous ore addition- water mass in each layer

5.10 Summary

The froth sampling experiments were originally designed to obtain the composition of the froth interstitial suspensions. The compositions, once determined, allowed preparation of bulk samples of froth interstitial suspensions ex-situ on which rheological measurements could be carried out. However, in addition, the data from these experiments provides valuable insights into transport mechanisms of particles of various shapes.

1. When 50% platy mica (of all size fractions) was mixed with 50% fine silica and used in nascent froth sampling experiments, higher total gangue mass, and higher water mass in the froth zone was obtained, as compared to when 50% globular silica (of same size fractions) was added to fine silica.
2. Effect of particle size is readily apparent, with coarser mica resulting in less total gangue mass in the froth zone.
3. When hydrophobic particles (chalcopyrite with adsorbed collector) are added in a mixture of 49% platy mica (of all size fractions) and 49% fine silica, total gangue mass in concentrate is still higher than when 49% globular silica is used (in place of the mica). However, when mica content is decreased down to 24%, the transport is dominated by the fine silica and the differences disappear. Certainly this is one of the problems of running froth sampling experiments without actual ore, but the tradeoff is that precise compositions of the froth zone can be obtained as a function of depth in the froth zone.
4. When steady state sampling (5 minute delay- upward drag and drainage balanced) was conducted, it was observed that in 50:50 mixtures with fine silica, the total gangue mass decreased for fine sized mica, but actually increased when the mica size was 100-150μ, as compared to the nascent froth sampling experiments.

5. Nascent froth sampling experiments were also conducted with fibrous ore (containing the fibrous mineral serpentine) mixed with fine silica. The amount of gangue in the froth zone was significantly more than when mica or silica of any size was used. It was also found that the amount of value chalcopyrite was significantly less than when mica or silica were used, especially when the fibrous ore content was increased to 7%.
6. Under steady state conditions (delayed sampling) for fibrous ore mixtures , it was observed that the total gangue mass actually decreased, as compared to the mass obtained under nascent sampling conditions. Value chalcopyrite content actually increased during the steady-state conditions (as compared to nascent), suggesting that the draining silica allowed for more chalcopyrite to be transported into the froth.

5.11 Additional froth sampling experiments- smaller data sets

Addition froth sampling experiments were conducted with mica of a wide particle size distribution (as identified in the materials and methods section), ultrafine mica (-2μ) procured from the mine, as well as the needle-like mineral wollastonite. The results from these tests are shown in this section.

5.11.1 Nascent froth sampling with mixtures of comparably sized fine mica with fine silica

The next set of experiments was conducted with mica that was fine and slightly coarser than the ultrafine size mica. This very fine mica was 10μ in size and the size was comparable to that of the fine silica. The results from these tests are shown in figures 5.22 and 5.23 below. The data suggests that gangue mass in the froth increases as more of this fine mica replaces fine silica. In addition, the mica:silica ratio in the froth increases as more mica is mixed with the fine silica. However, the increase in the mica:silica ratio is only observed starting at 40% mica addition. At 20%, the ratios in the pulp and froth are similar.

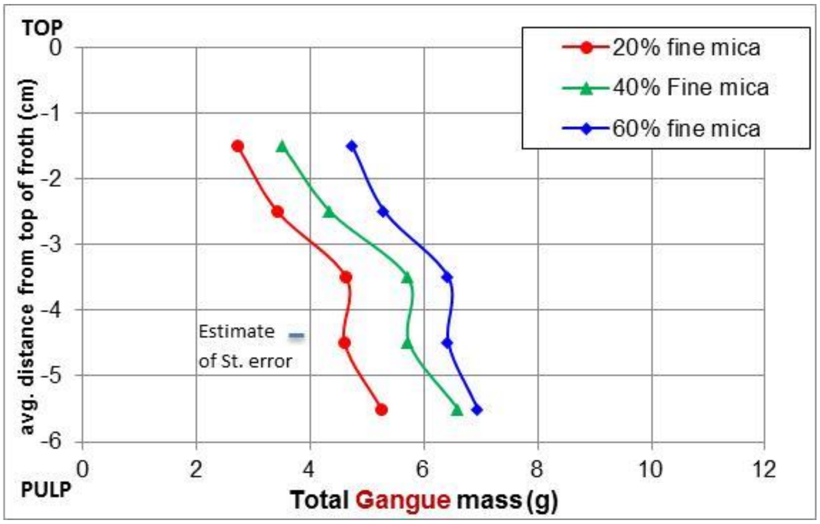

Figure 5.22: Nascent froth sampling experiments- fine mica in various ratios mixed with fine silica (comparably sized). Data shows that total gangue mass increases as more fine mica replaces fine silica in the mixture; solids concentration in the pulp is 35%(w/w)

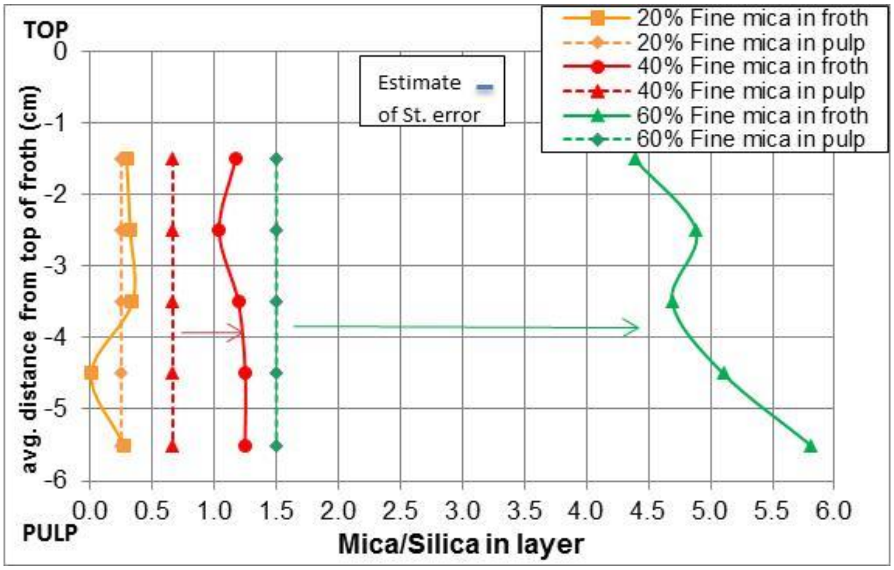

Figure 5.23: Nascent froth sampling experiments- addition of fine mica in various ratios mixed with base fine silica. Data shows that ratio of mica to silica in the froth is higher than what is in the pulp, but this only occurs when at least 40% mica is present.

5.11.2 Addition of wide PSD mica in the absence of chalcopyrite

These experiments were conducted to ascertain the effect of a wide-particle size distribution (PSD) mica sample obtained from a mica mine. Various amounts of this mica were mixed in with the fine silica, and froth sampling experiments were conducted. The data is plotted in Figures 5.24 and 5.25. The data shows that the total gangue transported to the froth decreases as the amount of wide-PSD mica transported increases. This suggests that either: a) the coarse mica (part of WPSD mica) does indeed slow the rate of transport of even the fine mica (that is part of WPSD mica) to the froth zone or that the froth stability is reduced due to the presence of coarse mica particles (that are present in WPSD mica). The ratio of mica to silica also decreases from the pulp to the froth zone, and the difference is greater for when more mica is transported to the froth zone.

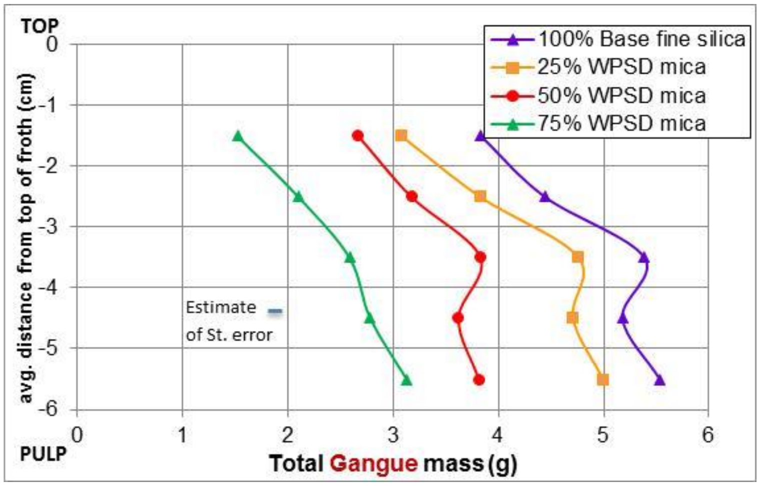

Figure 5.24: Nascent froth sampling experiments- addition of wide particle size distribution mica (WPSD) in various ratios mixed with base fine silica. Data shows that total gangue mass decreases as more WPSD mica is added to the mixture.

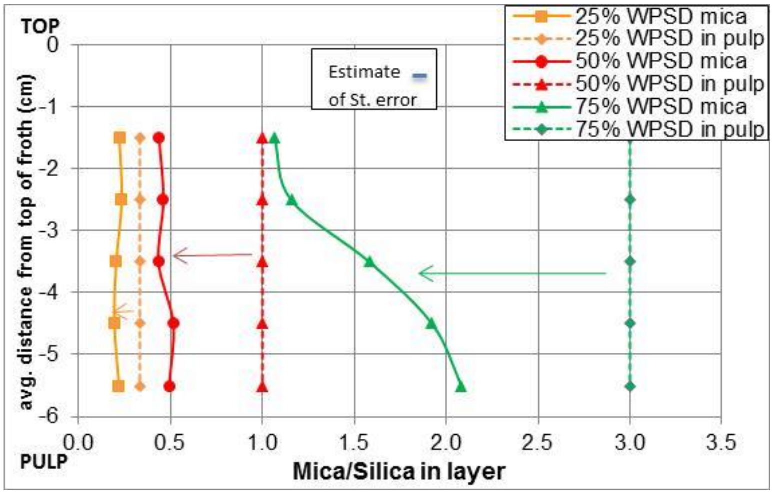

Figure 5.25: Nascent froth sampling experiments- addition of wide particle size distribution (WPSD) mica in various ratios mixed with fine silica. Data shows that ratio of mica to silica in the froth is lower than what is in the pulp, with the difference being larger when more WPSD mica is in pulp; 35% solids concentration in pulp

5.11.3 Nascent froth sampling with mixtures of ultrafine mica with base fine silica

Experiments were then conducted with ultrafine mica finer than 2μ in size. The results are plotted in figures 5.26 and 5.27. The data shows a complete opposite trend from that observed for the WPSD mica in section 5.10.2, and highlights the critical role of particle size, which is more significant than shape when comparing globular and platy morphologies. The amount of total gangue in the froth zone actually increases as more ultrafine mica is added. In addition, it is observed that the ratio of mica to silica is actually higher in the froth zone than in the pulp for all ratios of ultrafine mica to fine silica.

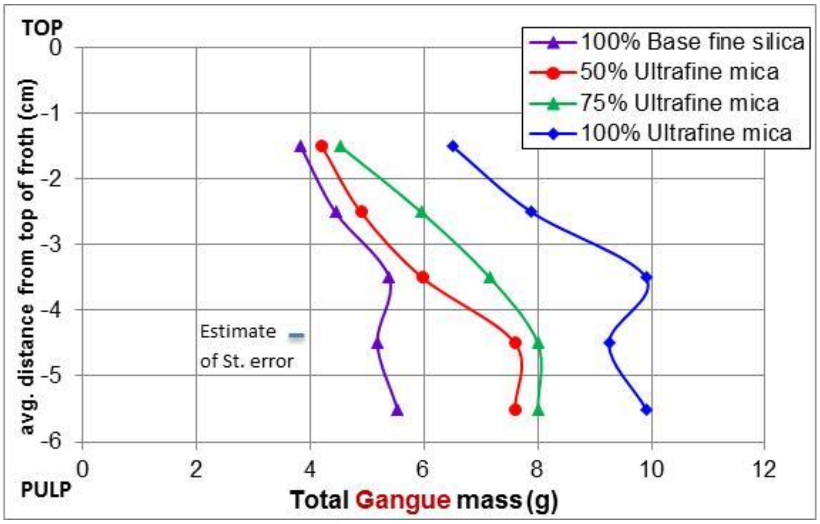

Figure 5.26: Nascent froth sampling experiments- addition of ultrafine mica in various ratios mixed with base fine silica. Data shows that total gangue mass increases as more ultrafine mica is added to the mixture; 35% solids concentration in pulp

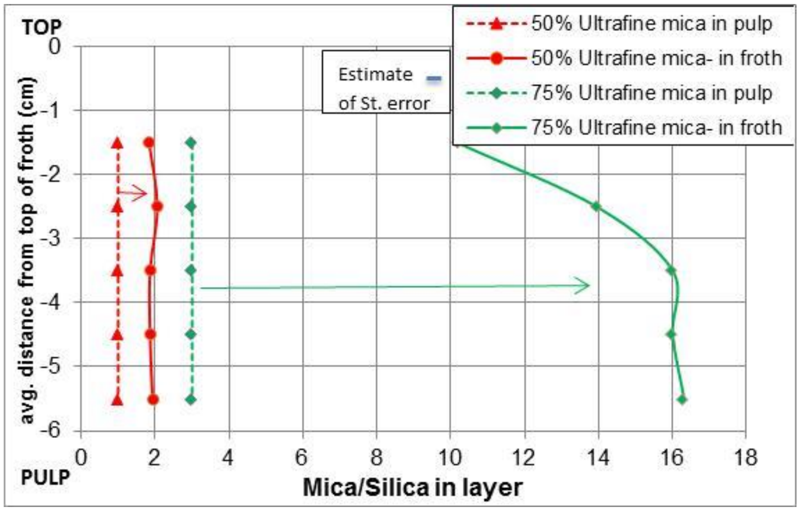

Figure 5.27: Nascent froth sampling experiments- addition of ultrafine mica in various ratios mixed with base fine silica. Data shows that ratio of mica to silica in the froth is higher than what is in the pulp, with the difference being greater for when more ultrafine mica is present; 35% solids concentration in pulp

5.11.4 Nascent froth sampling of wollastonite/fine silica mixtures in the absence of chalcopyrite

The mineral wollastonite has needle shaped particles and thus a higher aspect ratio than mica (platy morphology). Mixtures of wollastonite base fine silica were studied under nascent froth sampling conditions to ascertain the effect of these particles on gangue transport to the froth zone. The results from these tests are shown in figure 5.28 below. The data shows that wollastonite on its own does is not transported to the froth zone efficiently. Even when it is mixed with the fine silica, its transport rate appears to be similar to that of the fine silica, but not more than it. The wollastonite particles are significantly larger than the silica particles, which may explain the observations. In addition, the plank-like wollastonite particles cannot entangle like the fibrous minerals to form a strong network like structure.

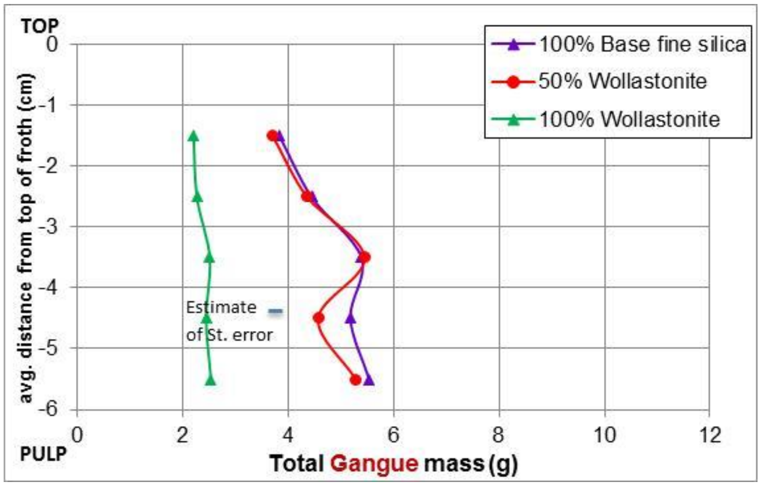

Figure 5.28: Nascent froth sampling experiments conducted on mixtures of wollastonite obtained from a commercial producer mixed with base fine silica. Data shows that on its own, wollastonite transports significantly less than the base fine mica. This may be because of its size, which is coarser than the base fine silica.

5.11.5 Nascent froth sampling experiments with fibrous ore in the absence of chalcopyrite

Nascent froth sampling experiments were also conducted in the presence of chalcopyrite. The results from these tests showed the same trends as observed in the presence of chalcopyrite. The results are shown in figures 5.29, 5.30 and 5.31 below. The data shows an increased in solids concentration, total gangue mass as well as water mass when the amount of fibrous mineral containing ore is increased. This is consistent with the mechanism of transport for fibrous mineral mixtures as "network transport via bubble flux and bubble entrapment", even in the presence of 2% (w/w) hydrophobic particles.

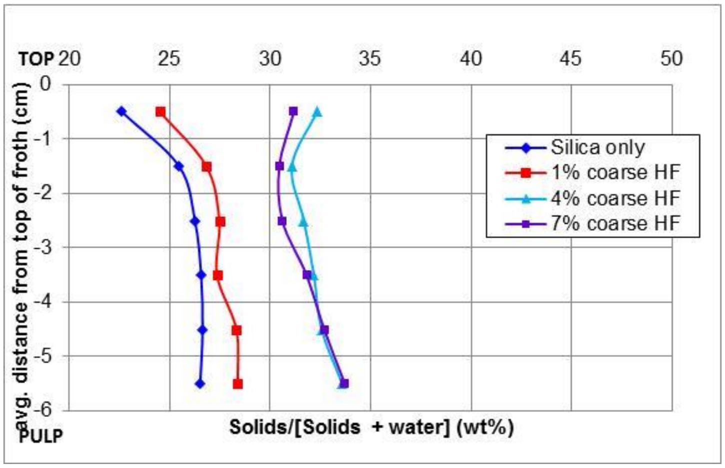

Figure 5.29: Nascent froth sampling of mixtures of Fibrous ore at 1%, 4% and 7% respectively mixed with fine silica. Solids concentration was 35% and no chalcopyrite was used. Data shows froth suspension solids concentration approaching the pulp solids concentration.

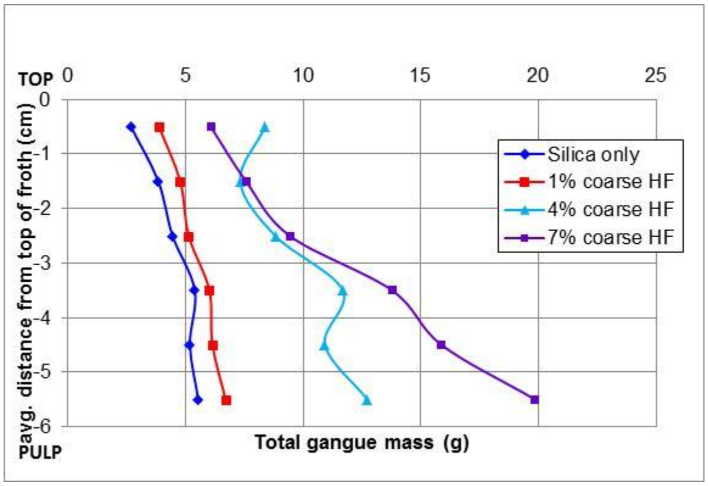

Figure 5.30: Nascent froth sampling on mixtures of Fibrous ore at 1%, 4% and 7% respectively mixed with fine silica. Solids concentration in the pulp was 35% and no chalcopyrite was used. Data shows total gangue mass reporting to the concentrate at each level increasing as the amount of fibrous ore added increases, more so in the lower layers.

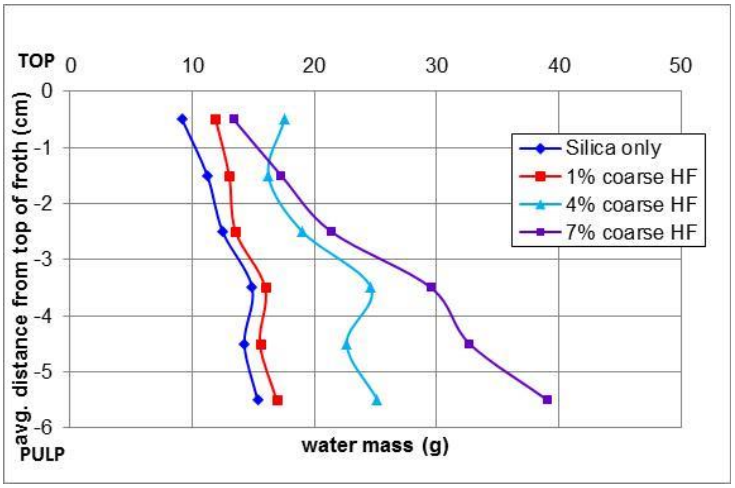

Figure 5.31: Nascent froth sampling on mixtures of Fibrous ore at 1%, 4% and 7% respectively mixed with fine silica. Solids concentration in the pulp was 35% and no chalcopyrite was used. Data shows water mass to the concentrate increasing as the amount of fibrous ore added increases, more so in the lower layers.

6 Rheology Measurements

In this chapter, bulk rheological measurements are conducted on the compositions obtained from the froth sampling experiments. The reason for measuring rheology at a wide solids volume-density range is to be able to obtain sufficient points to model the rheological data to extrapolate to points that cannot be physically measured (i.e. low volume fractions) due to settling. In addition the fit of the data to the rheological models will provide valuable insights that can be used to identify the maximum packing fraction (ϕ_{max}) as well as the intrinsic viscosity (B, also referred to sometimes as $[\eta]$), which are used in this work to identify the role of viscosity in the interstitial fluid drainage. The effect of particle shape on bulk viscosity is readily apparent.

6.1 Rheology measurements as a function of shear rate

Rheological measurements at the selected shear rates were then conducted on a number of different samples. Samples were chosen to span the entire space of compositions that was obtained from the froth sampling tests and so mixtures of silica, chalcopyrite, mica of various particle sizes and distributions, wollastonite of one size, and the fibrous ore sample were conducted. Using this data, a model of the predicted rheological properties of any desired combination of mineral species could be generated. Rheograms (plot of stress at a series of shear rates) were generated for a series of volume fractions for each mixture of samples, prepared using tap water. In order to calculate the volume fraction (ϕ), the mass of the material was divided by its density. The plots for silica are shown in the graph below.

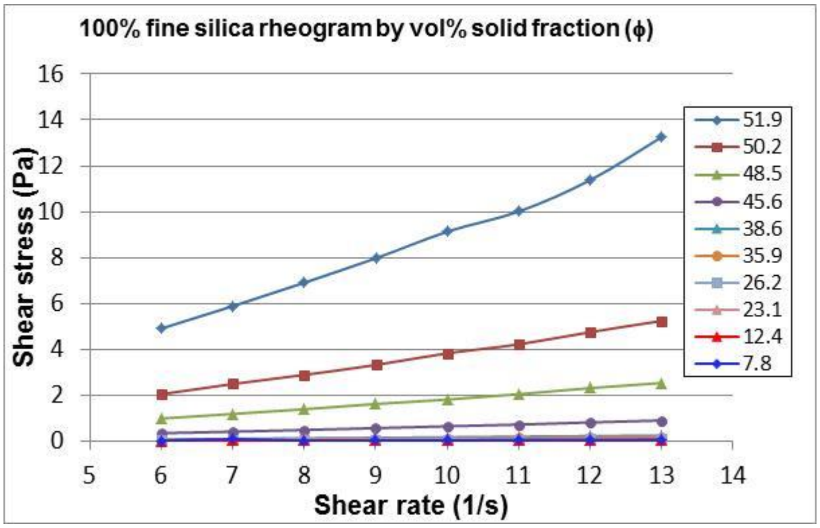

Figure 6.1: Rheogram for silica as a function of Vol % solids

The data suggests a step change in viscosity for when the volume fraction is increased to above 45 vol.% solids (69 wt.% solids for silica). While this concentration was not observed in the froth, it is possible that these vol. % concentrations occur locally in the plateau borders or interstitial fluid.

6.2 Rheology-Volume Fraction relationships

Existing models of slurry viscosity in the literature are reviewed in the chapter 3. The review outlines how the viscosity of suspensions can be described by a universal relation as follows

$$\eta_r = f(\phi) \qquad (1)$$

Where n_r is the viscosity and ϕ is the volume fraction of solids. As is clear from the review, the function f(ϕ) increases rapidly at large volume fractions until the suspension flow ceases at a finite volume fraction, described as the maximum packing fraction or ϕ_{max}. The value may be obtained by fitting an empirical relationship to the η_r, (ϕ) data. Sudduth (1998) described a generalized viscosity-ϕ relationship with a parameter σ.

$$\frac{d\eta}{\eta} = (5/2)(1 - k\varphi)^{-\sigma} d\varphi \qquad (2)$$

By setting σ to 0, 1, 2 and 3, various equations identified by authors over the past 80 years may be found. Setting the parameter to 1 yields the Krieger-Doherty relationship

$$\eta_r = (1 - \frac{\phi}{\phi_{max}})^{-B\phi_{max}} \qquad (3)$$

Finally, setting the parameter to 2 yields the Mooney equation

$$\eta_r = e^{\left(\frac{B\phi}{1-\frac{\phi}{\phi_{max}}}\right)} \qquad (4)$$

The viscosity is to be studied as a function of particle concentration. The tests described above at a number of different shear rates were conducted on slurries of varying volume concentrations (Vol. % or ϕ).

The plot of relative viscosity vs volume fraction for a shear rate of 13/s is shown below and illustrates the expected steep rise in relative viscosity when the volume fraction is increased to above 45%.

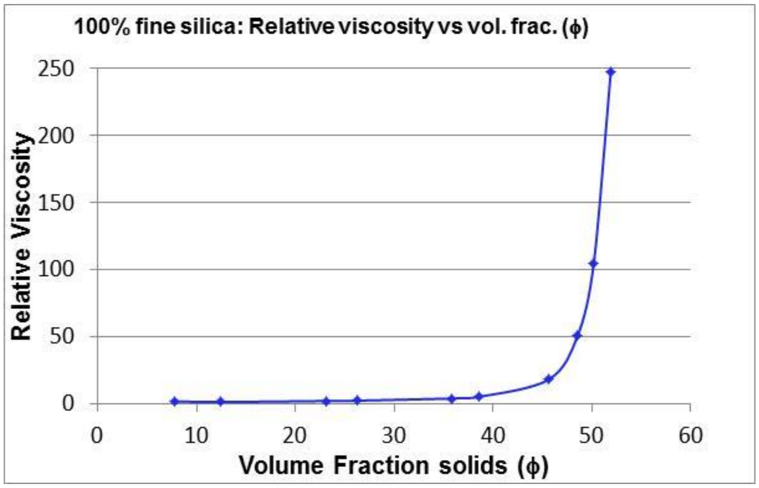

Figure 6.2: Relative viscosity vs volume fraction for fine silica only

This data is typically plotted with the relative viscosity expressed in the natural logarithmic form. The relative viscosity in the logarithmic form is shown below in Figure 6.3 for two experimental runs of two fine silica samples. The plot suggests that the results are reproducible.

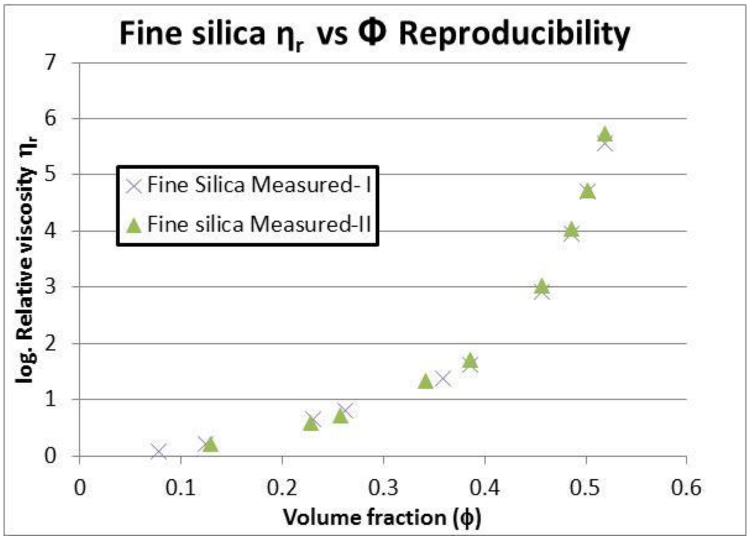

Figure 6.3: Reproducibility of data from fine silica experiments- log. Relative viscosity vs shear rate

Finally, the data from the first test is plotted with all shear rates included. The data shows that the shear rate has a very small impact on the shape of the curve.

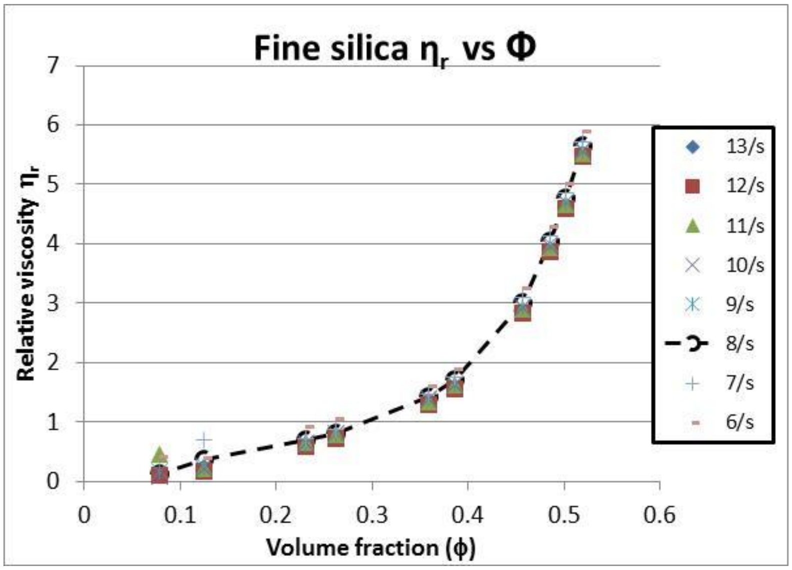

Figure 6.4: Fine silica η_r vs volume fraction ϕ for a range of shear rates

Given that the dependence on shear rates is low, the remainder of the analysis will focus on shear rates of 10/s. Next, the data was fit to the various rheological models, namely the Krieger-Doherty, Mooney, Quemada, and Maron-Pierce models (see literature review section). Although these were originally designed for hard spheres, they fit the data well for some asymmetrical particles as well (Mueller, 2010). All these models are two parameter models, i.e. the viscosity-relative volume fraction relationship can be defined using two parameters. As is apparent in the equations above, the first parameter is the intrinsic viscosity (B). This term correlates to polymer molecular weight when rheology of polymers is studied, however, in the case of suspension rheology, it is used largely as a fitting parameter and may be an indicator for effective volume (Pabst, 2004, Jeffrey and Acrivos, 1996). The other parameter is the maximum packing fraction or ϕ_{max}. This term refers to the maximum volume concentration of particles that can be added to a suspension before flow ceases. When studying perfect spheres in a density matched medium, the value for ϕ_{max} will depend on the packing, i.e. face centered cubic or hexagonal close packing. Values between 0.6 and 0.65 have been reported for spheres.

The model fitting was done using the Statistical Software JMP using its ‘non-linear modeling’ function. The observed viscosity (shear stress/shear rate) is normalized by the viscosity of water to give the relative viscosity η_r, and the logarithm of that value was taken. The Gaussian-Newton method was used to fit the data to each model, and the parameters ϕ_{max} and B were obtained. It is readily apparent from the plots below that the data fits both Krieger-Doherty and Mooney models.

The goodness of fit of the two parameters B and f are shown below:

Table 6.1: Goodness of fit for parameters B and ϕ_{max}

Fit	Parameter	Estimate	Approx. Std. Err.
K-D fit	B	2.873	0.161
Mooney fit	B	2.063	0.082
K-D fit	ϕ_{max}	0.530	0.00395
Mooney fit	ϕ_{max}	0.630	0.00651

Of the two, the B parameter was found to have a lower standard error for the Mooney fit than for the Krieger Doherty fit. Thus, the Mooney model is slightly better than the Krieger-Doherty and is used hereafter to fit the data.

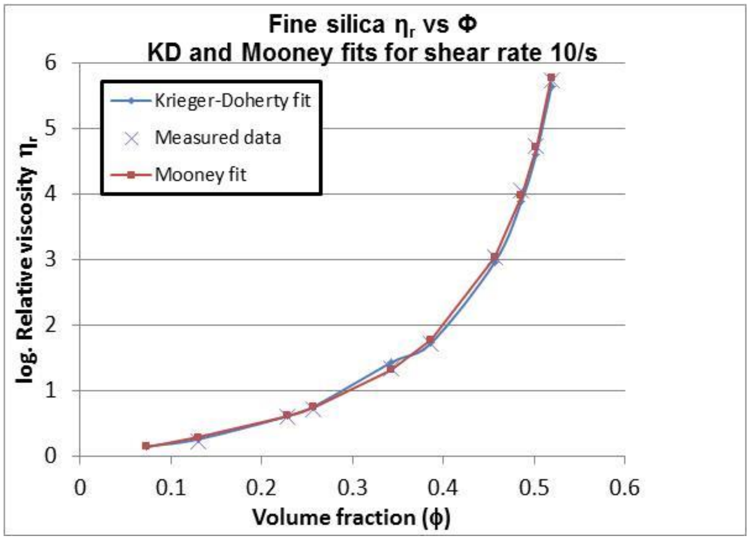

Figure 6.5: Fine Silica Data fit to the Krieger-Doherty and Mooney models

6.3 Rheology of mineral mixtures

The effect of platy minerals (mica) is studied first. Mica of wide particle size distribution (abbreviated hereafter as WPSD mica) is studied first. Fine silica was mixed with 50% wt% of WPSD mica. A test was also conducted for 100% wide PSD mica. Log. Relative viscosity-volume fraction relationship for 10/s shear rate is shown in Figure 6.6 below.

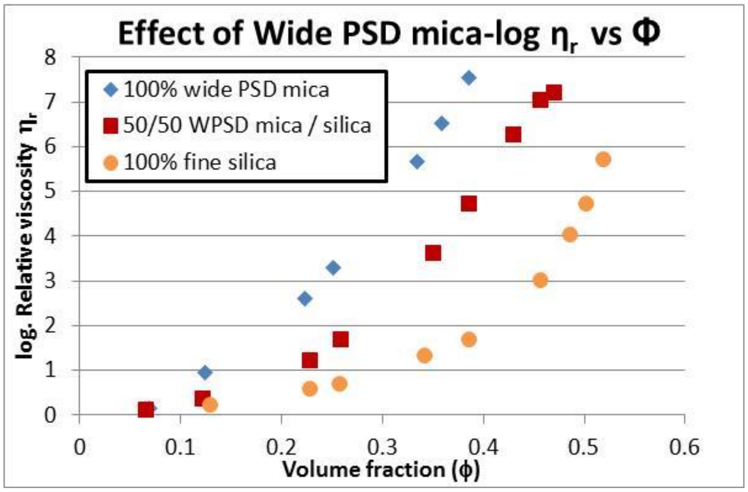

Figure 6.6: Effect of Wide PSD mica on η_r vs (ϕ) relationship for 10/s shear rate

The data suggests the following: a) the curve of relative viscosity vs volume fraction rises at a lower ϕ for wide PSD mica than for the fine silica. The relative viscosity at any given volume fraction is also higher for both WPSD mica and the WPSD mica containing silica than for the test with silica alone. The data was then modeled using the Mooney function, with the fit lines shown in the plot in Figure 6.7 below. The data shows that the rheology log. Relative viscosity curve for the 50% (wt%) WPSD mica bisects that of the 100% silica and 100% WPSD mica in half, suggesting that there is no synergistic or antagonistic effect for the mixture rheology.

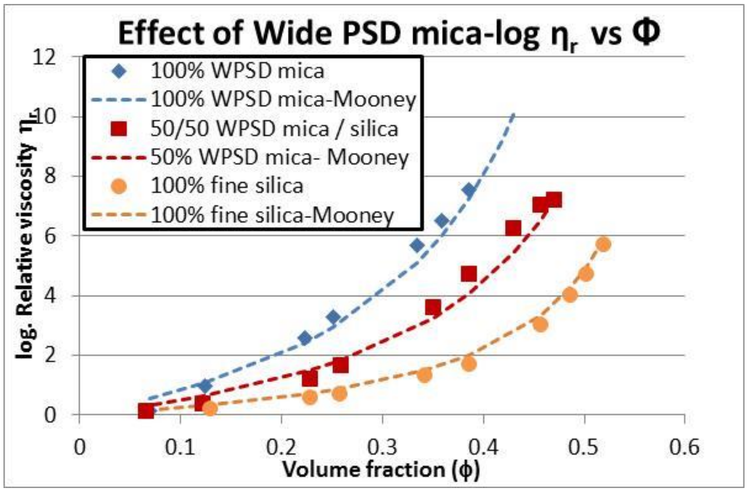

Figure 6.7: Effect of wide PSD mica on rel. viscosity-volume fraction relationship with fits to Mooney eqn at 10/s shear rate

The next step was to study the effect of mica particle size on the relative viscosity-volume fraction relationship. In figure 6.8 below, we show the effect of mica size by adding to the fine silica 50% by weight of mica of the desired size. As discussed earlier, the mica of various size fractions was prepared by carefully wet sieving the wide-PSD mica sample described above. For the sake of clarity, only the Mooney fits to the data are shown in figure 6.8 below.

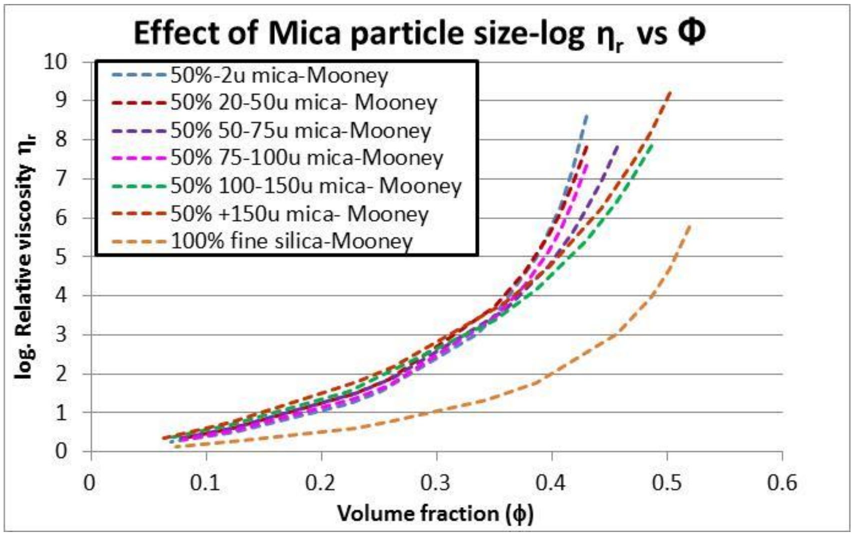

Figure 6.8: Effect of mica particle size on relative viscosity- volume fraction relationship for 50% addition (with fine silica) at 10/s shear rate

The data show that there is an effect of particle size of mica on the relative viscosity-volume fraction relationship. Mica that is below 50µ (either ultrafine below 2µ or relatively coarser at 20-50µ) displays a steeper increase in relative viscosity with increasing volume fraction than mica of coarser sizes. Note that the curves for all mica sizes follow the same pattern for volume fractions below 0.35, with the divergence observed only after this volume fraction. The constants for the Mooney fit, B and ϕ_{max} are shown in the table below.

Table 6.2: B and ϕ_{max} parameters for 50% mica addition of all sizes

Sample	ϕ_{max}	B
Base fine silica	0.61	1.64
50% 2-20µ mica	0.49	2.99
50 % 20-50µ mica	0.54	3.8
50% 50-75µ mica	0.59	4.0
50% 75-100µ mica	0.53	3.4
50% 100-150µ mica	0.68	4.68
50% +150µ mica	0.66	6.38

An interesting trend is observed, with the B and ϕ_{max} values. For the 100-150µ mica size, there is an increase in the ϕ_{max} values, which is above that of silica. The physical meaning is that more particles can be packed in a mixture that contains mica particles that are larger than 100µ, as you approach the maximum packing fraction. The other parameter B (intrinsic viscosity) also registers a significant increase in this region. B is essentially inverse density, so the increase suggests that effective volume of the mica particles is higher than calculated from a simple mass concentration and mineral density.

The same experiments were completed for 25% mica addition.

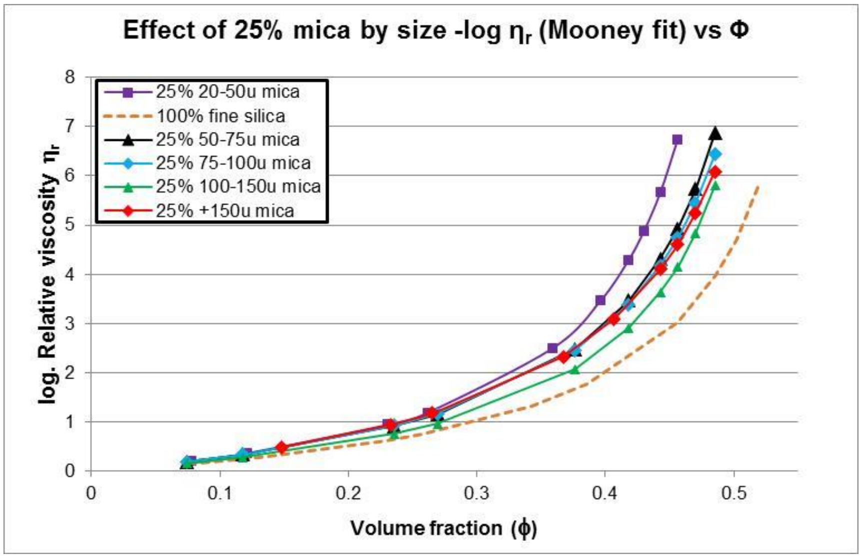

Figure 6.9: Effect of mica particle size on relative viscosity- volume fraction relationship for 25% addition (with 75% fine silica) at 10/s shear rate

The B and ϕ_{max} constants are shown in the table below.

Table 6.3: B and ϕ_{max} parameters for 25% mica addition to fine silica of all sizes

Sample	ϕ_{max}	B
Fine silica only	0.61	1.64
25% 20-50u mica	0.54	2.36
25% 50-75u mica	0.58	2.317

25% 75-100u mica	0.59	2.368
25% 100-150u mica	0.57	1.93
25% +150u mica	0.65	1.56

For this table too, it is apparent that there is some unusual behavior. Here, it is seen that the B and ϕ_{max} values up to 100μ size stay at the same level. At the 100-150μ mica addition level, there is a decrease in B values, but no change in ϕ_{max}, and at the +150μ mica size, there is an increased in ϕ_{max}, as well as B values.

6.1. Effect of addition of fibrous ore

Fibrous ore was prepared as described in the earlier sections. It is noted, again, that this ore contains about 1% of the mineral chrysotile which is fibrous in nature. In order to cover the volume fractions obtained in the froth sampling tests, three concentrations of coarse-ground fibrous ore were chosen, namely 0.75%, 1.25% and 2.5%. As mentioned in the froth sampling tests, the highest fibrous content obtained in any test was 2.5%. The results from the rheology data are summarized in the relative viscosity-volume fraction plot shown below.

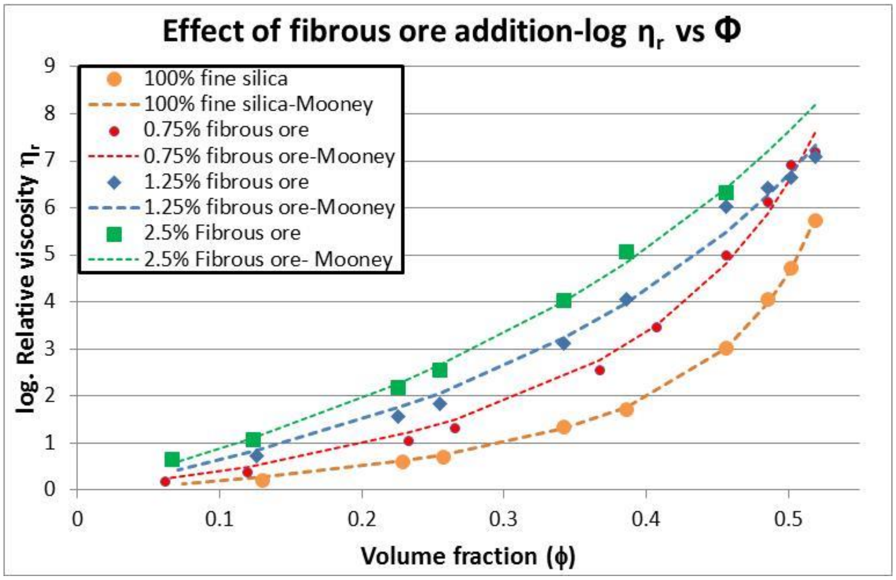

Figure 6.10: Effect of fibrous ore addition to silica on rheology-volume fraction relationship and Mooney fit at 10/s shear rate

The constants B and ϕ_{max} from fitting the data to the Mooney equation are shown in the table below.

Sample	ϕ_{max}	B
0.75% CHF ore	0.67	3.5
1.25% CHF ore	0.87	5.8
2.5% CHF ore	1.03	7.9

The data suggests a clear increase in viscosity as the fibrous ore is added to the fine silica sample. However, this plot is significantly different from the ones obtained with mica, with significant increases in both B and ϕ_{max} observed. Note that the ϕ_{max} values observed are greater than one for the 2.5% CHF ore addition. This is an artifact of the fit used for the measurements- the Mooney equation was designed for non-colloidal hard spheres and does not consider kind of interactions resulting from fibrous ore mixtures. However, with the goal being to compare the various mineral mixtures, the data is fit to the same equation. The extracted parameters are to be used as indicators for “expected metallurgical outcomes”.

6.2. Relative viscosity volume fraction data for silica-mica mixtures found in the froth fractions

The amount of mica present in the froth zone ranged between 15 and 30%, with the volume fraction in the froth ranging from 2 to 8% (volume fraction being calculated by dividing mass by density). At these volume fractions and concentrations of mica, it is sufficient to review the relative viscosity-volume fraction relationship for 25% mica added at 0.075 volume fraction, demonstrated in figure 11 below.

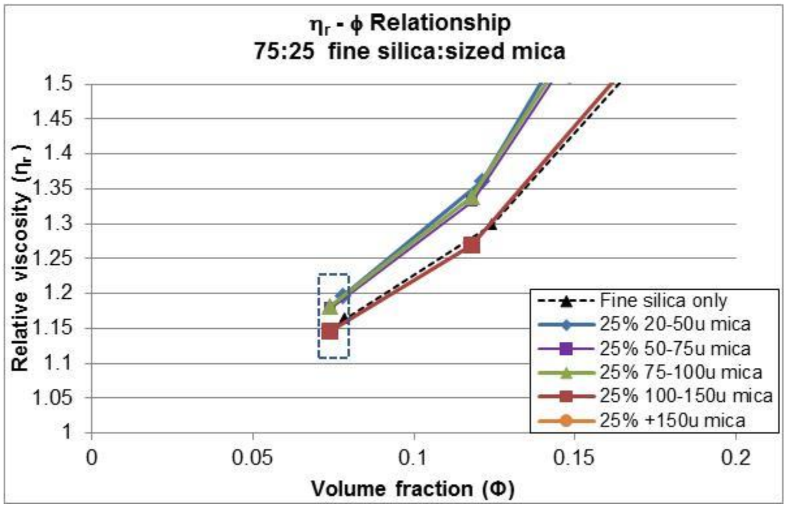

Figure 6.11: Relative viscosity- volume fraction for 25% sized mica (75% fine silica) compared to fine silica only. The difference between 25% mica/75% fine silica and 100% fine silica tests appears is about 0.3 to 0.5 units regardless of size

The data shows the following:

a. For 20-100μ size, there is no difference in relative viscosity at 0.075 ϕ. It is about 0.1 units (10%) higher than that for silica alone.

b. For 100-150 and +150μ there is a small difference, with the relative viscosity being slightly less than for 20-100μ.

The plots comparing mica and silica addition to the base fine silica for 20-50, 50-75 and 75-100μ sizes are shown in figure 12 below. To obtain these plots, the constants from the Mooney equation were used to obtain a model relative viscosity as the settle rate at 0.075 ϕ was too fast for accurate measurement. The data also suggests a 0.1 unit or 10% difference in relative viscosity when mica is added as compared to silica.

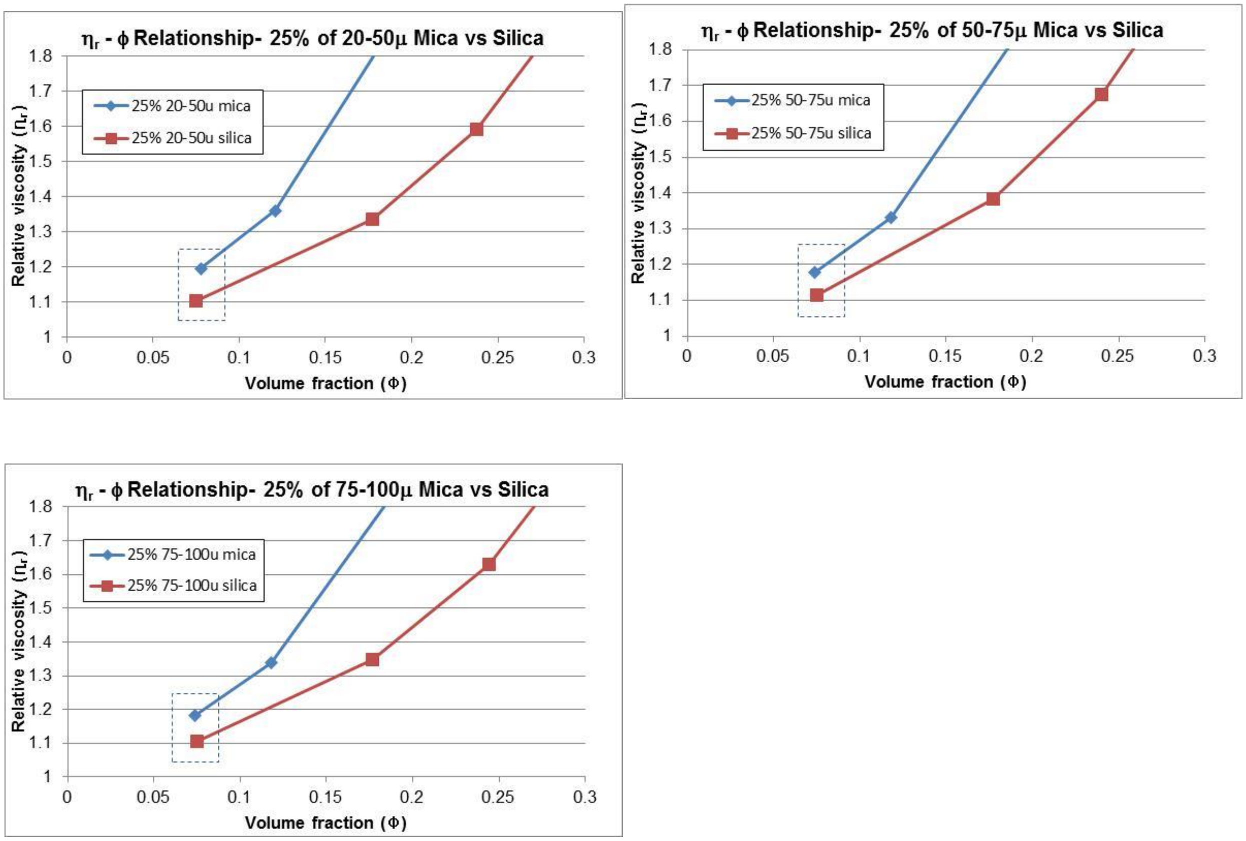

Figure 6.12: Relative viscosity (η_r) vs volume fraction (ϕ) for 25% mica or silica of 20-50μ (a), 50-75μ (b), 75-100μ (c), mixed with 75% base fine silica. At 0.075ϕ, the difference between mica and silica addition is about 0.1 units or approximately 10%, which is very small.

In comparison, the effect of addition of fibrous ore is shown in figure 12 below.

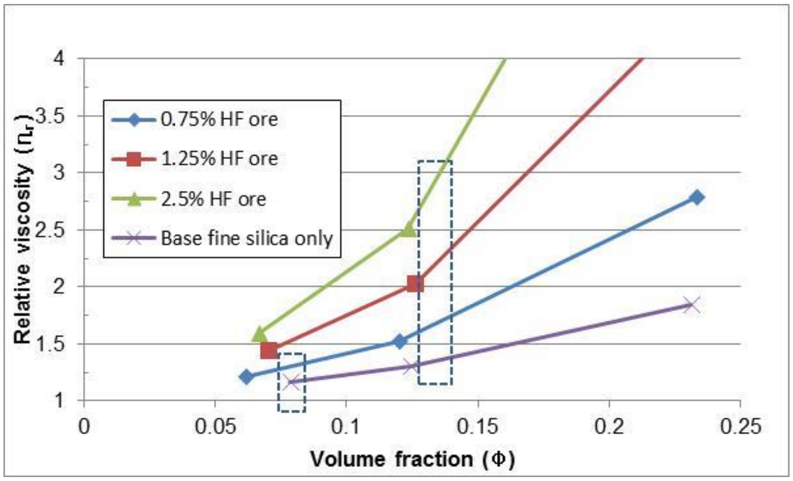

Figure 6.13: Relative viscosity vs volume fraction f for addition of 0.75% , 1.25% and 2.5% fibrous ore to fine silica. The data shows that the relative viscosity increases by about 100% for small increases in fibrous ore content

The data suggests that the small difference in relative viscosity for muscovite cannot explain the significant difference in degree of entrainment observed between mica and silica of various sizes. In addition, there is actually a decrease in relative viscosity when 100-150m mica is used, but in the flotation tests, there was an increase in degree of entrainment/gangue transport observed. It must therefore be concluded that the difference in slurry viscosity cannot explain the differences in flotation performance and the trends for the degree of entrainment curves.

6.4 Summary

1. An improved technique of measuring the rheological properties of suspensions of minerals was identified. This involved the use of the helical ribbon impeller/geometry, which helps maintain slurry flow upwards during the measurement. The disadvantage of this is the early onset of Taylor vortices. However, given that the shear experienced by the froth interstitial fluid suspension is rather low, the operating shear for the rheometer is still prior to the onset of turbulent flow. The accuracy of the measurements was found to be better than with the vane geometry.
2. A protocol was set up in the instrument which allowed for adequate mixing prior to each measurement. Viscosity-volume fraction relationships for mixtures of mica/silica of various sizes and ratios, as well as those of mixtures with fibrous ores are obtained.
3. The viscosity-volume fraction relationship for the mixtures fit the Mooney equation well. The extracted parameters B and ϕ_{max} were used to model relative viscosities at low volume fractions where settling was too rapid for accurate measurements to be made.
4. The results from these plots suggest that the relative viscosity measured using bulk rheological measurements of mica/silica mixtures at the concentrations of mica and the volume fractions of the solids is only very slightly different. In addition, there is a

decrease in relative viscosity for the coarsest sizes, even though flotation tests suggest that the gangue recovery is higher.

5. For the fibrous ore, the fit shows a linear relationship between the two parameters as a function of concentration of fibrous ore, which can be used as an indicator for viscosity mediated effects.

6.5 Wollastonite behavior

Wollastonite of fixed size fraction as defined in the earlier section was mixed with 75% and 50% by weight of silica and the same rheology experiments were conducted. The results from these studies, along with their fit lines to the Mooney equation are shown in figure 6.12 below. The values of the two constants B and ϕ_{max} are also shown. The data shows that the addition of wollastonite has a significant impact on the rheological properties of the suspension with a much steeper rise in relative viscosity with volume fraction.

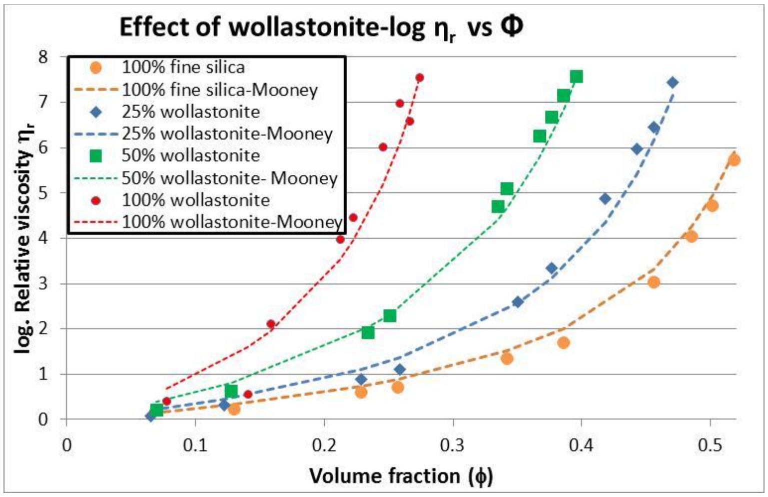

Figure 6.14: Effect of wollastonite addition on relative viscosity-volume fraction relationship

7 Discussion

7.1 Outline

This section calls upon the results from the flotation tests, the froth sampling tests, as well as the rheological measurements to test the hypotheses developed in Chapter 2. Changing the particle shape and size leads to different rates and mechanisms of transport of particles in three phase froths, driven by the changing dominant forces. The impact of the plate-shape mineral mica on flotation response, as a function of average size and concentration was critically evaluated. The critical platy mica or rounded silica concentrations, as a function of average particle size, needed to impact flotation are discussed. This is followed by a discussion on results from both nascent and steady-state froth sampling experiments conducted on pure mineral mixtures (sized platy mica with fine silica, sized silica with fine silica) to obtain compositional information of froths to identify mechanisms driving transport of each particle shape. A separate discussion section follows, with various mechanisms of transport and confinement effects included.

7.2 Effect of mica on flotation response

From the flotation test results shown in figure 4.1 and 4.2, it is readily apparent that platy mica affects flotation concentrate grade (i.e. the amount of copper-containing minerals relative to the total flotation product). When half of the mass of a typical copper-containing ore is substituted with mica of various size-fractions, and a flotation test is run on the mixture, there is a negative impact on concentrate grade, compared to when low-aspect ratio silica is used to prepare the mixture. The impact is also observed when 25% of the ore is replaced with mica. However, at 12.5% mica addition, an impact on recovery is not observed. For this reason, the critical amount of mica needed to impact flotation outcome is in between 12-25% of the total ore solids. It is also noted here that the recovery (i.e. the total amount of copper-containing minerals obtained in concentrate product relative to the amount in the original feed ore) is not affected by mica addition, with data showing equivalent recoveries regardless of mica content added. In other words, some of the added mica ended up in the flotation product, thereby diluting the value mineral of interest, but it did not suppress the amount of value mineral recovered.

7.3 Effect of mica size on flotation response

The effect of particle size on transport and recovery of non-sulfide gangue minerals to the froth and concentrate has been discussed in detail in the literature review section. If the main mechanism for non-sulfide gangue minerals to be recovered into the concentrate is entrainment, then the effect of size of the gangue mineral needs to be considered, as recovery by entrainment depends significantly on particle size. To this end, the results from flotation tests illustrate that when compared to the silica of the same size, the mass recovery is always higher and the concentrate grade is always lower when mica is used. This appears to be the case in all situations for both the 25% addition and the 50% addition. This illustrates that the addition of mica certainly results in lower grade regardless of size.

A review of figure 4.7, which shows the degree of entrainment/entrainment factor (overall ENT for a mixture of gangue particle sizes) as a function of size of mineral added to ore shows that the curve for mica mixture always lies above the one for a silica mixture. In other words, the amount of gangue recovered in the concentrate per unit mass of water recovered is higher when mica is present instead of silica. This could be attributed to either mica assisting in transport of other mineral species, or mica being transported faster to the froth, or draining slower than silica.

To answer this question, the data from the froth sampling experiments is used and will be described in section 7.2.1.

Secondly, the data suggests that there is a decrease in ENT as the size of mica added is increased. This relates well to the traditional entrainment vs PSD curve, which is generated by splitting a concentrate by size fractions and assaying each fraction for non-sulfide gangue mineral content. This is well documented (Wang, 2015) and is attributed to action of the froth phase as a classifier; the probability of a particle transporting into the froth zone and being recovered decreases as its size increases. However, there is an unusual effect at the very coarse sizes. It is seen that the ENT actually increases when the size of added mica is about 150μ, going from 0.25 to 0.3, while the ENT for silica addition continues to decline. Furthermore, at 50% addition rate, this increase in ENT starts at a smaller size, increasing slightly at 100-150μ, and increasing further at +150μ mica size.

The overall degree of entrainment could be biased if the content of hydrophobic particles is very high in the first concentrate (bubbles loaded with hydrophobic particles have narrower plateau borders). This is not the case for the fourth concentrate, where value mineral content is low since much of it is collected in the first three concentrates. The degree of entrainment for the fourth concentrate, i.e. C4 ENT for 25% mica addition, is shown in figure 4.9. In this plot too, a decrease in ENT was observed, along with the unusual increase at +150μ. In figure 4.10, the C4 ENT is shown for 50% mica or 50% silica addition, and here too, the same trends as figure 4.8 are observed, i.e. an increase in ENT past 75μ, and a significant increase at +150μ for both mica and silica. While the trend for mica is the same in both 25% and 50% addition tests, the trend for silica is different: an increase in ENT is observed for silica as well, with the increase becoming more significant only for the +150μ sized silica. Given this divergence, it is critical to examine other possible confounding effects, starting with froth stability, before we can determine the effect of gangue particle shape.

In section 2.2 the froth stability and factors driving it are reviewed. Corin (2011) mentions that water recovery is a reasonable proxy for froth stability, and for this reason, water recovery data is plotted in figure 7.1 below. It is expected that there is a slight effect of particle size on water recovery, i.e. as the froth may be less stable as particle size increases. This is the case for 25% mica or 25% silica addition. However, for the 50% silica addition, at the +150μ size there is a substantial decrease in water recovery, even as the water recovery for mica, at the same addition rate, remains constant. This decrease in water recovery for silica at 50% addition rate at the +150μ size suggests that there is a significant decrease in froth stability attributed to the insufficient presence of finer sized particles necessary to stabilize the froth zone. The decrease in water recovery is linked to the rapid drainage of water from the froth. Since the drainage of particles is always slower than the water due to hydrodynamic drag experienced by the particles, the resulting ENT curve is artificially inflated in the case of 50% 150μ silica addition. This effect likely contributes to the observed significant upward shift for silica. For mica, on the other hand, it is observed that the water recovery curve decreases slightly as expected. Thus, we may attribute the coarse silica (+150μ) effect to reduced froth stability, but this explanation does not apply for mica addition.

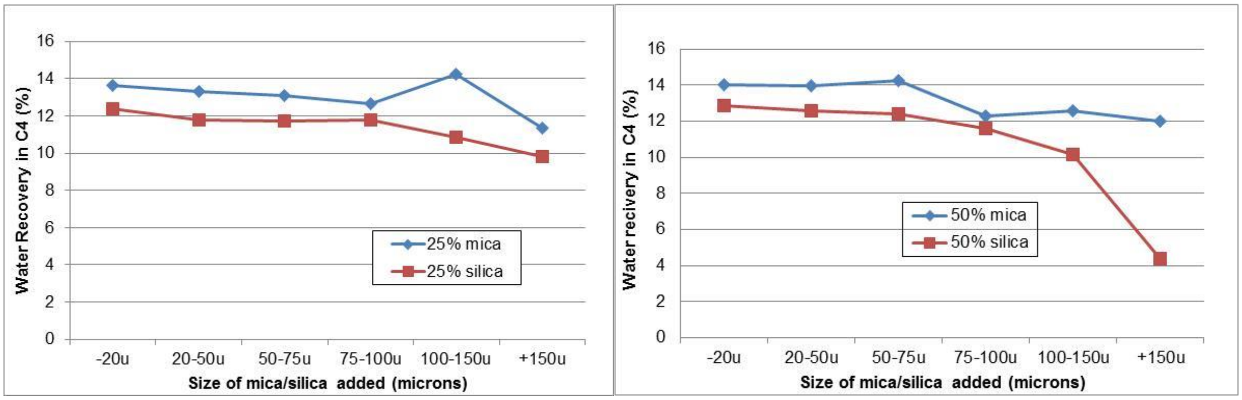

Figure 7.1: Flotation tests- Water recovery in the fourth stage of flotation for addition of (a) 25% and (b) 50% mica and silica to 75% and 50% base ore as a function of particle size

In order to understand the mechanisms resulting in the degree of NSG transport curves noted above, it is necessary to obtain compositional information on the froth zone i.e. the species that are being transported and the evolution of their transport rates over time. Obtaining the composition of the froth as a function of height can contribute to an understanding of the mechanisms at play. In order to obtain precise compositions, froth sampling tests were conducted on mixtures of pure minerals: fractionated mica mixed with fine silica, and fractionated silica mixed with the fine silica. Note: both platy particles and globular (low aspect ratio) silica particles are mixed with the same fine silica to obtain deep froths.

7.3.1 Nascent froth sampling results

The goal of conducting experiments under nascent sampling conditions was to test the hypothesis that platy mica particles experience more upward drag and/or are influenced lesser than low aspect ratio silica particles. This was done by sharply increasing airflow rate resulting in high drag conditions. The results for tests conducted with 50% mixtures of fractionated mica and fine silica as shown in figure 4.4 for nascent sampling (i.e. high drag conditions) illustrate (i) the decrease in total gangue mass when coarser sized mica is added and (ii) greater recovered gangue mass. In Figure 7.2 below, the results from Figure 4.4 are plotted with average particle size fraction on the x-axis. The data shows the decrease in floated mass with increasing particle size for 50% -mica or silica mixed with fine silica (and no chalcopyrite). It also shows that at froth layer 2 (near the top of the froth), there is a very small increase in mass, but in layer 5 (near the bottom of the froth), there is a significant increase in mass when mica is added instead of silica. This suggests that indeed platy mica particles experience more drag and/or are influenced less by gravitational settling than low aspect ratio silica particles.

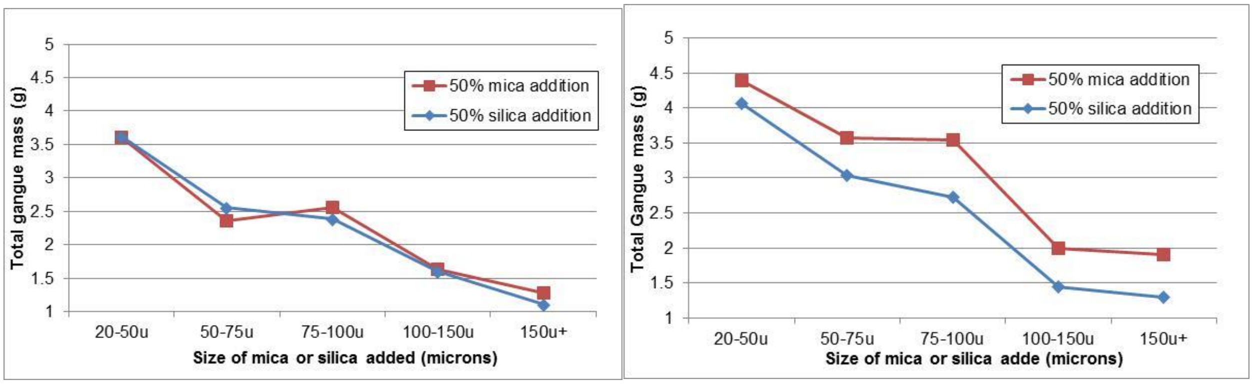

Figure 7.2: Nascent froth sampling- Total gangue mass with 50% mica or silica addition to 50% base fine silica for two select layers: a) layer 2 (near top of froth) and b) layer 5 (near bottom of froth). Gangue mass is higher when mica is added as compared to when silica is added in layer 5, while there is no significant difference observed in layer 2. Solids concentration in the pulp is 35%, and no chalcopyrite (value mineral) is present.

Figure 7.3 shows the solids concentration (solids mass/water mass) in froth layers 2 and 5, whose trends appear similar to those in Figure 7.2. Figure 7.3 is similar to the plot of ENT, except it is not normalized by the pulp water or solids. Recalling ENT plots from figure 4.7 and 4.8, it is expected that there would be an increase in ENT in the 100-150μ and +150μ size range. However, this is not observed, with only the gradual decrease seen. Thus, the increase in ENT is likely not due to increased drag forces.

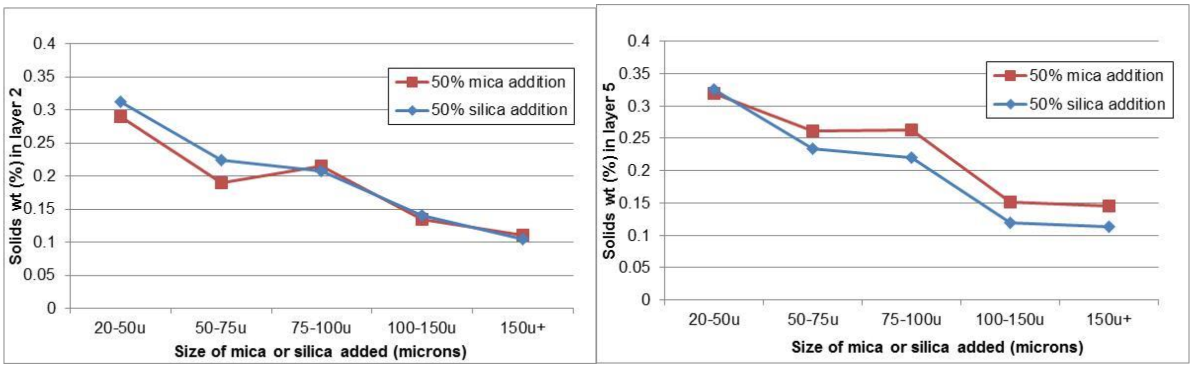

Figure 7.3: Nascent froth sampling- Solids concentration (w/w) with 50% mica or silica addition to 50% fine silica for two select layers: a) layer 2 (near top f froth) and b) layer 5 (near bottom of froth). Solids concentration is higher when mica is added as compared to when silica is added for layer 5, but there is no difference for layer 2. Solids concentration in the pulp is 35%, and no chalcopyrite (value mineral) is present.

Figure 7.4 below shows the water mass in two froth layers as a function of average particle size for various fractions of mica or silica mixed 50:50 with fine silica. While there is a difference between mica and silica, the actual difference is very small (note the expanded scale) and this may be attributed to increased froth stability with the platy mica compared to the lower aspect ratio silica. Lesser water is present in layer 2 as expected because water drains from the upper layers as the froth builds up. There is a very small decrease in the water mass recovered in either layer going from fine size to coarse size, similar to what was noticed in the ore flotation tests in figure 7.1 above, suggesting that the results from flotation tests and nascent froth sampling display the same trends. However, the significant drop observed in ore flotation tests for the +150µ silica is not observed in the froth sampling tests with coarse silica. This is likely attributed to the greater airflow rate used in the nascent froth sampling tests.

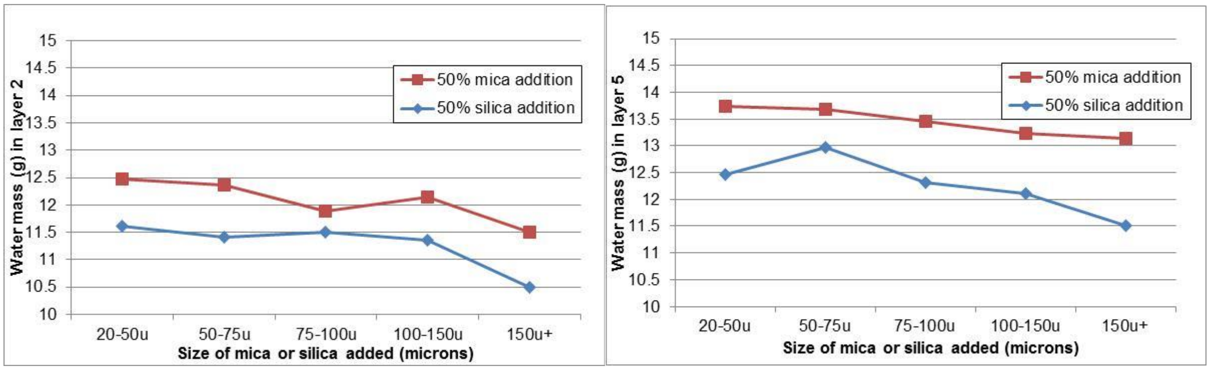

Figure 7.4: Nascent froth sampling- Water mass (g) with 50% mica or silica addition to 50% base fine silica in two select layers: a) layer 2 (near the top of froth) and b) layer 5 (near the bottom of froth). Water mass is always only slightly higher for when mica is added as compared to when silica is added for the same size. Solids concentration in the pulp is 35%, and no chalcopyrite (value mineral) is present.

In the ore flotation tests, the concentrate is collected continuously, whereas the nascent froth sampling tests are a snapshot of the froth zone at a particular point in time immediately after the froth is raised to its full height.

7.3.2 Steady-state sampling results

The next set of froth sampling tests were conducted by raising the froth and waiting for an extended period of time before sampling, which is meant to emulate the steady-state froths as described in chapter 2.11. Under these conditions, the upward drag forces and drainage are in balance. Tests with 50-75μ mica, 75-100μ mica and 100-150μ mica, mixed 50:50 with fine silica only, were conducted in this manner.

Figures 5.10, 5.11 and 5.12 in chapter 5 highlight the key differences between the steady-state tests and the nascent sampling tests. The data show that for 50-75μ or the 75-100μ silica mixed 50:50 with fine silica, there is a decrease in the amount of material retained in the froth held under steady state conditions for 5 minutes compared with the comparable nascent sampling condition. This suggests that in a steady-state froth, when **silica** of those sizes (50-75 and 75-100μ) is present, the rate of drainage is faster than the rate of upward transport into and through the froth. This is also the case for the 50-75µ **mica**. However, for the 75-100µ **mica**, there are nearly equal masses of mica captured as a function of depth in the froth for the nascent and steady-state samples, suggesting that the drainage rates and upward transport rates balance each other. In the 100-150µ **silica** case, however, there is a very small increase after time, which is within the range of experimental error. For the **100-150µ mica** case, it is observed that there is a substantial increase in the captured mass after 5 minutes, suggesting a buildup of gangue particles over time. The data may be summarized in the figure 7.5 below, with the red arrow highlighting the reversal in trend for the total gangue mass (i.e. increasing rather than decreasing after 5-minute delayed sampling).

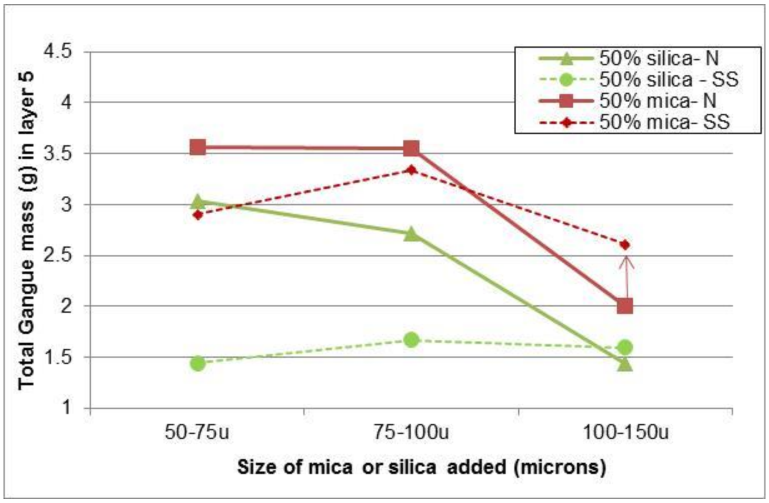

Figure 7.5: Total gangue mass in layer 5 (near bottom of froth) in froth sampling tests for nascent (N) and steady state (SS) sampling conditions- 50% of 50-75µ, 75-100µ or 100-150µ mica or silica mixed with 50% fine silica. Solids concentration in the pulp is 35%, and no chalcopyrite (value mineral) is present.

The trend for solids concentration (gangue mass/water mass) is shown in Figure 7.6 below. It shows the same trends as above, suggesting that the reversal for larger platy mica is not attributed to increased froth stability.

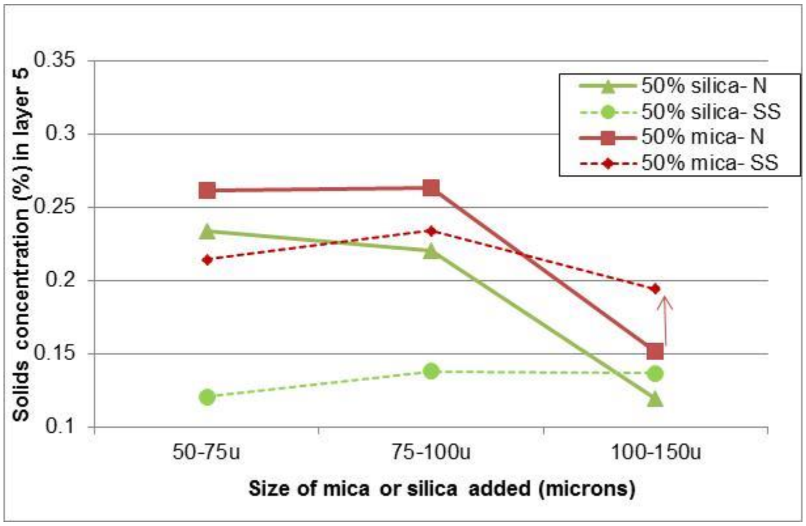

Figure 7.6: Solids concentration (wt.%) in layer 5 (near bottom of froth) in froth sampling tests for nascent (N) and steady state (SS) sampling - 50% of 50-75μ, 75-100μ and 100-150μ mica or silica mixed with 50% fine silica. Solids concentration in the pulp is 35%, and no chalcopyrite (value mineral) is present.

The data for the delayed froth sampling tests thus mirrors the observations in the flotation tests. However, in order to elucidate the mechanisms responsible for these trends, the compositions of the froths needed to be analyzed. The compositions determine whether the mica and fine silica behave independently of each other or not, and the mechanism of their transport to the froth zone can be further elucidated.

7.3.3 Compositions of froth zone

Figure 5.4 shows that, for the same size classes, the total gangue mass is always greater when platy mica is present as compared to rounded silica, the difference being only slightly greater at the finer sizes, and much greater at the coarser sizes. The compositions in the froth zone were obtained as a function of height and the masses of sized platy mica and rounded silica are plotted in figure 7.7 below. Only results for 75-100μ size and 100-150μ size mica/silica mixed 50:50 with fine silica are shown. The data shows that the sized mica mass is significantly more than the sized silica mass. However, the fine silica mass remains almost constant (see figure 7.8).

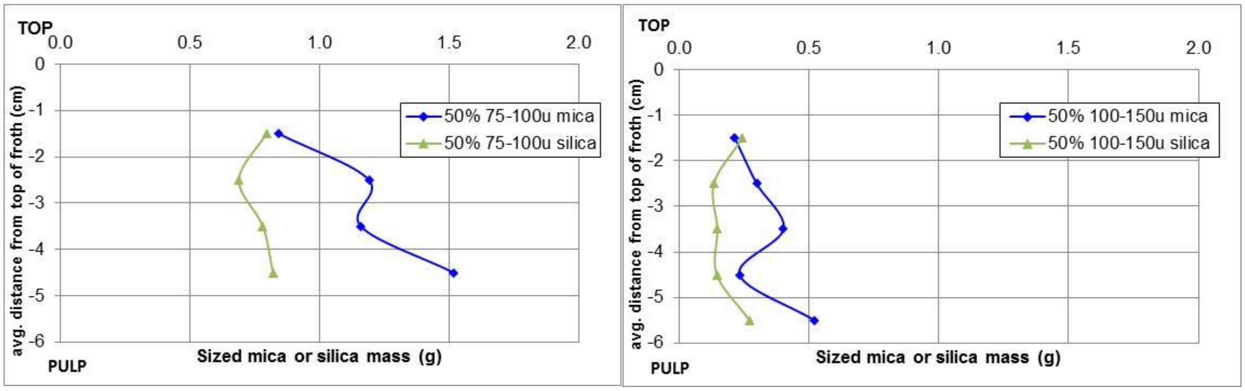

Figure 7.7: Nascent Froth sampling tests compositional analysis- 50% fine silica mixed with 50% (a) 75-100µ mica or silica, (b) 100-150µ mica or silica. Data shows sized silica or mica mass in each layer of froth. Mica mass is always more than silica of the same size. Solids concentration in the pulp is 35%, and no chalcopyrite (value mineral) is present. Data from layer 6 is removed in some cases because of errors. Data from layer 1 is excluded because of large uncertainty associated with it.

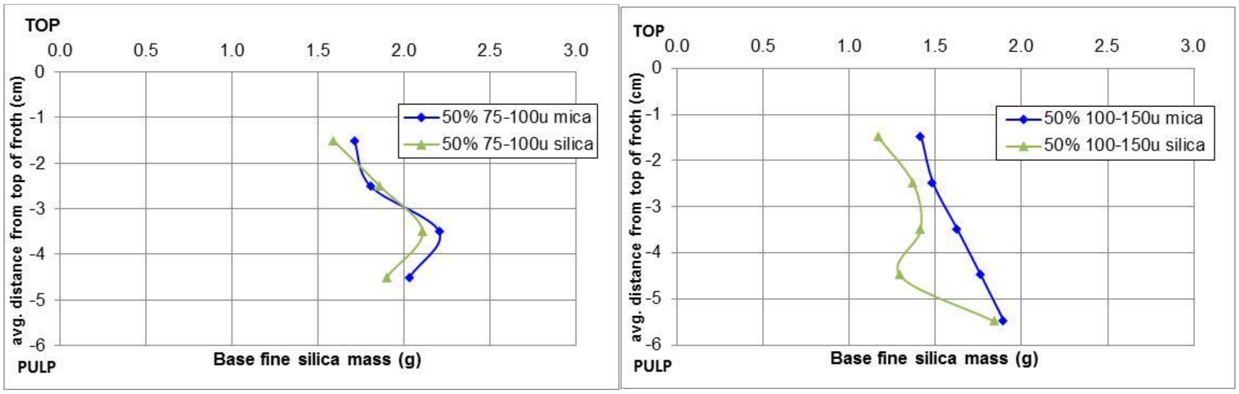

Figure 7.8: Nascent Froth sampling tests compositional analysis- 50% fine silica mixed with 50% (a) 75-100µ mica or silica, (b) 100-150µ mica or silica. Data shows fine silica mass in each layer of froth. fine silica mass is the same for mica or silica addition for both sizes. Solids concentration in the pulp is 35%, and no chalcopyrite (value mineral) is present. Data from layer 6 is removed in some cases because of errors. Data from layer 1 is excluded because of large uncertainty associated with it.

This suggests that the increased mass is attributed to additional platy mica being transported to the froth during the nascent froth sampling. It also indicates, perhaps, that the transport rate of each of the species is driven by their size or shape/morphology, alone. However, this is not the case certainly for the fine silica. Figure 7.9 shows the transport rates of fine silica as a function of height in the froth for each size fraction of mica that it (fine silica) was mixed with. It shows that the upward transport rate of the base fine silica appears to decrease with increasing mica size.

There are two possibilities for this result: a) the froth is less stable for coarser mica size, and hence fine particles drain rapidly, and/or b) as the coarser particles make their way to the pulp/froth interface, and are unable to the enter the froth zone, they accumulate at the interface and create a barrier for the fine silica particles to be transported into the froth. It is well known that the pulp froth interface is a turbulent region (Ata, 2004) so the likelihood of mica accumulation at the interface is very low, and thus the first possibility is more plausible.

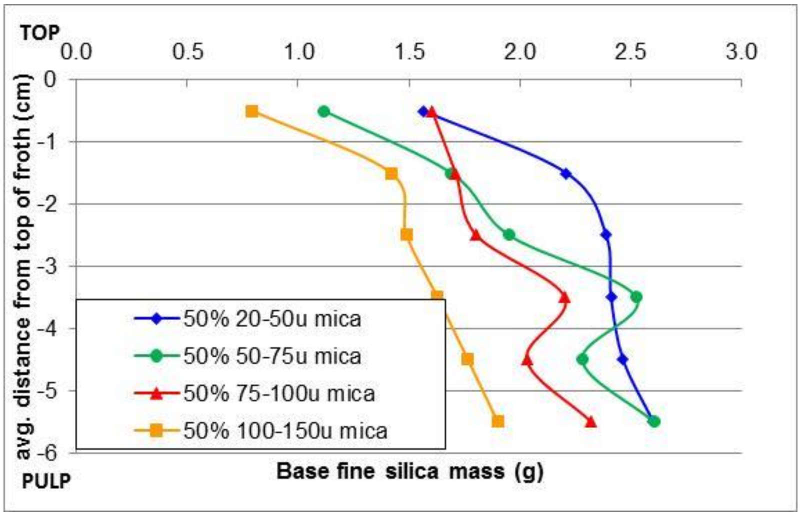

Figure 7.9: Nascent froth sampling tests- 50% base fine silica mixed with 50% sized platy mica as noted in legend. Data shows that mass of base fine silica decreases slightly as the size of mica added is coarser, and this may be attributed to increased froth stability.

Finally, the compositions of the tests where platy mica of various sizes was added for nascent and steady-state sampling are plotted below. It was shown in figure 7.6 that the total mass in each layer was increasing for the steady-state sampling. Figure 7.10 shows the mica mass for various sizes in layer 2 (a) and layer 5 (b). The data shows that for the 50-75µ mica size and the 75-100µ mica size the mica content does not appear to change significantly over time in both layers, suggesting the rate of mica transport to the froth is balanced by its drainage rate. However, for the 100-150µ mica size, there is a substantial increase in mica mass over time, as indicated by the red arrow in both plots. This suggests that the increased mass is attributed to additional mica being retained in the froth over time. The silica masses for nascent froth vs steady-state froth sampling are also shown in figure 7.11. The data shows that the silica masses are almost the same for the nascent froth sampling and steady-state froth sampling with very small differences. This suggests that the base fine silica transport and drainage rates are in balance, and the base fine silica transport is not affected by increasing/decreasing mica mass. Thus, only coarse mica is retained in the froth.

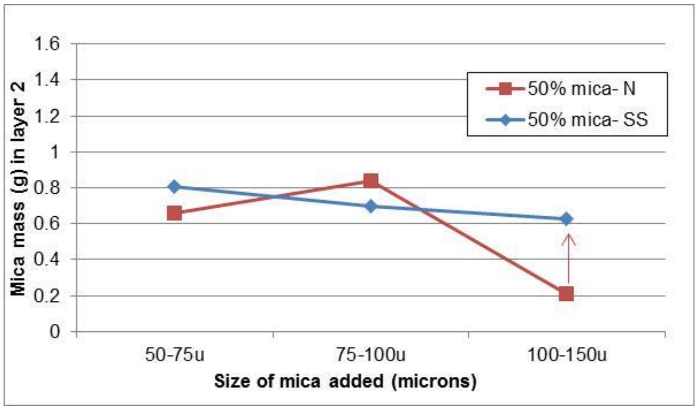

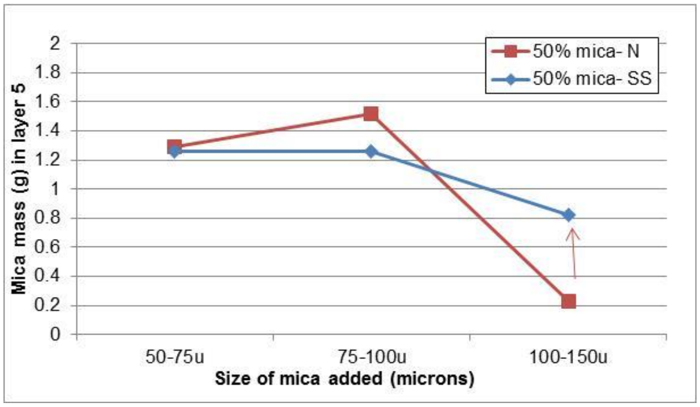

Figure 7.10: Nascent froth sampling vs steady-state froth sampling- 50% (w/w) sized mica mixed with 50% base silica- Mica mass in (a) layer 2 and (b) layer 5. Data shows that mica mass for the nascent and steady state sample is the same for sizes 50-75µ and 75-100µ for both layers. However, the mica mass increases for steady state sampling when 100-150µ mica is added. (Solids concentration in pulp is 35%, and no chalcopyrite was added)

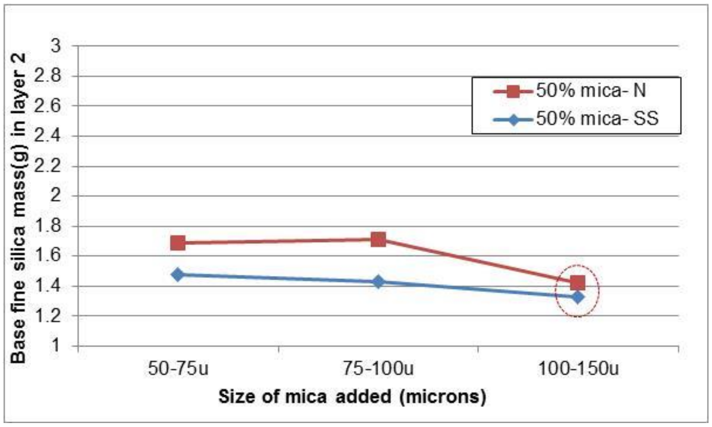

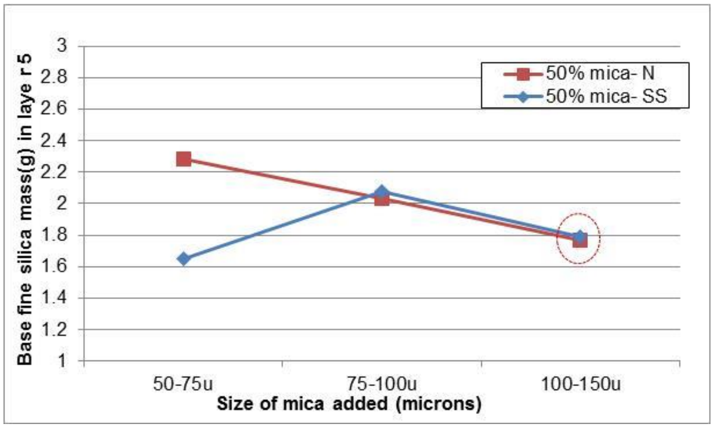

Figure 7.11: Nascent froth sampling vs steady-state froth sampling- 50% (w/w) sized mica mixed with 50% fine silica- Fine silica mass in (a) layer 2 and (b) layer 5. Data shows that base fine silica mass for the nascent and steady state sample is almost the same for all sizes, suggesting that its transport rate to the froth is balanced by drainage and is unaffected by increase/decrease in mica transport (Solids concentration in pulp is 35%, and no chalcopyrite was added)

7.3.4 Summary

a. More platy mica (as compared to the rounded silica of the same size) is transported to the froth as determined from the upward transport (drag)-dominated nascent froth sampling experiments. This suggests that under high drag conditions more platy mica is transported to the froth than low aspect ratio silica.

b. In the nascent froth sampling experiments, the mica transport and silica transport both decrease as a function of particle size.

c. In the drainage dominated steady-state sampling regime the mica sized below 100μ appears to drain freely, as ascertained from its decreased concentration (as compared to the nascent sampling).

d. Mica sized above 100μ appears to be retained in the froth as ascertained from its increased concentration in the drainage dominated steady-state sampling regime (as compared to nascent sampling).

e. The results from flotation, and a combination of nascent and steady-state sampling are self-consistent.

7.4 Mechanisms

7.4.1 Confirming hypothesis that increased drag is experienced by platy particles

In order to confirm the hypothesis that platy particles of all sizes experienced significantly more drag than low aspect ratio silica particles, the only possible way was to increase the drag forces significantly. This was accomplished in the nascent froth sampling experiments, by raising the froth at a high airflow rate rapidly, and then sampling immediately when the froth height reached the maximum height possible. Under these conditions, it was observed that for almost all sizes, more platy mica was transported to the froth than low aspect ratio silica particles, thus proving the hypothesis.

7.4.2 Confirmation of confinement effects and hypotheses

It has been demonstrated both at laboratory and plant scale that entrainment should decrease with size, so the effect of increase at coarse sizes is highly unusual, and finds only a single mention in the literature: Zheng (2006) observed that the degree of entrainment vs particle size curve, instead of going to 0 between 40-70μ as noted by other authors in the area, stays at 0.1 for coarser sizes. Zheng attributes this to the entrapment of coarse particles in the froth zone (as opposed to entrainment). Smith and Warren (1989) note that it is difficult to imagine entrainment in situations other than when the concentration of hydrophobic particles is significant. Entrapment in the traditional sense is certainly plausible given the experimental conditions in Zheng's work, i.e. sampling the flotation feed, conducting tests on a single cell where the hydrophobic particles dominate the froth zone. In Zheng's work, the coarse gangue would be trapped in between bubbles under high bubble loads (highly mineralized froths), as the channels between the froths would be too narrow to allow free drainage (the typical channel size is shown to be between 30-300 microns in size, depending on impeller speed, airflow rate, frother dosage, and concentration of hydrophobic particles). In this work, ENT curves vs particle size of the 4th stage are drawn, where the concentration of hydrophobic particles are considerably lower than in the first and second concentrates, the bubble loads are lower, and thus the plateau border channels should allow larger particles to drain, but we continue to see this effect. So it is to be recognized that the mechanism of transport of coarse mica to the concentrate (and to a significantly less extent the coarse silica) is related to the reduced drainage rates as the coarse particles are trapped in the froth phase and this phenomena occurs irrespective of the presence of hydrophobic particles. The reduced drainage rates for the coarse mica are likely related to bridging of the plateau borders, which would be possible if the shortest axis of the coarse mica particles is perpendicular to the direction of water flow. This alignment would be consistent with the observation that coarse mica particles appear to slow down the rate of transport of fine silica particles, as demonstrated in figure 7.9. Finally, while this effect is observed, in the equilibrium from sampling experiments it may be slightly subdued because in a steady-state froth, the volumetric flow of water at any level is completely balanced by downward flow by drainage, but in a flotation froth, there is a net upward flow of water.

The rheological profiles of relative viscosity vs particle volume fraction for the various sizes of mica mixed with fine silica at 25:75 ratio are shown in Figure 7.12 below (red circle shows volume fraction found in the froth. The data suggests that while there is a change in the viscosity of the interstitial suspension, it is far too insignificant to contribute to the increased transport in the froth phase by the mechanism of network transport via bubble flux. The viscosity-volume fraction relationship of 0.75% fibrous ore mixed with 99.25% fine silica is graphed on the same plot (blue circle shows volume fraction found in froth). The implication is that in the case of mica there is no phenomenon that results in aggregation of particles to form a network structure. At the same time, it can also be said that the bulk viscosity measurements of interstitial suspension, which we have used to explain network transport by bubble flux, likely cannot explain the mechanisms that result in recovery of mica in the concentrate.

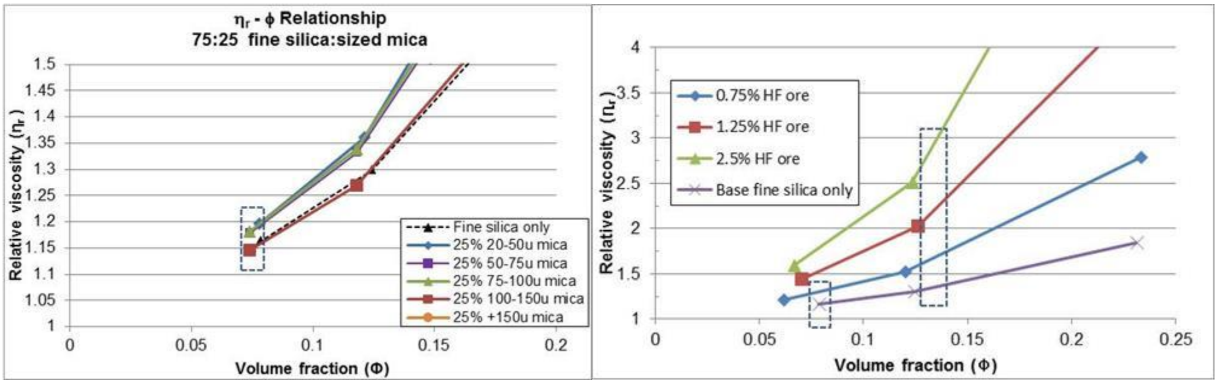

Figure 7.12: Relative viscosity vs volume fraction (a) 75:25 fine silica: sized mica, and (b) addition of increasing amounts of fibrous ore. The relative viscosity is substantially higher for fibrous ore as compared to mica addition, even at much higher mica concentrations. The blue dotted boxes show the volume fractions in the froth zone obtained from froth sampling experiments.

For the network transport via bubble flux to occur, the mineral species must create a light network-like structure in the pulp phase, which gets lifted to the froth phase via bubble flux. This is the case with fibrous minerals like chrysotile, which entangle in the pulp zone to create a network like-structure which cannot be broken up because of turbulence damping the pulp zone. This network carries with it the other non-fibrous gangue minerals to the froth. In this situation, the first wave of material arriving at the top of the lip cannot be distinguished from the pulp phase; gas holdup is extremely low. When the froth sampling experiments were completed on fibrous ore under nascent and steady-state conditions, it was observed that the amount of non-sulfide gangue (silica) actually decreases under steady-state sampling as compared to nascent sampling. This is because under the steady-state sampling conditions (waiting for 5 minutes), air bubbles are able to penetrate the network-like structure, destabilize it, resulting in the drainage of silica particles that were carried to the froth zone. However, in the actual flotation process, as the froth is removed continually the likelihood of particles draining over time decreases substantially. In other words, as mentioned earlier, the steady-state sampling exaggerates the drainage rate of the interstitial suspension as compared to flotation froths. Also note that the effects are significant at as low as 7% fibrous ore by weight, which translates to about 0.7% by weight of fibrous mineral (XRD- section 3.5). It is also noted here that the chrysotile fibers flexibility plays a critical role in the entanglement process and thus network transport via bubble flux, with the interactions driven by inter-fiber frictional forces (Patra, 2013).

It is to be noted how different this result is for the mica or silica. In this case, the viscosity is not very high so there is no turbulence damping, and the probability of transport of a particle to the froth zone is dictated by its size and shape. The pulp-froth interface acts as a classifier, slowing down the transport of particles as a function of size, with coarse particles less likely to be transported to the froth zone. However, the shape of mica results in it experiencing increased drag forces (Wiese, 2016, section 2.9.3. in this work), and thus having a higher probability of making it to the froth zone. Once they are in the froth zone, then the drainage rate is also directly proportional to their size, density and shape. Given that most non-sulfide gangue consists of silicate minerals, their specific gravity is in the narrow range of 2.6-2.8 and so rounded particles over 60μ are likely to drain rapidly even as they can barely be transported to the froth zone. As particles becomes increasingly asymmetrical (e.g. platy), the probability of their transport to the concentrate increases, but is still a function of size. Their drainage properties are also related to their shape, with particles under a critical size draining rapidly. However, at the +100μ size range, they are entrapped in the plateau borders, and build up in the froth over time and contaminate the concentrate. Thus, entrapment in plateau borders, even in the absence of hydrophobic particles, is the reason coarse mica particles are retained in the froth, and this increased retention (or reduced drainage) is what is responsible for coarse mica transport to the concentrate.

In the process of determining the mechanisms resulting in transport of particles to concentrate, a distinction must be made between the two separate sub-processes, namely, the transport of particles upward into the froth phase, and the drainage of particles from the froth. The current definition of entrainment refers to the net outcome from both these processes and this definition forms the basis for most models of non-sulfide gangue transport to concentrate. This works reasonably well for particles below a certain size range (i.e. 100μ) beyond which the drainage rates start to diverge. However, coarse particles start to accumulate in the froth via entrapment (i.e. drain slower), and this becomes significant particularly for asymmetric particles like mica (platy morphology). The existing models need to be altered to explain this phenomenon. The degree of entrainment should perhaps be termed “degree of gangue recovery”. Also, the mechanism of entrapment which is usually referred to as the mechanism as illustrated by

Konopacka (2010): particles being trapped in the channels when froths are loaded with hydrophobic particles should be expanded to cover the situation when there are no hydrophobic particles, i.e. entrapment of coarse gangue in plateau borders. Entrapment, thus, is a mechanism resulting in reduced drainage, and is not involved with particle transport to the froth zone.

Finally, these experiments (addition of specific size fractions) were conducted specifically with the goal of illustrating the various mechanisms contributing to transport of mica to the concentrate. In real ores, it is expected that a combination of these mechanisms is at play, depending on the size of the various mineral species and their shape/morphology. However, it is noted that mica in particular, tends to be coarser in size when ground in a tumbling mill relative to other silicate minerals owing to their platy morphology- sheets of mica have high tensile strength and stretch when impacted by grinding media (section 2.8.1).

7.5 Channel dimensions to confirm confinement effects

In order to confirm that the increased transport of coarse mica is related to its confinement in plateau borders, experiments were done to measure the dimensions of the plateau borders using a prism mounted onto the fixed piece of the froth sampler. The image analysis software Spot (v8.1.) was used to measure the size of the plateau borders. Only channels that are not touching the glass prism were used for measurements, i.e. those visible through the bubbles that were touching the glass prism. The data shows that the channel dimensions ranged from 150 to 350μ in size. This is in agreement with Hemmings (1971), who found that the dimensions for the drainage channels/plateau borders (he refers to them as interbubble film thickness) to be between 30 and 300 microns.

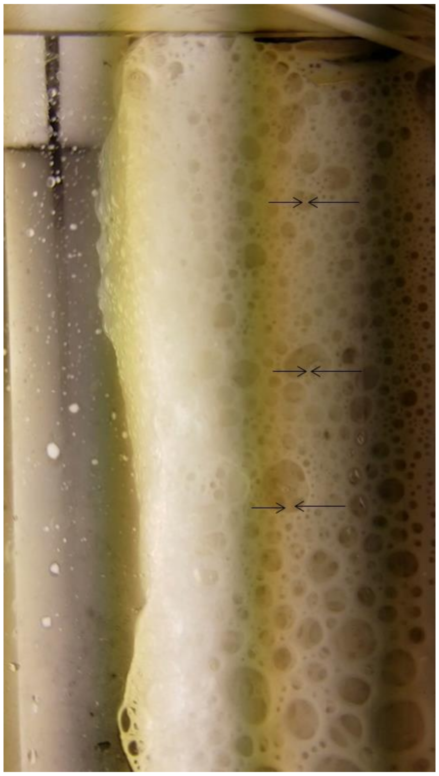

Figure 7.13: Measuring dimensions of plateau borders in froths. Data showed that the size of the plateau borders ranged from 100-300 microns in size.

In this case, we can use the confinement parameter λ, which is identified as the ratio of the diameter of the particle to the diameter of the constriction the particle needs to pass to drain through the channels, to study the drainage behavior of muscovite. The ENT from the flotation tests is plotted against λ in figure 14, with the assumption that the diameter of the constriction is 100μ. The data shows that the confinement is significantly higher for mica as compared to silica. In addition, the onset of confinement related effects appears to be delayed for 25% mica addition, as compared to 50% mica addition. Confinement effects are not observed for silica at 25% addition rate.

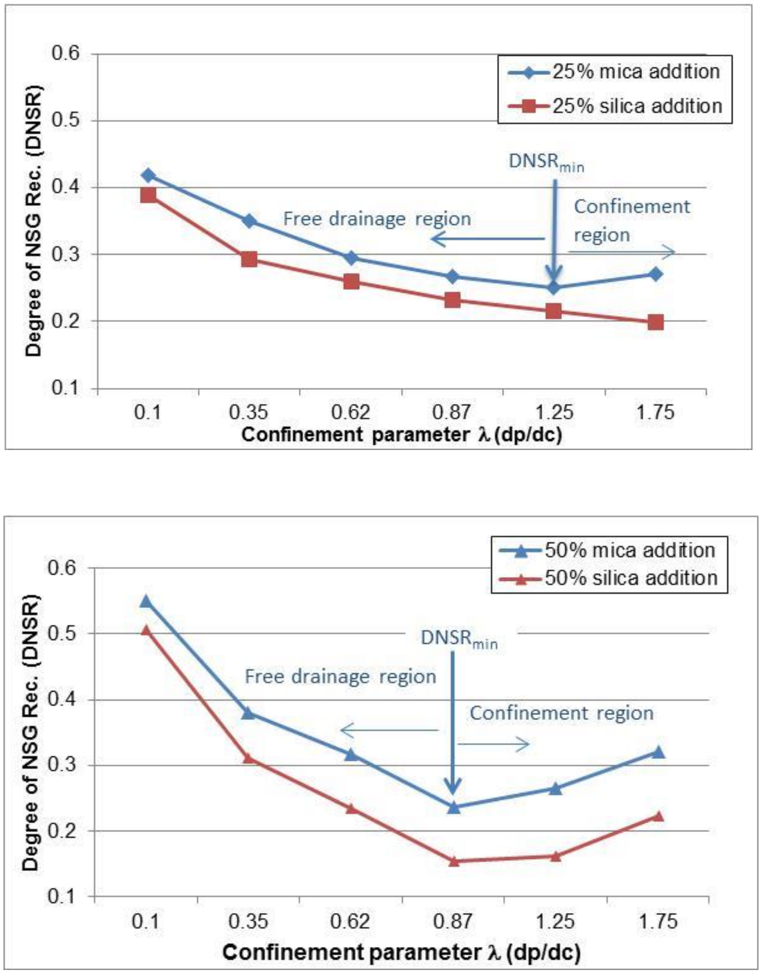

Figure 7.14: Degree of Non-sulfide Gangue Recovery (DNSR) vs confinement parameter generated from flotation tests with the assumption that the size of the constriction is 100 microns: DNSR for (a) 25% mica addition, and (b) 50% mica addition. The onset of confinement related effects appears to be delayed for 25% mica addition, as compared to 50% mica addition. Confinement effects not observed for silica at 25% addition rate.

A critical confinement parameter λ_c can thus be identified, which predicts the onset of confinement effects at the 25% and 50% addition rates for mica and silica. The λ_c values for the various experiments are shown in Table 7.1 below. It is recognized, of course, that mineral froths are unstable and have a wide size distribution of plateau border sizes. In addition, the bubbles are coated with hydrophobic particles resulting in narrower constrictions. As such, these results are only an estimate of the expected behavior. When an effort is made to model the flow of platy particles in cellular foams, it is expected that the λ_c values will be lower than those obtained for spherical particles, perhaps very significantly.

Table 7.1: Critical confinement parameter for 25% and 50% addition rate of mica

Experiment	Critical confinement parameter λ_c
25% mica (75% base fine silica)	1.75
25% silica (75% base fine silica)	N/A
50% mica (50% base fine silica)	1.25
50% silica (50% base fine silica)	1.75

The modes of particle transport and drainage in flotation froths as obtained from this work are illustrated in figure 14 below.

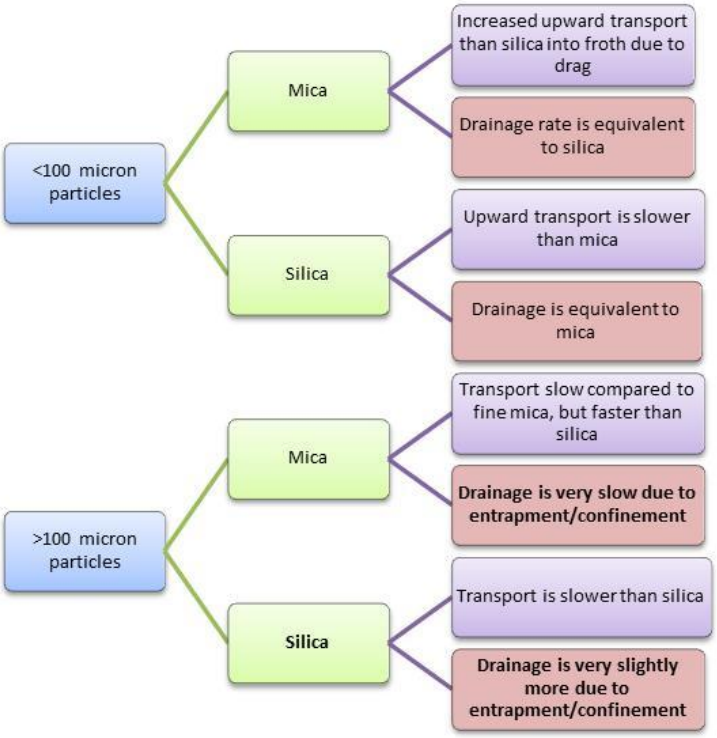

Figure 7.15: Modes of particle transport and drainage for mica and silica

Using the above data, it is possible to identify the regions of entrainment and entrapment/confinement mediated transport for mica minerals. This is shown in figure 7.16. The shade of red indicates the extent of gangue recovery by entrainment, and the boundaries identify regions of gangue recovery where entrainment and confinement/entrapment dominate. It also identifies the region for lowest gangue recovery.

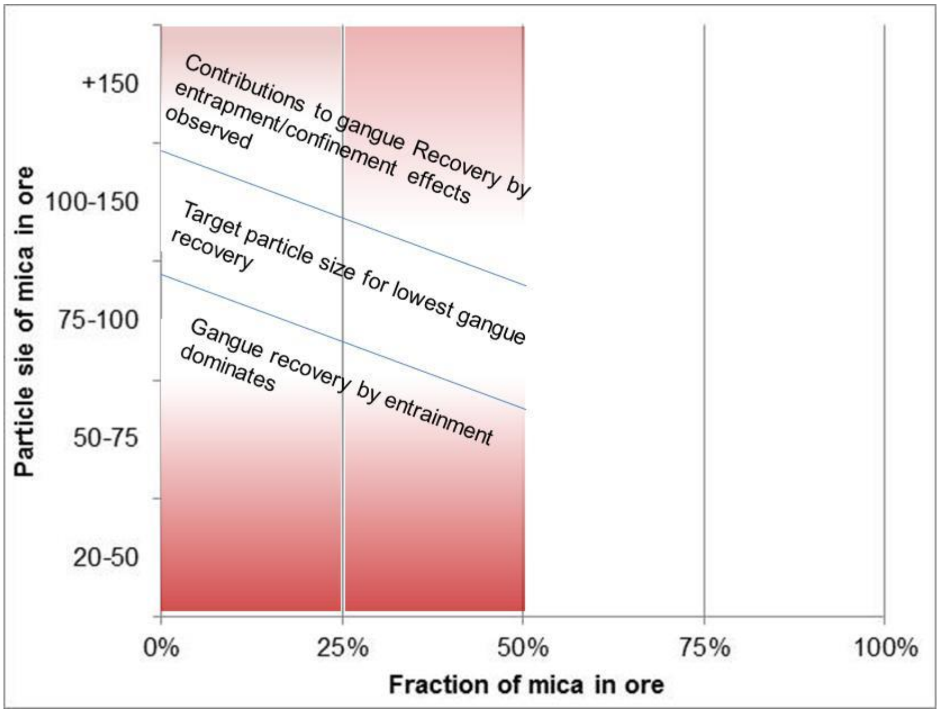

Figure 7.16: Illustration of various modes of particle transport to froth zone as a function of mica size and content in ore. The map illustrates the region where entrainment dominates, the region where entrapment/confinement effects start to contribute to gangue recovery, and the region of target particle size for minimal gangue recovery.

7.6 Using rheological properties as a function of volume fraction as indicators of transport via bubble flux and bubble entrapment for fibrous ores

Chapter 6 shows how the material properties of the mineral, i.e. shape and morphology, affect the viscosity-volume fraction relationship. It is noted that the shape of the viscosity-volume fraction curves may be used as an indicator for the type of mechanism responsible for particle transport and retention in the froth phase, and, by extension, a predictor for the flotation response of the ore. This is illustrated in figure 7.16 below.

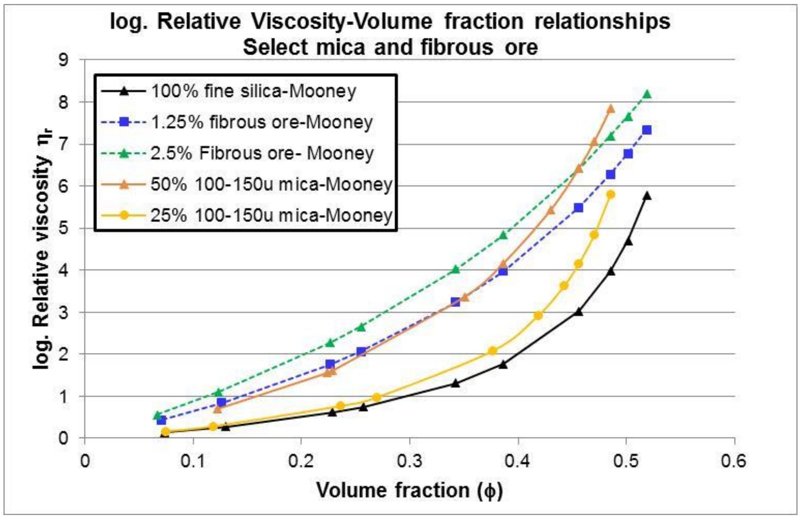

Figure 7.17: Relative viscosity-volume fraction relationships for select fibrous/silica and mica/silica mixtures

Note the similarities in the shapes of the Mooney-fit curves for silica and silica-mica mixtures, and the significant difference in the shape of the curves for the silica with fibrous ore. While the relative viscosity deviates from the silica curve with volume fraction starting at a ϕ value of 0.35 or so for silica/mica mixtures, it increases at an ϕ value of about 0.05 for the fibrous ore mixtures. In fitting the data to the Mooney equation (the Krieger-Doherty equation may be used as well), the two constants obtained, namely B and ϕ_{max} can be can be plotted on a graph to identify the areas corresponding the various mechanisms of transport as shown in Figure 7.14 below. When the ϕ_{max} and B parameter both increase, it corresponds to a system that is likely to result in the network-transport by bubble flux. In all other situations, entrainment and entrapment are likely to be the mechanisms for transport of non-sulfide gangue mineral to the froth zone. It is important to recognize the benefits of this outcome: prior to this work, all that was known that increasing viscosity leads to a problem, but this was not quantifiable. In this work, the data has been fit to a model, which is applicable under all circumstances and ores, and conditions under which the phenomenon of network transport via bubble-flux will result in poor concentrate grade.

It is also noted that if particles of the same aspect ratio as the fibers are used, but they are not flexible, they cannot entangle to form a network, for transport by bubble flux. This is illustrated in the case of wollastonite, where it is seen that the ϕ_{max} values decrease with increasing wollastonite concentration.

Finally, differentiating the region for entrapment vs entrainment (as in the case of mica) cannot be done because the mechanism of transport is not driven by the viscosity of the suspension, but by the confinement of particles in the plateau borders and vertices. There are some indicators, however, that the parameters B and ϕ_{max} may provide clues for how the particles behave in confinement. For example, it is seen that at 25% mica addition rate, the +150μ mica B value increases (Table 6.2), which does not happen for any other size fraction. This is also the case for 50% mica addition, where it happens for 100-150μ as well as +150μ size fractions.

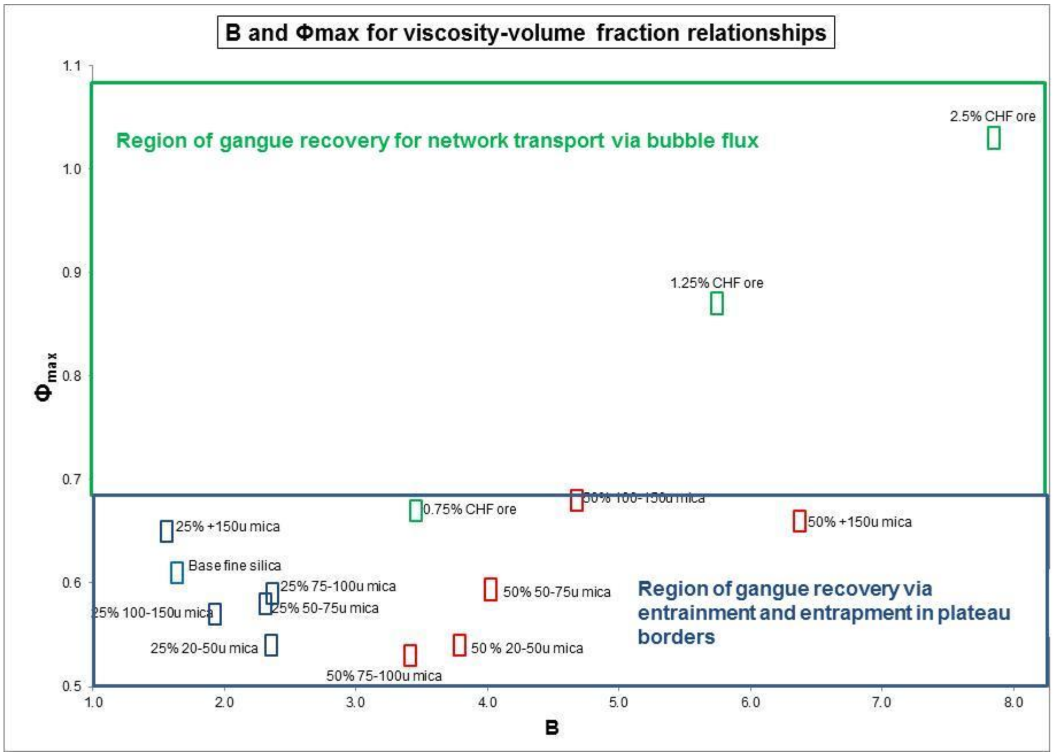

Figure 7.18: Relationship between Mooney fit to rheology data and mechanisms for gangue transport to concentrate

It is also noted here that the chrysotile fibers flexibility plays a critical role in the entanglement process and thus network transport via bubble flux, with the interactions driven by inter-fiber frictional forces (Patra, 2013). If particles of the same aspect ratio as the fibers are used, but they are not flexible, they cannot entangle to form a network for transport by bubble flux. This is illustrated in the case of wollastonite, where it is seen that the ϕ_{max} values are below 0.6, which is the critical point below which the likely mode for gangue recovery is rapid transport into froth (hydraulic entrainment) and entrapment. However, in the absence of sized wollastonite, it is difficult to conclude whether the coarse wollastonite is recovered by entrapment or not.

7.7 Summary

The results show that the modes of mineral recovery are related to particle size and shape. The upward transport dominated nascent froth sampling experiments and drainage dominated steady-state froth sampling experiments provide unique insights into the transport mechanisms for platy and rounded particles of various sizes.

1. When sized platy mica is mixed with an ore, the recovery of all non-value (gangue) minerals is higher than when rounded silica of the same size is used. There is a decrease in gangue recovery with increasing particle size for both types of particles.
2. Froth sampling experiments were used to obtain the composition of the nascent froths prepared containing sized platy particles (mixed with silica) and pure rounded silica particles (mixed with silica). Increased mass with mica was also observed in this mixture of pure minerals.
3. The solids concentration (volume fraction of solids) in the froth sampling experiments was found to be very low. The bulk viscosity values at these volume fractions with mica

addition are not significantly different from those obtained with silica addition of the same size. Thus, the hypothesis that the bulk viscosity differences alone could explain the increased transport of mica to the froth zone was proven to be false.

4. For fibrous minerals containing ore, constants obtained by fitting the data to the Mooney equation and the shapes of (ln) relative viscosity-volume fraction provide a clear indicator for transport of these minerals by the mechanism “network transport by bubble flux” as outline in Patra (2013).
5. This led to the revised hypothesis, which states (firstly) that increased transport of platy particles is related to the high drag forces experienced by the platy particles, as well as reduced influence of gravitational forces (less weight per particle). In order to magnify the effect of drag, the airflow rate was increased resulting in a very high drag regime. Under these conditions, it was observed that more platy mica was transported to froth zone as compared to low aspect ratio silica, thus proving the hypothesis.
6. The second part of the revised hypothesis was the confinement of particles in the plateau borders could explain the additional transport of coarse mica. The widths of the channels were measured using simple imaging techniques using a prism assembly. The plateau borders were of the order of 100-150μ, and the vertices ranges from 300-500μ.
7. Steady state froth sampling experiments were then conducted. In these experiments, once the froth is built up, the airflow rate is reduced significantly leading to a drainage and drag balanced regime. The results from the steady state froth sampling were compared to the nascent froth sampling. It was found that the gangue mass decreased for platy mica that was sized finer than 100μ, and this may be attributed to the drainage dominated regime. However, the gangue mass for steady state sampling increased for platy mica that

was sized coarser than 100μ. The composition of the froth shows that mass of platy mica was increasing, and fine silica mass was constant. This suggested that the coarse mica being transported upwards was transporting slower or once transported did not drain well. In comparison, the silica drained very well and its mass decreased in steady-state sampling. It is apparent that free drainage occurs until the size of the particle approaches the size of the channels (i.e. confinement parameter λ ~1). Thus, confinement effects appear to be the cause of coarse platy mica (100μ) being recovered in the froth. For finer sized platy mica (finer than 100μ), their increased transport may be attributed to increased drag forces resulting in higher transport rates to the froth zone. For coarse silica, the shape allows for gravitational drainage to dominate.

8. The region of minimal gangue recovery was thus identified for the amount of platy mica added (25% and 50%). Recall that rejecting particles (gangue) is the objective in mineral froths, but not in the case of foams used in other applications like ceramics. For non-mineral systems it is apparent that increasing aspect-ratio of particles (i.e. using non spherical particles) will lead to a more stable froth.

8 Summary, Conclusions and Recommendations for future work

Three-phase froths (containing solid, liquid and gas) are of great importance in a number of industries. In these froths, complex fluids (suspensions) flow through tortuous channels that may be lined with hydrophobic particles attached to bubbles. Unattached particles in these channels experience drag and gravitational forces, and are subject to confinement effects in the channels, all of which determine their transport through the froth. Understanding the role of shape and size on the particle motion through a froth is a scientific area of great interest to many industries. An attempt is made in this work to advance the knowledge in this area with a focus on the froth flotation process for separation of base and precious metal values from ores. Transport of platy mica and rounded silica through froth channels is studied.

In the industrial flotation process for the beneficiation of sulfide mineral ores, the ubiquitous *hydrophilic* phyllosilicate gangue (non-value) mineral muscovite (of the mica subgroup) is transported into and through the froth zone into the value mineral concentrate, thereby reducing its grade (product purity or quality). While the transport of fine mica (<50microns) into and through the froth zone may be understood in terms of traditional entrainment mechanism, transport of coarse mica (>50u) is not understood. The first objective of this thesis was to identify the nature and extent of the problem attributed to platy mica. To this end, flotation tests were conducted with mixtures of an ore and platy mica or rounded silica (control) of various sizes at two concentration levels. The results from these tests show that under almost all conditions (size ranges and ratios), there is a negative impact on concentrate grade when mica is mixed with the ore, as compared to when silica is mixed, but there is no impact on value mineral recovery or flotation kinetics (i.e. the rate of bubble transport of hydrophobic value sulfide mineral particles). The effect of size is more significant than shape at particle size <50μ, with finer sized species affecting concentrate grade, which is the well-known entrainment mechanism of transport of hydrophilic gangue to concentrate. When the fibrous mineral chrysotile is added to the ore, even at 4 wt.% addition there is a significant impact on concentrate grade. High aspect ratio minerals are thus problematic.

The degree of entrainment is defined as the ratio of non-sulfide gangue mass to water mass in the froth divided by the mass of non-sulfide gangue mass to water mass in the pulp. This ratio is an indicator of the extent of entrainment, which is the major process by which hydrophilic minerals transfer to the concentrate by the water through the froth. The amount of non-sulfide gangue and water in each concentrate was calculated, and the linear fit was used to obtain the degree of entrainment. The degree of entrainment vs. particle size curve shows that the non-sulfide gangue content of the concentrate when mica is added is always higher than when silica is added, regardless of size.

The second objective of this thesis was to understand pathways and mechanisms by which the concentrate grade was diluted. A decrease in grade is to be attributed to increased entrainment/transport of these particles to the froth zone and into the concentrate. Mica has a platy shape/morphology; SEM images confirmed this for the sample used in this strudy. *The preliminary hypothesis, based on a review of the literature, was that the asymmetric shape results in a modification of the rheological properties of the froth interstitial suspension, resulting in slower drainage of the suspension in the froth zone, which contributes to the overall transport of these species to the concentrate.*

In order to test the hypothesis that the rheological properties of the froth interstitial suspension were affected when platy mineral mica was present, froth sampling experiments were conducted using a cell specially designed for the purpose. A technique for raising froth and collecting samples without causing any leaks was perfected for conducting these experiments. Mixtures of pure mica, silica and chalcopyrite were used to enable quantitation of all species. A froth 6 cm deep was raised without any collection, and sampling conducted immediately. *This is termed nascent froth sampling in this work.* The results from the immediate froth sampling (or nascent froth sampling) tests showed that total gangue transport to the froth zone is greater than silica transport for the same size, and that the increased mass is attributed to the larger transport of mica. For comparison, froth sampling tests were also conducted by mixing the base ore with an ore containing large amounts of chrysotile, a mineral whose effect on slurry rheology (not interstitial froth) is known, and the transport mechanism has been identified as “network transport by bubble flux” (Patra et al., 2010).

The compositions were used to conduct bulk rheological measurements. A carefully calibrated helical ribbon geometry was used, for the first time in mineral suspensions, to obtain the rheological properties of suspensions as a function of volume fraction, and a protocol developed to alleviate measurement challenges associated with rapid settling of mineral particles, which is a common problem in practical ore/mineral slurries. The results from these experiments showed that at the volume fractions observed in the sampling experiments, the viscosity of the silica-mica mixture suspensions does not suggest networking effects, which are readily observed for suspensions with fibrous minerals. This showed that interstitial suspension viscosity could not explain the higher transport of mica compared to silica. For the fibrous ore mixtures, the constants obtained by fitting the relative viscosity data for ten different volume fractions to the Mooney equation provide clear indicators of the “network transport by bubble flux” mechanism.

It was then hypothesized that the increased transport of platy mica was related to increased drag forces (reduced gravitational settling forces) experienced by platy particles as compared to low aspect ratio silica particles, and that increased transport of coarse platy mica was related to the increased confinement of particles in the plateau borders. To prove the first part of the hypothesis, froth sampling experiments were conducted under very high drag conditions. It was observed that under these high drag conditions mica transport was always more than silica transport.

For the second hypothesis, referring back to the degree of entrainment curve obtained from the flotation tests, an unusual trend was observed. According to most prevailing studies on degree of entrainment, it has been observed that the degree of entrainment typically falls to zero at a certain (40-70μ) particle size. This is because a) the pulp-froth interface acts as a classifier, slowing down transport of coarser particles upwards, while letting the finer particles transport faster and b) the drainage rates of the coarser particles far exceeds the rate of transport to the froth zone through the interface. In this work, it was observed that for mica this was not the case, with the degree of entrainment first decreasing in a regular manner, and then increasing past 100μ for the 50% mixture (with base ore) and past +150μ for the 25% mixture. However, this effect was not observed in the nascent froth sampling tests, with recovery continuing to decrease as a function of size all the way to +150μ.

When sampling tests were conducted on steady state froths (sampling after a 5-minute waiting period), it was observed that when the relatively finer sized mica particles (50-75 μ) were mixed with the base fine silica, the total solids mass in froths was reduced compared to nascent sampling. This is because for steady state froths, the upward transfer (controlled using airflow rate) is slowed to maintain the froth bed, leaving the drainage rate to dominate and take over the net transfer rate. For the intermediate platy mica size (75-100μ) mixture, the solids mass in the froth remains the same. However, for the 100-150μ-sized platy mica mixture, the solids mass actually increases for the steady state sample as compared to the nascent froth sample. The compositional analysis revealed that the additional mass came from additional platy mica being present, suggesting that the drainage rate for the coarse platy mica suspension is so slow that despite the very slow transport rate to the froth under the steady state conditions (low airflow rate), it is able to build up in the froth over time. Thus, the increased transport of coarse mica has to be related to the confinement/entrapment of these large particles in the plateau borders and vertices. This entrapment is not subject only to situations where bubble loads (hydrophobic particles coating bubbles) are high, but even to low bubble load situations, such as scavenger cells or the last few rougher cells in a bank. This happens to a significantly less extent for coarse silica (globular/rounded) particles as well. Thus, the mechanism for transport of fine mica is related to increased transport to the froth zone because of increased drag attributed to its shape, while at the coarse size (+100μ) there is a significant contribution from entrapment/confinement.

Modeling the confinement of asymmetrical particles in froth has proven to be a significant challenge. Very little has been done with the modeling of the confinement of spherical particles in froths, and that too only under forced drainage conditions in very stable froths with immobile interfaces (mineral froths are known to be extremely mobile and unstable). A key parameter driving the drainage is the confinement parameter λ (Haffner, 2015) which compares the size of particles contained in the interstitial phase to the size of passage through the constrictions in the interstitial network: $\lambda = d_p/d_c$. The critical λ value for mica was estimated to be 1.25 suggesting that mica would confine more than silica, and this information could be used in future modeling efforts.

Given that mica tends to remain in the coarse fraction when ground, it is possible that this mechanism is a significant contributor to the presence of large amounts of mica in concentrates, which is the root cause of poor concentrate grades observed at many large operations globally. It is easy to see, thus, that one possible solution to eliminating this problem is to ensure that mica is in the right size range such that entrapment/confinement effects do not occur and entrainment is minimized, and a preferred range is presented for this. Of course, the extent of entrapment is subject to the size of the channels in the froth zone, which is a function of frother type and dosage, impeller speed, airflow rate, and the concentration of hydrophobic particles.

8.1 Recommendations for future work

In light of the findings from this work, the following recommendations can be made

1. These findings may be applicable in the field of cellular foams. Increasing particle aspect ratio can be used to stabilize foams. Foams with wider plateau borders (higher water content) may be prepared for the same solids content without compromising foam half-life or stability.
2. In order to better understand the behavior of these minerals under confinement, a systematic study must be conducted using these mineral mixtures at various ratios at the same size ranges as used in this work, under a wide range of variables that influence the confinement, i.e. the channel widths. This includes
    a. the concentration of hydrophobic minerals (which pack at the liquid air interface),

   b. the airflow rate or more specifically, the superficial air velocity (frequently abbreviated in the industry as J_g),
   c. the frother type and dosage (both of these influence the thickness of the bubble films and consequently, the channel widths)
3. With the information developed in this work, it would be possible to develop a semi-empirical model of confinement/entrapment behavior. The above derived parameters would be critical, as would be the particle size. It is expected, based on results in this work that platy particles below 100μ will not be subject to the confinement effects.
4. Methods should be developed to distinguish the entrapment mechanism for transfer of particles to the froth zone at the plant scale. Identifying the problem will lead to the development of mitigating actions to alleviate the problems associated with these minerals.
5. To understand whether these confinement effects are specific to platy minerals like mica, experiments should also be conducted with mixtures of silica with various sizes of wollastonite. A key challenge here is the size separation of wollasonite, which is difficult to do by sieving. As such, it is expected that the particle size distributions will be wider than those obtained for the silica experiments.

References

Amelunxen, P., et al. (2018). "A phenomenological model of entrainment and froth recovery for interpreting laboratory flotation kinetics tests." Minerals Engineering 125: 60-65.

Arnold, B., Aplan, F., 1986a. The effect of clay slimes on coal flotation, part I: The nature of the clay. International Journal of Mineral Processing, 17, 225–242.

Ata, S. (2012). Phenomena in the froth phase of flotation - A review. International Journal of Mineral Processing, 102-103, 1-12.

Ata, S., Ahmed, N. and Jameson, G. J. (2003). A study of bubble coalescence in flotation froths. International Journal of Mineral Processing 72(1-4): 255-266.

Ata, S., Ahmed, N., Jameson, G. J., 2004. The effect of hydrophobicity on the drainage of gangue minerals in flotation froths. Minerals Engineering 17, 897–901.

Aveyard, R., Binks, B.P., Fletcher, P.D.I., Peck, T.G., Rutherford, C.E., 1994. Aspects of aqueous foam stability in the presence of hydrocarbon oils and solid particles. Advances in Colloid and Interface Science. 48, 93–120.

Bakker, C.W., Meyer, C.J. and Deglon, D.A. 2010, "The development of a cavern model for mechanical flotation cells", Minerals Engineering, vol. 23, pp. 968-972.

Barbian, N., Cilliers, J. J., Morar, S. and Bradshaw, D. J. (2007). Froth imaging, air recovery and bubble loading to describe flotation bank performance. International Journal of Mineral Processing 84(1-4): 81-88.

Barnes, H. A., Hutton, J. F. and Walters, K. (1989). An introduction to rheology, Elsevier, Amsterdam.

Basnayaka, L., Subasinghe, N., and Albijanic, B., 2017, “Influence of clays on the slurry rheology and flotation of a pyritic gold ore.” Applied Clay Science, 136. pp. 230–238.

Batchelor, G., & Green, J. (1972). The determination of the bulk stress in a suspension of spherical particles to order c2. Journal of Fluid Mechanics, 56(3), 401-427. doi:10.1017/S0022112072002435

Bikerman, J. J. (1973). Foams. Springer-Verlag, New York.

Bisshop, J.P., White, M.E., 1976. Study of particle entrainment in flotation froth. Transactions of the Institution of Mining and Metallurgy C85, C191–C194.

Chen, G., Grano, S., Sobieraj, S., Ralston, J., 1999a. The effect of high intensity conditioning on the flotation of a nickel ore, part 2: Mechanisms. Minerals Engineering 12,1359–1373.

Cilliers, J., J., Asplin, R. A. and Woodburn, E. T. (1998). Kinetic flotation modelling using froth imaging data. In: Laskowski, J. A., Woodburn, E. T. (Eds), Frothing in Flotation II. Gordon and Breach Science Publishers, The Netherlands.

Cohen-Addad, S. and Höhler, R. (2014). Rheology of foams and highly concentrated emulsions. Current Opinion in Colloid & Interface Science 19(6): 536-548.

Connelly, D. 2011, “High clay ores – a mineral processing nightmare”, In Australian Journal of Mining, July/ August edition: Mineral processing-Flotation and Separation, pp. 28-29.

Cutting, G.W., Watson, D., Whitehead, A., Barber, S., 1981. Froth structure in continuous flotation cells: relation to the prediction of plant performance from laboratory data using process models. International Journal of Mineral Processing 7, 347–369.

Cutting, G.W., Devenish, M., 1975. A Steady State Model of Froth Flotation Structures. SME AIME. (75-B-56).

Cruz, N., Peng, Y. J., Farrokhpay, S. and Bradshaw, D. (2013). Interactions of clay minerals in copper–gold flotation: Part 1 – Rheological properties of clay mineral suspensions in the presence of flotation reagents. Minerals Engineering 50-51: 30-37.

Deer, W.A., Howie, R.A. and Zussman, J. 1992, An introduction to rock forming minerals, Addison Wesley Longman Limited, England.

Dixon, J.B. and Weed, S.B. 1977, Minerals in soil environments, eds. Dixon, J.B. and Weed, S.B. Soil Science Society of America, Madison, Wisconsin, USA.

Edwards, C.R., Kipkie, W.B. and Agar, G.E. 1980, “The effect of slime coatings of the serpentine minerals, chrysotile and lizardite on pentlandite flotation”, International Journal of Mineral Processing, vol. 7, pp. 33-42.

Engelbrecht, J., Woodburn, E., 1975. The effects of froth height, aeration rate and gas precipitation on flotation. Journal of the Southern African Institute of Mining and Metallurgy 76, 125–132.

Falutsu, M., Dobby, G.S., 1989. Direct measurement of froth drop back and collection zone recovery in a laboratory flotation column, Minerals Engineering 2 (3), 377–386.

Farrokhpay, S. (2011). The significance of froth stability in mineral flotation - A review. Adv Colloid Interface Sci 166(1-2): 1-7.

Farrokhpay, S. (2012). The importance of rheology in mineral flotation: A review. Minerals Engineering 36-38: 272-278.

Farrokhpay, S. and Zanin, M. (2012). Synergic effect of collector and frother on froth stability and flotation recovery - an industrial case. 11th Mill Operators' Conference 2012, Hobart, Australia.

Farrokhpay, S., et al. (2016). "Behaviour of swelling clays versus non-swelling clays in flotation." Minerals Engineering **96-97**.

Farrokhpay, S., et al. (2018). Behavior of talc and mica in copper ore flotation. Applied Clay Science DOI: 10.1016/j.clay.2018.02.011

Fuerstenau, D., Gaudin, A., Miaw, H., 1958. Iron oxide slime coatings in flotation. Transactions of American Institute of Mining and Metallurgy, 211, 792–1783.

Forbes, E., Davey, K. J. and Smith, L. (2014). Decoupling rehology and slime coatings effect on the natural flotability of chalcopyrite in a clay-rich flotation pulp. Minerals Engineering 56: 136-144.

Finch, J.A., Dobby, G.S., 1990. Column Flotation. Pergamon Press: Oxford Pergamon Press, Oxford.

Genc, A. M., Kilickaplan, I. and Laskowski, J. S. (2012). Effect of pulp rheology on flotation of nickel sulphide ore with fibrous gangue particles. Canadian Metallurgical Quarterly 51(4): 368-375.

Gorain, B. K., Franzidis, J.-P. and Manlapig, E. V. (1995). Studies on impeller type, impeller speed and air flow rate in an industrial scale flotation cell--Part 1: Effect on bubble size distribution. Minerals Engineering 08: 615-635.

Gorain, B. K., Franzidis, J. P. and Manlapig, E. V. (1997). Studies on impeller type, impeller speed and air flow rate in an industrial scale flotation cell. Part 4: Effect of bubble surface area flux on flotation performance. Minerals Engineering 10(4): 367-379.

Gorain, B. K., Harris, M. C., Franzidis, J.-P. and Manlapig, E. V. (1998). The effect of froth residence time on the kinetics of flotation. Minerals Engineering 11(7): 627-638.

Hadler, K. and Cilliers, J. J. (2009). The relationship between the peak in air recovery and flotation bank performance. Minerals Engineering 22(5): 451-455.

Haffner, B., et al. (2015). "The drainage of foamy granular suspensions." Journal of Colloid and Interface Science **458**: 200-208.

Harvey, P. A., Nguyen, A. V., Jameson, G. J. and Evans, G. M. (2005). Influence of sodium dodecyl sulphate and Dowfroth frothers on froth stability. Minerals Engineering 18(3): 311-315.

Hemmings, C.E. (1980). An alternative viewpoint on flotation behaviour of ultrafine particles. Transactions of the Institute of Mining and Metallurgy, 89, C113.

Herzhaft, B. (1999). Rheology of aqueous foams - a literature review of some experimental works. Oil & Gas Science and Technology - Revue d'IFP Energies nouvelles 54: 587-596.

Ireland, P.M., 2009. Coalescence in a steady-state rising foam. Chemical Engineering Science 64 (23), 4866–4874.

Johansson, G. and Pugh, R. J. (1992). The influence of particle size and hydrophobicity on the stability of mineralized froths. International Journal of Mineral Processing 34(1): 1-21.

Johnson, N. W., 1972. The flotation behaviour of some chalcopyrite ores, PhD thesis, The University of Queensland, Brisbane, Australia.

Johnson, S.B., Franks, G.V., Scales, P.J., Boger, D.V. and Healy, T.W. 2000, "Surface chemistry–rheology relationships in concentrated mineral suspensions", International Journal of Mineral Processing, vol. 58, pp. 267-304.

Johnson, N. W., 2005. A review of the entrainment mechanism and its modelling in industrial flotation processes. Centenary of Flotation Symposium. Brisbane, Australia.

Jorjani, E., Barkhordar, H.R., Tayebi Khormani, M. and Fazeli, A. 2011, “Effects of aluminosilicate minerals on copper-molybdenum flotation from Sarcheshmeh porphyry ores”, Minerals Engineering, vol. 24, pp. 754-759.

Jowett, A., 1966. Gangue mineral contamination of froth. British Chemical Engineering 11, 330–333.

Kaptay, G., 2006. On the equation of the maximum capillary pressure induced by solid particles to stabilize emulsions and foams and on the emulsion stability diagrams. Colloids and Surfaces A: Physicochemical and Engineering Aspects. 282+283, 387–401.

Kawatra, S. K. and A. K. Bakshi (1996). "On-line measurement of viscosity and determination of flow types for mineral suspensions." International Journal of Mineral Processing 47(3): 275-283.

Kirjavainen, V. M., 1996. Review and analysis of factors controlling the mechanical flotation of gangue minerals. International Journal of Mineral Processing 46, 21–34.

Klein, B. and Pawlik, M. 2005, “Rheology modifiers for mineral suspensions”, Minerals and Metallurgical Processing, vol. 22, pp. 83-88.

Klein, C. and Dutrow, B. 2008, Manual of Mineral Science, 23rd edition, John Wiley and Sons Inc., New York, pp. 456-467; 519-534.

Klein, C. and Hurlbut, C. S. 1993, Manual of Mineralogy (after J.D. Dana), 21st edition .Wiley and Sons, New York.

Klimpel, R. R. (1999). The selection of wet grinding chemical additives based on slurry rheology control. Powder Technology 105: 430-435.

Konopacka, Z. and J. Drzymala. 2010. Types of particles recovery—water recovery entrainment plots useful in flotation research. Adsorption 16(4):313-320

Krieger, I. M. and Maron, S. H. (1952). Direct Determination of the Flow Curves of Non-Newtonian Fluids. Journal of Applied Physics **23**(1): 147.

Laskowski, J.S. and Pugh, J.S.1992, Chapter 4- Dispersion stability and dispersing agents in Colloid Chemistry in mineral processing, edited by Laskowski, J.S. and Ralston, J.S. Elsevier Science Publishers B.V., Amsterdam, Netherlands, pp. 151-161.

Lee, H. T., et al. (2005). "Particle and liquid dispersion in foams." Colloids and Surfaces A: Physicochemical and Engineering Aspects 263(1): 320-329.

Levine, S., Bowen, B. D. and Partridge, S. J. (1989). Stabilization of emulsions by fine particles I. Partitioning of particles between continuous phase and oil/water interface. Colloids and Surfaces 38(2): 325-343.

Li, C. An investigation of flotation froth rheology, PhD. Thesis. The University of Queensland., 2016

Ma, C., Zhao, P., Zhang, Y., Xueyong, C., Wang, S., 2014. Study on influence of gypsum on flotation process in the yechangping wolfram-molybdenum ore. J. China Min. 23, 117–119.

Maestro, A., Santini, E., Zabiegaj, D., Llamas, S., Ravera, F., Liggieri, L., Ortega, F., Rubio, R. G. and Guzman, E. (2015). Particle and Particle-Surfactant Mixtures at Fluid Interfaces: Assembly, Morphology, and Rheological Description. Advances in Condensed Matter Physics 2015: 1-17.

McFarlane, A., Bremmell, K. and Addai-Mensah, J. 2005, "Microstructure, rheology and dewatering behaviour of smectite dispersions during orthokinetic flocculation", Minerals Engineering, vol. 18, pp. 1173-1182.

Meloy, J. R., et al. (2007). "Geometric dispersion of unattached particles in foams." Colloids and Surfaces A: Physicochemical and Engineering Aspects 309(1): 246-253.

Mewis, J. and Wagner, N. J. (2012). Colloidal suspension rheology. Cambridge, New York, Cambridge University Press.

Mooney, M. (1951). "The viscosity of a concentrated suspension of spherical particles." Journal of Colloid Science 6(2): 162-170.

Moudgil, B. M. (1993). Correlation between froth viscosity and flotation efficiency Minerals and Metallurgical Processing 294: 24-27.

Moys, M. H. (1978). A Study of a Plug-Flow Model for Flotation Froth Behaviour. International Journal of Mineral Processing 5: 21-38.

Moys, M. H. (1984). Residence time distribution and mass transport in the froth phase of the flotation process. International Journal of Mineral Processing 13: 117-142.

Ndlovu, B., Forbes, E., Farrokhpay, S., Becker, M., Bradshaw, D. and Deglon, D. (2014). A preliminary rheological classification of phyllosilicate group minerals. Minerals Engineering 55: 190-200.

Ndlovu, B. (2013). The effect of phyllosilicate mineralogy and surface charge on the rheology of mineral slurries, Ph.D. thesis. University of Cape Town.

Neethling, S. J. and J. J. Cilliers (2002). "Solids motion in flowing froths." Chemical Engineering Science 57(4): 607-615.

Neethling, S. J. and J. J. Cilliers (2002). "The entrainment of gangue into a flotation froth." International Journal of Mineral Processing 64(2): 123-134.

Neethling, S. J. and Cilliers, J. J. (2009). The entrainment factor in froth flotation: Model for particle size and other operating parameter effects. International Journal of Mineral Processing 93: 141-148.

Ney, P. 1973, "Applied mineralogy in zeta potentials and flotability of minerals", Springer-Verlag, Vienna/ New York, vol. 6, pp. 214.

Nguyen, Q.D. and Boger, D.V. 1985, "Direct Yield Stress measurement with the vane rheometer", Journal of Rheology, vol. 29, pp. 335-347

Nguyen, A. V., Harvey, P. A. and Jameson, G. J. (2003). Influence of gas flow rate and frothers on water recovery in a froth column. Minerals Engineering 16(11): 1143-1147.

Nguyen, Q. D. and Boger, D. V. (1983). Yield Stress Measurement for Concentrated Suspensions. Journal of Rheology 27(4): 321-349.

Patra, P., Bhambhani, T., Nagaraj, D.R. and Somasundaran, P. 2010,"Effect of morphology of altered silicate minerals on metallurgical performance: transport of Mg silicates to the froth phase", In Proceedings of the 8th UBC-McGill-UA International Symposium on the fundamentals of mineral processing: rheology and processing of fine particles, editor. Pawlik, M. The Canadian Institute of Mining, Metallurgy and Petroleum, Vancouver, British Columbia, Canada, pp. 31-42.

Prestidge, C.A. 1997, "Rheological investigations of ultrafine galena particle slurries under flotation-related conditions", International Journal of Mineral Processing, vol. 51, pp. 241-254.

Rahman, R. M., Ata, S. and Jameson, G. J. (2013). Froth recovery measurements in an industrial flotation cell. Minerals Engineering **53**: 193-202.

Ross, V. E., 1989. Determination of the contributions by true flotation and entrainment during the flotation process. Int. Colloquium: Developments in Froth Flotation. Southern African Institute of Mining and Metallurgy, Gordon's Bay, South Africa.

Ross, V. E. (1990). A study of the froth phase in large-scale pyrite flotation cells. International Journal of Mineral Processing **30**: 117-142.

Ross, V. E. (1991). "An investigation of sub-processes in equilibrium froths (I): the mechanisms of detachment and drainage." International Journal of Mineral Processing 31(1): 37-50.

Ross, V. E. (1997). Particle-bubble attachment in flotation froths. Minerals Engineering **10**(7): 695-706.

Runge, K., Crosbie, R., Rivett, T., McMaster, J., 2010. An evaluation of froth recovery measurement techniques. XXV International Mineral Processing Congress, Brisbane, Australia, Brisbane, Australia.

Savassi, O. N. (1998). Direct estimation of the degree of entrainment and the froth recovery of attached particles in industrial flotation cells. PhD Thesis, The University of Queensland.

Savassi, O. N., Alexander, D. J., Johnson, N. W., Franzidis, J. P. and Manlapig, E. V. (1997). Measurement of froth recovery of attached particles in industrial flotation cells. The 6th Annual Mill Operators Conference, Kalgoorlie, Australia.

Somasundaran, P., Smith, E.L. and Harris, C.C. 1975, “Dewatering of phosphate slimes using coarse additives”, Mineral Processing Congress, Caligri, Italy, pp. 1301.

Somasundaran P., Processing Mineral Fines, Engineering and Mining Journal. 180: 64-68.

Somasundaran P., Roussev, R. Morphology of mineral fines produced under different grinding conditions Particulate Science and Technology. 4: 305-320. DOI: 10.1080/02726358608906461

Shabalala, N.Z.P., Harris, M., Leal Filho, L.S. and Deglon, D.A. 2011, “Effect of slurry rheology on gas dispersion in a pilot scale mechanical flotation cell”, Minerals Engineering, 24, pp.1448-1453.

Shaw, D. J. 1992, Introduction to colloid and surface chemistry, Butterworth Heinman.

Shi, F. N. and Napier-Munn, T. J. (1996). A model for slurry rheology. International Journal of Mineral Processing **47**: 103-123.

Shi, F. N. and Napier-Munn, T. J. (1999). Estimation of shear rates inside a ball mill. International Journal of Mineral Processing **57**: 167-183.

Shi, F. N. and Napier-Munn, T. J. (2002). Effects of slurry rheology on industrial grinding performance. International Journal of Mineral Processing **65**: 125-140.

Shi, F. N. and Zheng, X. F. (2003). The rheology of flotation froths. International Journal of Mineral Processing **69**(1-4): 115-128.

Smith, P. G., Warren, L. J., 1989. Entrainment of Particles into Flotation Froths. Mineral Processing and Extractive Metallurgy Review 5, 123–145.

Szatkowski, M., and Freyberger, W. L. (1985). Kinetics of flotation with fine bubbles. Transactions of the Institute of Mining and Metallurgy, 94(C61-C70).

Szatkowski, M., 1987. Factors influencing behavior of flotation froth. Transactions of the Institute of Mining and Metallurgy, Section C 96, 115–122 (September).

Trahar, W. J., 1981. A rational interpretation of the role of particle size in flotation. International Journal of Mineral Processing 8, 289–327.

Vasudevan, M., Bhambhani, T.,Nagaraj, D.R., Farinato, R., (2012) Impact of dissolved gangue species and fine colloidal matter in process water on flotation performance. Water in Mineral Processing-Proceedings of the 1st International Symposium, 247-259

Verbist, G.; Weaire, D., Kraynik, A., The foam drainage equation, Journal of Physics: Condensed Matter 8 (1996) 3715–3731.

Wang, L., et al. (2016). "Entrainment in froth flotation: The degree of entrainment and its contributing factors." Powder Technology 288: 202-211.

Warren, L. J., 1985. Determination of the contributions of true flotation and entrainment in batch flotation tests. International Journal of Mineral Processing 14, 33–44.

Weaire, D. (2008). The rheology of foam. Current Opinion in Colloid & Interface Science 13(3): 171-176.

West, J., 2011. Decreasing metal ore grades. Journal of Industrial Ecology 15, 165–168.

Wiese, J., Harris, P. and Bradshaw, D. 2011, "The effect of the reagent suite on froth stability in laboratory scale batch flotation tests", Minerals Engineering, vol. 24, pp. 995-1003.

Wiese, J., et al. (2015). "An investigation into the relationship between particle shape and entrainment." Minerals Engineering 83: 211-216.

Wiese, J. G. and C. T. O'Connor (2016). "An investigation into the relative role of particle size, particle shape and froth behaviour on the entrainment of chromite." International Journal of Mineral Processing 156: 127-133.

Wills, B., A., and Napier-Munn, T. J. (2006). Wills' Mineral Processing Technology: An introduction to the practical aspects of ore treatment and mineral recovery (7th ed.): Elsevier Ltd.

Yianatos, J., Contreras, F., 2010. Particle entrainment model for industrial flotation cells. Powder Technol. 197 (3), 260–267.

Yu, Y., Cheng, G., Ma, L., Huang, G., Wu, L., Xu, H., 2017. Effect of agitation on the interaction of coal and kaolinite in flotation. Powder Technology. 313, 122–128.

Zanin, M., Wightman, E., Grano, S.R., Franzidis, J.P., 2009. Quantifying contributions to froth stability in porphyry copper plants. International Journal of Mineral Processing 91 (1–2), 19–27.

Zhang, M. and Peng, Y. J. (2015). Effect of clay minerals on pulp rheology and the flotation of copper and gold minerals. Minerals Engineering 70: 8-13.

Zheng, X., Franzidis, J. P. and Manlapig, E. (2004a). Modelling of froth transportation in industrial flotation cell Part I. Development of froth transportation models for attached particles. Minerals Engineering 17: 981-988.

Zheng, X., Franzidis, J. P. and Manlapig, E. (2004b). Modelling of froth transportation in industrial flotation cells: Part I. Development of froth transportation models for attached particles. Minerals Engineering 17(9-10): 981-988.

Zheng, X., Franzidis, J.P., Johnson, N.W., 2006a. An evaluation of different models of water recovery in flotation. Miner. Eng. 19 (9), 871–882.

Zheng, X., Johnson, N.W., Franzidis, J.P., 2006b. Modelling of entrainment in industrial flotation cells: water recovery and degree of entrainment. Miner. Eng. 19 (11), 1191–1203.